CORRELATION OF FULL-SCALE DRAG PREDICTIONS WITH FLIGHT MEASUREMENTS ON THE C-141A AIRCRAFT - PHASE II, WIND TUNNEL TEST, ANALYSIS, AND PREDICTION TECHNIQUES

Volume 1 - Drag Predictions, Wind Tunnel Data Analysis and Correlation

by D. G. MacWilkinson, W. T. Blackerby, and J. H. Paterson

Prepared by
LOCKHEED-GEORGIA COMPANY
Marietta, Ga. 30063
for Langley Research Center

1. Report No. NASA CR-2333	2. Government Accession No.	3. Recipient's Catalog No.
4. Title and Subtitle CORRELATION OF FULL-SCALE DRAG PREDICTIONS WITH FLIGHT MEASUREMENTS ON THE C-141A AIRCRAFT - PHASE II, WIND TUNNEL TEST, ANALYSIS, AND PREDICTION TECHNIQUES. VOLUME 1 - DRAG PREDICTIONS, WIND TUNNEL DATA ANALYSIS AND CORRELATION		5. Report Date February 1974
		6. Performing Organization Code
7. Author(s) D. G. MacWilkinson, W. T. Blackerby, and J. H. Paterson		8. Performing Organization Report No. LG73ER0058
9. Performing Organization Name and Address Lockheed-Georgia Company Marietta, Georgia		10. Work Unit No. 501-06-09-01
		11. Contract or Grant No. NAS1-10045
12. Sponsoring Agency Name and Address National Aeronautics and Space Administration Washington, D. C.		13. Type of Report and Period Covered Contractor Report
		14. Sponsoring Agency Code

15. Supplementary Notes

This is one of two final reports.

16. Abstract

A research program has been conducted to determine the degree of cruise-drag correlation on the C-141A aircraft between predictions based on wind-tunnel test data, and flight test results. Volume 1 contains an analysis of wind-tunnel tests which were conducted in the NASA Langley 8-foot transonic wind tunnel on a 0.0275 scale C-141A model at Reynolds numbers up to 3.05 x 10⁶/MAC. Model support interference corrections were evaluated through a systematic series of tests, and the fully-corrected model data analyzed to provide details of the model component interference factors. Detailed estimates of profile drag were conducted, including a review of flat plate skin friction, airfoil and wing form drag.

It is shown that predicted, subcritical minimum profile drag of the complete configuration agrees within 0.7% of flight test data, through a wind-tunnel extrapolation method based on flat plate skin friction and component shape factors which, in turn, were based on average supervelocity calculations. The full-scale estimated roughness drag is, therefore, assumed to be substantially correct from this correlation. An alternative method of extrapolation, based on computed profile drag from a subsonic viscous theory, resulted in a prediction which was four percent lower than flight.

17. Key Words (Suggested by Author(s)) Wind-Tunnel/Flight Correlation Model Support Tares C-141A Drag Estimates Wind-Tunnel Model Extrapolation	18. Distribution Statement Unclassified-Unlimited		
19. Security Classif. (of this report) Unclassified	20. Security Classif. (of this page) Unclassified	21. No. of Pages 164	22. Price* Domestic, $4.75 Foreign, $7.25

CONTENTS

CORRELATION OF FULL-SCALE DRAG PREDICTIONS WITH FLIGHT MEASUREMENTS ON THE C-141A AIRCRAFT -PHASE II, WIND TUNNEL TEST, ANALYSIS, AND PREDICTION TECHNIQUES

VOLUME 1 – DRAG PREDICTIONS, WIND TUNNEL DATA ANALYSIS AND CORRELATION.

By D. G. MacWilkinson, W. T. Blackerby,
and J. H. Paterson

SUMMARY

A research program has been conducted to determine the degree of cruise – drag correlation on the C-141A aircraft between predictions based on wind tunnel test data, and flight test results.

Tests were conducted in the NASA Langley 8-foot transonic wind tunnel on a 0.0275 scale C-141A model at Reynolds numbers up to 3.05×10^6/MAC. Model support interference corrections were evaluated through a systematic series of tests, and the fully-corrected model data analyzed to provide details of the model component interference factors. Detailed estimates of profile drag were conducted, including a review of flat plate skin friction, airfoil and wing form drag.

It is shown that predicted, subcritical minimum profile drag of the complete configuration agrees within 0.7% of flight test data, through a wind tunnel-extrapolation method based on flat plate skin friction and component shape factors which, in turn, were based on average supervelocity calculations. This assumes shape factors to be independent of Reynolds number. The full-scale estimated roughness drag is, therefore, assumed to be substantially correct from this correlation. An alternative method of extrapolation resulted in a prediction which was four percent lower than flight, based on computed profile drag from a subsonic viscous theory.

The drag-rise characteristics of the model from tests with transition fixed near the wing leading-edge were, in general, more adverse than the flight data, amounting to a decrease in drag-rise Mach number of 0.01. Closer agreement was obtained over a limited lift coefficient range from model tests with transition located just ahead of the main shock on the wing.

The program demonstrates that, to achieve this degree of correlation, careful attention must be paid to subscale wind tunnel-testing techniques. Model support interference is shown to be significant, resulting in corrections which are both lift coefficient and Mach number dependent. A remaining unknown factor in the correlation is identified as the degree of scale effect on component interference and separation drag for this configuration.

INTRODUCTION

During the relatively short history of aeronautics, aircraft performance prediction techniques have advanced to a high degree of sophistication. These have developed in parallel with the necessity for stringent performance guarantees required by both commercial and military customers of modern aircraft. Drag prediction of the full-scale vehicle is therefore of vital importance in this process, particularly for transport configurations, where, for example, long range cruise efficiency on aircraft such as the C-5A can be converted to an equivalent of approximately 1000 pounds (454 Kgs) in payload per airframe drag count, or $C_D = 0.0001$.

Two approaches to full-scale drag prediction of a new project are generally in use by industry teams. The first relies on an accumulation of flight test data from various configurations. These are converted into generalized design charts of parametric form for use on the new configuration. Wind tunnel tests are used primarily to refine the design and provide incremental data to apply to the base configuration. Secondly, some design teams have additionally attempted to use absolute values of total drag measured at low wind tunnel Reynolds numbers by extrapolating the data to full scale using estimated changes in profile drag.

During the decade of the 1960s, some concern was expressed by industry on the validity of using scaled wind tunnel data after serious discrepancies were noted on a number of subsonic transport designs. These were due principally to a combination of inadequate wind tunnel testing techniques, and to erroneous scaling procedures. The quality of flight test measured data has also left much to be desired. One method which therefore requires a continuing effort to substantiate the methods of full-scale drag prediction is to correlate accurately-determined and fully-corrected wind tunnel measurements with flight test data.

The Lockheed-Georgia Company, through its work on the C-141A and C-5A programs, has been involved in extensive theoretical and experimental research on large high subsonic speed transports. Available flight test data on the C-141A were considered to be of sufficient quality and quantity to form the basis of a correlation study. The company was contracted by the NASA Langley Research Center to analyse these data in detail to provide the necessary basis. Results of this initial phase were completed and reported in reference 1. A contract for Phase II of the program was awarded to the company in July 1970 to conduct analytical studies on drag estimation, and to obtain a new set of fully-corrected wind tunnel data on a 0.0275 scale C-141A model from the Langley 8-foot transonic tunnel. Experience gained on the C-5A program in new transition fixing techniques and on model support systems were to be applied to the C-141A test in order to obtain the required degree of test data accuracy.

This report presents the results of the test program, data analysis and analytical and correlation studies in two volumes. Volume 1 gives summary results of drag estimation procedures and a detailed profile drag estimate for the C-141A configuration, the wind tunnel test data analysis and correlation with flight test data. Volume 2 gives details of the test facility, model configurations, program and procedures, and the basic data obtained from two phases of testing.

SYMBOLS

A	aspect ratio
A_{HL}	inlet highlight area
A_o	entry stream tube at infinity
C_D	drag coefficient
C_{D_P}	profile drag coefficient
C_f	average flat plate skin friction coefficient
C_L	lift coefficient
$C_{L_{A-h}}$	tail-off lift coefficient
C_{L_W}	wing lift coefficient
C_{L_T}	tail lift coefficient based on reference area S
$C_{L_{TRIM}}$	trimmed lift coefficient
C_M	pitching moment coefficient
C_p	pressure coefficient
M	Mach number
MAC	mean aerodynamic chord
$P_{T_{2.5}}/P_{AM}$	nozzle pressure ratio

R_N Reynolds number

S wing area

S_H horizontal tail area

b wing span

c chord

c_{avg} average chord, S/b

c_d section drag coefficient

c_{d_p} section profile drag coefficient

c_f local skin friction coefficient

c_ℓ section lift coefficient

e span efficiency factor = ratio elliptical/non-elliptical induced drag

i_H horizontal tail incidence

t/c thickness to chord ratio

x/c nondimensional chordwise station

α_{FRL} angle of attack of the fuselage reference line

δ^* boundary layer displacement thickness

ϵ downwash angle at the tail

η nondimensional semispan station

$\theta_{T.E.}$ boundary layer momentum thickness at the trailing edge

H_{TE} δ^*/θ_{TE}

DRAG PREDICTION STUDIES

Wind tunnel tests on complete model configurations are generally limited in existing transonic facilities to Reynolds numbers in the region of 6×10^6 per foot (19.7×10^6 per meter). For a typical installation, there is therefore a considerable Reynolds number 'gap' between wind tunnel data and full-scale conditions. Estimation of all drag components which are Reynolds number dependent is thus required with a high degree of accuracy in order ot use wind tunnel data for full-scale prediction. Treatment of interference and separation drag measured at wind tunnel scale is rendered difficult due to the limitations of current theoretical methods. For minimum profile drag estimation flat plate skin friction formulae and appropriate thickness or shape factors are in general use. These are supplemented, where possible, by theoretical methods so as to gain further insight into the scale effects phenomena.

Initially, a review is given of the accuracy of existing flat plate skin friction test data which form the background to the widely used empirical laws. The intent is to identify the sources of inaccuracy in the data which have an influence on the predicted scale effects in the drag estimation procedure. Secondly, profile drag estimation is studied, with the emphasis on comparing the methods to be used in extrapolating the C-141A test data to flight Reynolds numbers.

Review of Flat Plate Skin Friction

The literature contains a vast amount of experimental data on plane surfaces at incompressible speeds. The experiments range from the early water tank towing experiments to modern wind tunnel tests using sophisticated measuring techniques. A significant number of tests are historical, having been conducted prior to 1950 by towing planks through water, primarily for use in ship design. Many of the early experiments are characterized by inconsistencies in testing and measuring techniques. Nevertheless, empirical skin friction formulae derived from these data have received widespread acceptance by hydro- and aerodynamicists. This is particularly true of the Karman-Schoenherr formula developed in 1932 and still widely used by aeronautical engineers. Appendix A contains a detailed review of the background testing and data on which this law is based. Comments in this section of the report are of a summary nature and emphasize the principal findings of the study which have a direct influence on the objective of this program.

A selection of average skin friction test data from both water and air experiments is given in figure 1. Referring to the water experiments (open symbols) it is seen that the majority of test data pertain to Reynolds number values of less than 40 million. Those of Froude (ref. 2), and Gebers (ref. 3 and 4), exhibit particularly wide scatter of the order of 15 percent. The Froude tests were conducted with planks of rather large l/b (31.6), which is the probable reason why the data appear high above $R_N = 6$ million. For the Gebers data, however, mixed laminar/turbulent flow was responsible for the low values of C_f. In both cases, the exact magnitude of these errors is unknown.

6

The data obtained by Kempf, (ref. 6) in 1929, is an important set, since they represent the only results for very high Reynolds numbers up to approximately 500 million. Average values of skin friction were obtained from measurements of local shear forces on movable plates set into the bottom of a long iron pontoon.

In the process of examining how Kempf's data in figure 1 compared with other skin friction results, an integration of the measured local skin friction must be made to obtain the average skin friction. Schoenherr, (ref. 7), in presenting Kempf's data, chose to evaluate the local skin friction values by differentiating the equation for his mean line. Schoenherr's mean line equation is:

$$\frac{0.242}{(C_f)^{1/2}} = \log_{10}(R_N \cdot C_f) \tag{1}$$

Since

$$c_f = \frac{d}{dx}(x \cdot C_f) \tag{2}$$

Then

$$c_f = \frac{0.558\, C_f}{0.558 + 2(C_f)^{1/2}} \tag{3}$$

Since Schoenherr's approach would tend to bias the results toward his mean line equation, a separate graphical integration based on Kempf's actual observations was made in the present analysis. The article by Falkner, (ref. 8), provided an excellent source for Kempf's original measurements. A mean line was faired through Kempf's observations for the case of an iron plate rubbed smooth and an iron plate lacquered, waxed and polished; the latter case being closer to the desired smooth flat plate. The results are also shown in figure 1 and indicate close agreement with the Schoenherr-derived data. Although these approaches give consistent results, it should be noted that the original Kempf data contain several sources of error affecting the magnitude of c_f and the variation of c_f with R_N. These have been identified in the present study as wave-making resistance, length of run in the towing tank tests, and pontoon nose shape causing an unspecified length of laminar flow.

A selection of test data from wind tunnel experiments (solid symbols) is included in figure 1 for comparison with the earlier water tank results. These are attributed to Gibbons, (ref. 9), Wieselsberger, (ref. 10), Jones and Williams, (ref. 11), Smith and Walker, (ref. 12), and Winter and Gaudet, (ref. 13). The tests of Smith and Walker are significant, as they represent good precision techniques (see appendix) and cover a Reynolds number range from 2 to approximately 50 million. Average skin friction data computed from local shear on a floating element, and integrated friction drag by the momentum defect method, were obtained and both these data are shown. Both sets of data are in fairly good agreement

7

over the whole Reynolds number range, the scatter amounting to about $\pm 1 \frac{1}{2}\%$. In the range from 3 to 30 million, the magnitude of C_f is about $1 - 2$ percent lower than the Schoenherr mean line with a result that the slope of the $C_f - R_N$ curve is somewhat lower that that of the earlier results.

Data obtained by Winter and Gaudet in 1966 extended the Reynolds number range up to 200×10^6 from tests on the sidewall of the R.A.E. 8' x 8' tunnel. Although a major limitation in these tests was the lack of information about the boundary layer ahead of the single measuring point (see appendix), they appear to confirm the values of C_f measured by Kempf up to 225 million.

The principal observations to be noted from this survey are:

(1) Of the test data available, which form the historical background to Schoenherr's "mean line" analysis, significant scatter exists ($\pm 10\%$) particularly over the Reynolds number range up to 40 million, where the majority of experiments were conducted. This range coincides with that for skin friction estimation on aircraft components, such as wings.

(2) The basis for the variation of C_f with R_N in the range 100 to 300 million is solely from Kempf's water tank tests of 40 years ago. Beyond 300 million no basic data exist, although Schoenherr used Kempf's integrated results to extend these levels by his empirical formula to 450 million.

(3) There is a strong suggestion from study of the experimental techniques and resulting data that the magnitude of C_f in the Reynolds number range up to 30 million is conservative mainly due to three-dimensional effects. This is confirmed by the work of Hughes, and to some extent by the data of Smith and Walker. In the range of R_N from 3 million to 40 million, the maximum difference in scale effect between all data is of the order of 0.0002 in C_f. This would represent an uncertainty in predicting full-scale profile drag of the C-141A wing of approximately ± 0.0005 in C_D.

(4) Although the Schoenherr mean line is a good representation of existing test data, substantiation of low and very high ($R_N \approx 500$ million) Reynolds number skin friction is required by further research programs.

Airfoil Profile Drag

Summary of test data and methods - One of the critical factors recognized in the process of extrapolating model data to full scale is the degree of scale effect on the profile drag of the aircraft components. Since the wing and empennage drag represent approximately 60 percent of the total airplane profile drag for the C-141A configuration, and typically will account for about 70 percent of the total airplane scale effect on components, special attention is required for these lifting surfaces. This section gives the results of a series of studies on the profile drag of airfoils in two-dimensional incompressible flow. It is assumed that for attached flow conditions,

$$c_{d_p} = c_{d_{P_{min}}} + c_{d_{P_{c_\ell}}} \tag{4}$$

where $c_{d_{Pmin}}$ is the minimum profile drag occuring at some optimum c_ℓ, and $c_{d_{Pc_\ell}}$ is the lift-dependent profile drag which is primarily a function of airfoil thickness, camber, and trailing edge angle. Both terms are Reynolds number dependent as a result of viscous modifications to the boundary layer and pressure distribution. For the purposes of this analysis, the first term in equation 4 can be further defined as

$$c_{d_{P_{min}}} = (S.F.) \times 2 C_f \tag{5}$$

where C_f is the skin friction of the equivalent flat plate with zero pressure gradient for the same transition location as the airfoil. Thus, in this analysis (S.F.) or shape factor accounts for the sum total of all the thickness and viscosity effects inherent in the airfoil characteristics and manifested as form drag.

Hoerner, (ref. 14), has shown, from a collection of early data, that the shape factor for sections with maximum thickness at 30 percent chord can be represented empirically by

$$(S.F.) = 1 + 2(t/c) + 100(t/c)^4 \tag{6}$$

where the second term represents the drag due to increase in local velocity over the section, or supervelocity. This can be shown for incompressible attached flow conditions to be approximated by

$$(t/c) \equiv (\Delta v/v_o) = \left\{ (1 - C_p)^{1/2} - 1 \right\} \tag{7}$$

9

The third term in equation 6 represents the viscous pressure drag effects.

Figure 2 presents a summary of a preliminary study in which the objective was t determine the method which provided the most realistic estimation of airfoil form drag, as represented by the factor (S.F.) in equation 5. Where possible, sections of thickness close to 12 percent have been chosen, typical of the average values used on modern transport aircraft wings.

The experimental data shown in figure 2 are derived from two sources: (1) NACA (ref. 15), and (2) Lockheed-Georgia. The study has shown that most of the early NACA data are not ideally suited to accurate assessment of airfoil form drag. This is because the testing techniques employed favored either natural transition or the application of an oversized roughness band applied around the leading edge. Hence, in the first instance, correlation of measured drag with transition location was in most cases not possible and, in the second, accurate estimation of roughness drag was not attempted. For the present analysis, the NACA data have been corrected for an estimated roughness drag of ten counts, which is considered reasonable for the low range of lift coefficients existent in the data.

The Lockheed-Georgia data are taken from a research program on a series of airfoils derived from the basic C-5A section. Profile drag was measured by the wake traverse method. For the purposes of this analysis, it is sufficient to note that these airfoils generally conform to the principles of obtaining high loading characteristics by leading and trailing edge modifications, and therefore differ somewhat from earlier, more conventional types. These data have been corrected for eight counts of roughness drag.

In addition to the experimental data, a number of estimates for the C-141A section at 0.389 x semispan and airfoil 8 of the Lockheed series are included. These are:

(1) Supervelocity as in equation 7, using measured pressure data.

(2) Thwaites' incompressible formula (ref. 16).

(3) Lockheed-Georgia Subsonic Viscous Flow Program.

The method of Thwaites is based on a first-order approximation of the boundary layer, and was shown in related studies (ref. 17), to give good agreement with experiment for some of the NACA airfoil data.

The recently developed Lockheed program is based on the well known Squire and Young formula (ref. 18), which, when rederived from the compressible momentum equation and using the Squire and Young assumption for variation of shape factor H in the wake, can be written as:

$$c_d = 2\theta_{TE} \frac{}{c} \left(\frac{M_{TE}}{M_\infty} \right)^{\left(\frac{H_{TE} + 5}{2} \right)} \left(\frac{(1 + 0.2 M_\infty^2)}{(1 + 0.2 M_{TE}^2)} \right)^{\left(\frac{H_{TE} + 15}{4} \right)} \tag{8}$$

10

The large spread in value of (S.F.) at $t/c = .12$, indicated in figure 2, is a result of parametric differences in camber, maximum thickness location and aft loading which all contribute to form drag. No attempt has been made to correlate the data for these effects. Certain features of the various methods are, however, noted;

(1)   In general, experimental form drag for the 12 percent airfoils lies within the 30 to 50 percent range above flat plate skin friction.

(2)   Estimates by the average supervelocity method for airfoil 8 and the C-141A section, using measured pressure data, are 10 - 15 percent lower than experimental data. The empirical result from equation 8 also produces a low value of (S.F.).

(3)   The experimental results are generally in better agreement with the range of values given from the R.Ae.S Data Sheets (ref. 19).

The results for the C-141A section at $\eta = 0.389$ can be summarized as follows:

<div align="center">

C-141A $\eta = .389$

NACA   0012 $a_o = .8$ (mod), $t/c = .12$

</div>

Method	(S.F.)
Hoerner	1.28
Thwaites	1.39
Av. Supervelocity	1.17
Lockheed Theory	1.32
Experiment (ref. 20)	1.34

The values of (S.F.) from experiment, Thwaites and Lockheed theory agree within five percent, whereas the value predicted by the mean supervelocity process is 13 percent lower than the average of these figures. It is concluded that if full account is to be taken of airfoil form drag from viscous effects in attached flow conditions, the boundary layer methods typified by the Lockheed theory should be used.

<u>Correlation of theory and experiment for two-dimensional airfoils</u> - The state-of-the art review presented in the previous section is now followed by the results of a correlation of $c_{d_{Pmin}}$ from experiment and Lockheed theory on selected airfoils.

Figure 3 presents a selection of measured and calculated airfoil section drag with transition fixed on both upper and lower surfaces. The data for Lockheed airfoils 3 and 8 have been selected because their geometrical characteristics are closer to the conventional types as, for example, are employed on the C-141A wing. In general, these results show that the theory predicts $c_{d_{pmin}}$ within about four percent for the selected comparisons. The value of c_ℓ for $c_{d_{pmin}}$ agrees closely with experiment, but the measured data exhibit larger values of the lift-dependent drag term $c_{d_{Pc_\ell}}$.

Uncertainties in the validity of the test data at higher values of c_ℓ, together with unknown roughness effects and transition movement, may be responsible for these discrepancies. Also, the test data drag increases at high c_ℓ due to supersonic flow onset. Emphasis is therefore placed only on the correlation of $c_{d_{Pmin}}$.

The validity of the calculation method to predict Reynolds number effects on profile drag is shown in figure 4. This comparison is limited to a range of Reynolds numbers up to 7.5 million, due to the sparse amount of good quality test data at higher Reynolds numbers. The transition-free results given in figure 4(b) illustrate that the relative movements of transition on upper and lower surfaces are in good agreement between theory and experiment, indicating that the boundary layer characteristics are predicted satisfactorily. For the transition-fixed comparison, the slight leveling-off in $c_{d_{Pmin}}$ of the test data may be indicative of an oversizing roughness for this Reynolds number range.

Figure 5 compares $c_{d_{Pmin}}$ from theory and experiment for 17 airfoils over a range of speeds from Mach = 0.20 to 0.70, and Reynolds numbers from 3.3×10^6 to 6.5×10^6. Generally, the theory underpredicts measured $c_{d_{Pmin}}$ for 80 percent of the test points; this is qualitatively the same result obtained by the more extensive analysis of Cebeci and Smith (ref. 21). The present work, however, has attempted a correlation of transition-fixed data only, and the scope has been limited due to the overall objectives of this program.

To summarize the analysis of profile drag on two-dimensional airfoils, existing empirical methods are shown to be inadequate and do not account for the full magnitude of the viscous pressure drag on modern airfoils. For similar reasons, the average super-velocity around the airfoil is only a first order approximation and is shown to underpredict $c_{d_{Pmin}}$ by approximately 13 percent. An analysis of 17 airfoils shows that the Lockheed-Georgia

iscous Flow Theory generally predicts $c_{d_{P_{min}}}$ to within five percent for data with transition fixed at low Mach number.

C-141A Drag Estimate

For estimation purposes, the total drag coefficient of the trimmed, rigid aircraft can be written as:

$$C_D = (\Sigma C_{D_{P_{min}}}) + C_{D_i} + C_{D_{trim}} + C_{D_{P_{C_L}}} + C_{D_C} + C_{D_{INT.}} + C_{D_R} \qquad (9)$$

where

$(\Sigma C_{D_{P_{min}}})$ = Summation of the minimum profile drag of the individual aircraft components, for smooth turbulent attached flow.

C_{D_i} = Wing vortex induced drag at a given wing lift coefficient corresponding to the spanwise distribution of lift, and is the net effect of elliptic and non-elliptic contributions.

$C_{D_{trim}}$ = Drag required to trim the aircraft about its center of gravity.

$C_{D_{P_{C_L}}}$ = Net aircraft lift-dependent profile drag, including major contributions from the wing and fuselage, and other components.

C_{D_C} = Compressibility Drag; this includes subcritical drag creep, wave drag, and shock-induced separation drag.

$C_{D_{INT}}$ = Drag due to interference between components.

C_{D_R} = Drag due to surface distributed roughness, steps, gaps, and significant protuberances.

A description of the estimation of wing vortex drag C_{D_i} and component minimum profile drag now follows.

<u>Wing vortex-induced drag</u>, C_{D_i} - The derivation of wing vortex-induced drag and the corresponding span efficiency factor is outlined in the previous study on flight test data

(ref. 1). Wing pressure data from wind tunnel tests, (ref. 22), on the C-141A .0275 scale model have been analyzed to give an indication of the effects of transition fixing and test Reynolds number on the span load distributions. These earlier tests were conducted with transition fixed on the wing by a four percent wide band of densely applied carborundum of nominal size 0.0020 in. (0.0051 cm), starting at five percent chord. It is not clear to what extent this technique "overfixes" transition. The data indicate, however, that the effect of roughness on the <u>shape</u> of the span load distribution at a given Reynolds number is insignificant.

Figures 6(a) and 6(b) present span load distributions showing the effects of Reynolds number over a range from 1.45×10^6/MAC to 4.9×10^6/MAC. A comparison of wind tunnel data at the same two Reynolds numbers and a flight test span load distribution is given in figure 7, at $C_L = 0.40$, $M = 0.700$. The flight test data are taken from reference 1, and are the "equivalent rigid" data used in that analysis. This shows good agreement between wind tunnel and flight test results outboard of $\eta = 0.5$. The inboard panel local load appears to be sensitive to scale effects. However, the computed values of span efficiency are shown from calculations to vary only one percent between all three conditions.

The computed values of span efficiency factor from the wind tunnel at $M = 0.700$ are shown in figure 8. The resulting values of 'e' agree closely with those computed from the flight test data analysis. Thus, for evaluation of profile drag, the data given in figure 34(b) of reference 1 are used.

The results of a brief study of flexibility effects on the 0.0275 scale model wing under typical wind tunnel load are summarized in figure 9. The maximum aeroelastic twist is 0.22 degrees at $M = 0.775$ and a dynamic pressure of 6.8 psi (46.9×10^3 N/m²). (Subsequent wind tunnel tests were conducted at 5.8 psi (40×10^3 N/m²). A similar analysis in reference 1 on the full-scale aircraft wing produced a maximum tip deflection of two degrees under high-load conditions. The effects of wing distortion on the wind tunnel model are regarded as insignificant, since the calculated effect on wing span efficiency is less than one percent or 0.5 drag counts ($\Delta C_D = 0.00005$) at cruise conditions.

<u>Component minimum profile drag estimates</u> – Wing: Four sources of profile drag estimation have been evaluated to determine the variation in predicted full scale drag of this component.

A. Use of the Karman-Schoenherr flat plate skin friction formula with shape factors derived from the super-velocity method using wind tunnel pressure data, and a wing strip analysis technique.

B. Predictions from the original C-141A Aerodynamic Substantiating Data Report (ref. 23), which were based on the Karman-Schoenherr formula and a Reynolds number based on wing MAC, and shape factors from the super-velocity method.

C. Use of a strip analysis and the Lockheed viscous theory to predict wing profile drag, from the Squire and Young formula, with pressure distributions from wind tunnel tests.

14

D. Calculation of the wing drag as in Method C, but using wing geometrical ordinates.

Examples of the spanwise variation of minimum profile drag from Methods A and C are given in figures 10 and 11. Method A provides a shape factor which is given as

$$
(S.F.) = \frac{\int_{.084}^{1.0} c_{f_{local}} \cdot (S.F.)_{local} \cdot {}^{c}/c_{avg} \, d\eta}{\int_{.084}^{1.0} c_{f_{local}} \cdot {}^{c}/c_{avg} \cdot d\eta}
\tag{10}
$$

The denominator of this equation represents the average wing skin friction for a planform of zero thickness based on the Karman-Schoenherr line and referred to gross wing area.

The principal results are summarized in figure 12, giving values of $C_{DP_{min}}$ versus Reynolds number at model transition for the four methods under review. Considerable variations in predicted minimum profile drag are shown. At $R_N = 3 \times 10^6/\text{MAC}$, this amounts to $\Delta C_D = 0.0021$ between the methods. The result from method A, the strip analysis using super-velocity shape factors, indicates low values consistent with the results of the airfoil analysis, and it further suggests that total wing form drag is underpredicted using this approach. The data from method C was computed from available wind tunnel pressures over a limited Reynolds number range of up to $4 \times 10^6/\text{MAC}$. In order to estimate scale effects beyond this range, the results from method D (predictions based on ordinates) were used. For this purpose, the data of figure 12 were converted to representative shape factors using a reference value of wing drag based on MAC Reynolds number, and shown in figure 13. These results show that both methods using the Lockheed viscous theory predict increasing shape factors, or form drag, at low Reynolds numbers. It was shown from the analysis of method D that this was primarily due to high pressure drag over the inboard panel of the wing. Evaluation of the boundary layer parameters at low R_N suggested that an increasing boundary layer thickness was leading to high form drag in this region. At high Reynolds numbers, method D gives values essentially constant as assumed by the standard method, (B). The extrapolation of method C data was based on the ratio

15

$$\frac{\left\{\left[\dfrac{C_{D_{P\ min}}}{C_{D_{\ MAC}}}\right] - 1\right\}_{R_N}}{\left\{\left[\dfrac{C_{D_{P\ min}}}{C_{D_{\ MAC}}}\right] - 1\right\}_{R_N = 4 \times 10^6/MAC}} \qquad \text{for method D}$$

The scale effects resulting from these different methods are summarized by comparing increments due to Reynolds number between $R_N = 3.05 \times 10^6/MAC$ and $35 \times 10^6/MAC$.

Method	ΔC_D
A	0.0022
B	0.0028
C	0.00305
D	0.00315

The increase in Reynolds number correction from use of viscous theory, (C), rather than the standard method, (B), amounts to $\Delta C_D = 0.00025$ for the wing. The estimated total effect for the complete configuration is calculated to be 0.0005 in ΔC_D.

Results from the viscous theory strip analysis technique, method C, to estimate wing total C_{DP} as a function C_L are shown in figure 14. The variation of C_{DP} with C_L for assumed attached flow conditions is seen to reduce with increasing Reynolds number. This effect is used in the subsequent scale corrections of the model data for correlation with flight results.

Wing-fuselage intersection fairing: The estimated profile drag for the wing-fuselage fairing inboard of $\eta = .084$ was based on an assumed shape factor of 1.20 from examination of wind tunnel pressure data.

Fuselage: In accordance with the definition of profile drag for estimation purposes, the fuselage term is defined as

$$C_{D_{P_{FUS}}} = C_{D_{P_{min_{FUS}}}} + C_{D_{V_{FUS}}} \qquad (12)$$

where

$$C_{D_{P_{min_{FUS}}}} = C_f \cdot \times (S.F.)$$

The first term represents the minimum profile drag of the equivalent body of revolution of the same cross-sectional area. This includes the effects of super-velocity around the body, and the form drag resulting from boundary layer growth toward the afterbody. The second term in equation (12) represents excess pressure drag due to deviations from the basic body of revolution. The major contribution to non-linear drag-due-to-lift of the fuselage, that due to afterbody upsweep, is included in this term.

The profile drag of generalized bodies of revolution was calculated by Young (ref. 24), and reasonable agreement demonstrated with experiment for bodies without parallel portions for Reynolds numbers on body length of up to 11×10^6. These data are summarized in figure 15, showing agreement between theory and experiment of within five percent. This method forms the basis of existing design charts (ref. 25), giving values of C_{D_P} as a function of d_{max}/l and Reynolds numbers up to 200×10^6. For use of these data in estimating C_{D_P} the effective fineness ratio is defined in the present analysis as

$$\frac{d_{max}}{l} = \frac{d_{max}}{l_A + l_C + 2d_{max}} \qquad (13)$$

where l_A = length of forebody and l_C = length of afterbody.

Transport fuselages typified by the C-141A configuration are often radical departures from the ideal body of revolution. Four types have been analyzed and $C_{D_{P_{min_{FUS}}}}$ estimated for each configuration using the charts given in reference 25, and the definition given in equation (13). The results are presented in figure 16 as effective shape factor $C_{D_{P_{min_{FUS}}}}/C_f$ (= S.F.). Transports 1 and 3 are typical commercial types, and 2 (C-141A configuration) and 4 represent cargo configurations with some degree of upsweep on the rear fuselage. All four designs have a parallel section B which varies in proportion to the total fuselage length, $l_A + l_B + l_C$. The estimated shape factors appear to be essentially constant over the Reynolds number range up to 200×10^6, although it should be noted that scale effects at these high Reynolds numbers have not been well substantiated due to lack of experimental data.

Measured data are also given in figure 16 (solid symbols). The points representing the two cargo transports (2 and 4) show good agreement with theory, although the validity of these data from early tests is in question because transition was not fixed on the fuselage and no corrections were made for sting support interference. Further, excess drag due to upsweep is not apparent from these comparisons, although some is anticipated even at cruise angle of attack. The single flight test point for transport 1, derived from boundary layer measurements (ref. 26), is seen to be approximately 3.5% higher than predictions; however, this was obtained at M = 0.86 and probably includes compressibility and roughness drag.

The results for the C-141A show that the profile drag of the equivalent body of revolution, $C_{D_{P_{min_{FUS}}}}$, is approximately ten percent above flat plate skin friction.

Wheel-well fairings: This component was reduced to two bodies of revolution, with the equivalent diameter d_{max} based on a circle with area equal to the maximum cross-sectional area of the fairing. The boundary layer was assumed to grow from zero at the leading-edge of the fairings, although the location on the fuselage will actually result in a boundary layer which is somewhat thicker than estimated. However, since the effects of pressure gradients on the boundary layer growth are unknown, the present method is assumed to be adequate.

Summary curves of the estimated $C_{D_{P_{min}}}$ for fuselage and wheel-well fairings are given in figure 17.

Pylons: Profile drag of the pylons was estimated using pressure data and the viscous theory described earlier, identified as method C.

External profile drag - isolated nacelle: The model nacelle profile drag was treated as a conventional body of revolution with an effective fineness ratio

$$\frac{d}{l} = \frac{(d^2_{max} - d^2_{jet})^{1/2}}{l} \tag{14}$$

where d_{max} = maximum external diameter and d_{jet} = diameter of the stream tube contained by the internal bore of the flow-thru nacelle. The isolated nacelle skin friction drag was thus estimated using existing charts (ref. 24), for the equivalent body of revolution.

Internal drag, flow-thru nacelle: The internal skin friction drag of the model nacelles was required in order to correct model wind tunnel data before correlation with full-scale data. A computer program has recently been developed at Lockheed-Georgia, to calculate internal drag of flow-thru nacelle configurations. In order to substantiate the validity of this method, it was necessary to correlate theory with experiment from a series of tests on a flow-thru nacelle representing a high by-pass ratio fan cowling. The Reynolds

18

number of these tests was 4×10^6, and the nacelle A_o/A_{HL} was 0.65. The comparison is given in figure 18, where it is shown that agreement of theory with experiment is within 1 to 1 1/2%, or 0.1 drag counts, at typical cruise angles of attack. The estimation of the C-141A 0.0275 scale-model nacelle internal drag was based on this method which, as shown in figure 18, gives good agreement with experiment. Figures 19(a) and 19(b) give the total estimated internal drag for the model transition at $x/1 = 0.14$ as a function of Reynolds number and angle of attack for Mach numbers ≥ 0.700. Although these Mach numbers represent the range of interest in the present program for correlation of cruise data, figure 19 shows that the maximum variation in ΔC_{D_p} between $M = 0.700$ and 0.825 is only 0.25 aircraft drag counts at $\alpha_{FRL} = 1°$, $R_N = 6 \times 10^6$.

Nacelle forebody additive drag: The requirement for a forebody additive drag correction on the C-141A was examined using test results from a high-speed, parametric cowl test program, conducted as a part of the C-5A nacelle development. The C-141A forebody design was selected purely from extrapolated, low-speed test results and later high-speed testing showed it to be a fairly conservative configuration. Based on the referenced data, the C-141A forebody should have a drag-divergence Mach number in excess of 0.85 with a critical mass flow ratio 7.5 percent below design. At lower Mach numbers, the allowable mass flow margin can be shown to increase. Thus, with the degree of conservatism present, no additive drag correction is necessary anywhere within the normal range of cruise operation. It is also of importance to note that the mass flow ratio of the model flow-thru nacelle is matched closely to the full-scale engine value, and for a normal cruise range it is approximately 0.60.

Nacelle afterbody pressure drag: The full scale afterbody pressure drag correction was shown to be a function of fan pressure ratio and Mach number (ref. 27). These data were obtained from C-141A development test results (ref. 28), and represent the pressure drag on the nacelle in isolation. A recently-published generalized correlation of afterbody data (ref. 29), has led to a brief study to substantiate the previous data.

Figure 20 shows a plot of both model and full-scale drag characteristics, and indicates the drag decrement due to shortening the model afterbody and opening up the model exit to permit inlet flow matching. Although the flow-through nacelle data are seen to be relatively insensitive to Mach number between $M = 0.600$ and 0.900, the full-scale estimates vary by a factor of two in this range. This variation is, effectively, that applied to the engine thrust level, so that to achieve compatibility of model and full-scale drag, the corresponding model estimate must be deducted from the wind tunnel measurements. The drag level calculated from the method given in reference 29 agrees closely with both model and full-scale data at $M = 0.900$, as shown in figure 20. Substantiation of the trends below this Mach number is not possible from the new method, since the data base correlation is entirely from Mach 0.900 data.

The data presented in figure 20 therefore represent the levels of pressure drag which have to be deducted from the model data. Wing-nacelle interference effects, which

will result in a significant variation in pressure drag with angle of attack, are assumed to be inherent in both model and full-scale aircraft drag levels, and, furthermore, are taken to be independent of scale effect.

Empennage – The procedure for calculating profile drag of the vertical and horizontal tail surfaces was based on method C, using the wind tunnel pressure data available from tests reported in Reference 22. Examples of the vertical and horizontal tail pressures are given on figures 21 and 22. The Lockheed theory was again used, as in the case of the wing calculation, to calculate boundary layer characteristics from measured pressure distributions. Local drag coefficients were integrated across the span to give overall profile drag.

Empennage bullet: The profile drag of the bullet was estimated using the method of reference 25, with the fineness ratio $d_{max}/1 = 0.146$ for the equivalent body of revolution.

Summary curves of the pylon-nacelles and empennage minimum profile drag estimates are presented in figure 23. Table 1 summarizes the component minimum profile drag estimates.
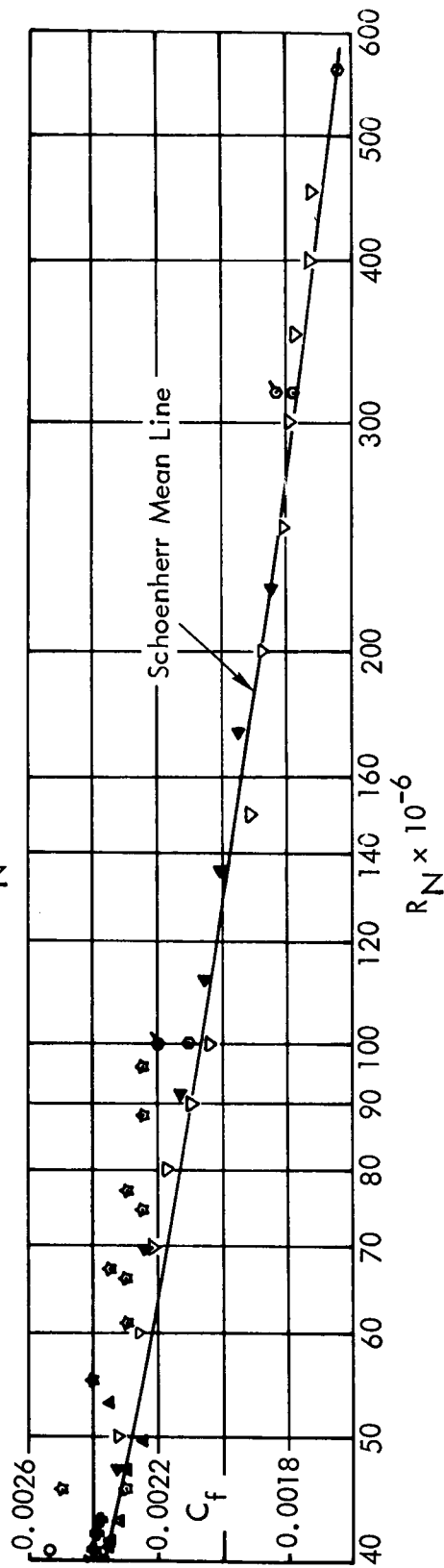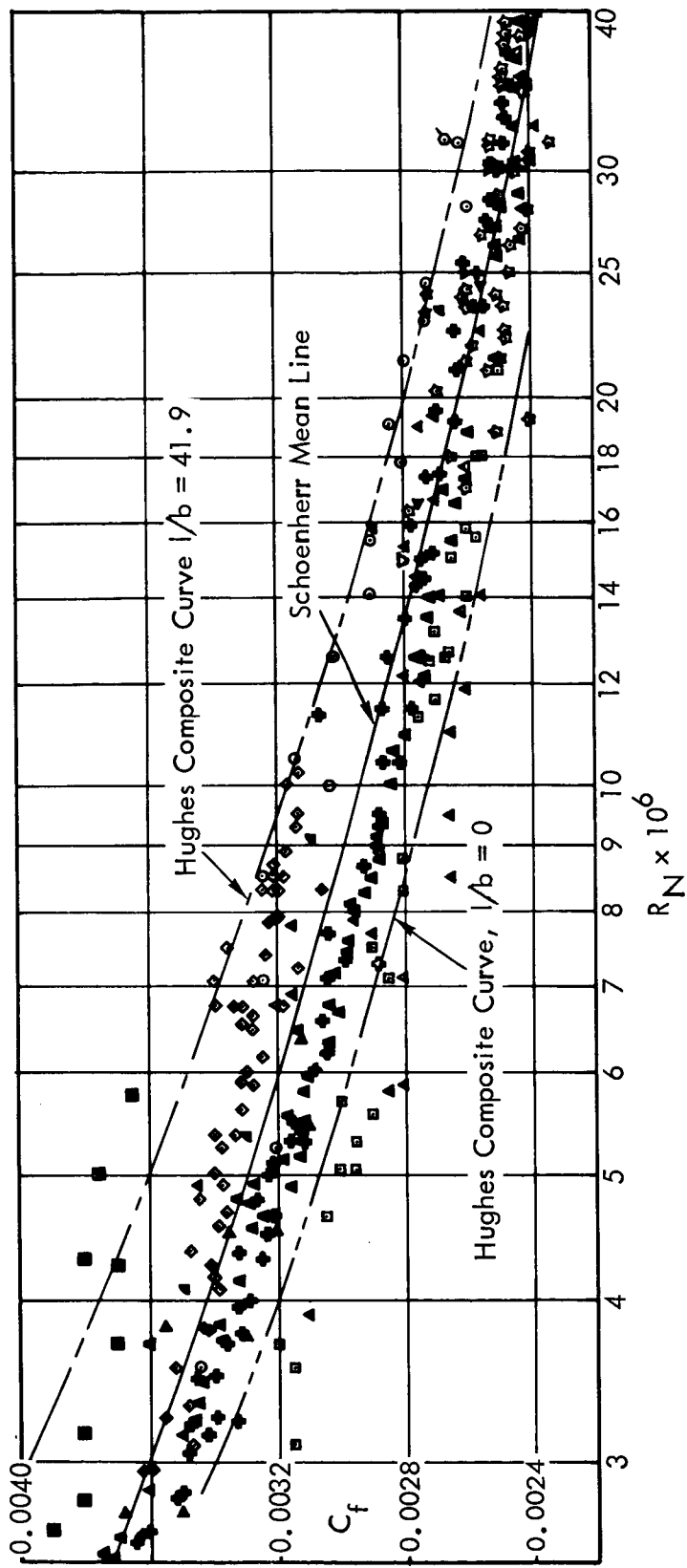
Figure 1(a). Summary of Experimental Research on Flat Plate Skin Friction. Incompressible Speeds.

21

Investigator/Description	Symbol

Tests in Water

Froude, 1872 -- 16, 28, and 50 foot varnished planks. ⊙

Gebers, 1908 -- 160, 360, 460, 652 cm. planks. ⊡

Froude Tank, NPL, 1915, -- 3, 8, 16 foot planks. ◈

Gebers, 1919 -- 125, 250, 500, 750, 1000 cm. planks. △

Kempf, 1929 -- Various plates, integrated by Schoenherr ▽
using the Schoenherr mean line.

Kempf, 1929 -- Basic local c_f data for iron plate, ◎
lacquered, waxed and polished; integrated
graphically.

Kempf, 1929 -- Basic local c_f data for iron plate rubbed ⬠
smooth, integrated graphically.

Washington Unpublished, 1932 -- 20, 30, 40, ✴
80 foot planks.

Hughes, 1952 -- NPL Tank; Composite curve for — -- —
$1/b = 0$.

Hughes, 1952 -- NPL Tank; Composite curve for — – —
$1/b = 41.9$

Tests in Air

Gibbons, 1915 -- 9.5 foot glass plate. ▶

Wieselsberger, 1925 -- 50, 100, 150, 200 cm. planes. ■

Jones & Williams, 1937, -- CAT, 2 foot plank. ◀

Smith & Walker, 1959 -- Flat plate, momentum ▲
defect method.

Smith & Walker, 1959 -- Flat plate, floating element ✚
method.

Winter & Gaudet, 1966 -- Sidewall of 8 x 8 foot ◀
RAE tunnel.

Figure 1(b). Summary of Experimental Research on Flat
Plate Skin Friction.
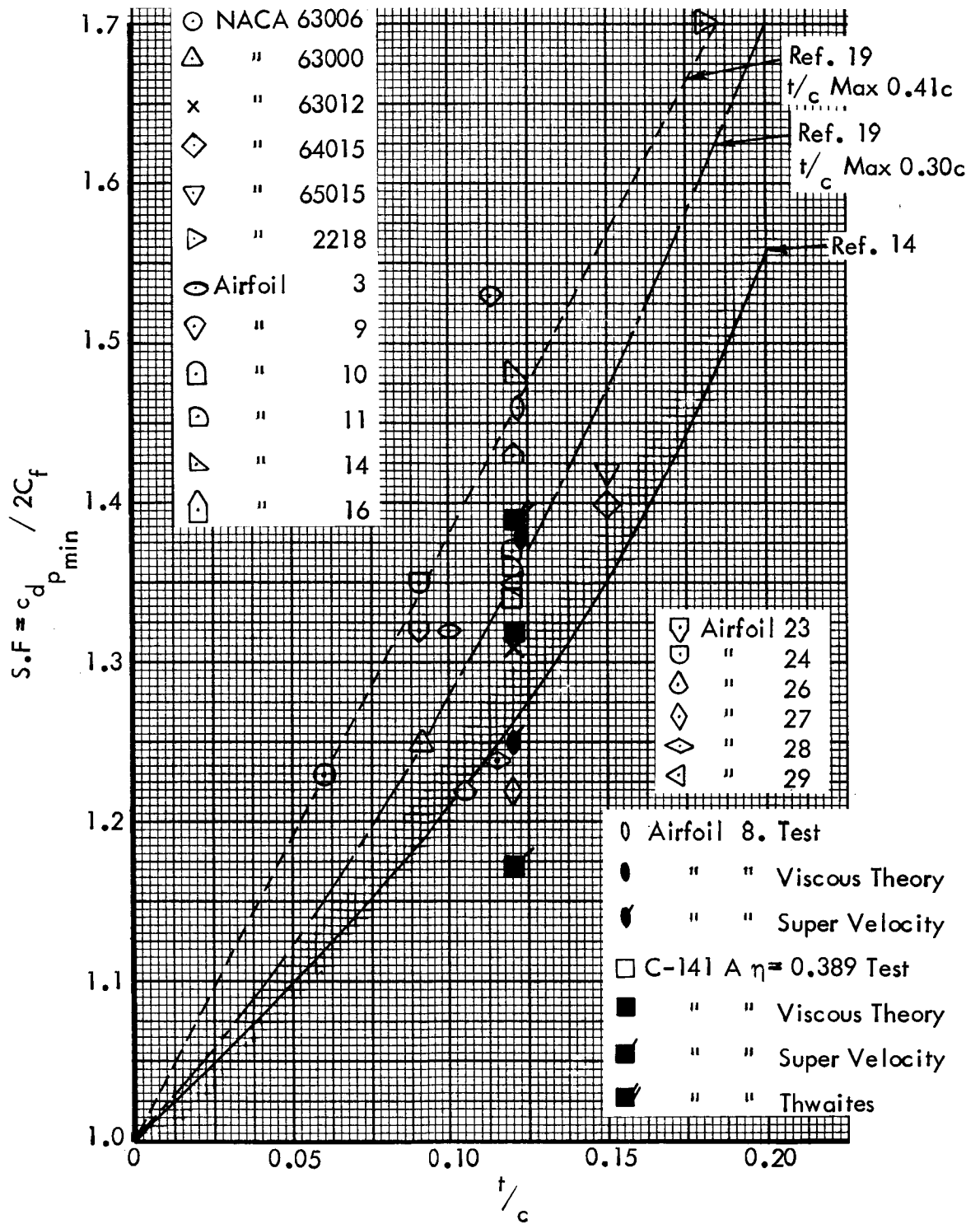
Figure 2.   Airfoil Shape Factors
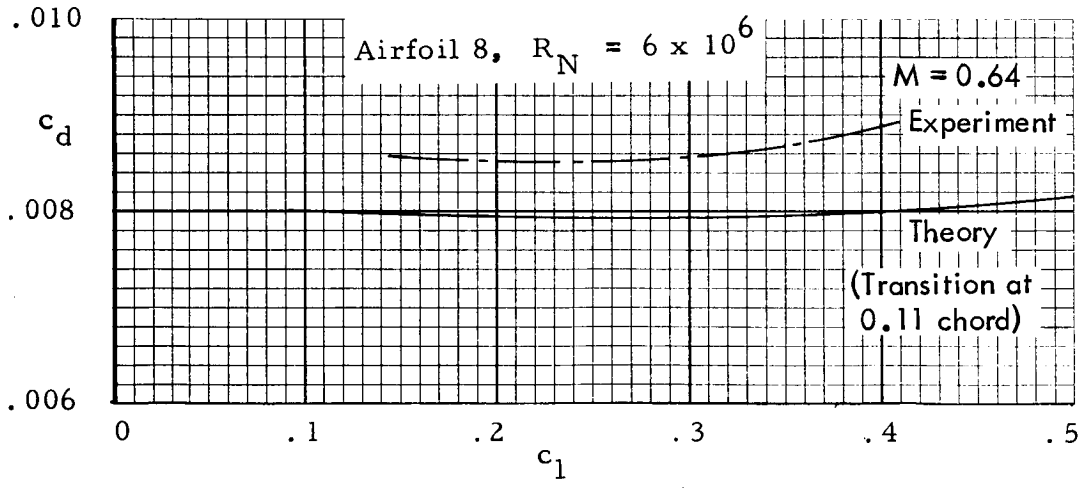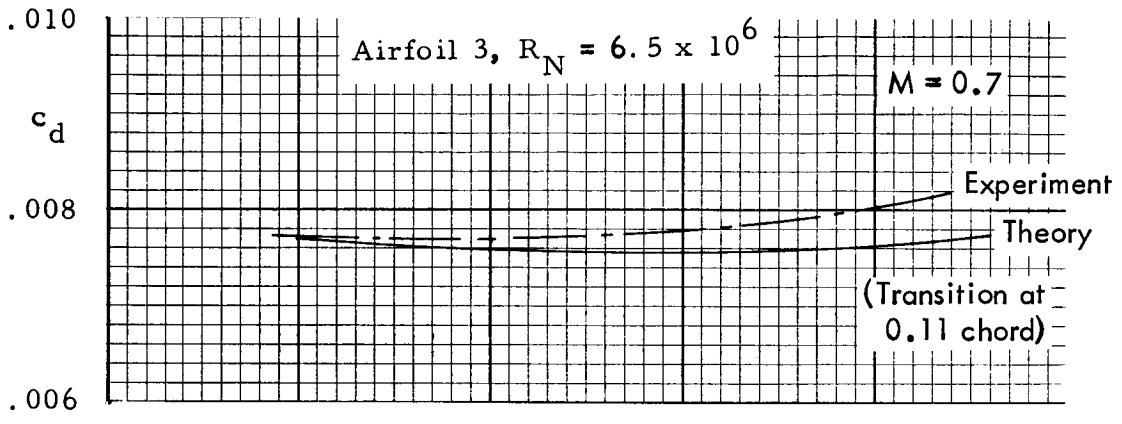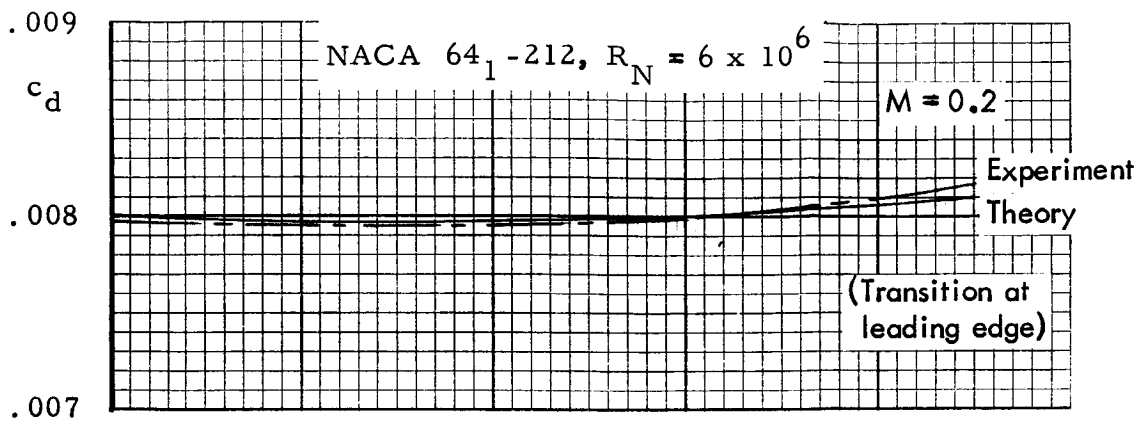
Figure 3(a). Airfoil Profile Drag. Comparison of Theory With
Experiment, Transition Fixed. Experimental
Data Corrected for Grit Drag.

NACA 66-209
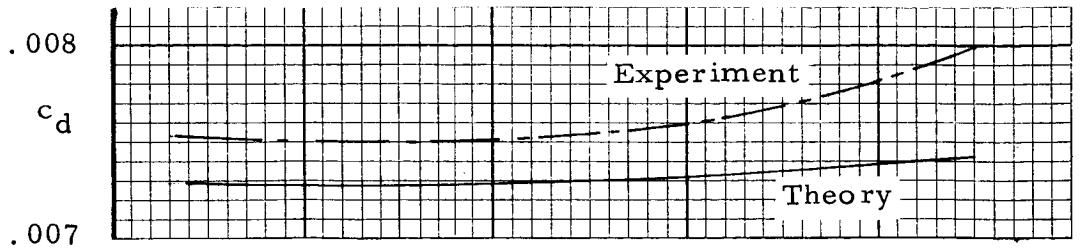
NACA 64_2-215
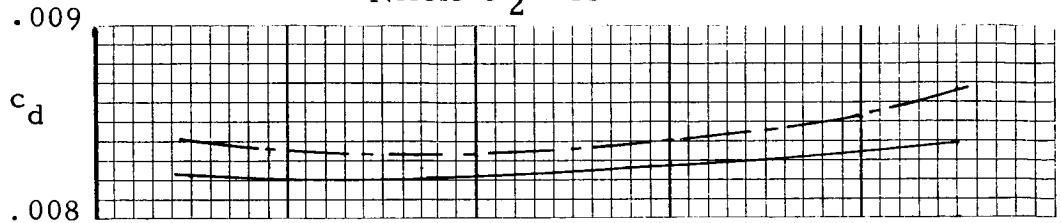
NACA 64-210
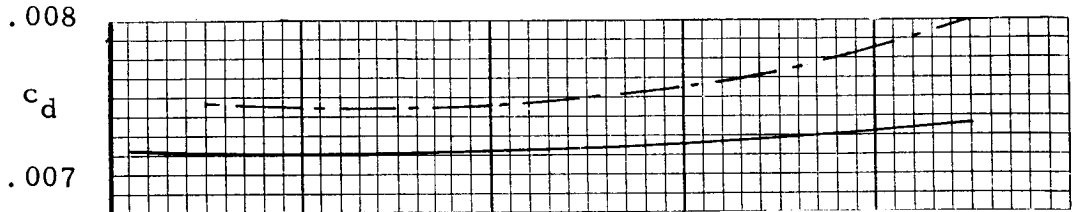
NACA 66_1-212
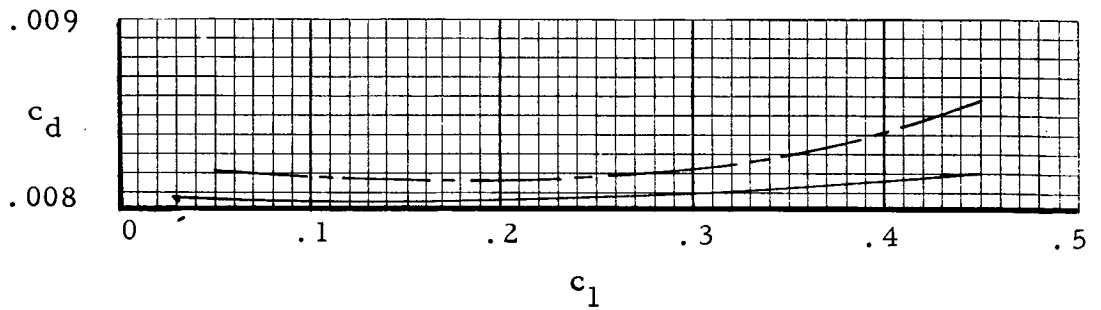
Figure 3(b). Airfoil Profile Drag. Comparison of Theory With Experiment, Transition Fixed. Transition at The Leading Edge, $M = 0.2$, $R_N = 6 \times 10^6$.
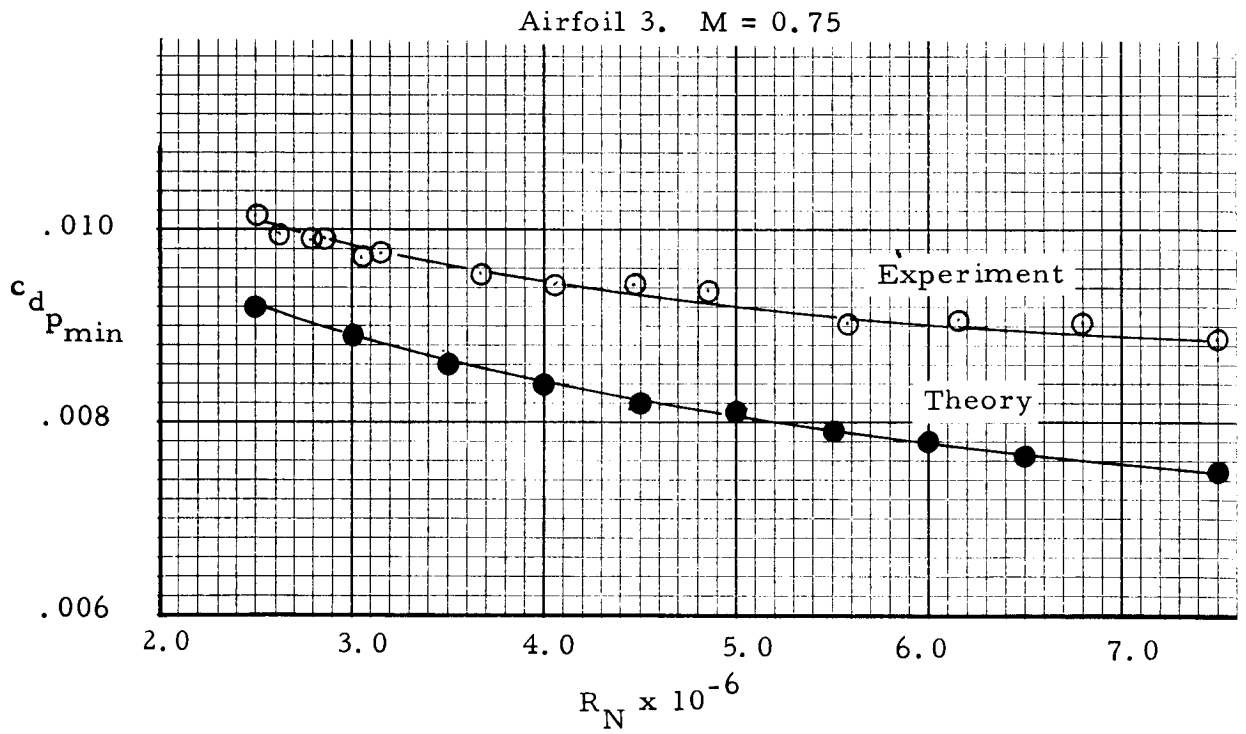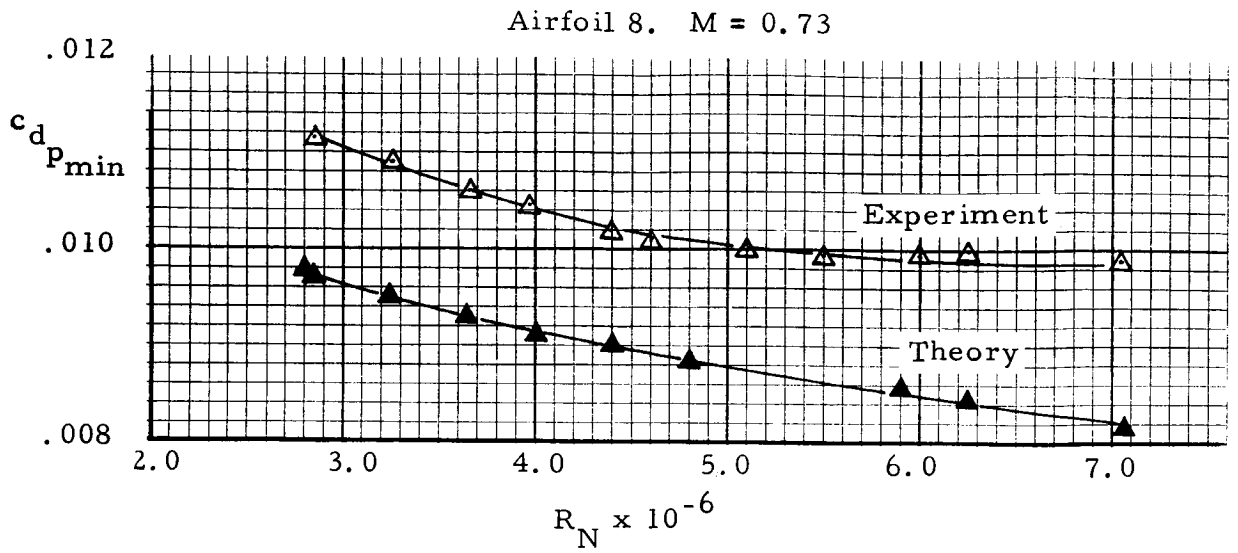
Figure 4(a). Reynolds Number Effects on Minimum Profile Drag.
Comparison of Theory and Experiment for 2-D Airfoils,
Transition Fixed at 0.11 chord. No Grit Drag Correction.

M = 0.2, Transition Free
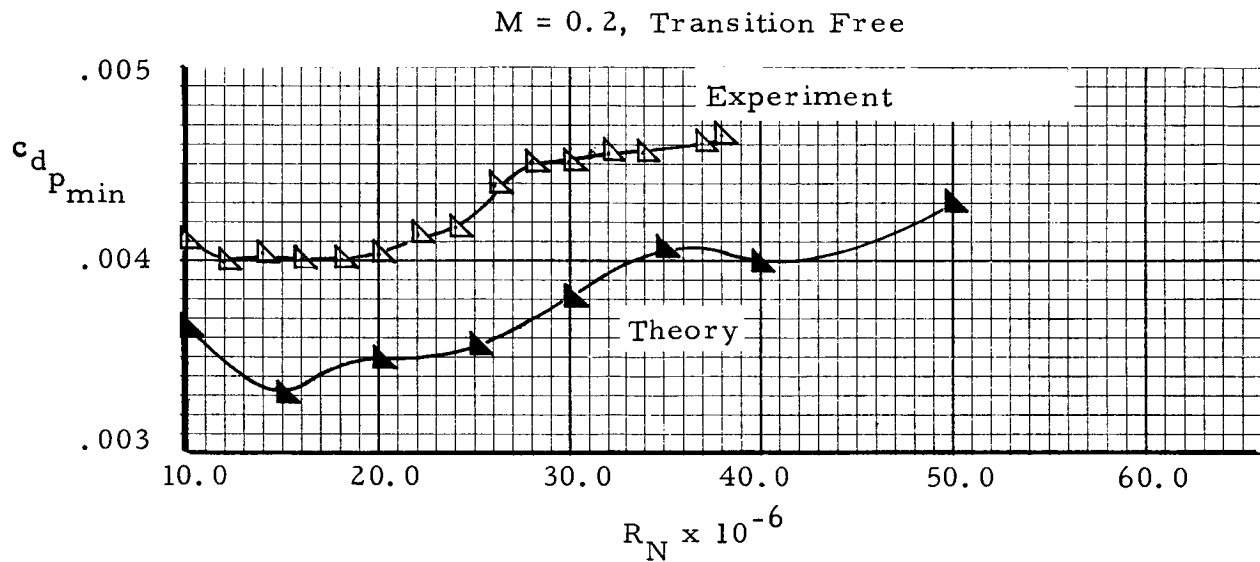
Figure 4(b). Reynolds Number Effects on Minimum Profile
Drag for NACA $65_{(215)}$-114 Airfoil.

	Airfoil	Mach No.	Reynolds No.
⊙	3	0.7	6.5×10^6
⊙	3	0.64	3.6×10^6
△	8	0.64	6.5×10^6
△	8	0.64	3.3×10^6
⊡	10	0.64	6.5×10^6
◇	11	0.64	6.5×10^6
▽	12	0.64	6.5×10^6
◁	26	0.64	6.5×10^6
◇	29	0.64	6.5×10^6
⊙	32	0.64	6.5×10^6
▽	27	0.64	6.5×10^6

	NACA		
●	$64_1\text{-}210$	0.2	6.0×10^6
■	$64_1\text{-}212$	0.2	6.0×10^6
▲	$64_2\text{-}215$	0.2	6.0×10^6
▼	66-206	0.2	6.0×10^6
◆	66-209	0.2	6.0×10^6
⬟	$66_1\text{-}212$	0.2	6.0×10^6
◣	$66_2\text{-}215$	0.2	6.0×10^6
⬢	0012-64	0.2	6.0×10^6

$(c_{d_{p_{min}}})_{th}$

.011

.010

.009

.008

.007

5% line

$(c_{d_{p_{min}}})_{Expt.}$

.008   .009   .010   .011
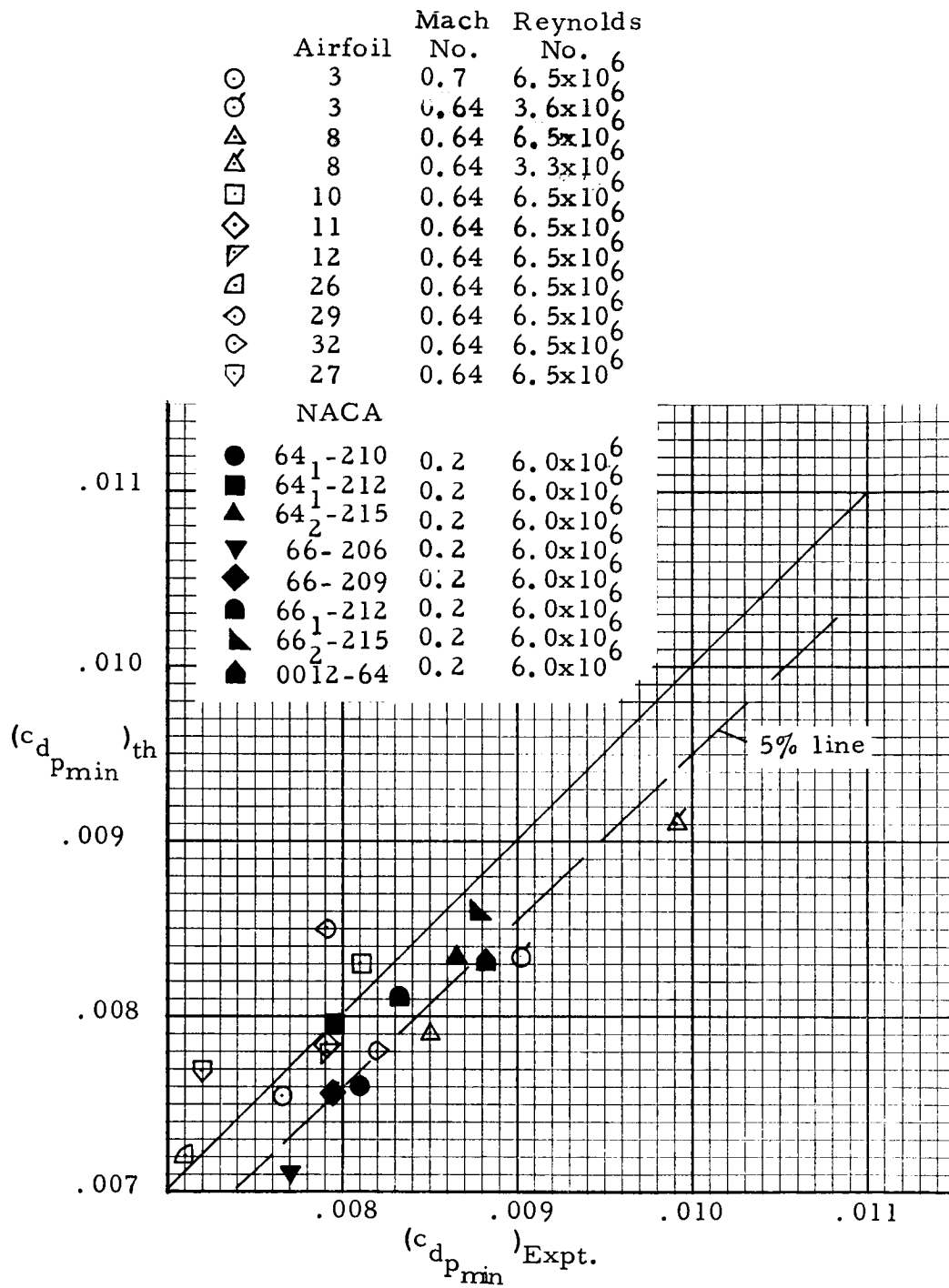
Figure 5.   Correlation of Airfoil Minimum Profile Drag. Transition Fixed. Corrected for Grit Drag.
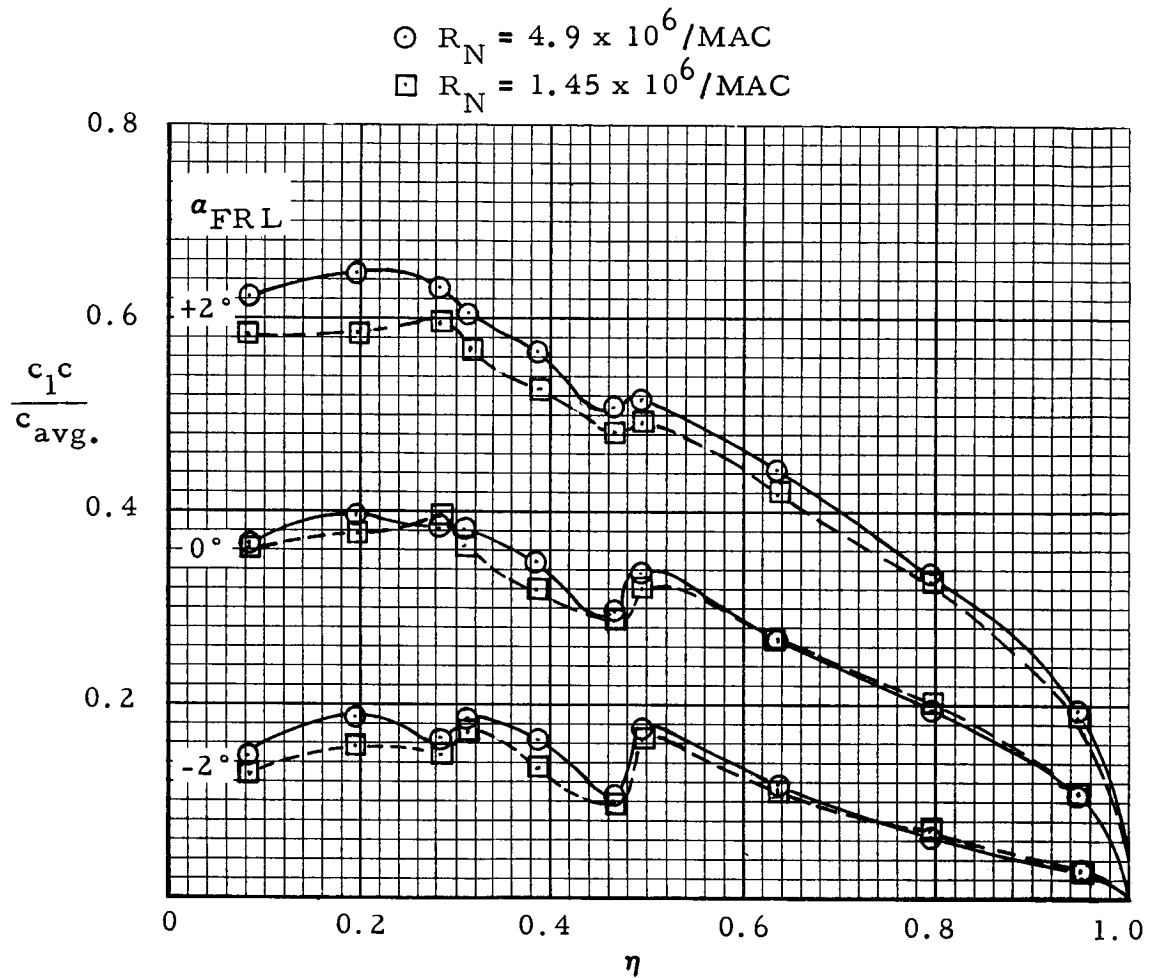
Figure 6. (a) C-141A. Effect of Reynolds Number on Wing Span Load Distribution. Wind Tunnel Data, Transition Fixed, M = 0.700.
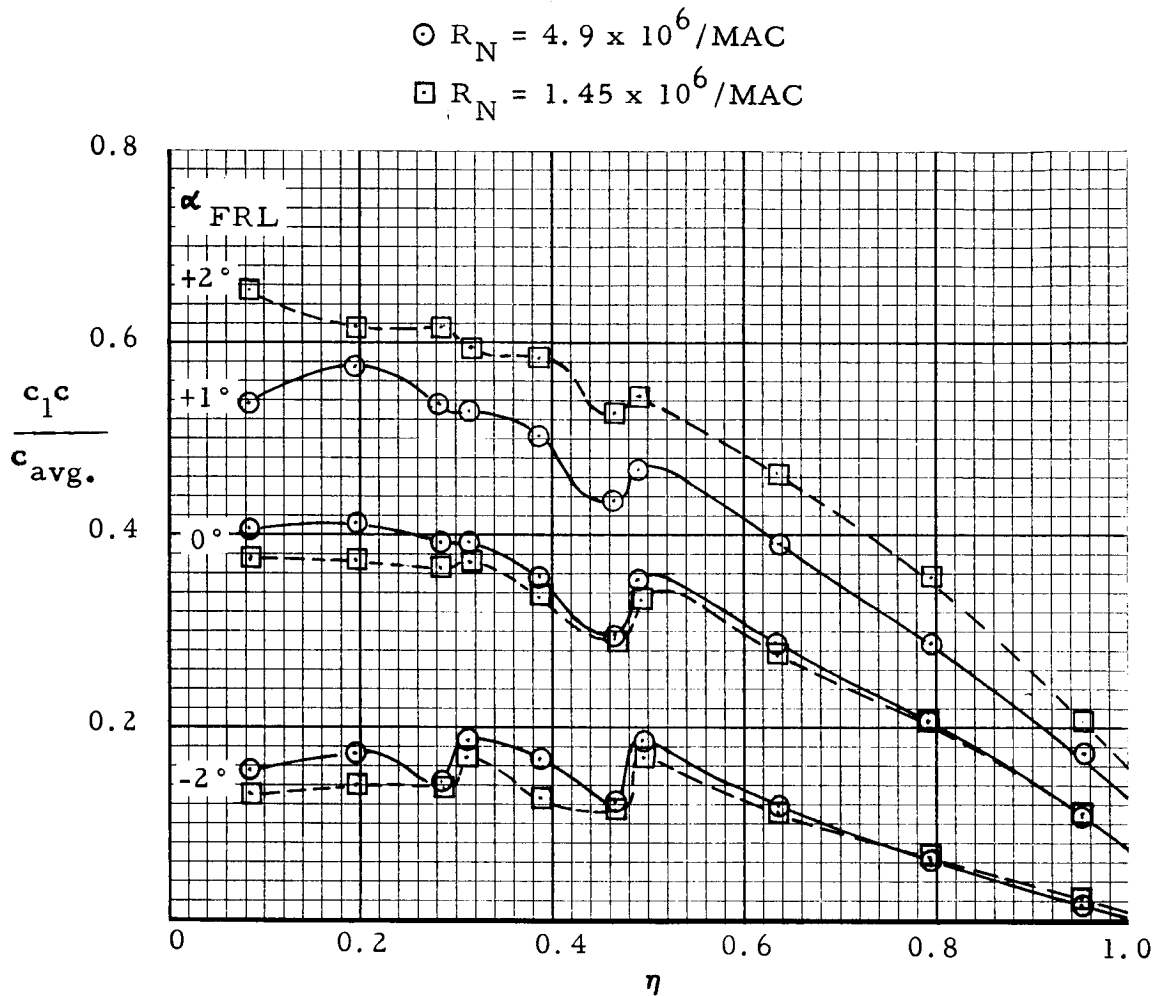
Figure 6. (b) C-141A. Effect of Reynolds Number on Wing Span
Load Distribution. Wind Tunnel Data, Transition
Fixed, M = 0.775

$$\frac{c_1 c}{c_{avg.}}$$
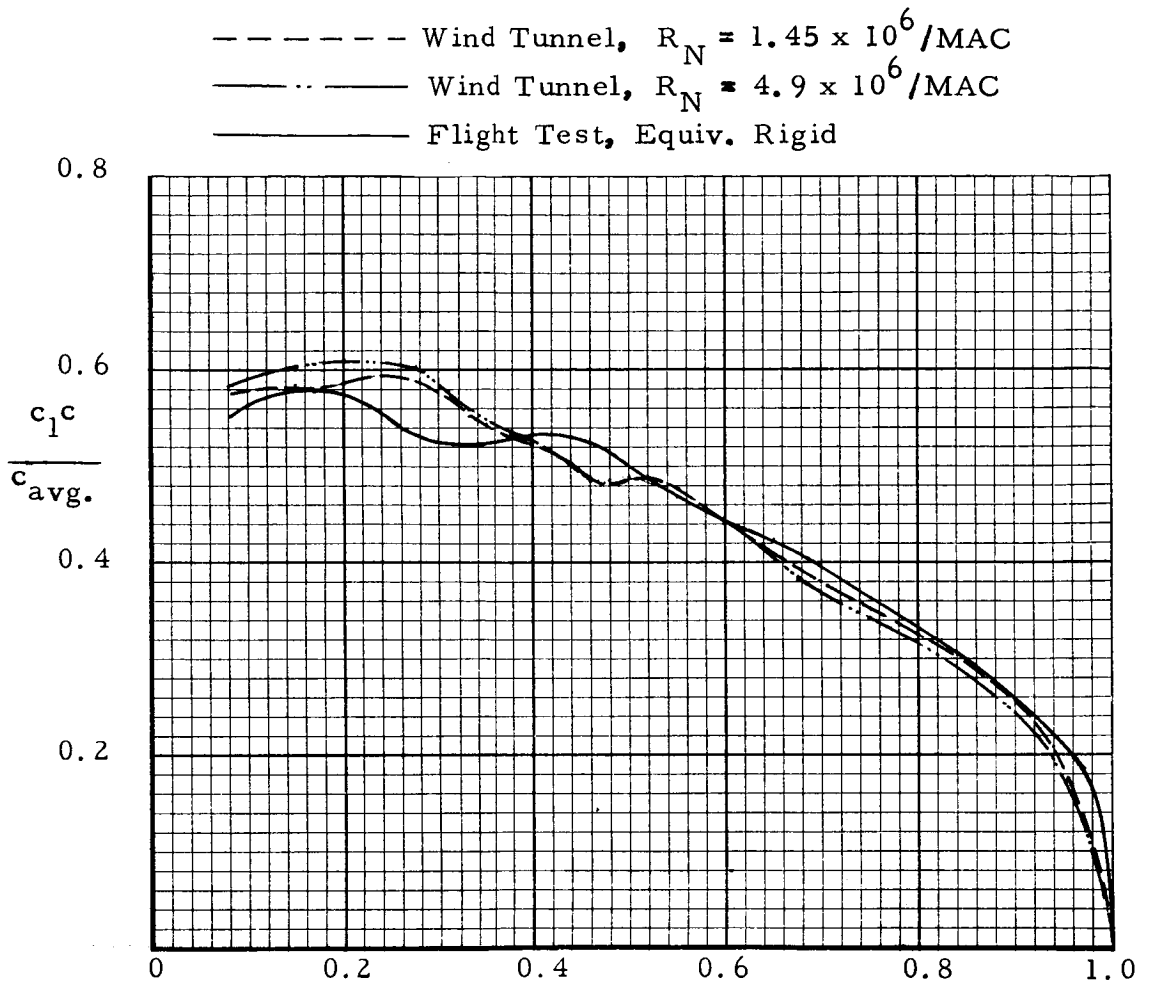
Figure 7. C-141A. Comparison of Wing Span Load Distribution, Wind Tunnel and Flight. $C_L = 0.400$, M = 0.700.

- - - - - - Wind Tunnel, $R_N = 1.45 \times 10^6$/MAC
———· ——— Wind Tunnel, $R_N = 4.9 \times 10^6$/MAC
——————— Flight Test, Equiv. Rigid
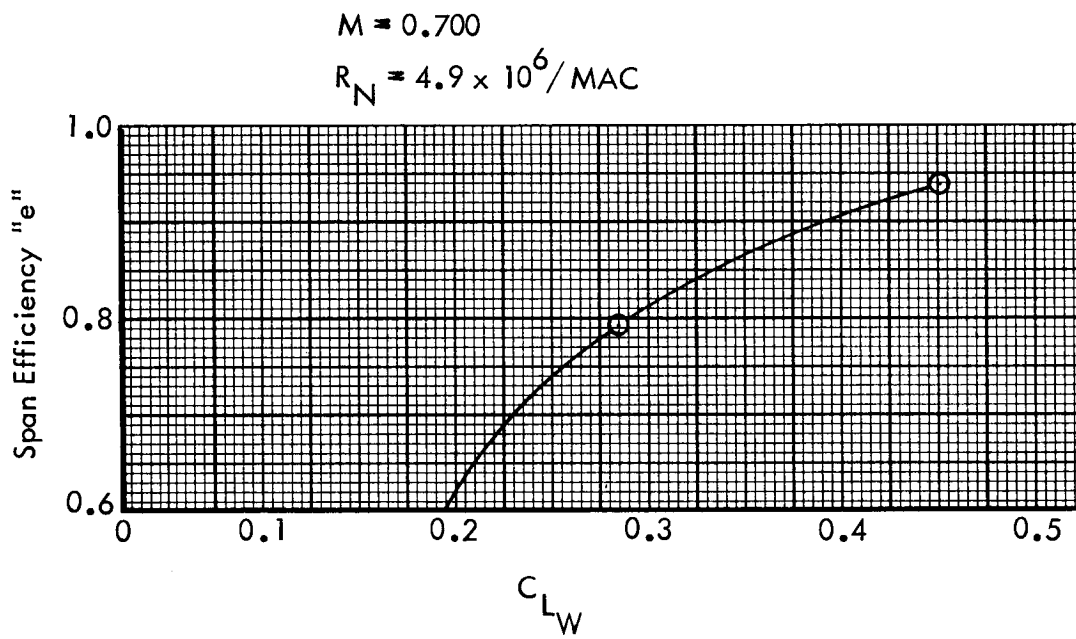
Figure 8. C-141A. Wing Span Efficiency Based on Total Wing Load
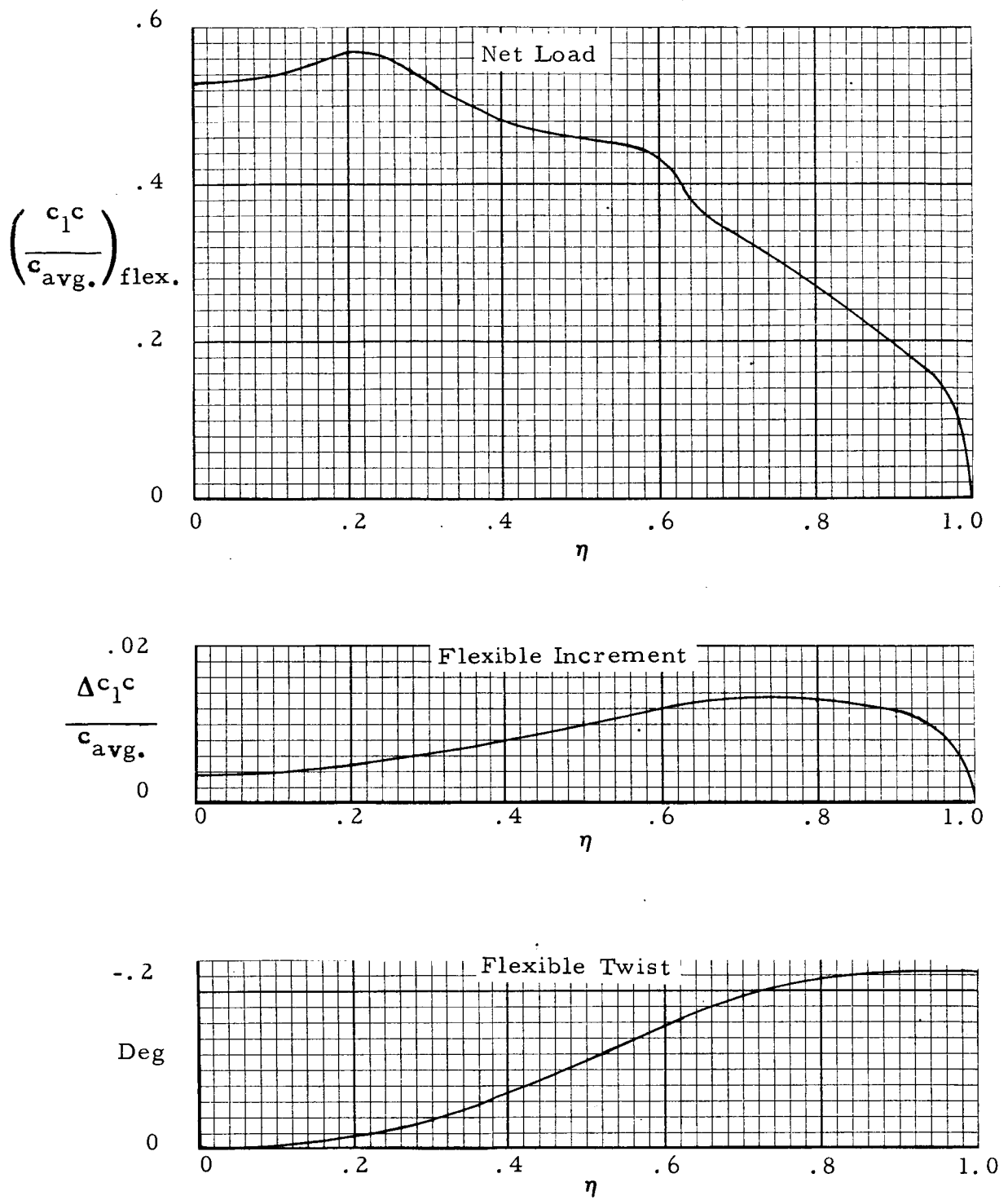
Figure 9.   C-141A.   .0275 Scale Model. Wing Flexibility Under
Wind Tunnel Load,   M = 0.775, q = 6.8 psi,
α_{FRL} = 1.0°.
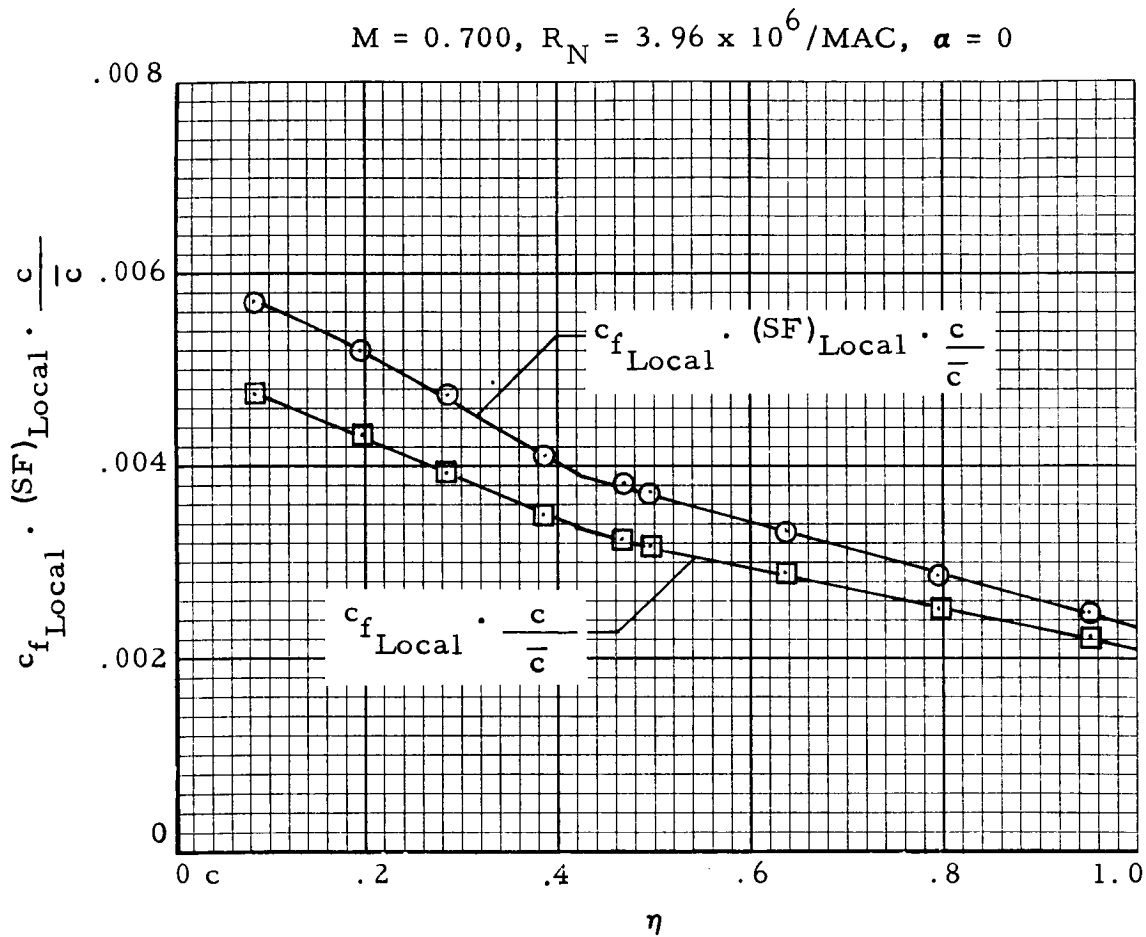
Figure 10. C-141A. Wing Average Shape Factor By
Supervelocity Method.

M = 0.700

$a_{FRL} = 0°$

Transition Fixed 6%c

	$R_N \times 10^{-6}$/MAC	C_d
▽	1.45	0.00925
⊙	3.96	0.00712
▢	25.0	0.00546
△	45.0	0.00488
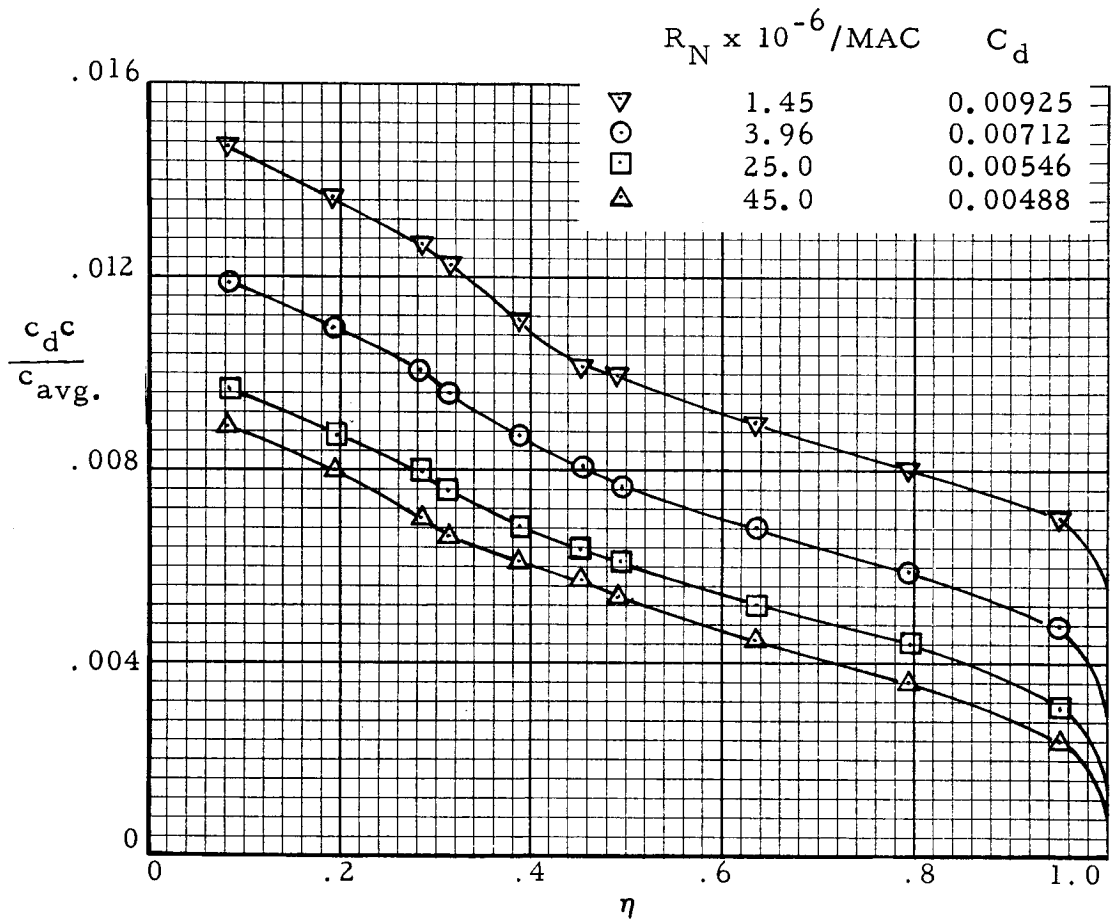
Figure 11.   C-141A. Spanwise Variation of Wing
Profile Drag From Theory.
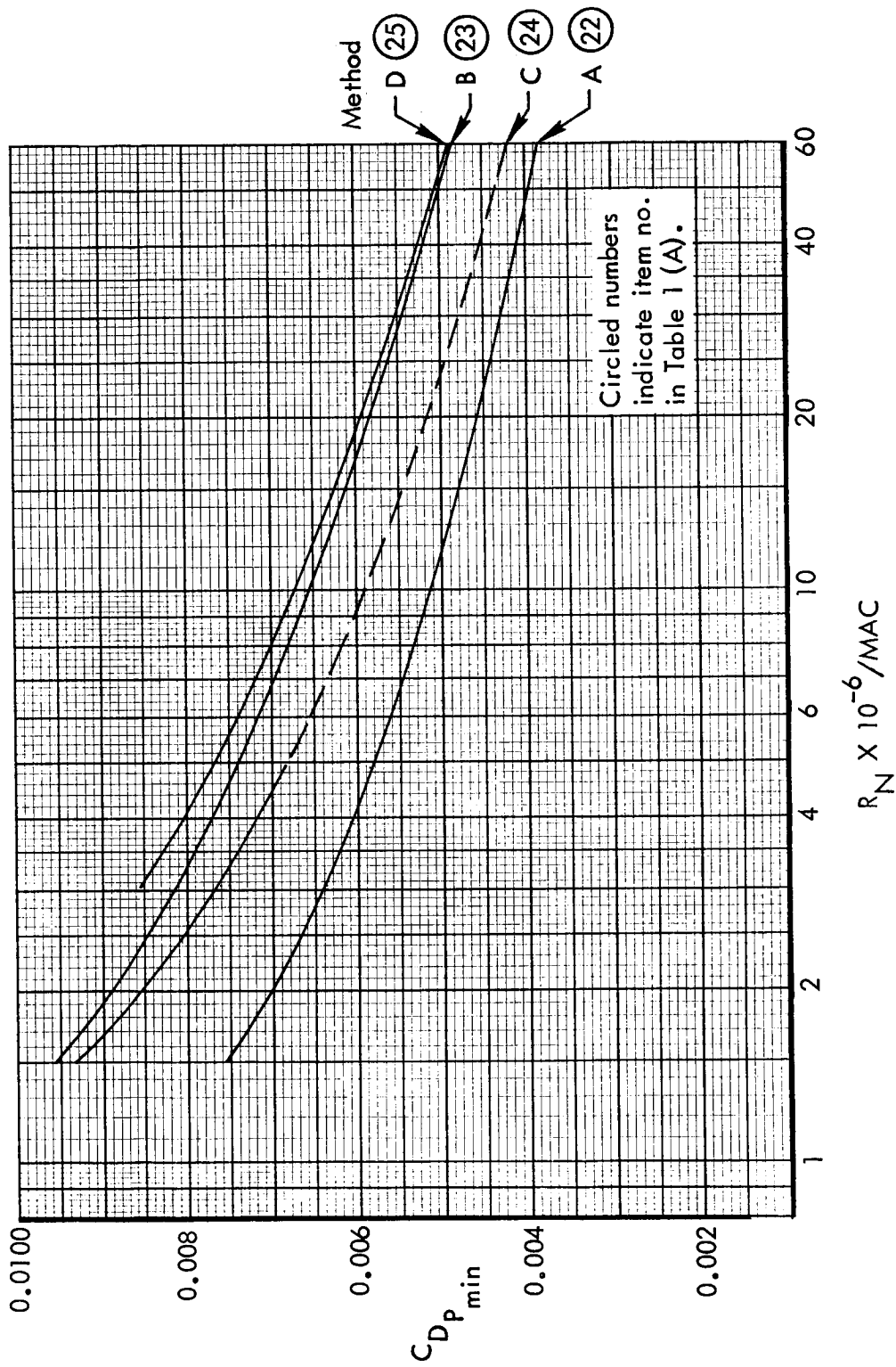
Figure 12.   Wing & Fillet Minimum Profile Drag Estimates.
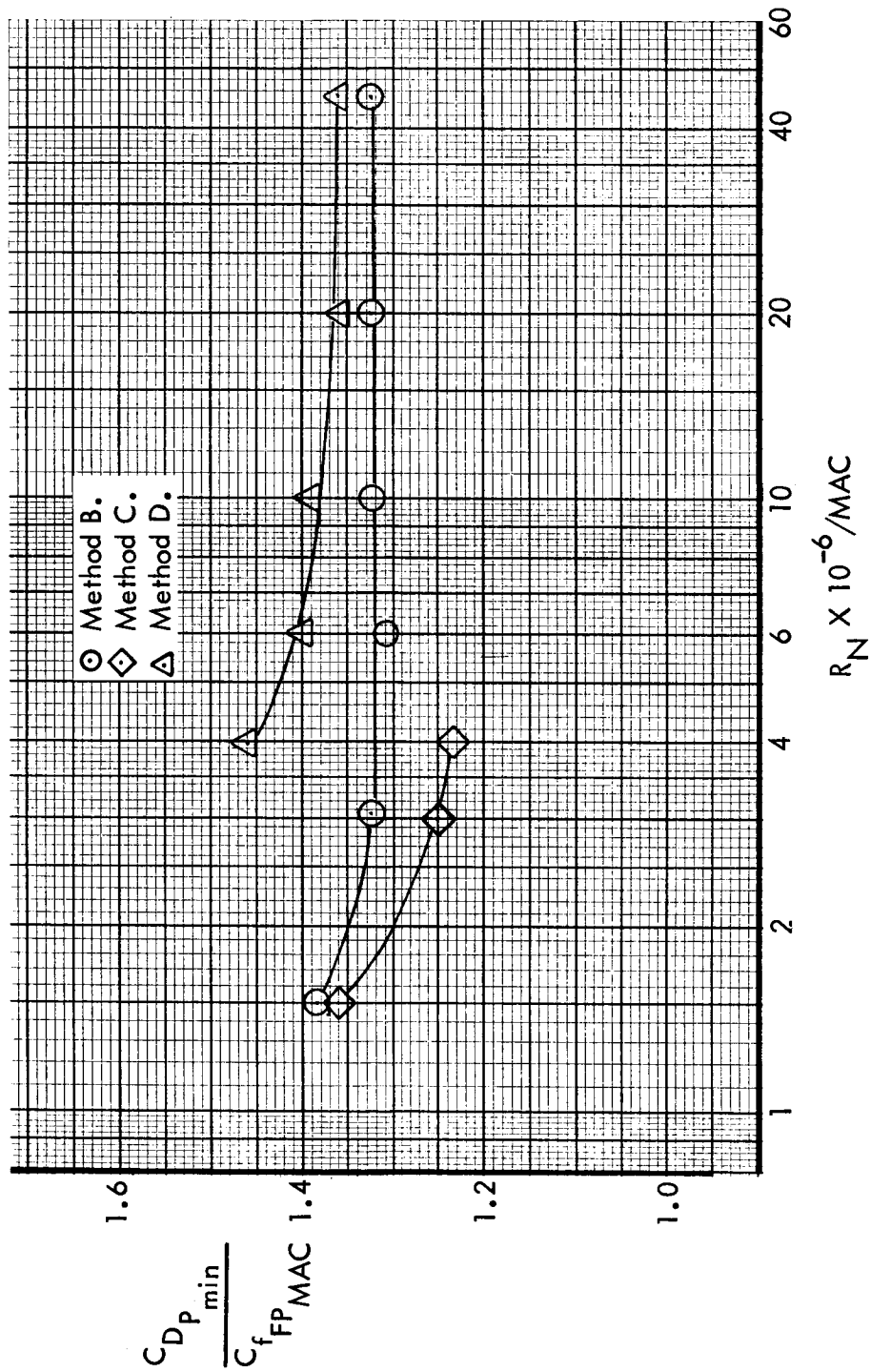
Figure 13.   Comparison of Wing Shape Factors.
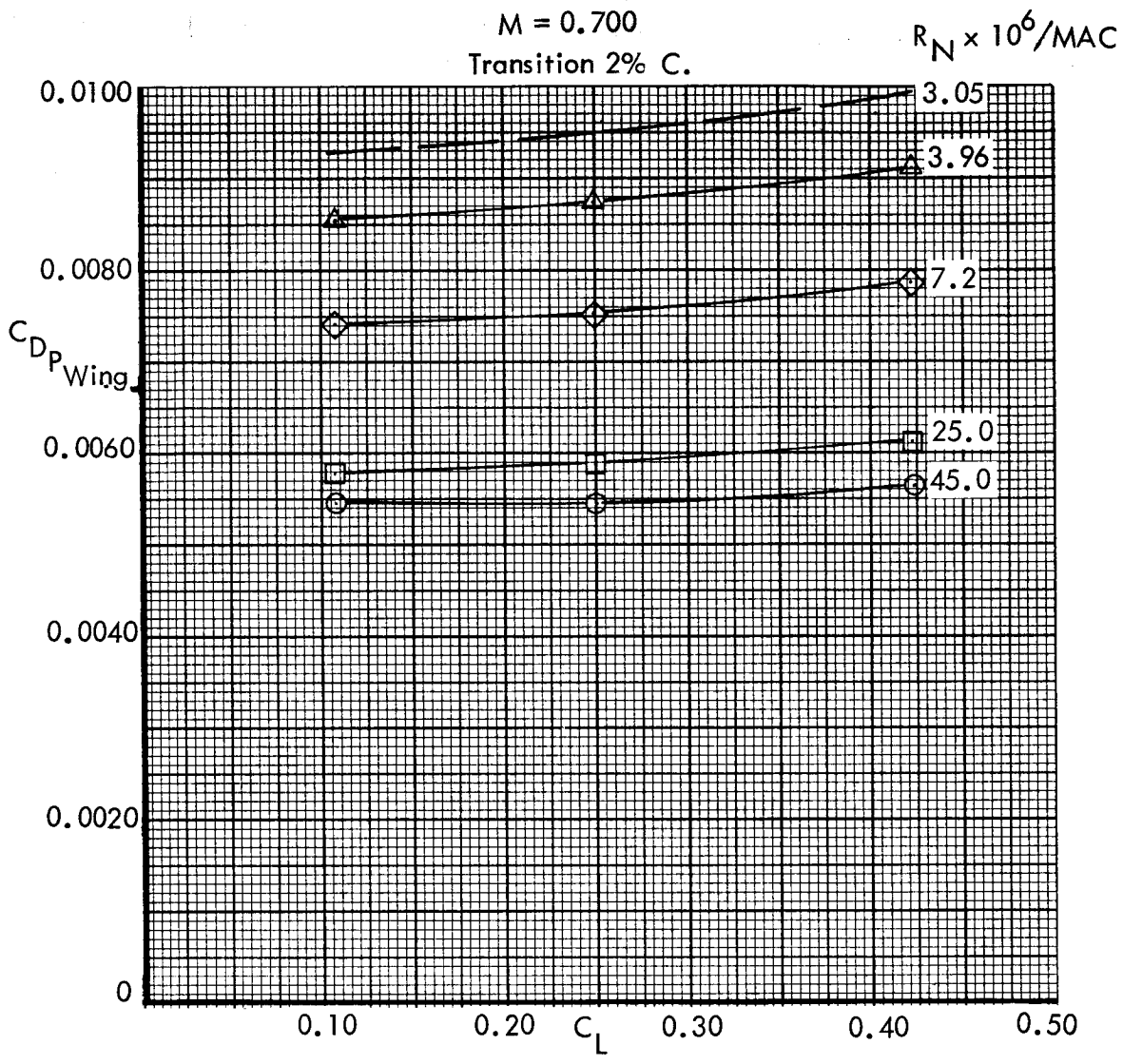
Figure 14. Predicted Wing Profile Drag Variation With Lift Coefficient. Method C.
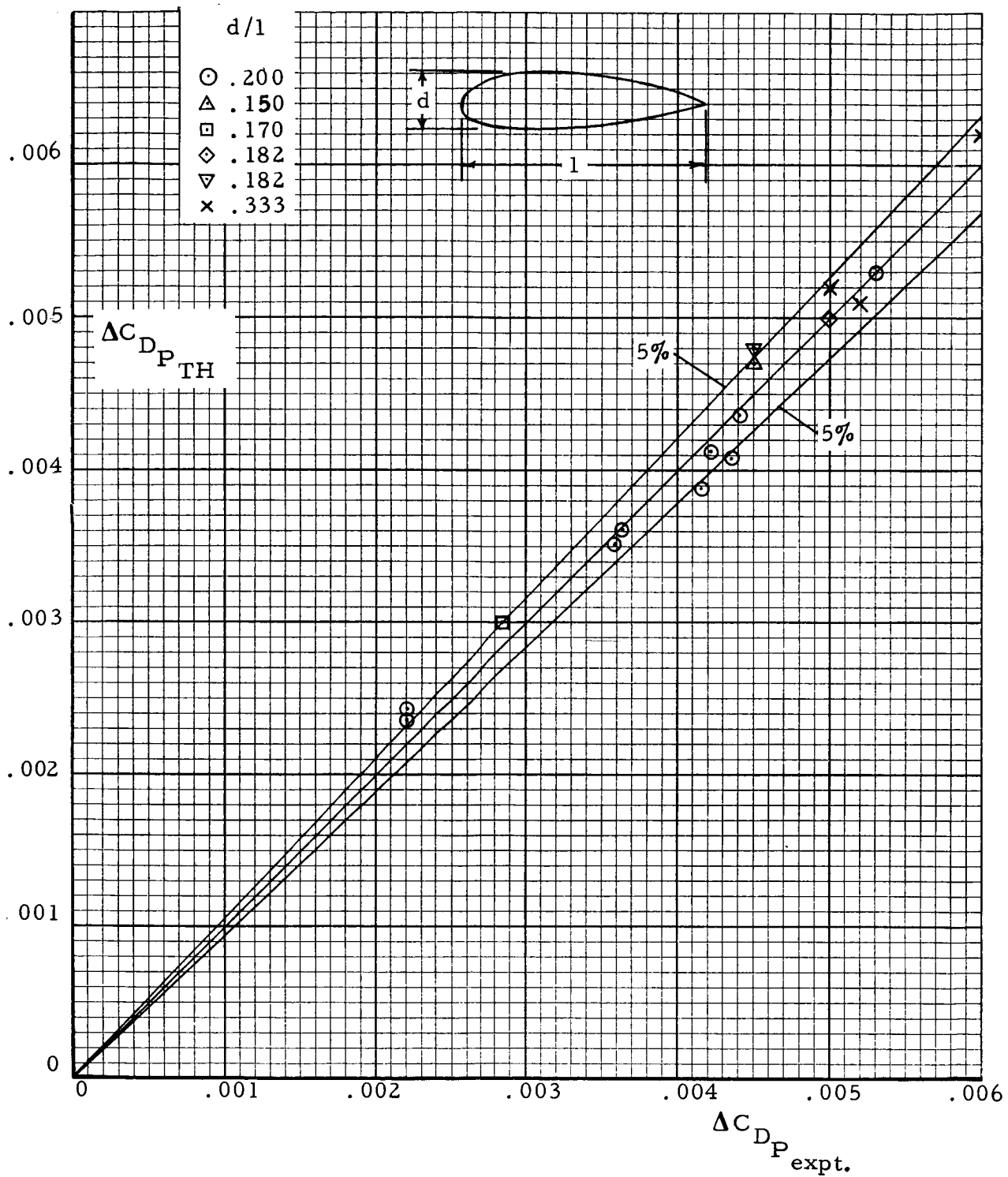
Figure 15.   Fuselage Profile Drag. Bodies of
Revolution.
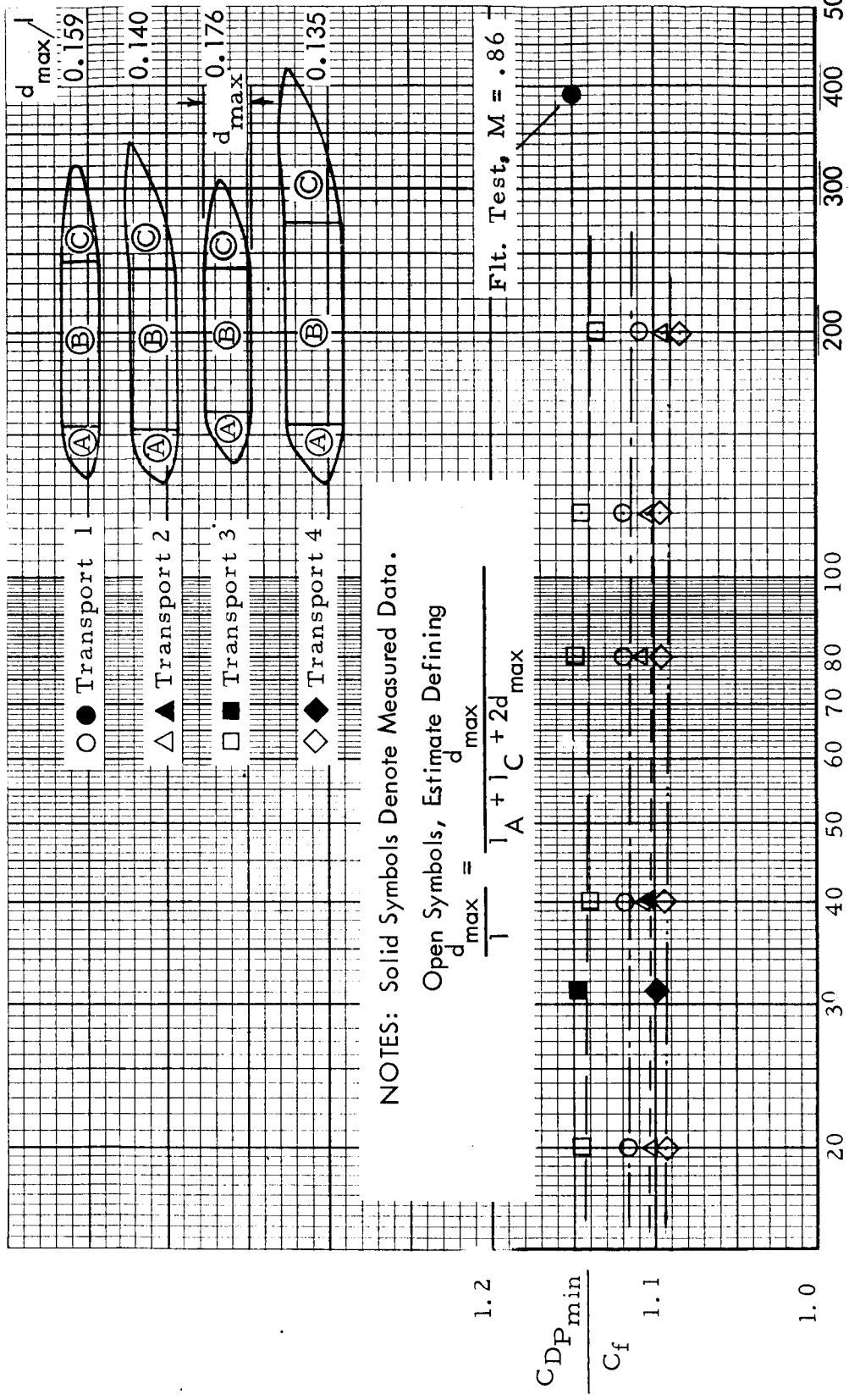
Figure 16.. Fuselage Shape Factors, $M \leq 0.700$
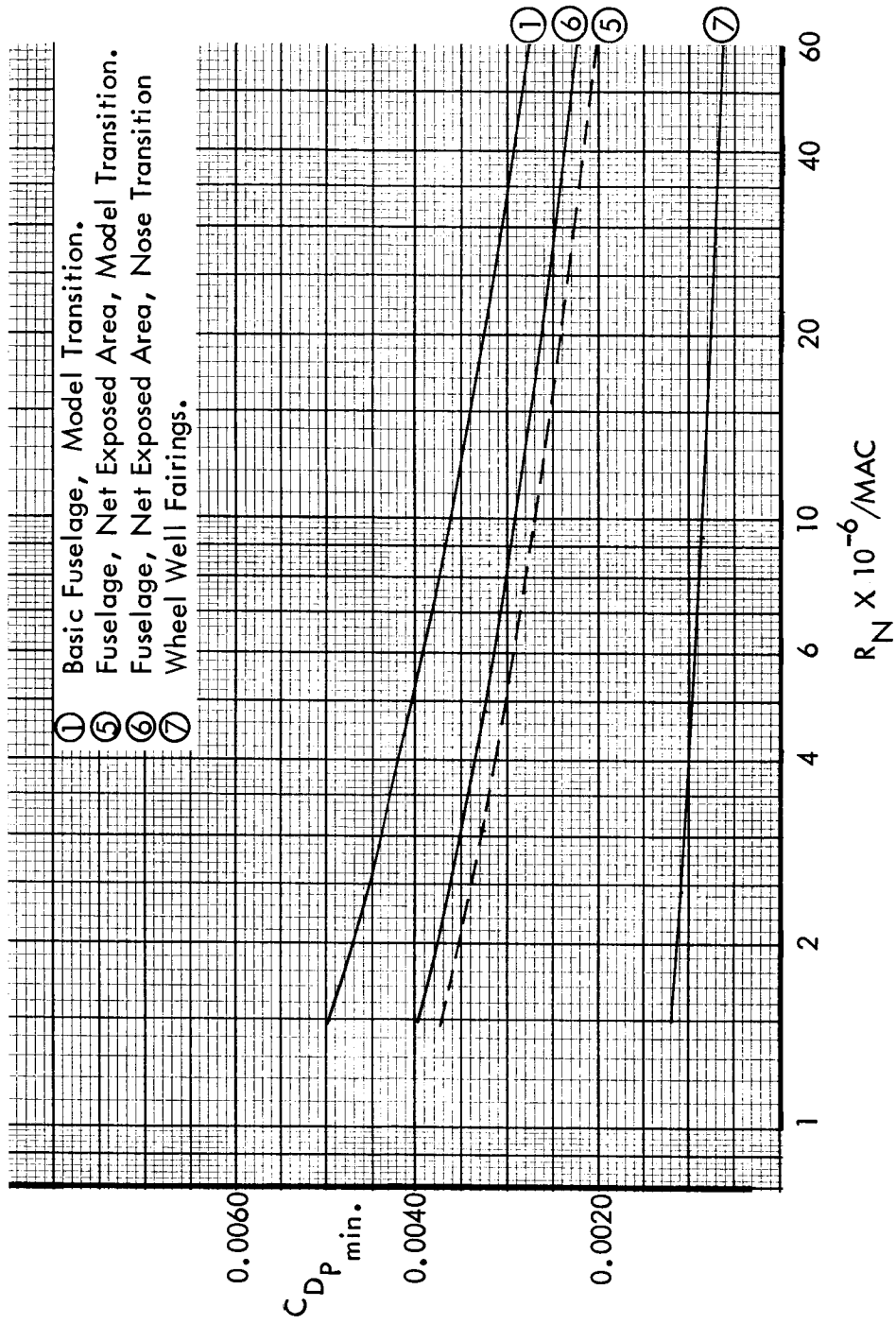
Figure 17. Fuselage, Wheel Well Fairing Drag Estimates

Legend:
- ① Basic Fuselage, Model Transition.
- ⑤ Fuselage, Net Exposed Area, Model Transition.
- ⑥ Fuselage, Net Exposed Area, Model Transition.
- ⑦ Fuselage, Net Exposed Area, Nose Transition
  Wheel Well Fairings.

$R_N \times 10^{-6}/MAC$

$C_{D_{P_{min.}}}$
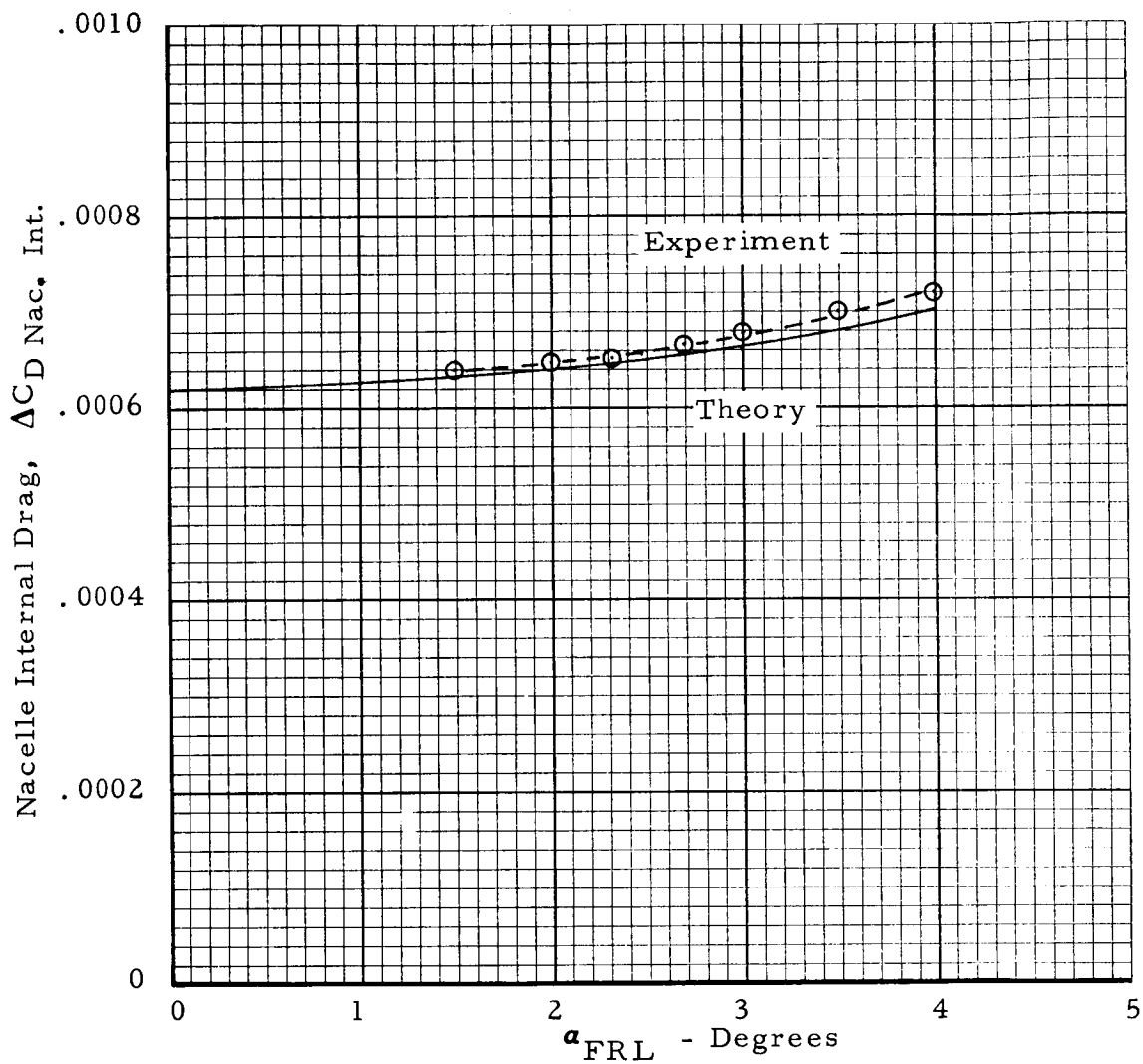
Figure 18.. Correlation of Nacelle Internal Drag. 1/20 Scale
Flow - Through Nacelle. $R_N = 4 \times 10^6$.
Ao/A_{HL} = 0.65.
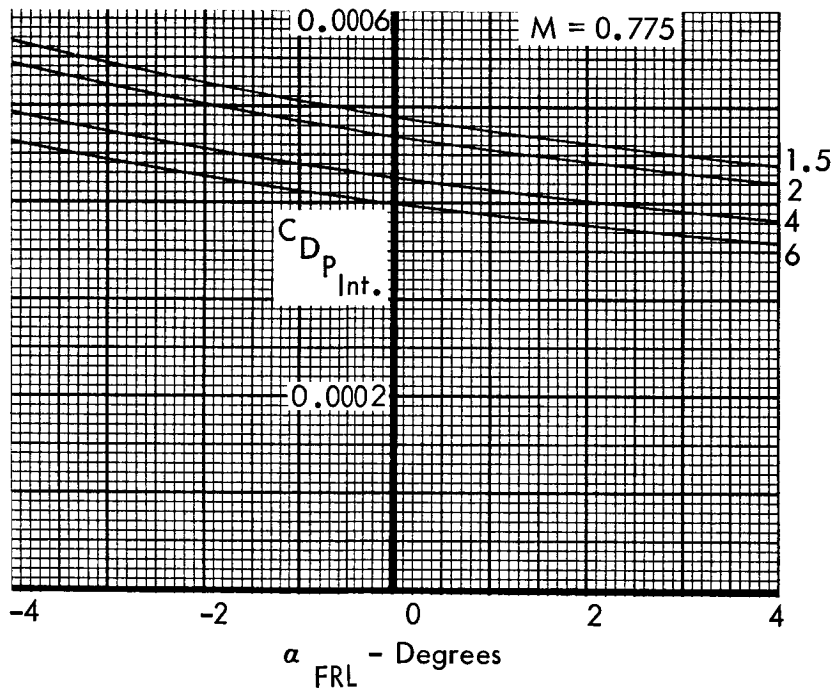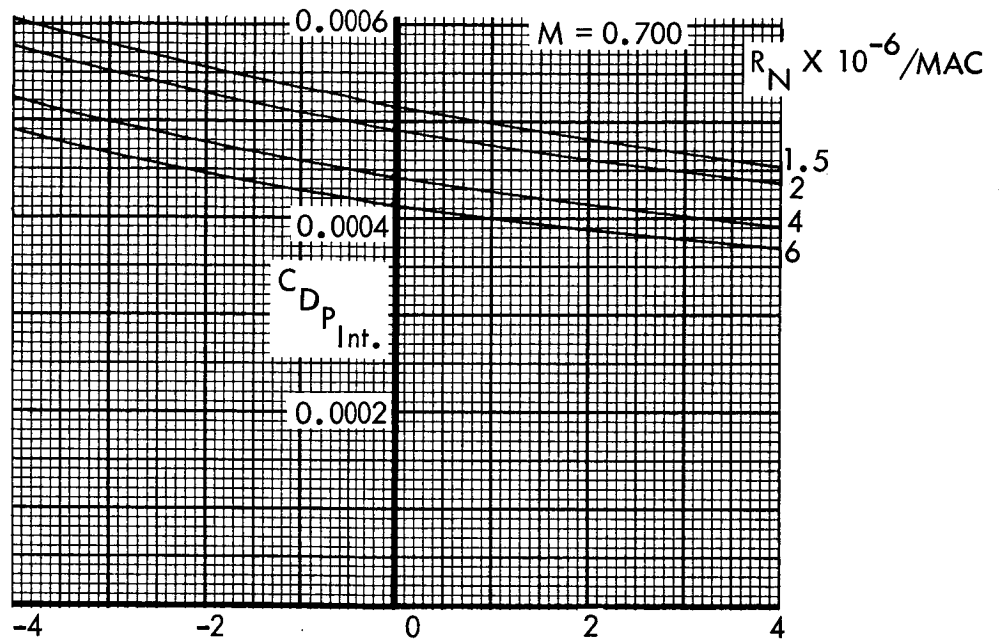
Figure 19　Model Nacelle Internal Drag Estimates
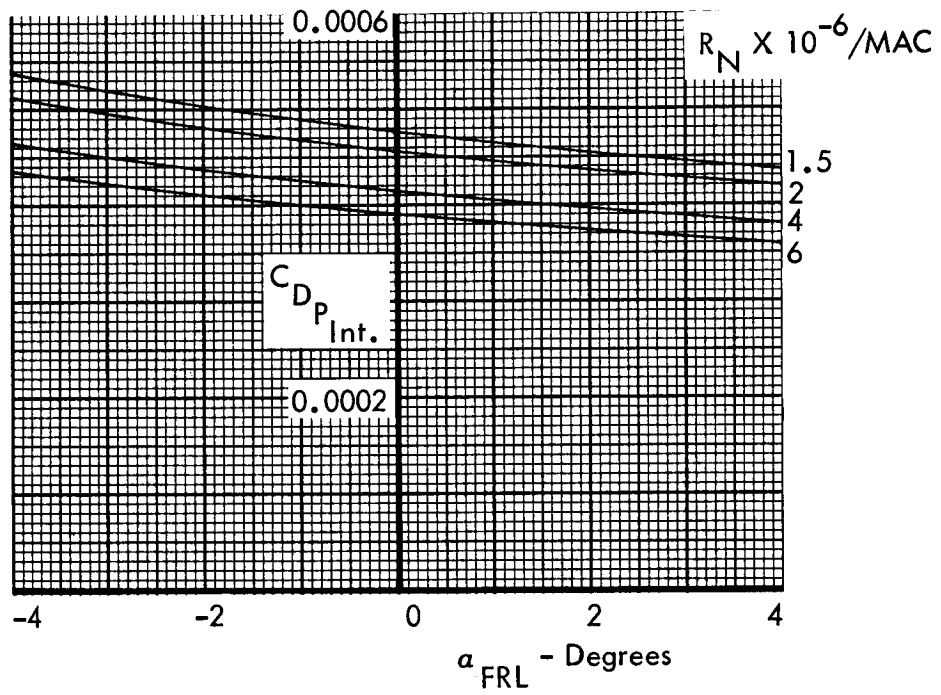
(b) M = 0.825

Figure 19.   Continued.
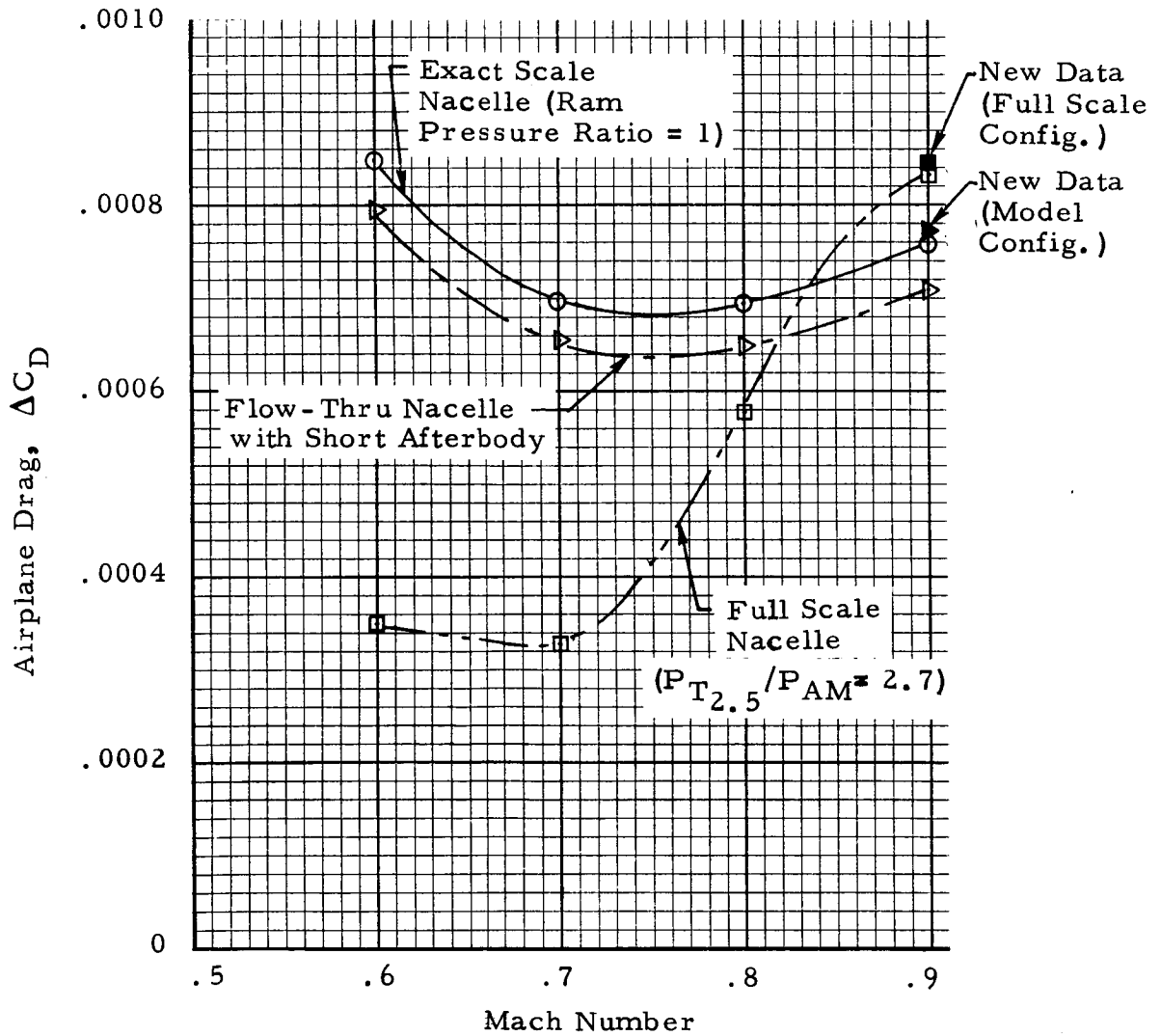
Figure 20.   C-141A. Nacelle Afterbody Pressure Drag.
.0275 Scale Model and Full Scale
Characteristics.
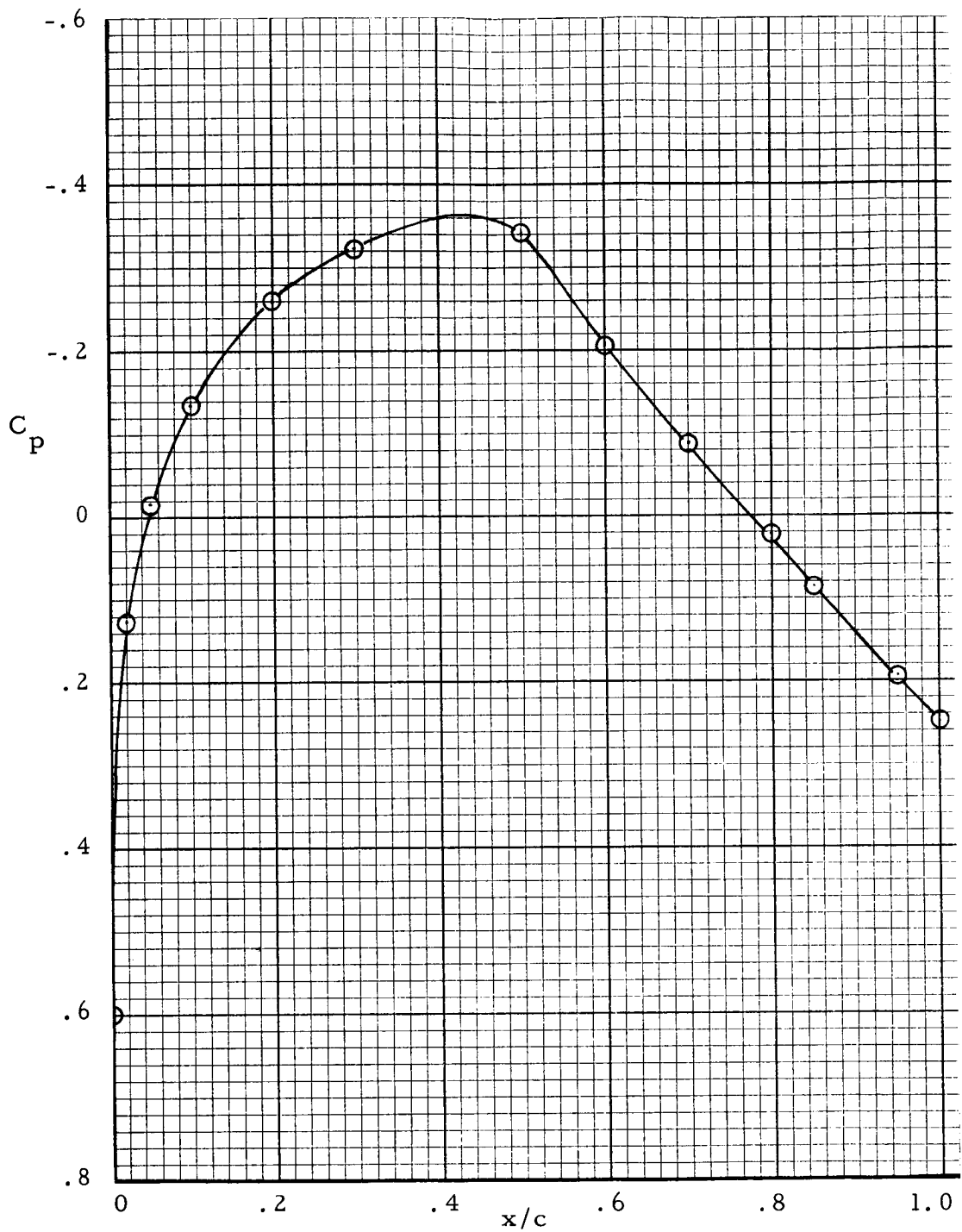
Figure 21. C-141A. Vertical Tail Pressure Distribution at 0.60 x Semispan. M = 0.700, α_{FRL} = 0°, R_N = 4.9 x 10^6/MAC.
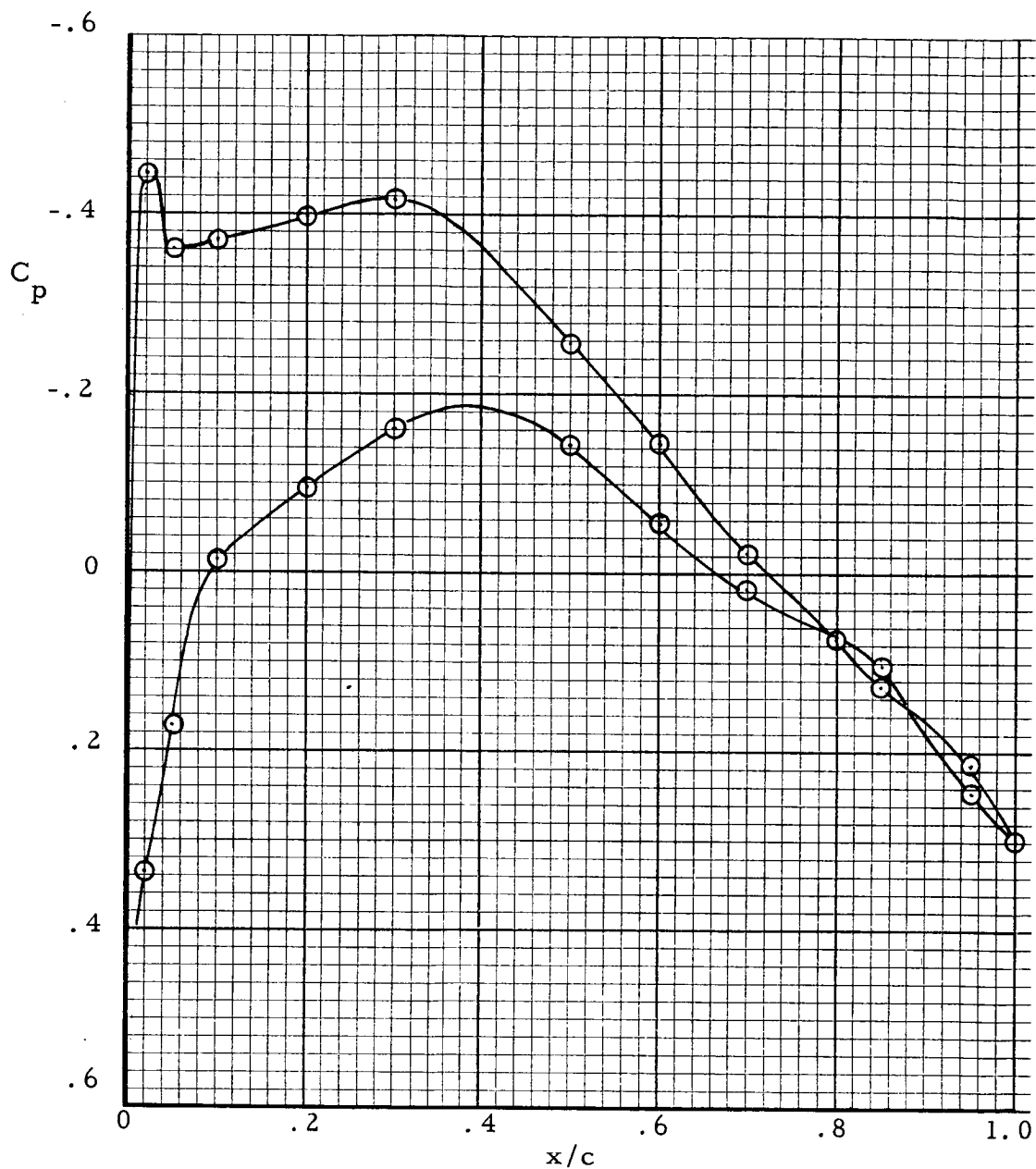
Figure 22.   C-141A. Horizontal Tail Pressure Distribution.
Wind Tunnel Data,   M = 0.700
$\alpha_{FRL} = 0°$, $R_N = 4.9 \times 10^6$/MAC.
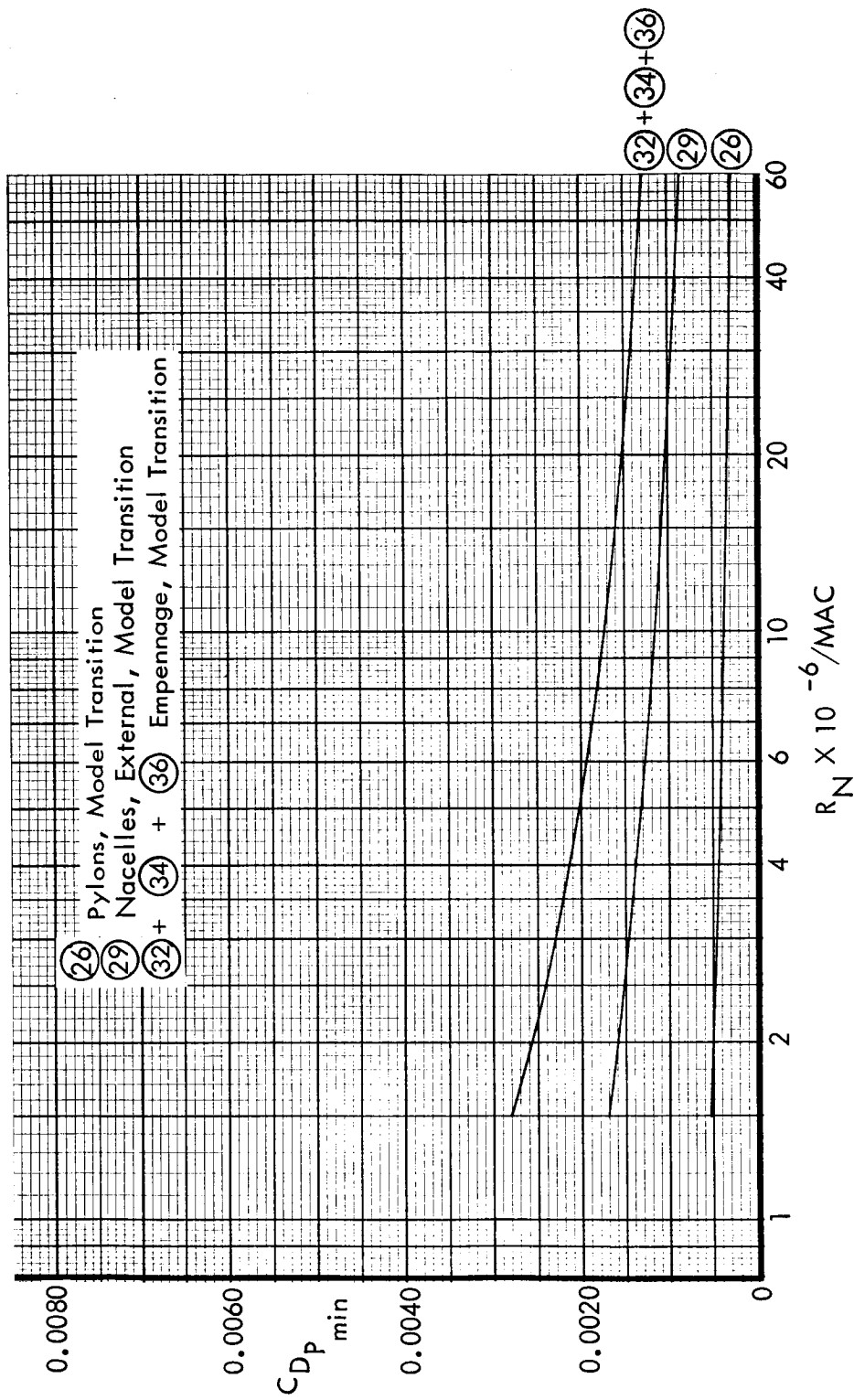
Figure 23.   Pylons, Nacelles, Empennage Minimum Profile
Drag Estimates.

TABLE I (A).
C-141A MINIMUM PROFILE DRAG ESTIMATES

Item	Component	Wetted Area, Ft²	Trans.	Method	$R_N \times 10^{-6}$/MAC				
					1.5	3.05	6.0	20	60
①	Fuselage (Basic)	5088	Model		.00498	.00439	.00392	.00329	.00276
②	① Less Blade Imprint	5026	"		.00492	.00433	.00388	.00325	.00273
③	② Less W.W.F. "	4680	"		.00458	.00404	.00370	.00302	.00254
④	③ Less Fillet "	4134	"		.00405	.00357	.00319	.00268	.00225
⑤	④ Less Emp. "	4064	"		.00398	.00350	.00313	.00263	.00221
⑥	As ⑤	4064	Nose		.00424	.00374	.00335	.00285	.00243
⑦	Wheel Well Fairings	822	Nose		.00119	.00105	.00093	.00076	.00064
⑧	Wing O/B η=.084	6600	Model	A	.00802	.00684	.00602	.00489	.00409
⑨	⑧ Less Pylon Imprint	6554	"	=	.00695	.00593	.00522	.00425	.00355
⑩	⑨ "Fus, Fillet Imprint	5688	"	=	.00690	.00588	.00518	.00421	.00352
⑪	⑧ "Total Imprint	5642	"	=					
⑫	As ⑨	6554	"	B (Includes Fillet)	—	—	—	—	—
⑬	As ⑩	5688	"	=	—	—	—	—	—
⑭	As ⑪	5642	"	=	.00953	.00811	.00716	.00581	.00485
⑮	As ⑨	6554	"	C	.01010	.00825	.00702	.00555	.00451
⑯	As ⑩	5688	"	=	.00875	.00715	.00609	.00480	.00391
⑰	As ⑪	5642	"	=	.00870	.00710	.00604	.00477	.00388
⑱	As ⑨	6554	"	D	—	.00930	.00802	.00641	.00533
⑲	As ⑩	5688	"	=	—	.00806	.00695	.00556	.00462

49

TABLE I (A).
C-141A MINIMUM PROFILE DRAG ESTIMATES

Item	Component	Wetted Area. Ft²	Trans.	Method	$R_N \times 10^{-6}$/MAC				
					1.5	3.05	6.0	20	60
20	As 11	5642	Model	D	–	.00800	.00690	.00552	.00458
21	Wing Fillet	424	Leading Edge		.00062	.00051	.00046	.00038	.00032
22	Wing + Fillet	5642	Model	A	.00752	.00639	.00564	.00459	.00384
23	=	=	=	B	.00953	.00811	.00716	.00581	.00458
24	=	=	=	C	.00932	.00761	.00650	.00515	.00420
25	=	=	=	D	–	.00851	.00736	.00590	.00490

50

TABLE I (B).
C-141A MINIMUM PROFILE DRAG ESTIMATES

Item	Component	Wetted Area, Ft²	Trans.	Method	$R_N \times 10^{-6}$/MAC				
					1.5	3.05	6.0	20	60
㉖	Pylons	438	Model	C	.00053	.00046	.00042	.00034	.00028
㉗	"	"	Leading Edge	C	.00058	.00050	.00046	.00038	.00031
㉘	Nacelles (Internal)	985	Model		.00051	.00047	.00042	-	-
㉙	"	"	"	=	.00171	.00147	.00128	.00104	.00085
㉚	Nacelles (External)	"	Leading Edge		.00183	.00160	.00141	.00117	.00097
㉛	"								
㉜	Horizontal Tail	894	Model	C	.00130	.00109	.00092	.00071	.00058
㉝	"	"	Leading Edge	=	.00155	.00133	.00115	.00094	.00079
㉞	Vertical Tail	819	Model	C	.00122	.00100	.00088	.000715	.00060
㉟	"	"	Leading Edge	=	.00132	.00109	.00096	.000785	.00067
㊱	Bullet	137	Model	=	.00018	.00016	.00014	.00011	.00010

RESULTS OF WIND TUNNEL DATA ANALYSIS

Background

Presentation of the basic wind tunnel results from tests 591 and 617 is to be found in Volume 2 of this report. Summary curves and discussion of the principal analysis work are presented in the following sections. The analysis was conducted at intervals over a period from June 1971 to March 1973, as a result of difficulties in scheduling the complete wind tunnel test program.

The results include those from the support tare and interference investigation, model trim drag and component interference evaluation. Pressure measurements taken on the fuselage afterbody are computed to provide afterbody pressure drag characteristics. These data are used principally to substantiate some of the support and component interference effects measured by the force balance.

Support Tare and Interference

A summary of the evaluation process for model support corrections is shown in figure 24. For the sting interference portion, the model was supported by a load-bearing thin blade to the lower fuselage, and a lower sting attached to the other extremity of the blade. This configuration measured the combined model load, L_M, and the interference terms $L_{I_{S-M}}$ and $L_{I_{B-M}}$, the interference of the sting on the model and blade on the model, respectively. The sting interference term, $L_{I_{S-M}}$, was obtained by extrapolating respective load data at each of four different sting displacement distances to an infinite displacement of model and sting, $D \rightarrow \infty$. This assumes that the sting interference effects on the model can be treated independently of the blade-model interference.

Figure 25 shows, diagramatically, the installation of the model in the wind tunnel (a) with the standard configuration in which the support sting was located approximately 12 inches (0.305 m) below the tunnel center-line and (b) with the sting axis on the tunnel center-line.

Summary curves of the lift, drag and pitching moment data for the standard tail-on configuration (with offset) are shown in figures 26, 27, and 28 respectively, for configurations 1, 2, 3 and 4. The variation of C_L with sting position at constant angle of attack is generally very small over the cruise Mach number range, and sting interference effects are not discernible from these data. The effect of sting position on drag, for convenience

plotted as $\left(C_D - \dfrac{C_L^2}{\pi A}\right)$, shows a consistent trend of decreasing drag for sting positions 1 (closest to model) to 3 for all Mach numbers. This effect increases slightly over the C_L range up to 0.55. Corresponding data from the integration of afterbody static pressures indicate an opposite effect of sting position, figure 29. This result confirms the expected sting taper effect on the afterbody due to the positive pressure field generated by the sting. The result for the complete configuration, however, is taken to be indicative of significant interference effects on the wing flow field from the sting. For sting position 4, the drag is seen to increase, being both C_L and Mach number-dependent. This abrupt change is also reflected in the pitching moment data of figure 28, where a nose-down change is shown at sting position 4.

The correct interpretation of these effects is important with regard to the final sting corrections to be applied to the basic model data. Figure 30 presents results of integrated afterbody pressure drag for the configurations shown in figure 25. These show that the presence of the offset bullet fairing in the standard configuration reduces the drag by approximately $\Delta C_D = 0.0003$. This effect is taken to be inherent in the sting interference corrections for the standard configuration.

Referring to figure 25 again, data are shown for the configuration with the central sting, where it is seen that the model was located at somewhat higher positions in the tunnel than the standard configuration. Selected results from these tests are given in figures 31 and 32. These data show magnified trends of the drag and pitching moment data noted in figures 27 and 28 as the model is positioned from configuration 1 to 4. These results suggest that a probable tunnel ceiling-interference effect is present in the data for the standard configuration 4 through a modification to the tailplane downwash field and resulting pitching moment. This is confirmed by the results shown in figures 33 and 34, giving tail-off data through the four sting positions for the standard configuration. The variation of drag and pitching moment with sting position does not indicate the abrupt changes noted in the tail-on results for position 4.

An additional study was conducted to evaluate the tunnel ceiling effects noted in the test data. A three-dimensional theoretical program, developed at Lockheed Georgia, was utilized to correlate tunnel ceiling effects on the tail with the test results. This program uses a vortex collocation method to compute total forces and moments from an input representing geometry of the wing-body-tail configuration, and the wind tunnel ceiling. The detailed geometry is then computed, followed by the circulation for the rectangular and horseshoe vortices which constitute the total vortex lattice of the system.

Pitching moment results for an incompressible condition at $\alpha_{FRL} = 0$ are shown in figure 35, giving the wing, body and tail contributions as a function of the parameter h/(semi width of tunnel), where h is the distance of the tail from the tunnel ceiling. No sting effects are included in these data. The effects of representing the longitudinal slots of the 8-foot tunnel ceiling are seen to be relatively small. The change in C_M over sting

positions 1-4 is of the order of 0.008 nose-down for the complete configuration, of which 0.006 is a result of tail effects. However, it should be emphasized that these results are for an inviscid case, and, therefore, the equivalent value of $h/(B/2)$ for correlation with test data would be somewhat less than the test figure, due to tunnel ceiling boundary layer. Figure 35(b), shows the values of $C_{M_{tail}}$ plotted as a function of $1/D^2$, as given in the test

results. These data indicate a significant reduction in C_M in the range $1/D^2 < 0.30$, and it is concluded that these trends confirm, qualitatively, the effect of a tunnel ceiling constraint on the test data for the standard model configuration.

Referring again to the pitching moment and drag results for the standard configuration, figures 27 and 28, corrections have been derived to drag by extrapolating the sting interference effects over the range of sting positions 1, 2 and 3 to $1/D^2 = 0$. The correction required to obtain equivalent free air data was then obtained by subtracting the value of C_D at $1/D^2 = 0$ from the level at sting position 4. The effects on drag are summarized in figure 36, for a range of Mach number and C_L combinations. In general, the pitching moment increments thus obtained resulted in negligible changes in trim drag and this component was neglected.

The blade interference effects on the model were obtained by comparing force data from configurations 5, 6 and 7 at constant α_{FRL}. The blade interference on the model, $L_{I_{B-M}}$, (figure 24), was obtained from tests with the model mounted on the dorsal strut. The total model and blade loads, mutual interference and dorsal interference are given by configuration 5. Configuration 5 is shown in figure 3 of Volume 2.

$$(1) \quad L_B + L_M + L_{I_{M-B}} + L_{I_{B-M}} + L_{I_{D-M}}$$

Configuration 7, shown in figure 4 of Volume 2 with the blade loads measured, gives

$$(2) \quad L_B + L_{I_{M-B}}$$

Configuration 6, which is configuration 5 without the blade installed, gives

$$(3) \quad L_M + L_{I_{D-M}}$$

Thus, the blade interference on the model was obtained by the resultant of (1) - (2) - (3), giving $L_{I_{B-M}}$. Figures 37(a) and 37(b) give the blade interference on the model, ΔC_L and ΔC_D. The drag interference is of the order of $\Delta C_D = 0.0004$ at low Mach number, zero at cruise Mach number, and shows an increasing angle of attack effect at higher Mach numbers, resulting in favorable interference at $M > 0.750$ and $\alpha_{FRL} > -1°$. The correction due to the

seal at the blade/fuselage junction is approximately $\Delta C_D = 0.0001$ at cruise angles of attack. The effect of the blade on model lift, figure 37(a), is to reduce C_L by approximately 0.01 - 0.02. Corresponding effects on pitching moment, given in figure 37(c), were small, of the order of -0.003 in C_M. The combined effect on a typical drag polar is shown in figure 38, giving the resultant blade interference.

The alternative method of evaluating support interference, by obtaining the effect of the dummy blade-sting combination (configuration 8, shown in figure 5, Volume 2) has not been used in this analysis. It was found that the cavity pressure levels for configuration 8 were not in agreement with the corresponding values for the live blade (configuration 5), indicating some degree of flow through the cavity. Also, the force data from configurations 6, 8 and 10 indicated a large mutual interference between the dorsal and lower sting, giving an invalid blade interference measurement. The computed afterbody pressure drag, given in Figure 39, substantiates these conclusions.

Trim Drag Results

The analysis of model trim drag data was conducted in the following stages.

The base drag level for the complete model configuration was taken from Test 617 results ($i_H = -1°$). Data from these runs (89-93) are contained in figure 35 in Volume 2 of this report. The model was supported by the "Standard" blade-sting configuration, as described earlier. These tests were conducted with the sting located in the No. 4 position. Since data were obtained for values of $i_H = -1°$ and $+2°$ only from test 617, results from the previous test series (591) for $i_H = -1°$, 0° and $+1°$ were utilized in order to determine a set of incremental values of lift, pitching moment and drag data for each tail setting, relative to the base configuration of $i_H = -1°$.

Before arriving at a set of trimmed drag polars for the model, it was necessary to correct the basic data for the blade support interference effects on the model. These corrections were applied at constant values of α_{FRL} by the following expressions:

$$C_L = C_{L_{Blade \atop on}} - \Delta C_{L_{Blade}} \tag{15}$$

$$C_D = C_{D_{Blade \atop on}} - \Delta C_{D_{Blade}} \tag{16}$$

$$C_m = C_{m_{Blade \atop on}} - \Delta C_{m_{Blade}} \tag{17}$$

Through an interim set of data corrected for the combined effects of varying tailsetting and blade interference, plots of C_D versus C_L and C_m versus C_L for values of $i_H = -1°$, $0°$, $+1°$ and $+2°$ were derived for a series of Mach numbers from $M = 0.600$ to 0.825. These are presented in figures 40 and 41. The sting interference drag corrections were applied to the trimmed drag polars at given constant C_L conditions, since discussion of these results has indicated that the sting interference effects on pitching moment resulted in negligible changes in trim drag. Model drag polars corrected for total support interference, and trimmed to a c.g. position of 25 percent MAC are shown in figure 42 for a Reynolds number of 3.05×10^6/MAC.

Effects of Aft-Located Transition Strip

Figure 43 presents oil flow visualization photographs of the wing upper surface at typical cruise conditions. These tests were conducted with natural transition on the wing, in order to identify the main shock location at drag-rise conditions. Transition was then fixed by 0.0054-inch (0.0136 cm) ballotini glass beads at a distance of ten percent local chord ahe of the most forward shock location for the appropriate range-of-cruise Mach number and angle of attack. This technique does not guarantee that transition remains fixed ahead of the shock for all Mach number and C_L combinations, and must be viewed as of limited use to a narrow range of conditions, where a more valid simulation of the full-scale shock and boundary layer interaction should be obtained.

The results of the investigation are shown in figure 44, which compares trimmed drag-rise characteristics for the model with standard transition fixing and the aft-located transition. The data for the revised technique have been corrected for the estimated reduction in wing upper surface profile drag due to the change in transition location. Incremental drag-rise, ΔC_D, between $M = 0.700$ and 0.760 are as follows:

C_L	0.30	0.40	0.50
Standard Transition	0.00090	0.0013	0.0029
Aft-Located Transition	0.00085	0.00085	0.00135

These results indicate that the drag-rise, including low Mach number drag-creep and wave drag onset effects, is reduced significantly at cruise values of C_L and above, suggesting that the revised technique is beneficial in reducing excess form drag and achieving a better simulation of the post-shock boundary layer characteristics at wind tunnel Reynolds numbers. These results are not conclusive, however, due to the limitations of the technique discussed earlier.

Model Component Drag Evaluation

Basic data from tests 591 and 617 have been analyzed to provide the effects of component build-up on the overall configuration drag. Figures 45(a) and 45(b) present results at M = 0.600, 0.700, 0.775 and 0.785 for the basic fuselage and wheel well fairing configurations. These were obtained from tests with the model supported by the standard technique through sting configuration 4. Comparison of the computed afterbody pressure drag results in figure 39 indicated that the effect of the dummy blade on the afterbody drag is insignificant. Although the blade could affect the fuselage super-velocities near the nose region, the resulting effects on overall fuselage drag are assumed to be negligible. Hence, in this analysis, the measured fuselage drag represents the expected interference free levels for this configuration.

The experimental data for the isolated fuselage exhibit increasing drag with decreasing angle of attack due to separation on the upswept afterbody. The wheel-well fairings cause additional drag at negative angles of attack; flow visualization photographs presented in figure 46 show separation at the base of the fairings. At positive angles of attack, the drag increment due to the fairings increases to the order of $\Delta C_D = 0.0010$, indicating some additional interference effects because of boundary layer confluence at the fuselage and fairing junctions.

The wing and fillet drag increments versus angle of attack, for Reynolds numbers of $1.83 \times 10^6/MAC$ and $3.05 \times 10^6/MAC$, are shown in figures 47(a), (b), (c) and (d). The measured scale effect on minimum drag is seen to be of the order of $\Delta C_D = 0.0008$ at M = 0.700. This compares with an estimated value of 0.0012 from method C given in table 1. The reason for this discrepancy is not known, but it should be noted that the discrepancies in drag between test 591 and 617 (see page 5, Volume 2) may be responsible for some of this effect. Also, although the size of ballotini used for these tests was estimated to be adequate for Reynolds numbers down to $1.83 \times 10^6/MAC$ ($3 \times 10^6/foot$), it is possible that some degree of laminar flow was present downstream of the transition strip for these conditions. The majority of the analysis and correlation studies, however, use the higher Reynolds number data where it has been established from detailed tests on a similar configuration, (C-5A), that transition was adequately fixed at all test conditions.

Measured drag increments for the pylon-nacelles and empennage (vertical, horizontal tails and bullet) are presented in figures 48(a), (b), (c) and (d). The drag increment for the pylon-nacelles (including internal drag) is seen to reduce with increasing angle of attack due to a favorable mutual interference between the wing and nacelle. The empennage increment for a tail setting of 0 degrees decreases with increasing fuselage angle of attack to minimum values in the region of $\alpha_{FRL} = 2.5°$, approximating to zero load on the tailplane.

The foregoing data are now used as a basis for evaluating component drag under trimmed complete model conditions throughout the cruise Mach number range. Figures 49 (a) and (b) present the variation of wing & fillet, fuselage, wheelwell fairing, pylon-nacelles and empennage drag with Mach number for aircraft values of C_L = 0.30, 0.40 and 0.50 at R_N = 3.05 x 10^6/MAC. These were obtained by evaluating the corresponding values of $C_{L_{A-h}}$ and α_{FRL} at each Mach number to maintain the total C_L at each condition. The resulting drag variation with Mach number reflects the degree of net component interference at each Mach number, including subcritical drag creep effects and wave drag onset at high Mach numbers. These give slightly different values of excess drag to those derived from trimmed conditions.

At a typical cruise C_L = 0.40, the fuselage drag, shown in figure 49 (a), is seen to increase by ΔC_D = 0.0005 over the Mach number range M = 0.700 to 0.775.

The drag increment due to the wheel-well fairings remains essentially constant over the Mach number range from M = 0.600 to 0.775.

The pylon-nacelles installation exhibits a reduction in drag of the order of ΔC_D = –0.0005 over the same speed range at C_L =0.40 and 0.50, as a result of the favorable interference effects noted previously. The empennage increment increases by ΔC_D = 0.0007. The component drag measured at R_N = 3.05 x 10^6/MAC is summarized in table 2 at C_L =0.40. It is shown that of a total model drag – rise of ΔC_D = 0.0037 at M = 0.775, the wing + fillet is responsible for an increment of 0.0031, the empennage 0.0007 and fuselage 0.0005. Favorable effects result from the pylon-nacelles (–0.0005) and wheel-well fairings (–0.0001).

The wing and fillet profile drag was obtained from these total C_D data by estimating and deducting the induced drag component (= $\dfrac{C_{L_{A-h}}^2}{\pi\, Ae}$), where values of 'e' were taken from reference 1. Resulting profile drag as a function of both C_L and Mach number is shown in figure 50. The steep rise in the variation of C_{D_p} with C_L above M = 0.700 is the result of boundary layer separation discussed in the previous section, and clearly seen on the inboard wing panel on the flow visualization photographs of figure 43. The levels of C_{D_p} for M = 0.785 result from strong rear separation and wave drag.

A comparison of the estimated profile drag with measured data for the configuration build-up at M = 0.700, $C_{L_{TRIM}}$ = 0.40, and R_N = 3.05 x 10^6/MAC is given in table 3. An exact correlation of estimated and measured data for each model configuration is not possible, since support interference effects were determined only for the complete model configuration. However, it is reasonably assumed that the presence of the blade-sting support did not affect the installation drag of the pylon-nacelles, although the possibility

58

of a mutual effect between blade-sting and empennage cannot be overlooked.

The results in table 3 show the excess drag of the fuselage-wheelwell fairing configuration to be $\Delta C_D = 0.0009$, or 0.00126 if the assumption is made that the wind tunnel buoyancy correction should be applied to this configuration. These data are, respectively, 30 percent or 37 percent above the flat plate skin friction value. The net excess drag increases by 0.00225 in C_D due to the addition of the wing and fillet, giving a total of 0.00315 for the wing-fillet, fuselage, wheelwell fairing configuration. This wing-fuselage interference is therefore 29 percent above the wing + fillet estimate based on method C. Previous wind tunnel development on the C-141A configuration during the design phase established that a revised wing-fillet fairing reduced the interference drag by approximately 0.0013 in C_D. This modification, however, was not incorporated into the production configuration. The wing-fuselage interference factor in this case would reduce to 12 percent of the estimated value.

The installed effects of the pylon-nacelles result in a net favorable interference of -0.00083. The net measured drag increase on the model due to the empennage is seen to be 0.0036, or 0.00135 in C_D above estimate. The excess drag due to the empennage results mainly from an interference effect on the upswept afterbody, as shown in the results of figure 51, where computed afterbody pressure drag shows an increase in C_D at cruise α_{FRL} due to installation of the empennage. Analysis of the static pressure data for these configurations indicates that the peak velocities generated at the fin maximum thickness location result in large increases in negative C_p values on the rearward facing surfaces of the afterbody, resulting in a pressure drag increment.

The total excess drag on the configuration of $\Delta C_D = 0.00374$ or 0.0034, when corrected for support interference and buoyancy, is thus primarily the result of wing-fuselage interference and empennage-afterbody interference factors. Some evidence of a reduction in afterbody pressure drag with Reynolds number is given by the data presented in figure 52, for the tail-off configuration. Similar results were also obtained with the tail-on data. The total axcess drag measured at $R_N = 3.05 \times 10^6/MAC$, therefore, may well contain elements of Reynolds number-dependent drag which cannot be evaluated from the limited range of test conditions.

Sting Interference Effects on Model

A. $L_{I_{S-M}} + L_M + L_{I_{B-M}}$ $L_{I_{S-M}}$ From Plot $1/D \longrightarrow 0$
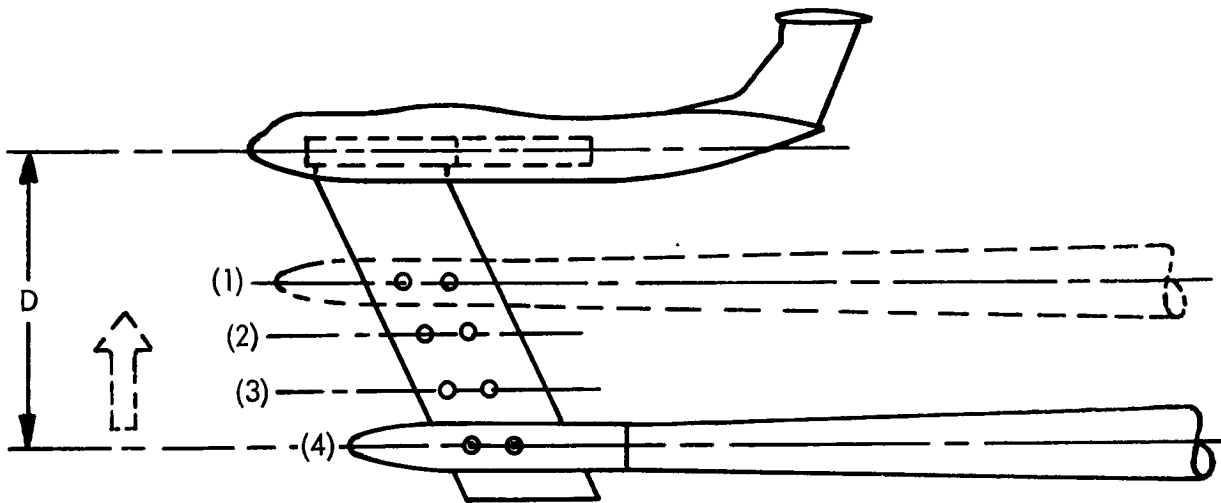
Blade Interference on Model

B. Dorsal Sting, Model & Blade Metric. $L_B + L_M + L_{I_{M-B}} + L_{I_{B-M}} + L_{I_{D-M}}$

C. Dorsal Sting With Metric Blade Only. $L_B + L_{I_{M-B}}$

D. Blade Out. $L_M + L_{I_{D-M}}$

E. $L_{I_{B-M}} = B-C-D$

$L_M = A - L_{I_{B-M}} - L_{I_{S-M}}$

Cavity at Blade/Model Junction
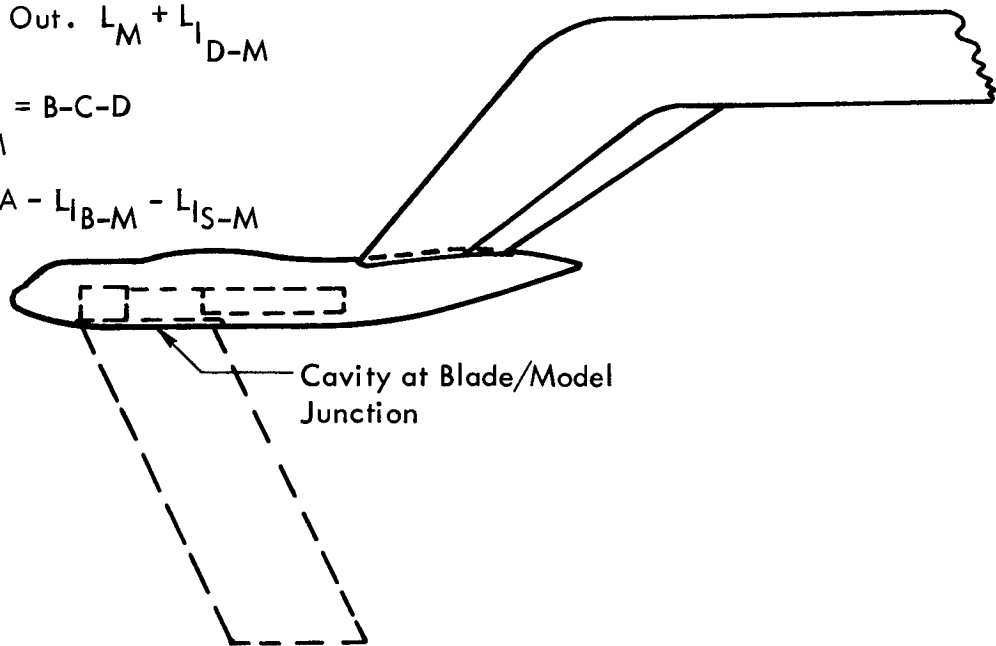
Figure 24.   Evaluation of Model Support Tare & Interference.
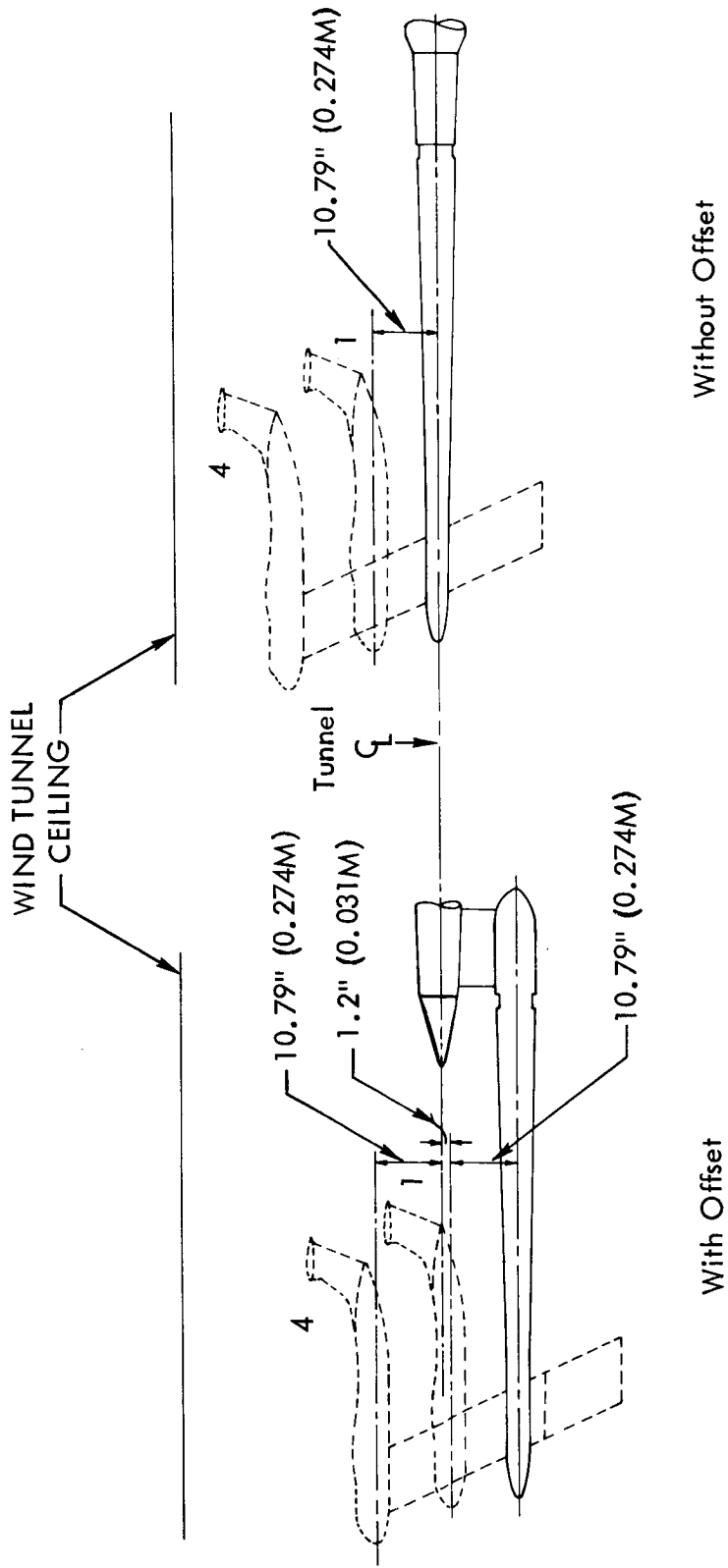
Figure 25. Comparison of Offset Sting and Central Sting Configurations
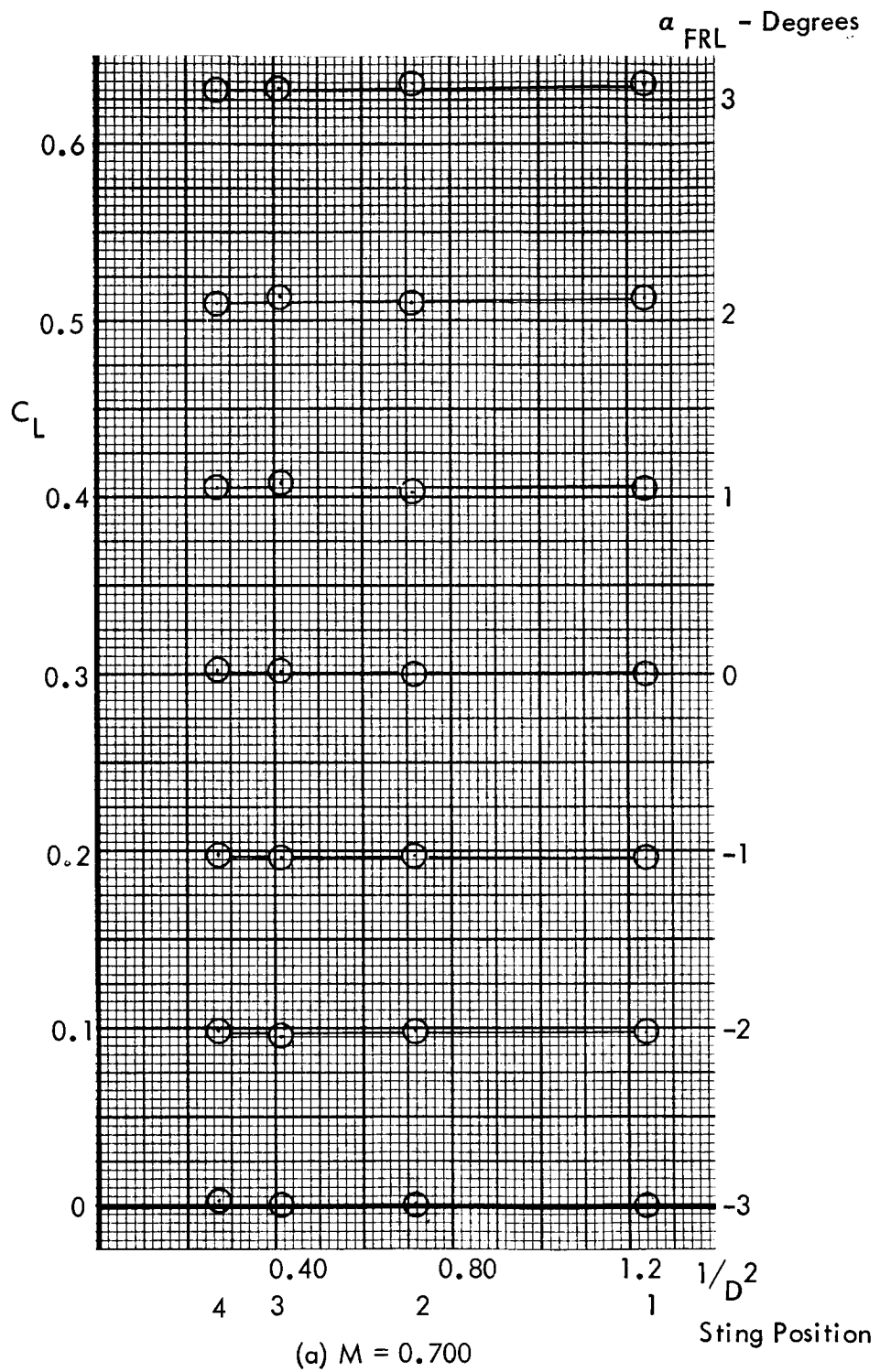
Figure 26.   Effect of Sting Position on Model
               Lift. Tail On.
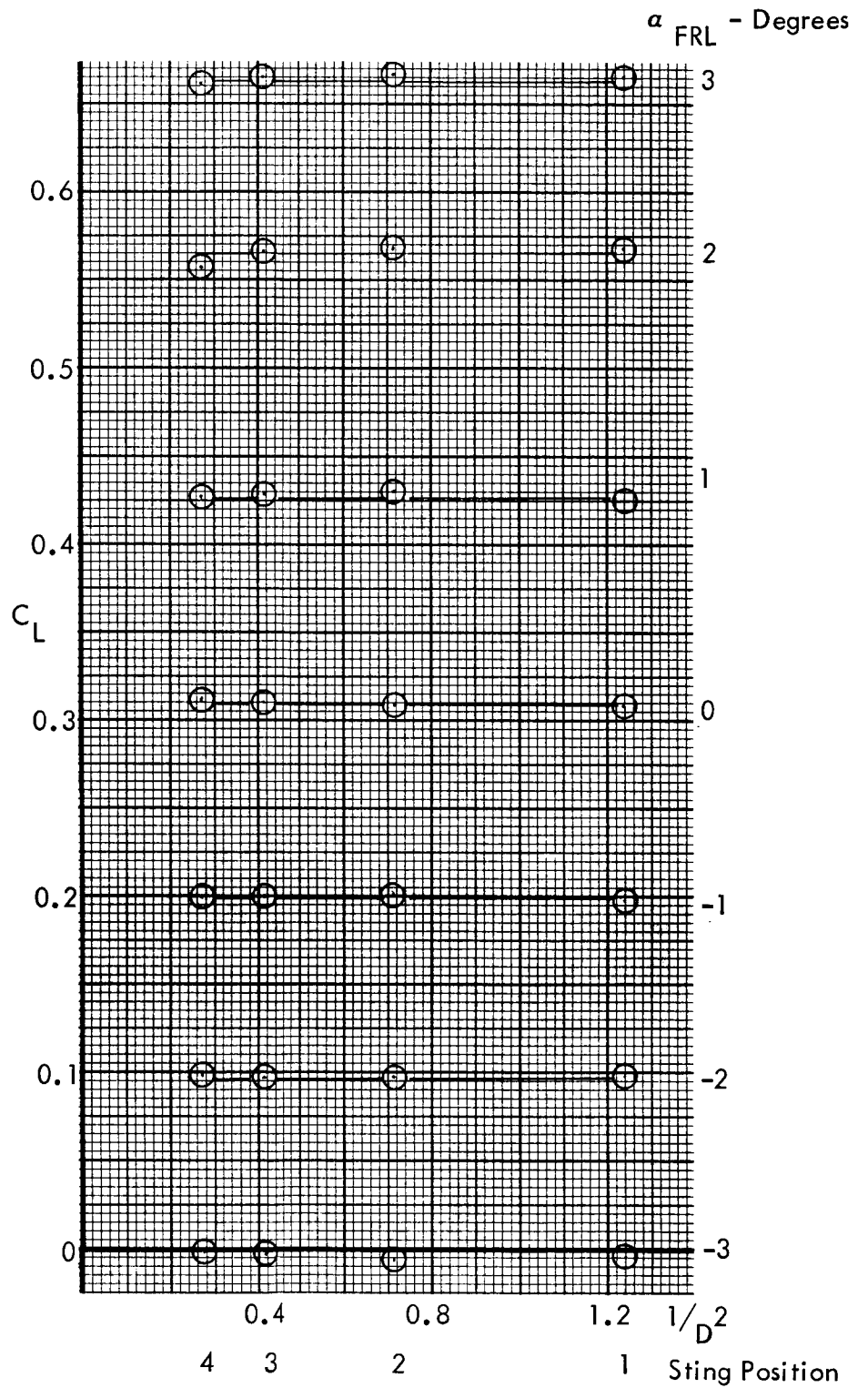
(b) M = 0.750

Figure 26.   Continued.

(c) M = 0.775

Figure 26.   Continued.

(d) M = 0.785
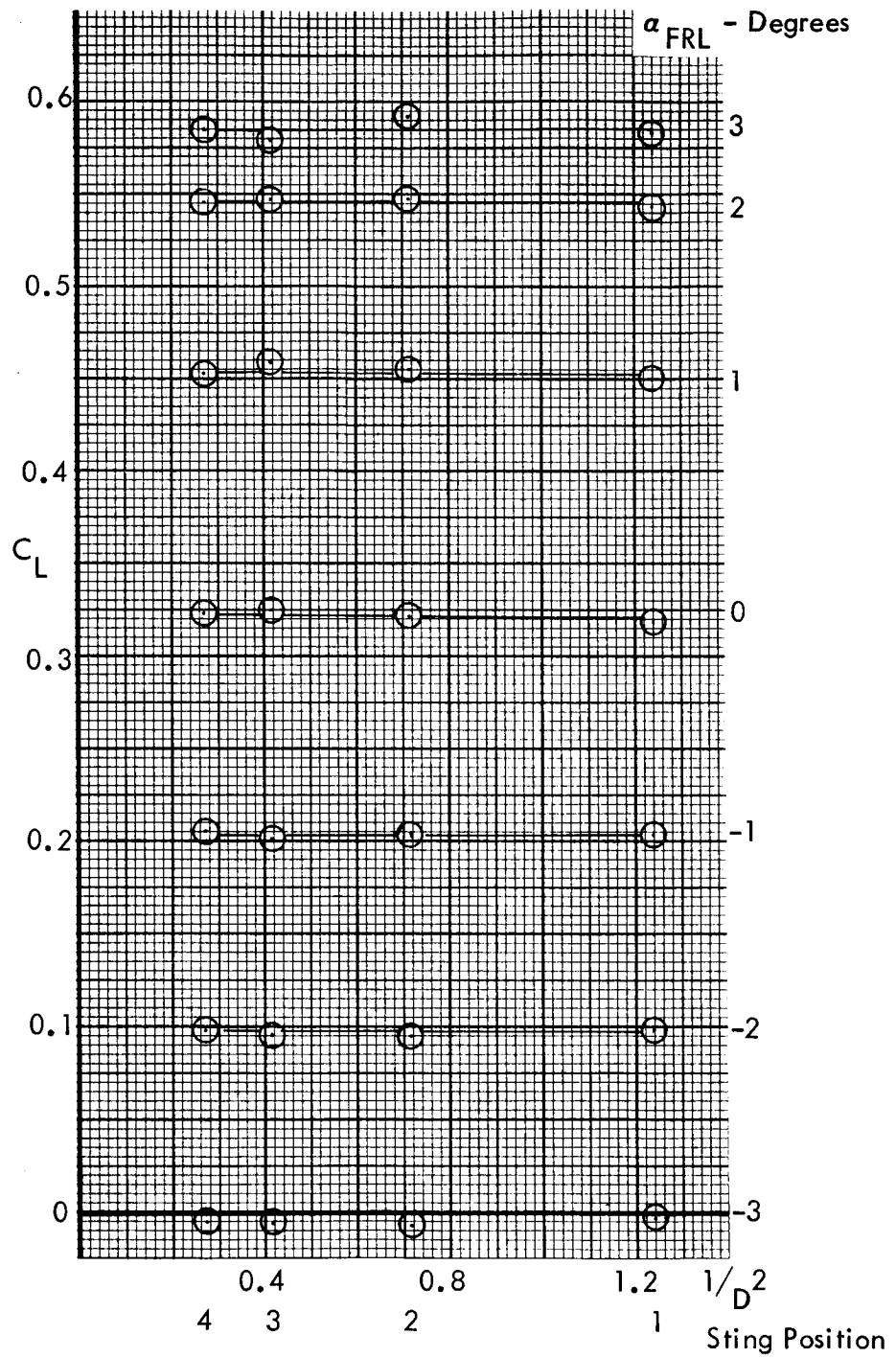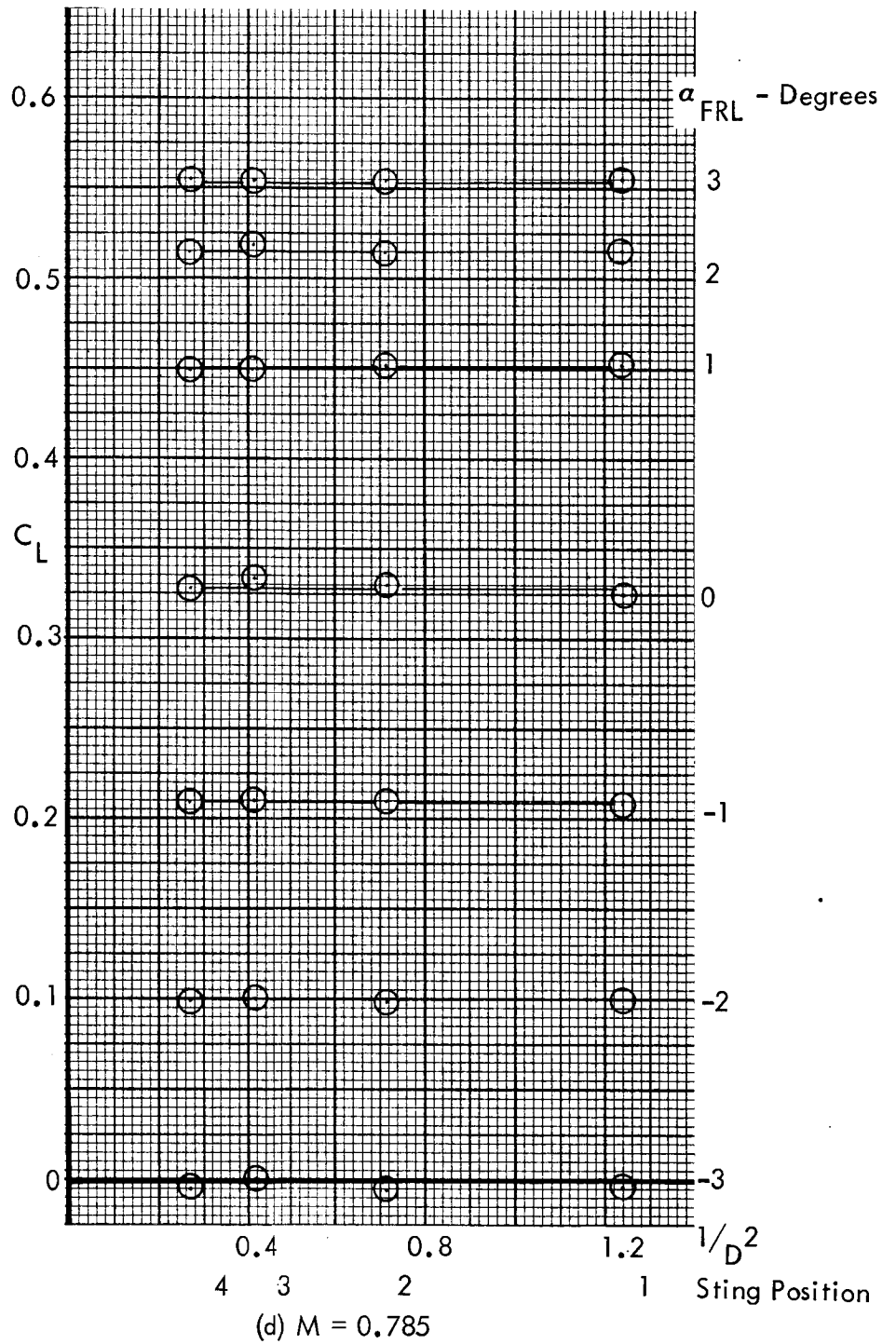
Figure 26.   Continued.
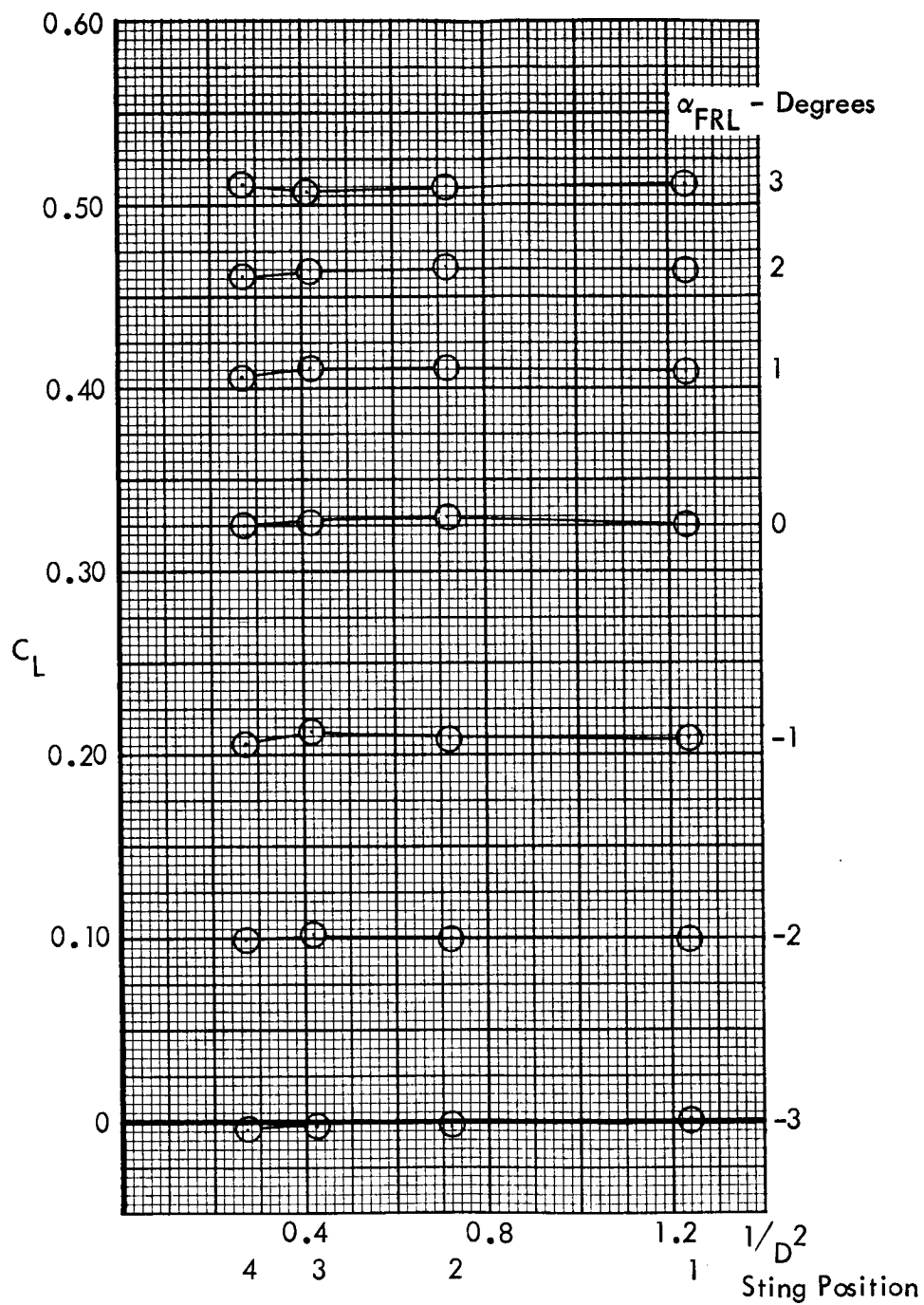
(e) M = 0.800

Figure 26. Concluded
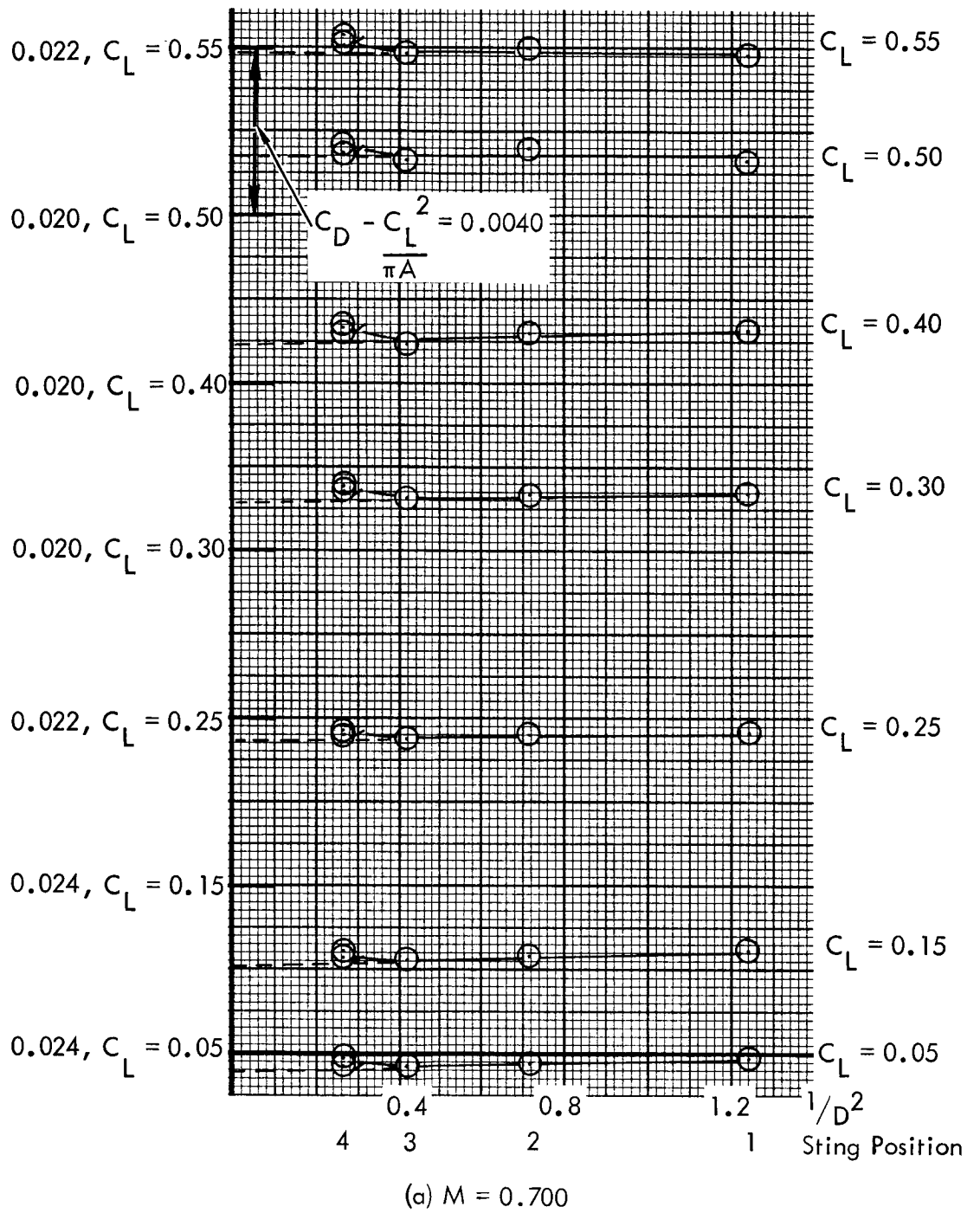
Figure 27.   Effect of Sting Position on Model
              Drag. Tail On.
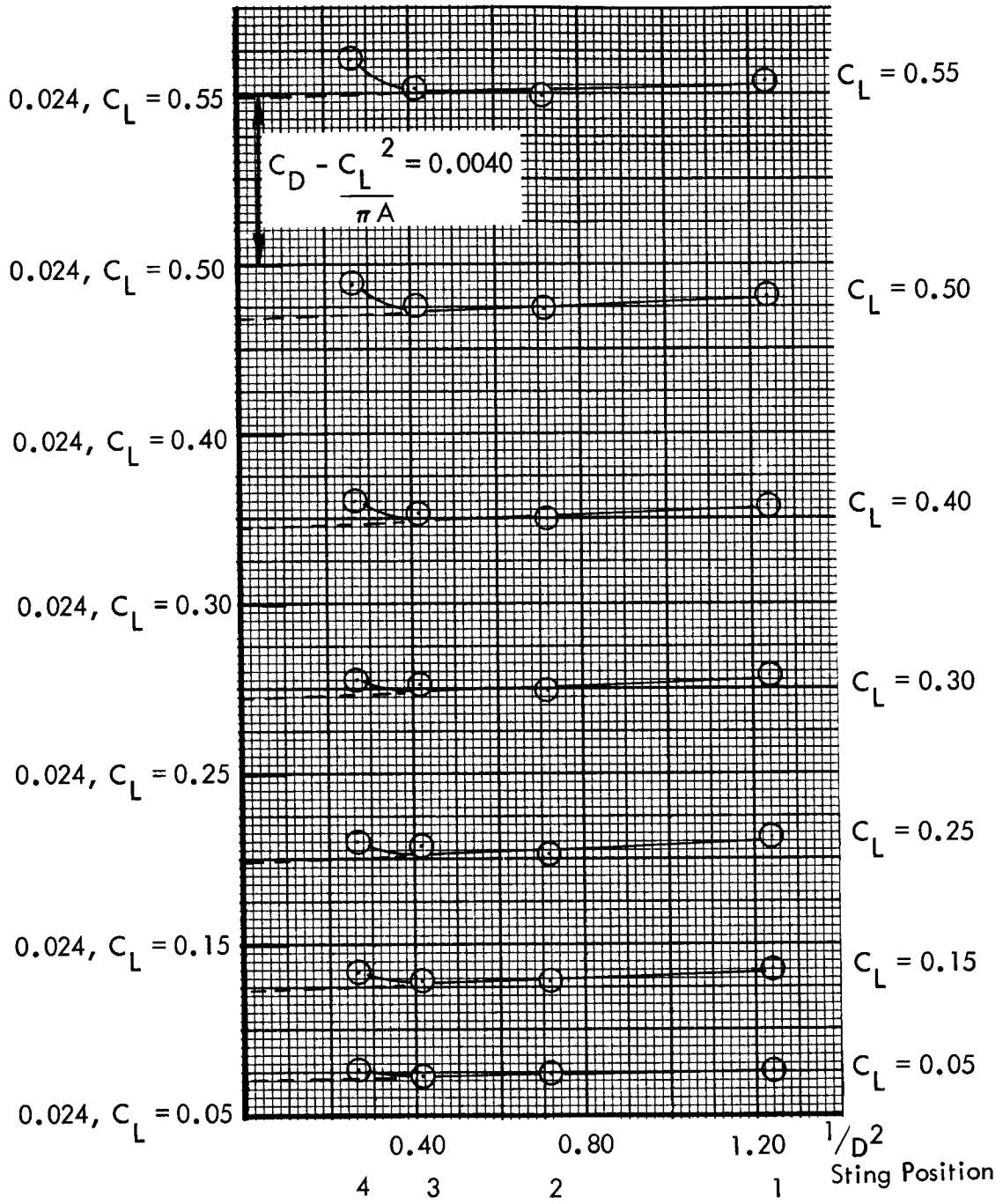
(b) M = 0.750

Figure 27.   Continued.
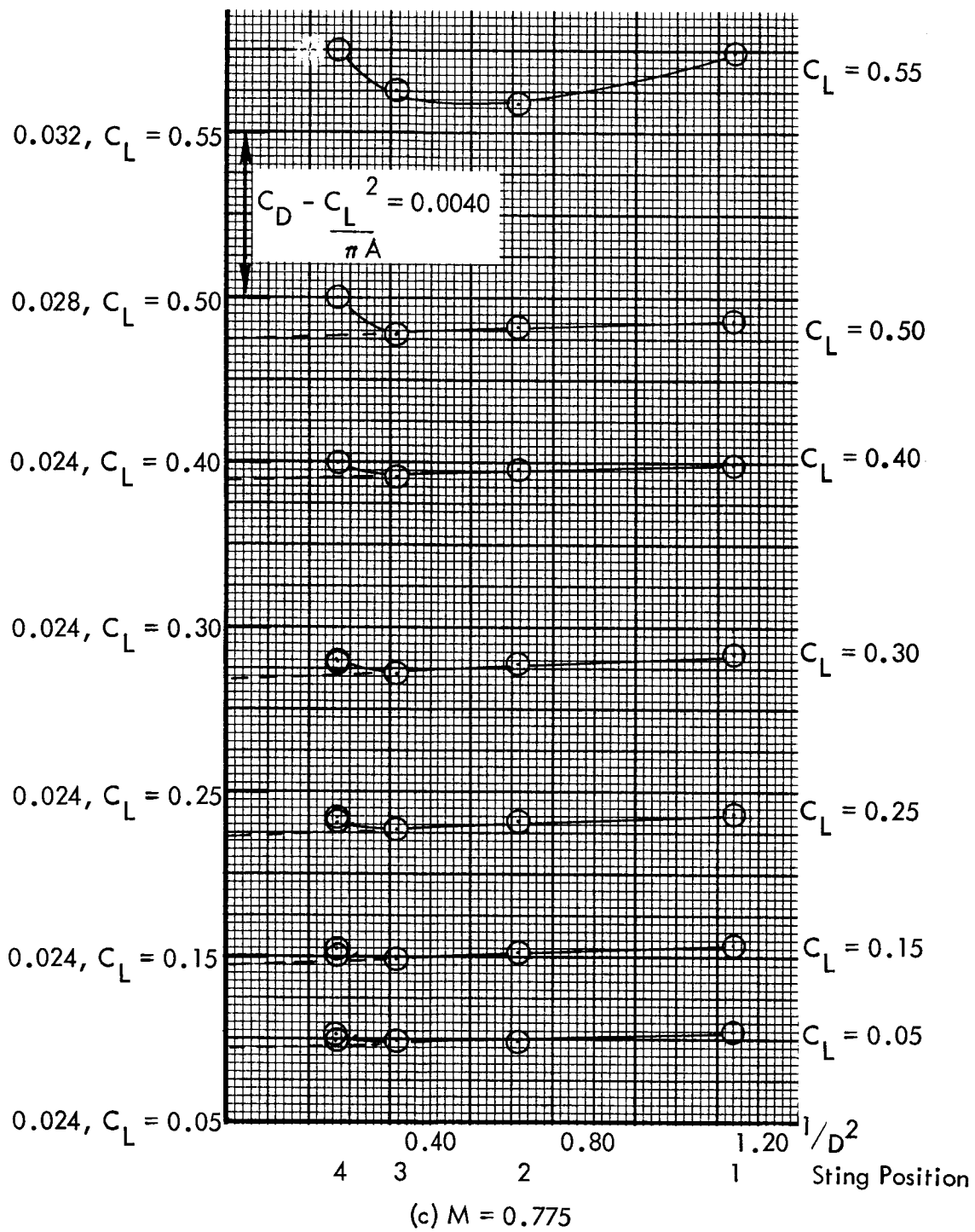
(c) M = 0.775

Figure 27. Continued

Figure 27.   Continued.

$$C_D - C_{L}^{2} = 0.0040$$
$$\hspace{1em} / \pi A$$

$C_L = 0.50$

$0.050, C_L = 0.50$

$C_L = 0.40$

$0.032, C_L = 0.40$

$C_L = 0.30$

$0.026, C_L = 0.30$

$C_L = 0.25$

$0.026, C_L = 0.25$

$C_L = 0.15$

$0.026, C_L = 0.15$

4   3   2   1   Sting Position

$C_L = 0.05$

$0.028, C_L = 0.05$

0.40   0.80   1.20 $1/_D{}^2$
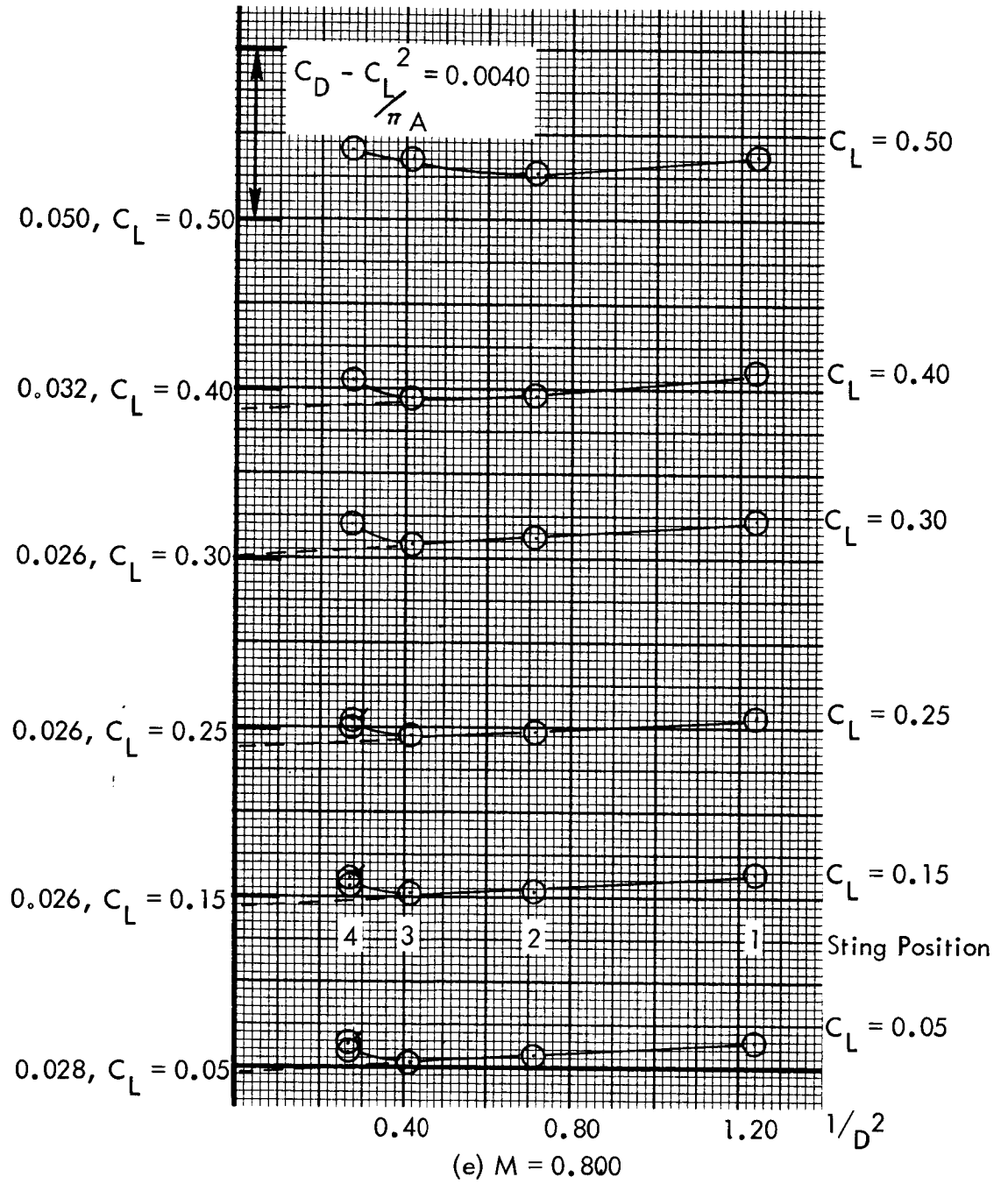
(e) M = 0.800
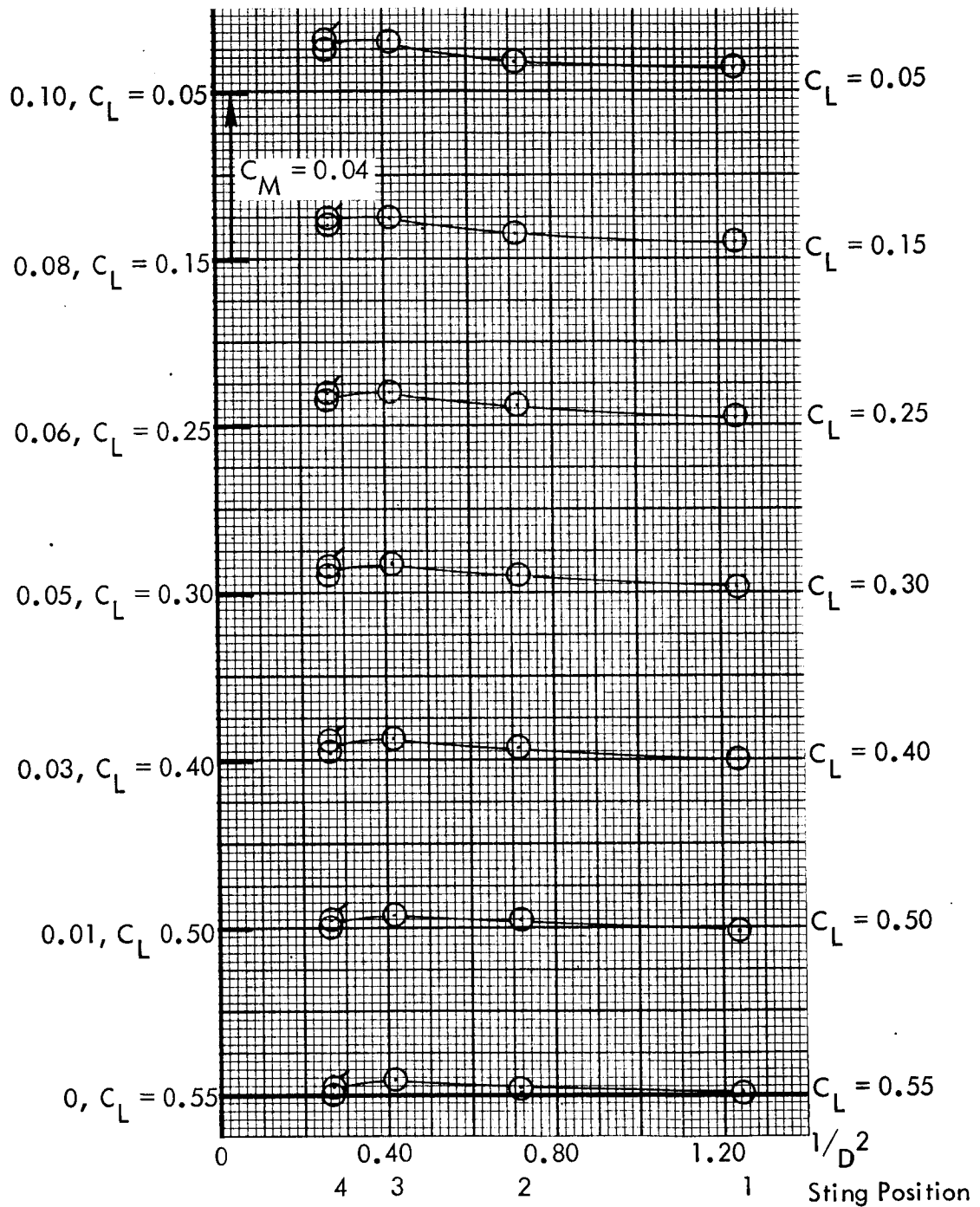
Figure 27.   Concluded.

Figure 28.   Effect of Sting Position on
Model Pitching Moment, Tail On.

(b) M = 0.750
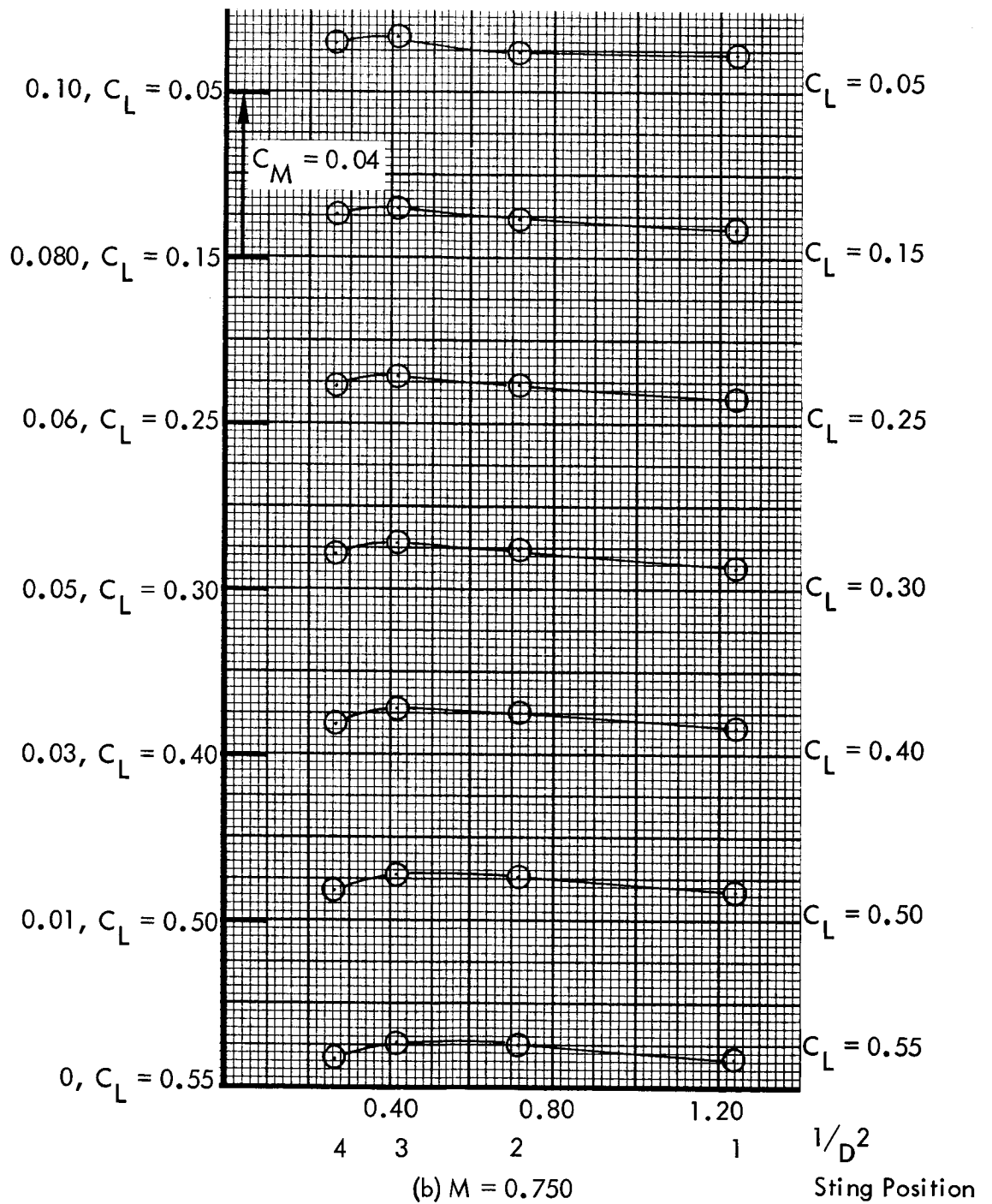
Figure 28.   Continued.
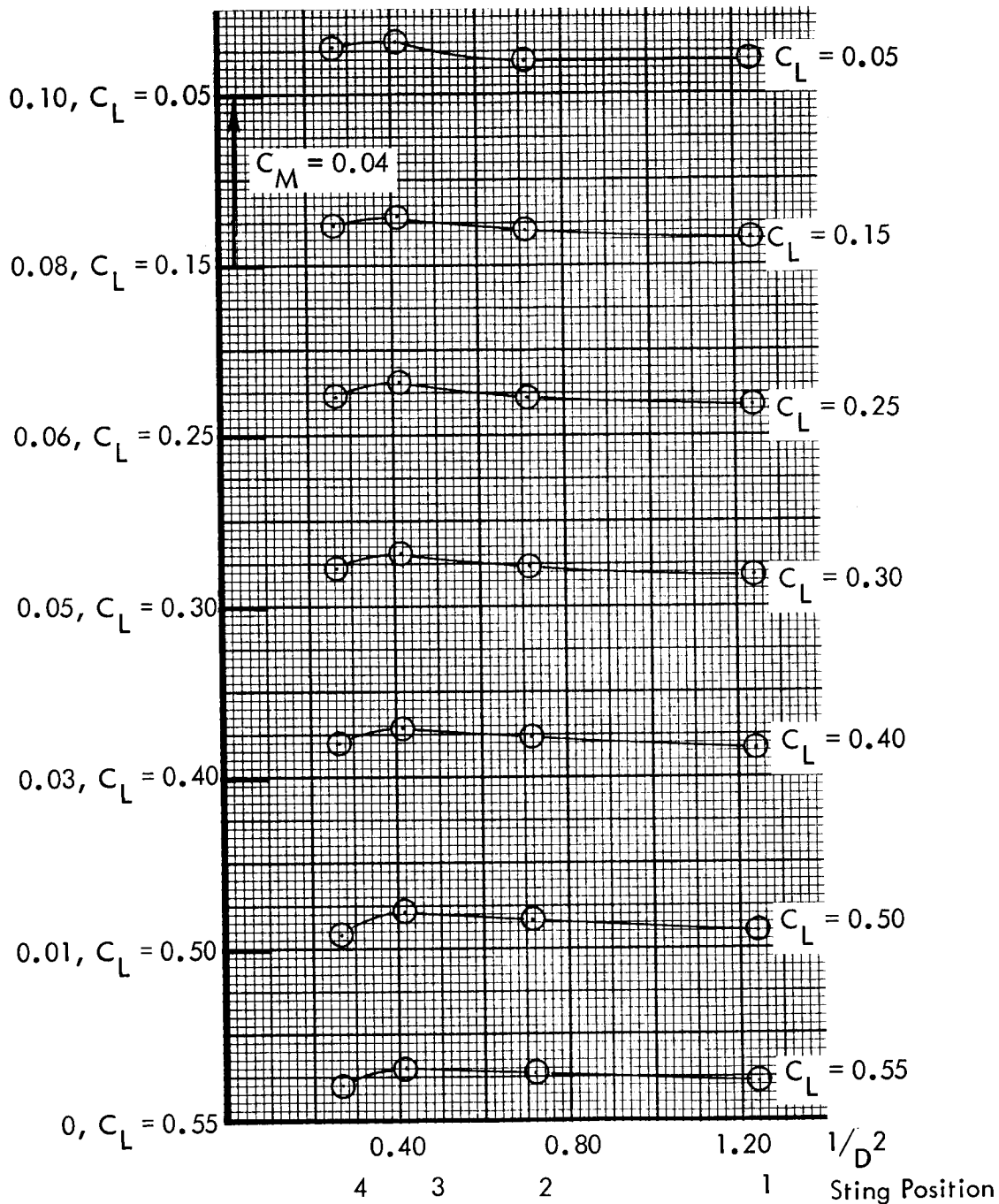
(c) M = 0.775

Figure 28.   Continued.
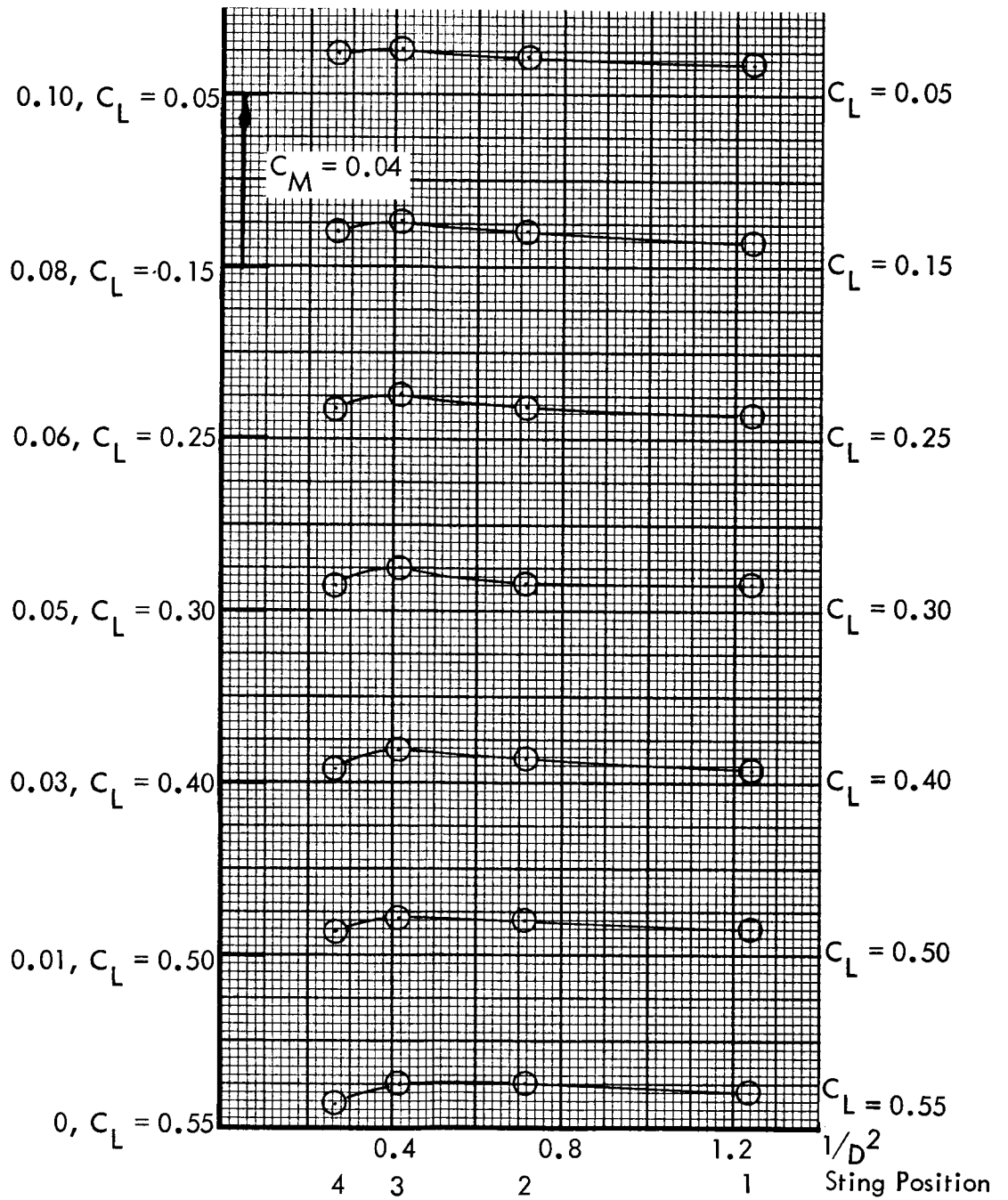
(d) M = 0.785

Figure 28.   Continued.
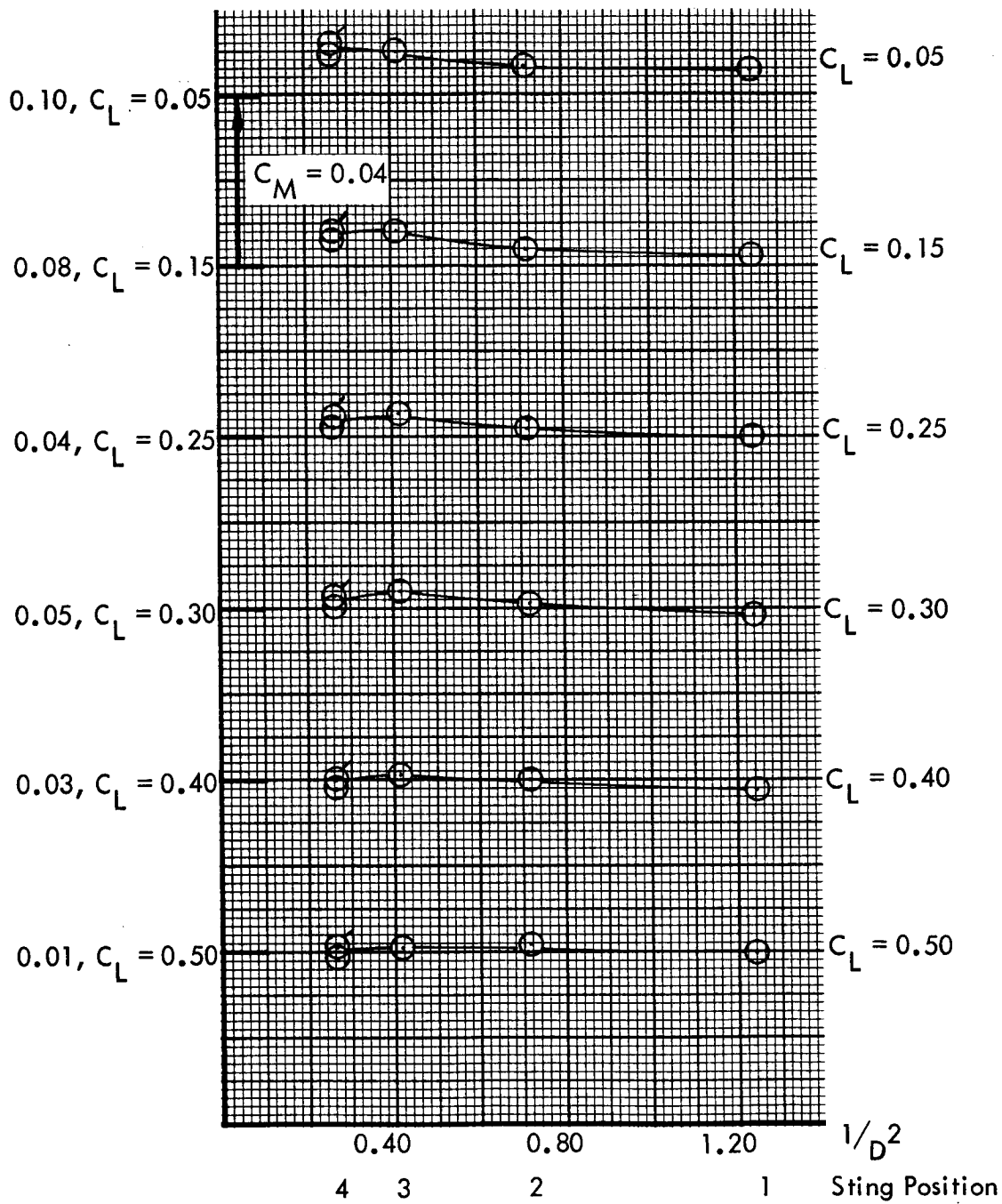
(e) M = 0.800

Figure 28.   Concluded.
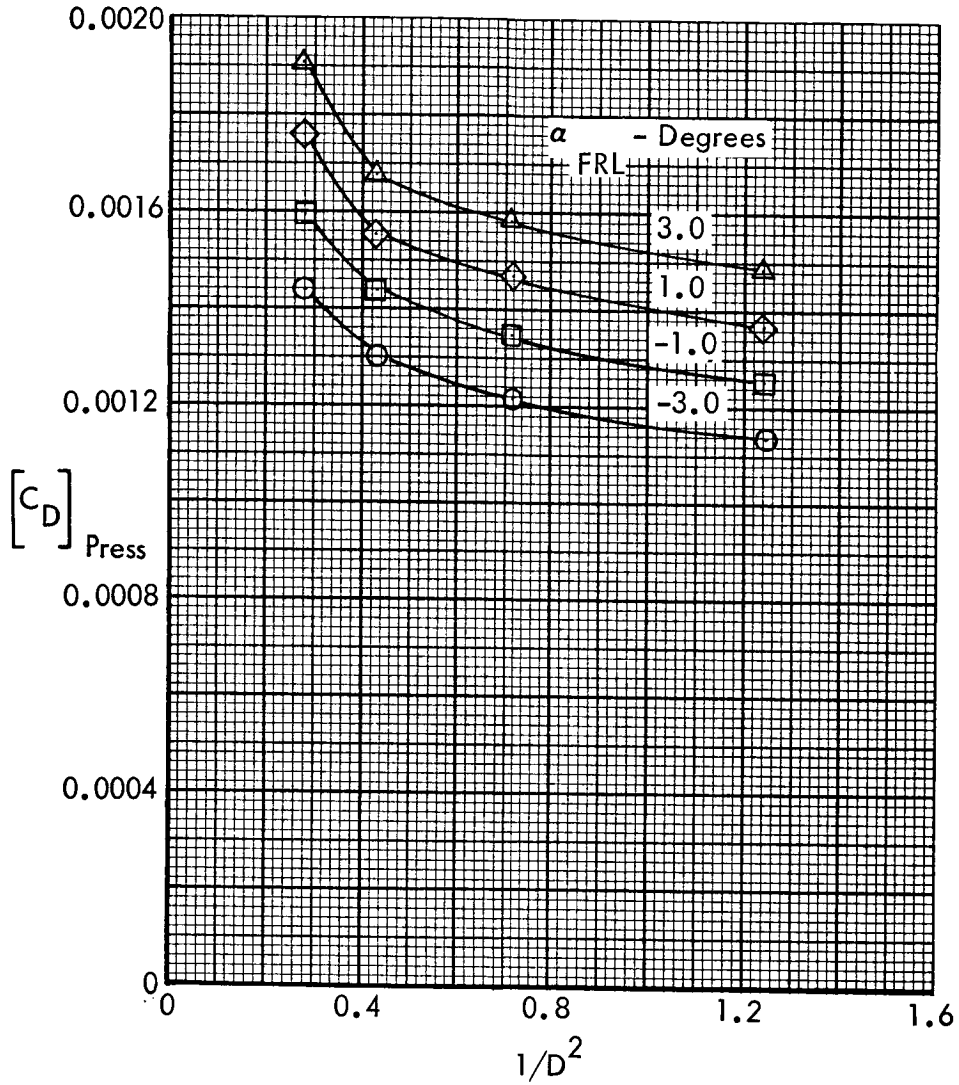
Figure 29.   Sting Interference Effect on Afterbody
Pressure Drag.
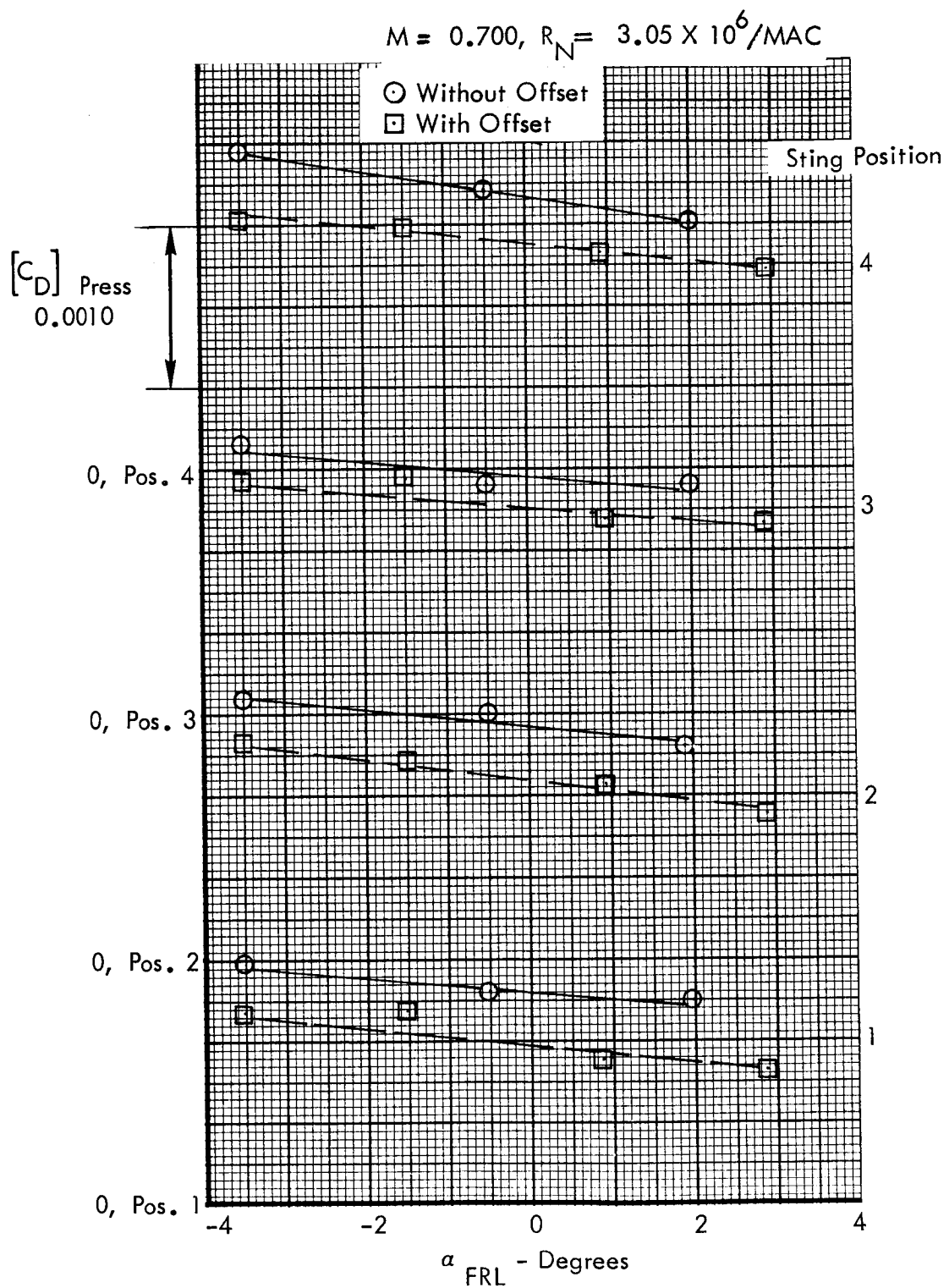
Figure 30.   Effect of Sting Offset Fairing on
Afterbody Pressure Drag.
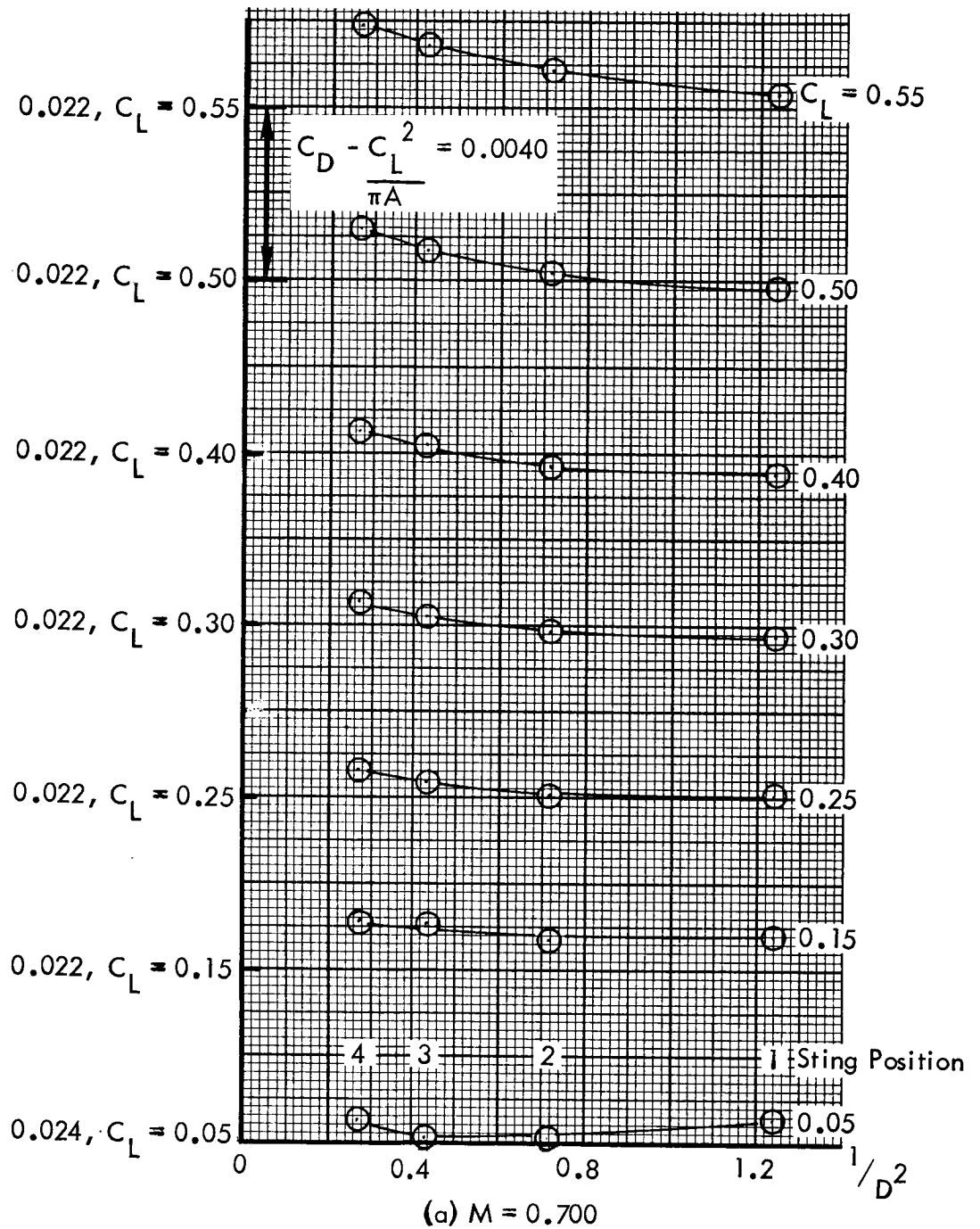
Figure 31. Effect of Sting Position on Model Drag. Tail-On
Central Sting, No Offset
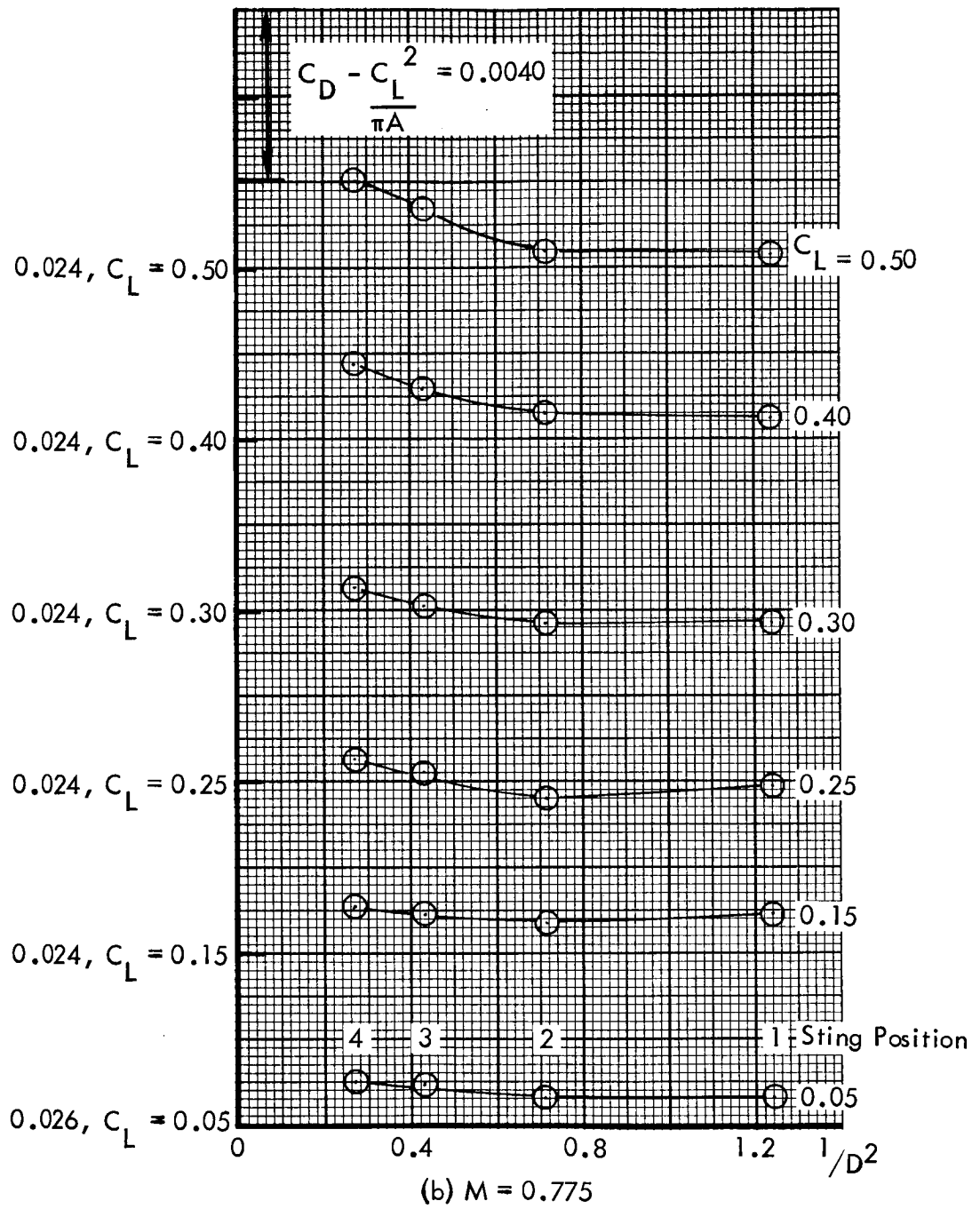
Figure 31. Concluded
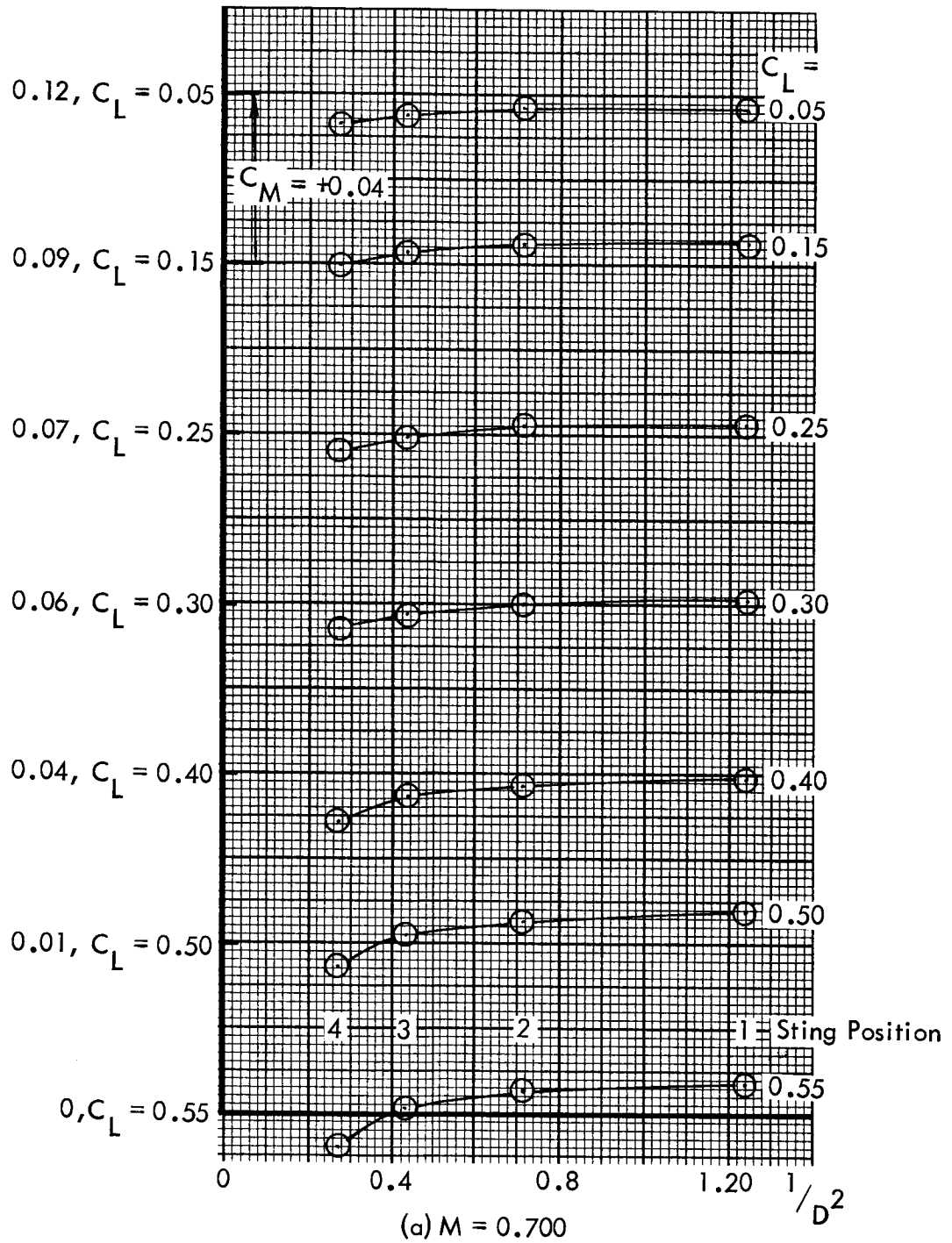
Figure 32. Effect of Sting Position on Model Pitching
Moment. Tail-on, Central Sting, No
Offset.
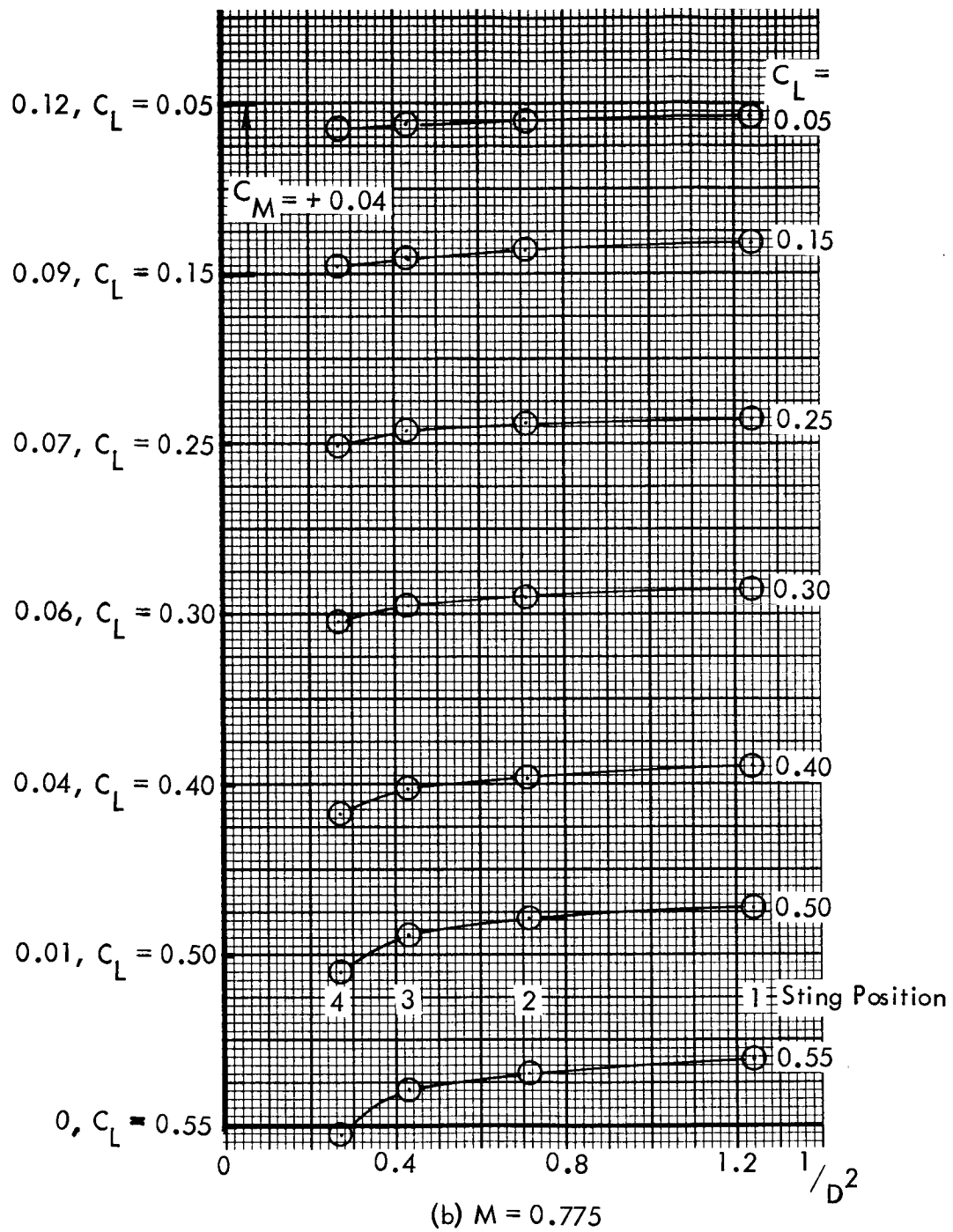
(b) M = 0.775

Figure 32. Concluded
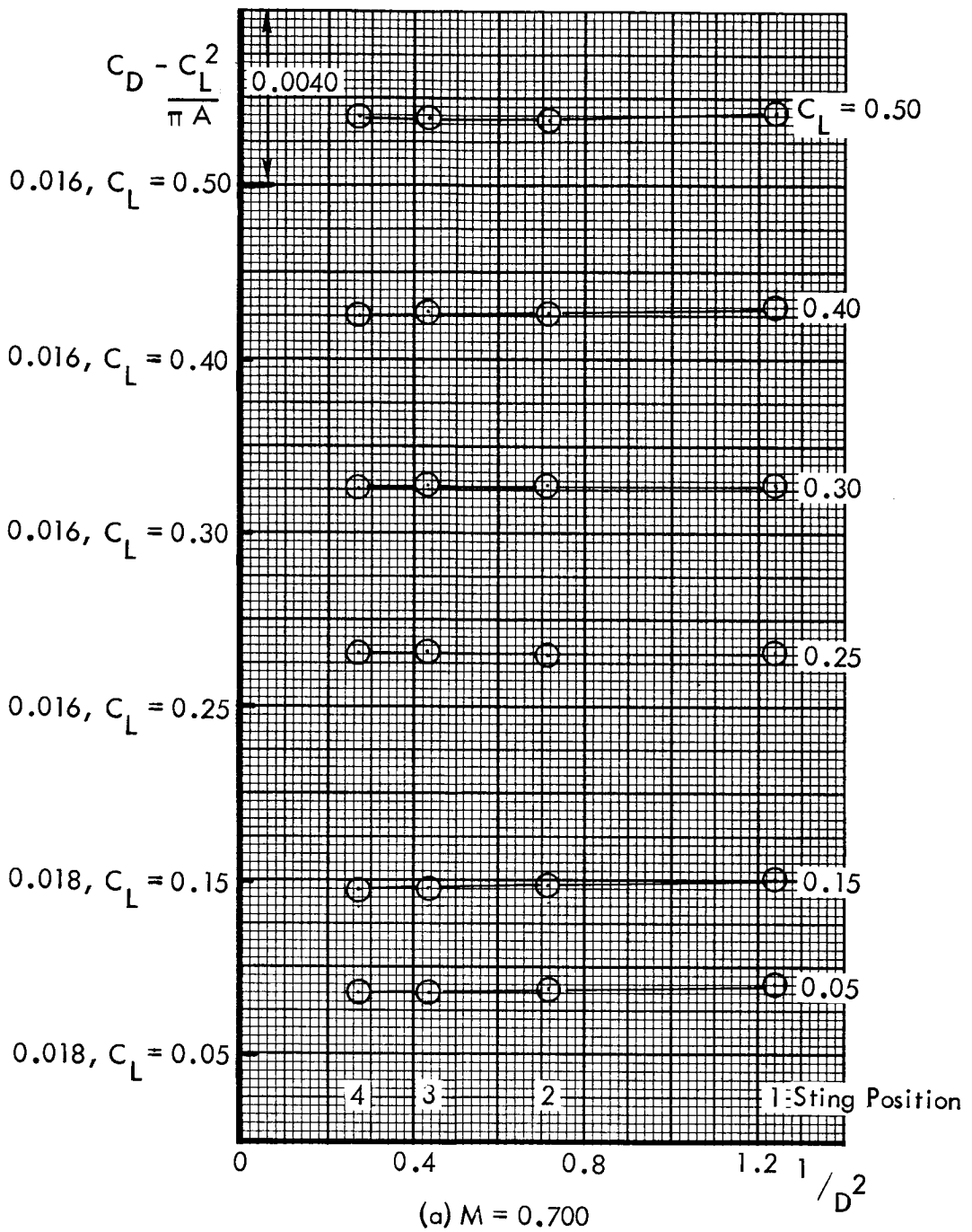
Figure 33. Effect of Sting Position on Model
Drag. Tail Off.
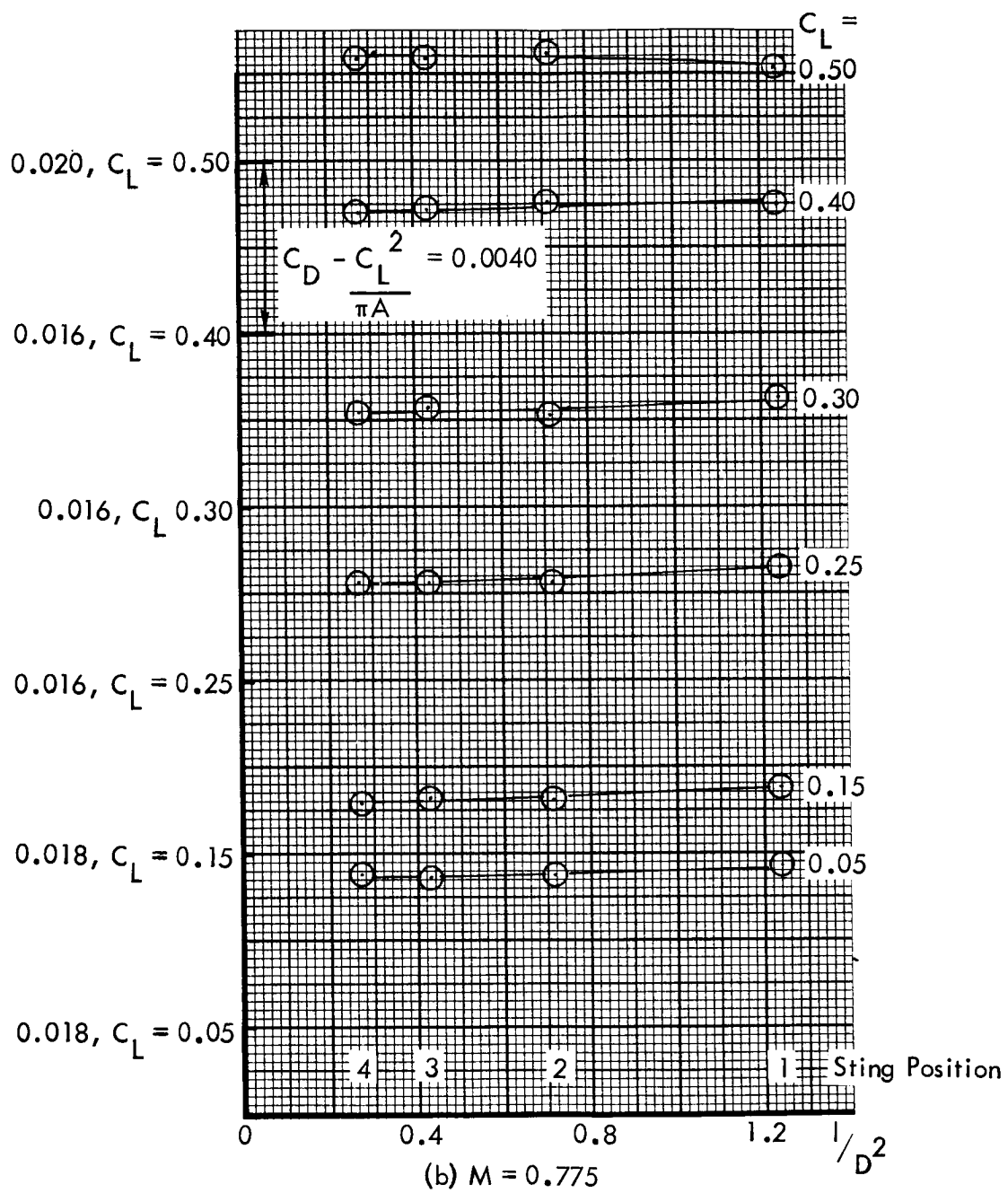
Figure 33. Concluded
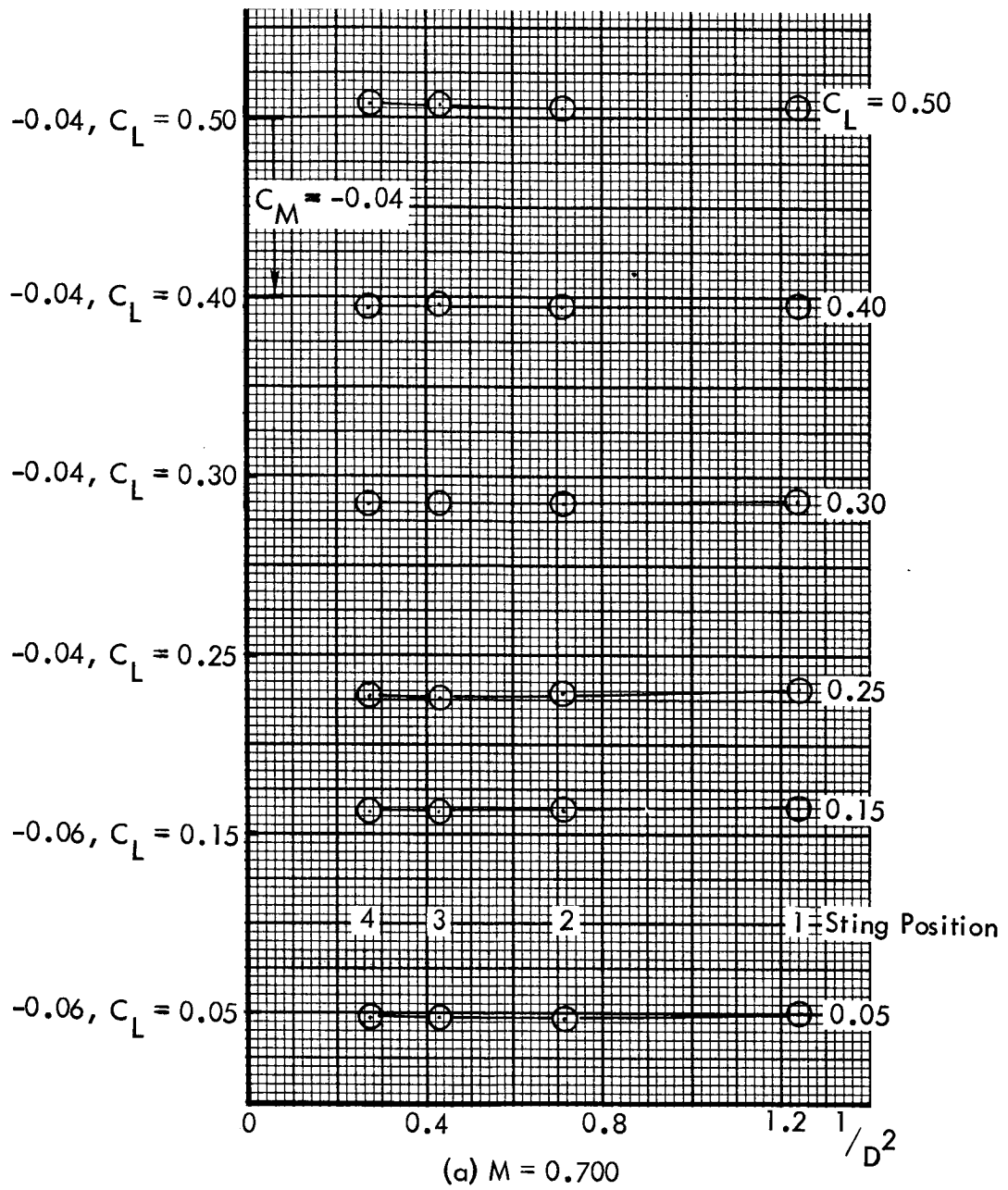
Figure 34. Effect of Sting Position on Model Pitching Moment. Tail Off.
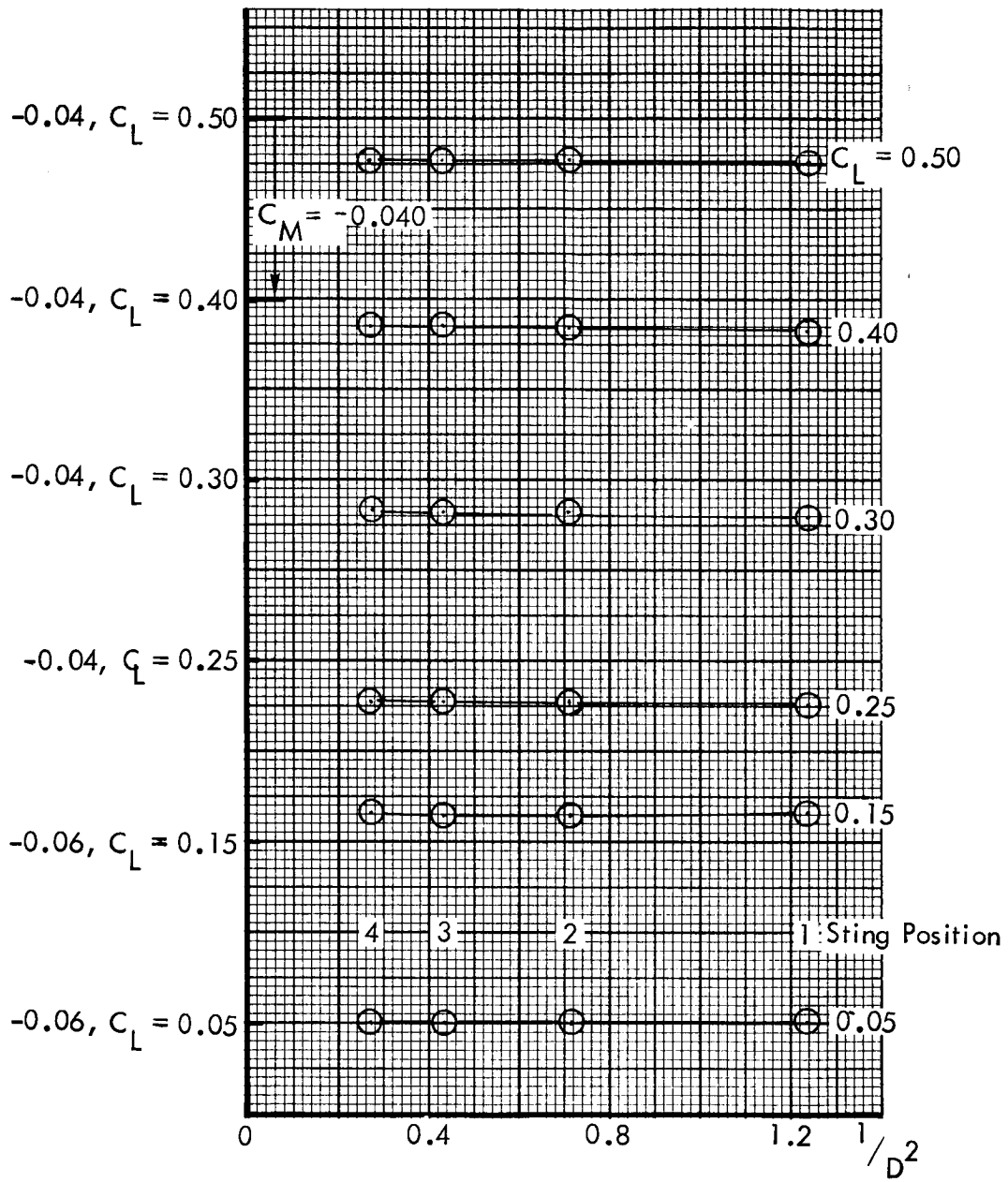
(b) M = 0.775

Figure 34. Concluded
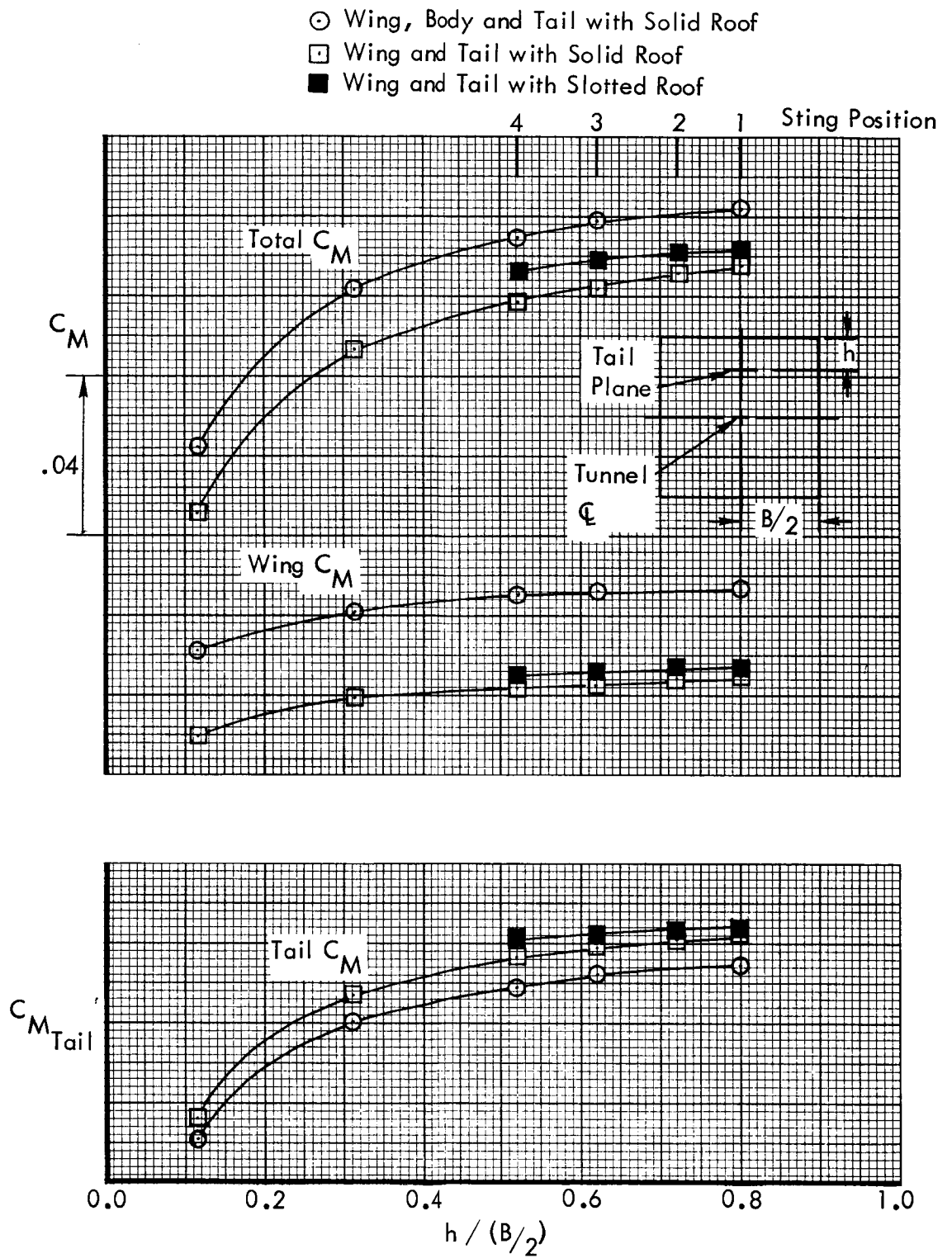
Figure 35(a). Theoretical Effect of Ceiling on Model Pitching Moment.
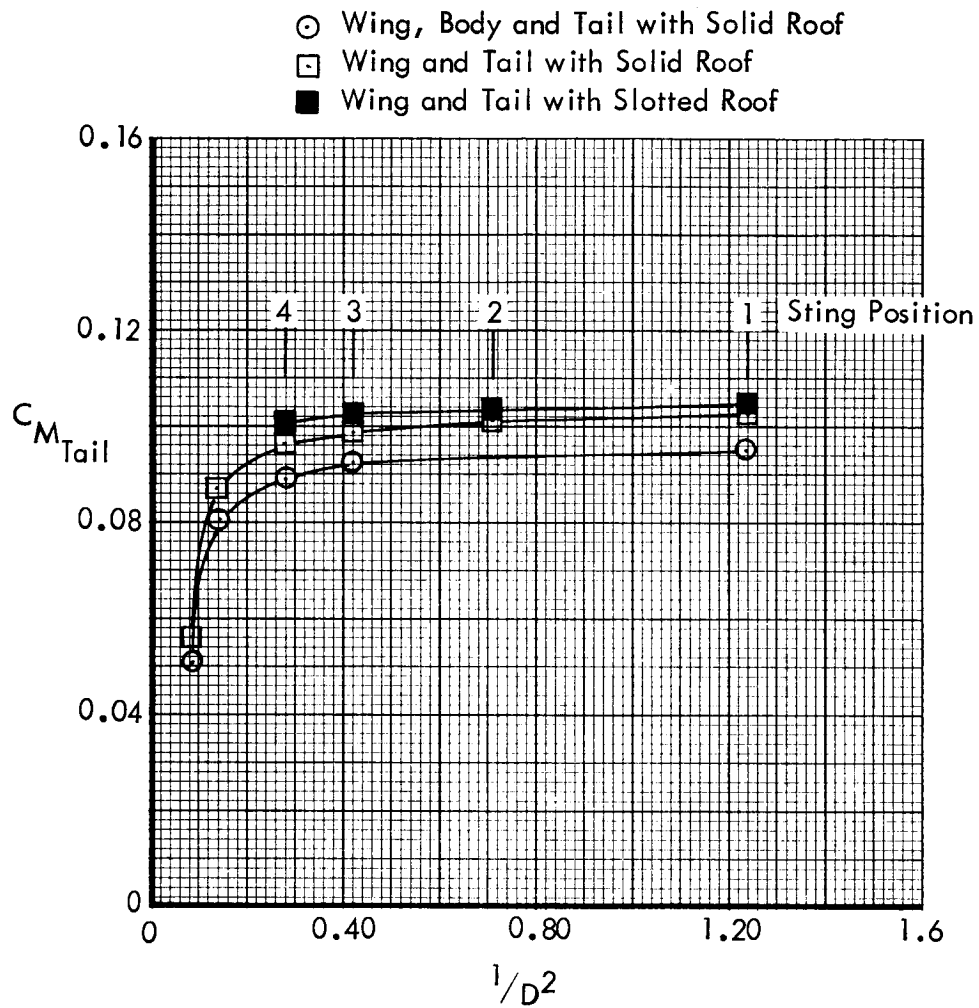
Figure 35(b). Theoretical Effect of Ceiling
on Tail Pitching Moment.
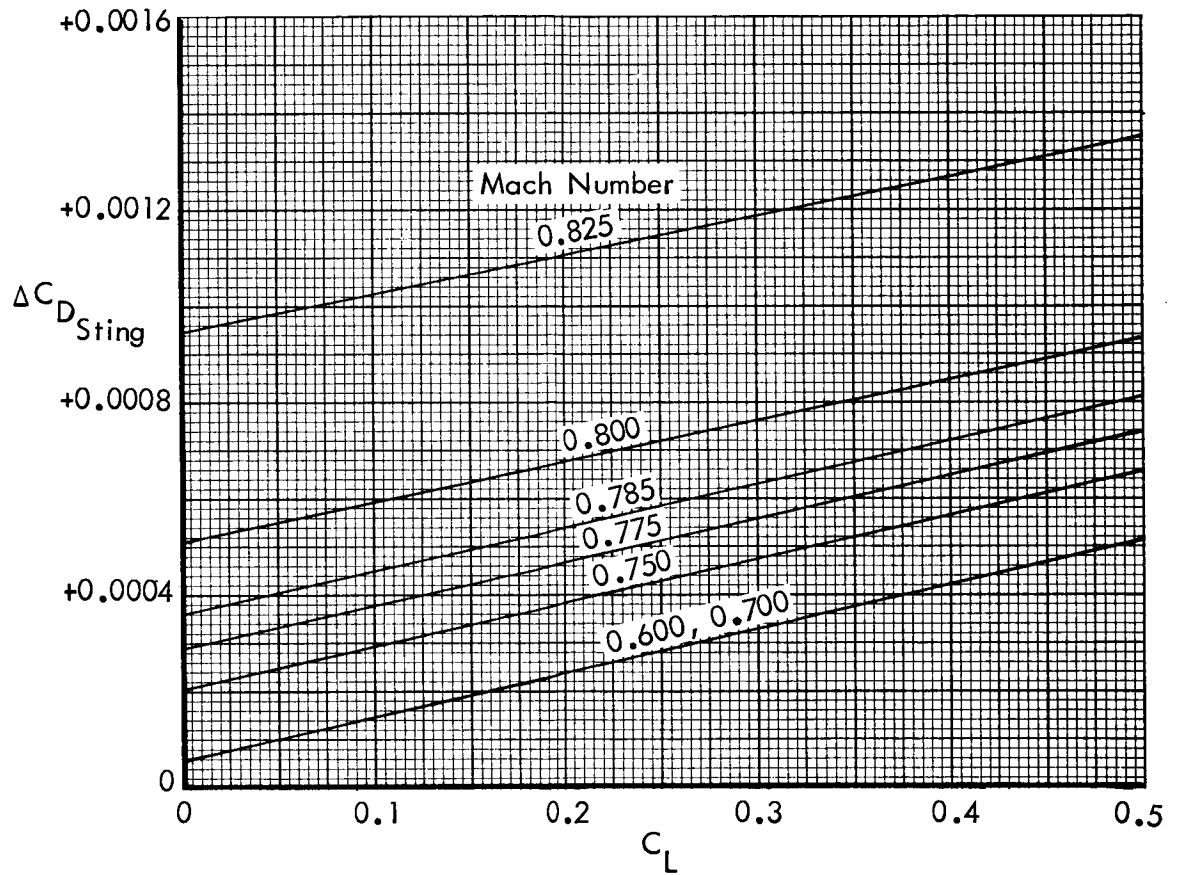
Figure 36. Sting Interference Corrections

$C_L = -0.04$

$\Delta C_L = 0.0, M = 0.825$

$\Delta C_L = 0.0, M = 0.800$

$\Delta C_L = 0.0, M = 0.785$

$\Delta C_L = 0.0, M = 0.775$

$\Delta C_L = 0.0, M = 0.750$

$\Delta C_L = 0.0, M = 0.700$

$\Delta C_L = 0.0, M = 0.600$

-4   -2   0   2   4

a_{FRL} - Degrees
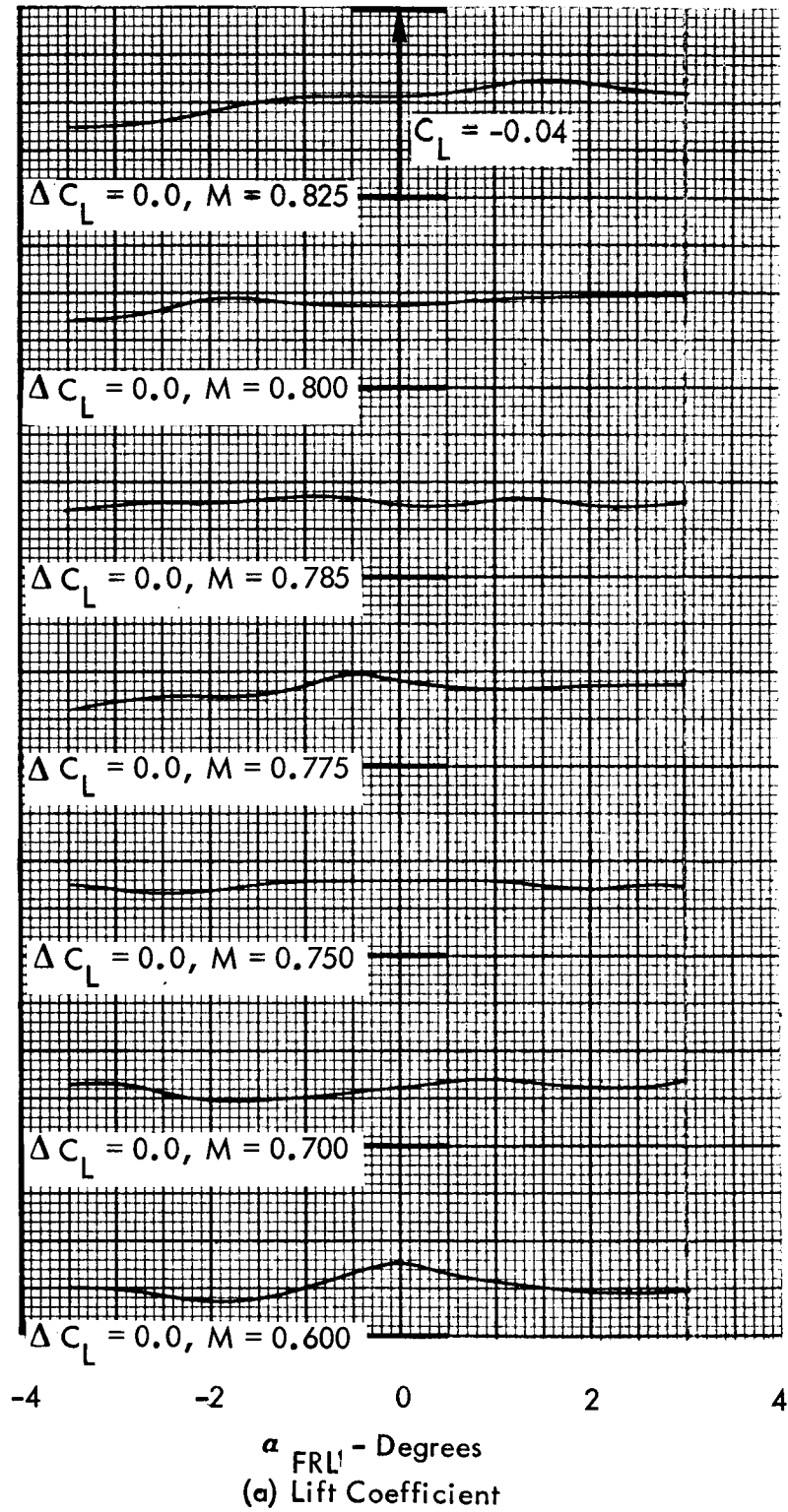
(a) Lift Coefficient

Figure 37.   Blade Interference on Model.
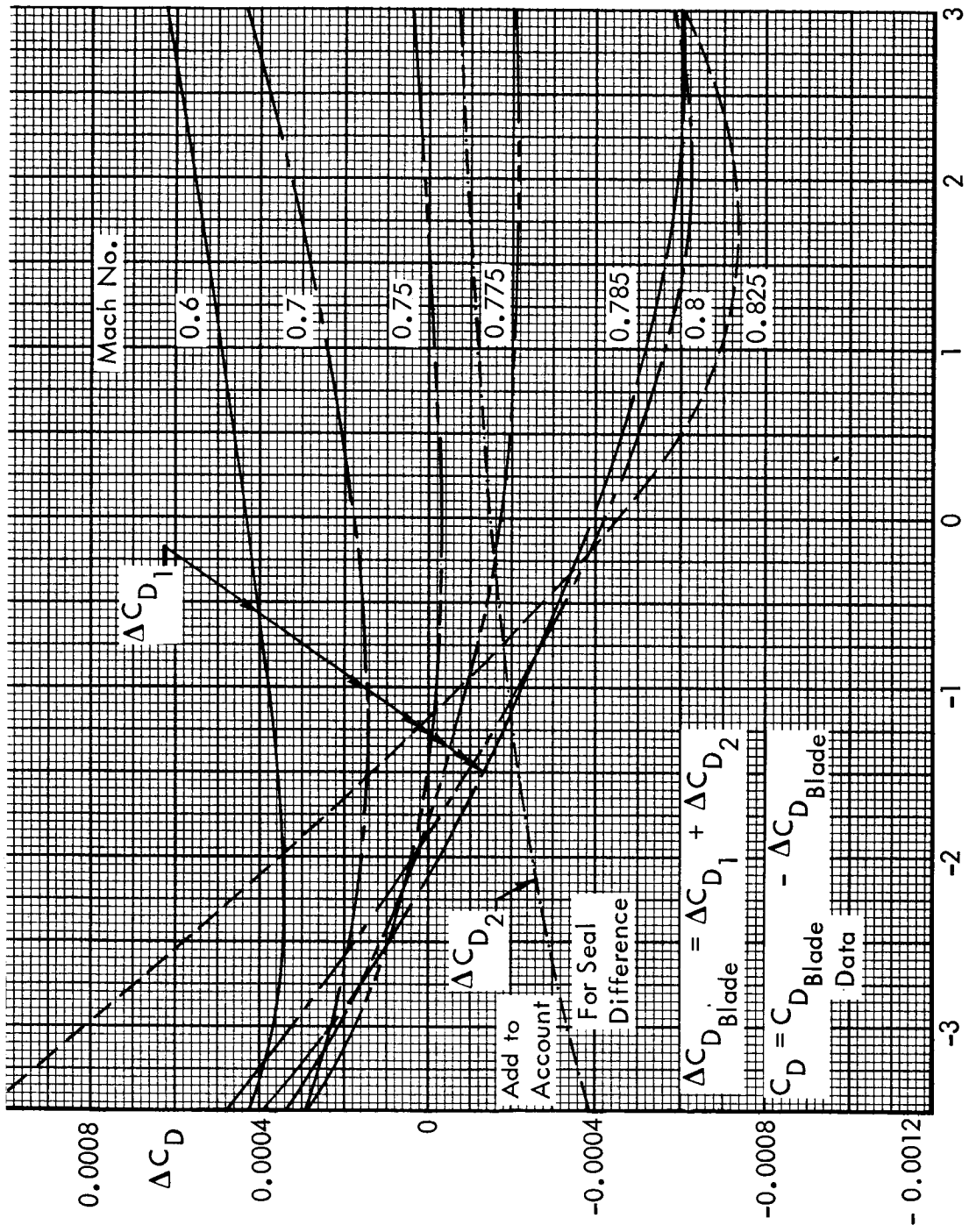
a_{FRL} - Degrees
(b) Drag Coefficient
Figure 37.   Continued.

$\Delta C_m = 0.0, M = 0.0$

$\Delta C_m = 0.0, M = 0.800$

$\Delta C_m = 0.0, M = 0.785$

$\Delta C_m = 0.0, M = 0.775$

$\Delta C_m = 0.0, M = 0.75$

$\Delta C_M = -0.04$

$\Delta C_m = 0.0, M = 0.700$

$\Delta C_m = 0.0, M = 0.600$
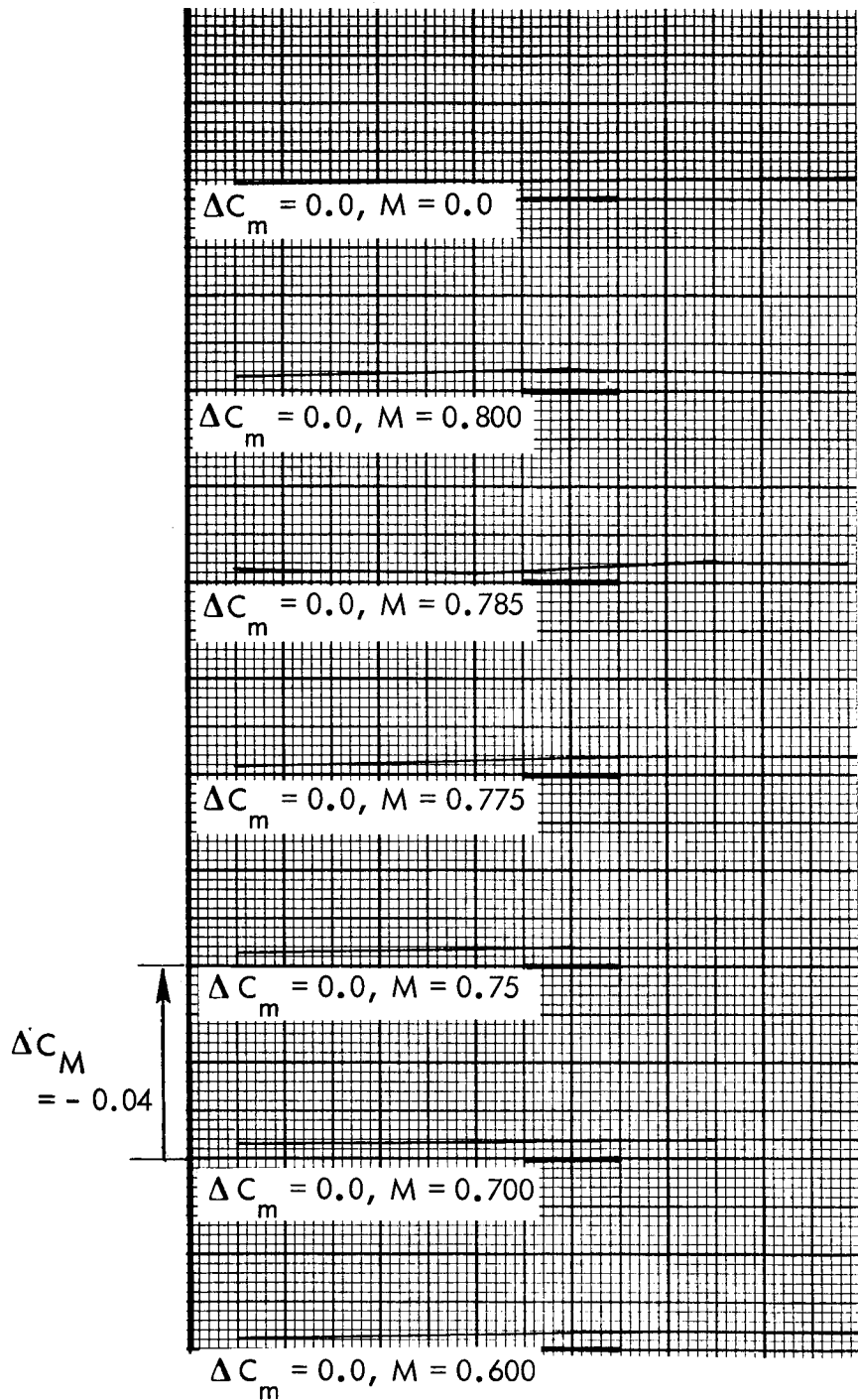
(c) Pitching Moment Coefficient

Figure 37.   Continued.

M = 0.600
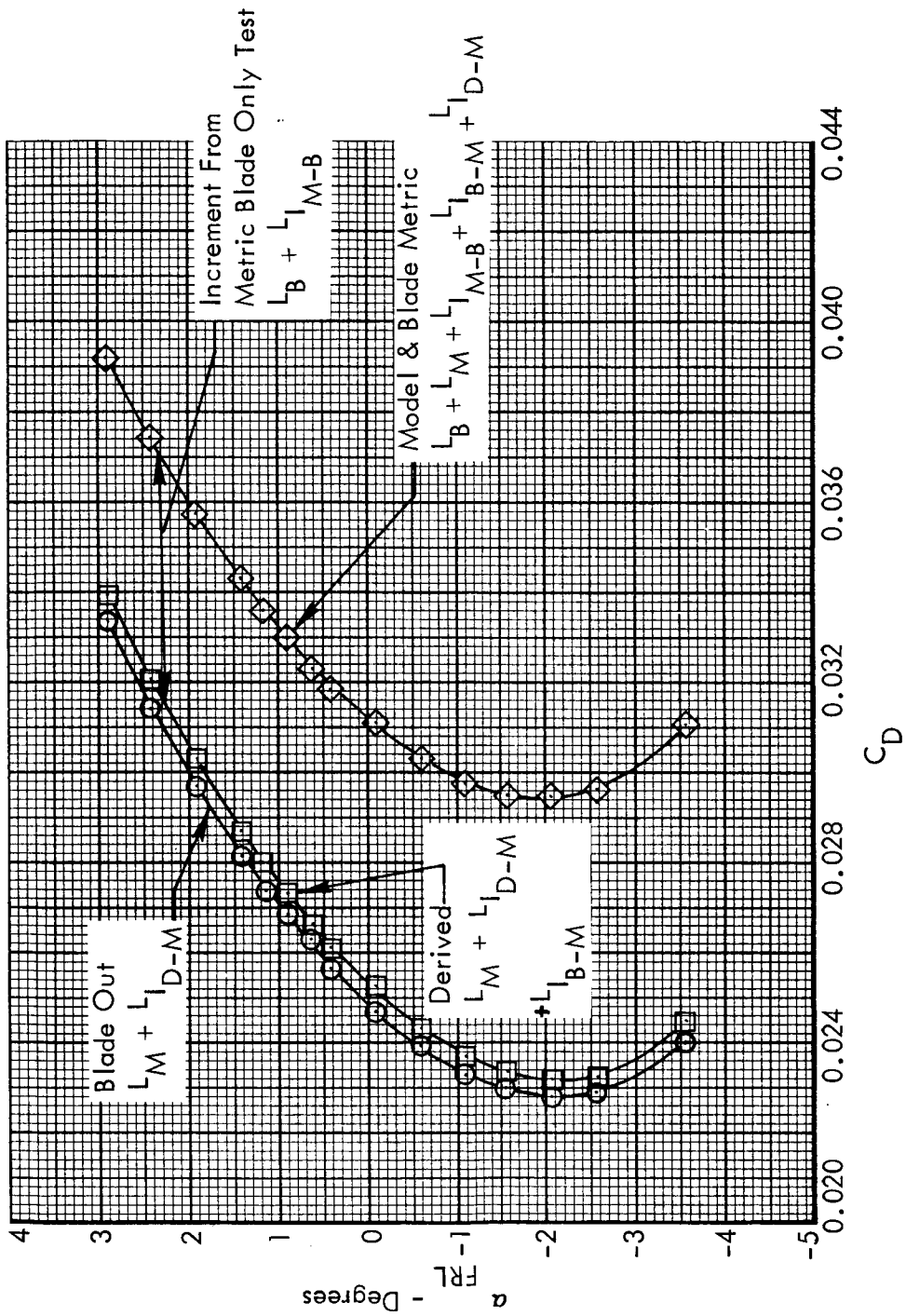
Figure 38.   Example of Drag Polar Evaluation to Determine
Blade Interference on Model.

$$M = 0.700$$

$$R_N = 3.05 \times 10^6/MAC$$

O Dorsal Mount Only
□ Dorsal Mount Only Dummy Lower Blade
◇ Dorsal Mount Only Dummy Lower Sting
△ Dorsal Mount Only Dummy Lower Blade & Sting
◣ Mounted on Lower Blade & Sting
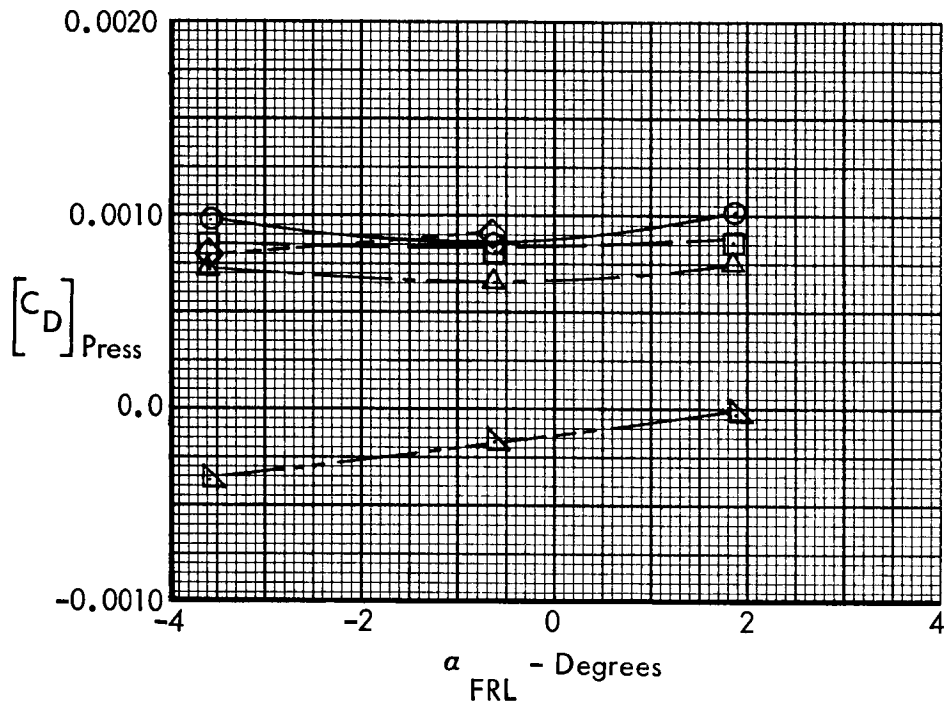
Figure 39.   Blade, Sting, Dorsal Effects on
Afterbody Pressure Drag.
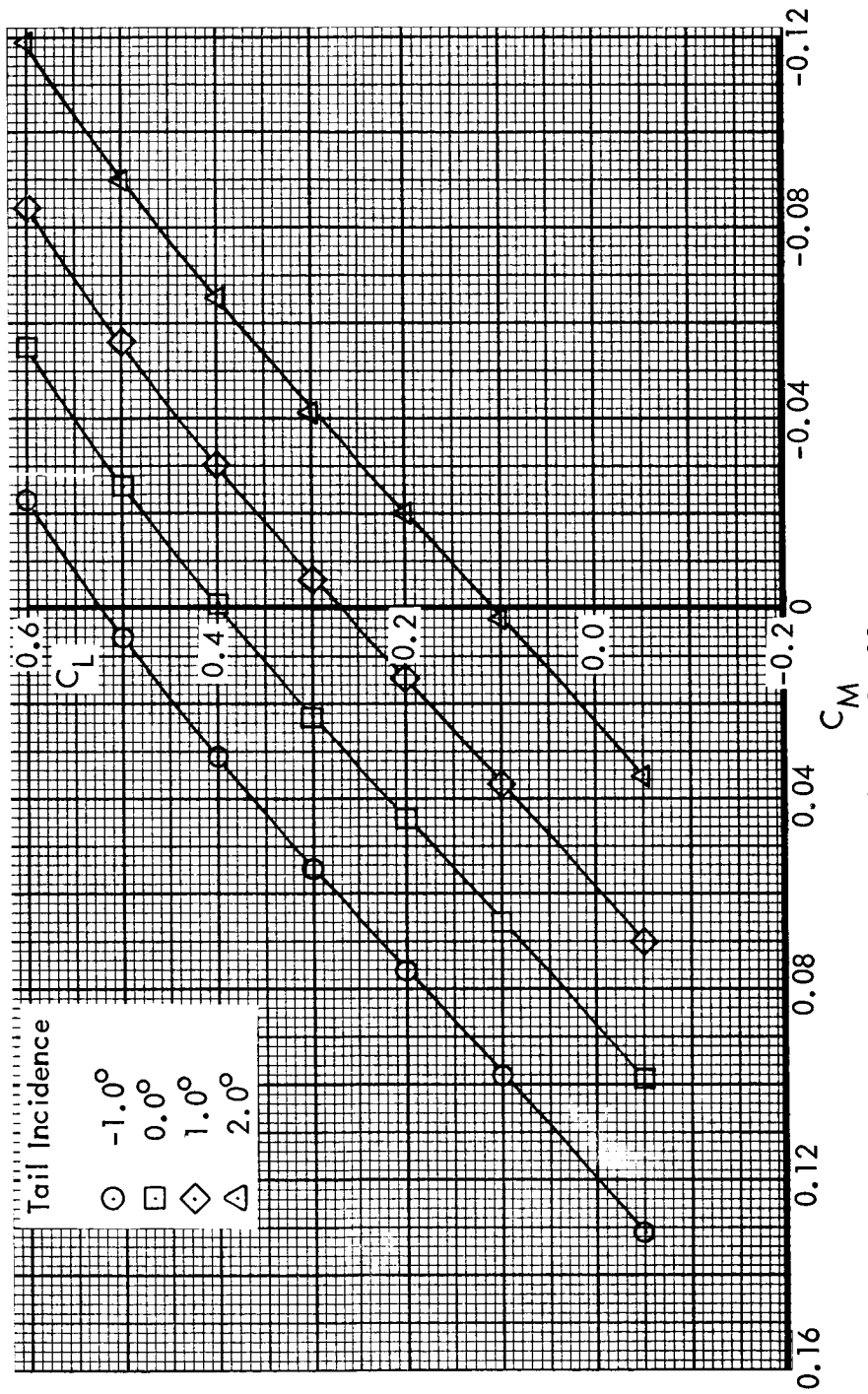
Figure 40. Effect of Horizontal Stabilizer Incidence on Pitching Moment – Data Corrected for Blade Tare and Interference.
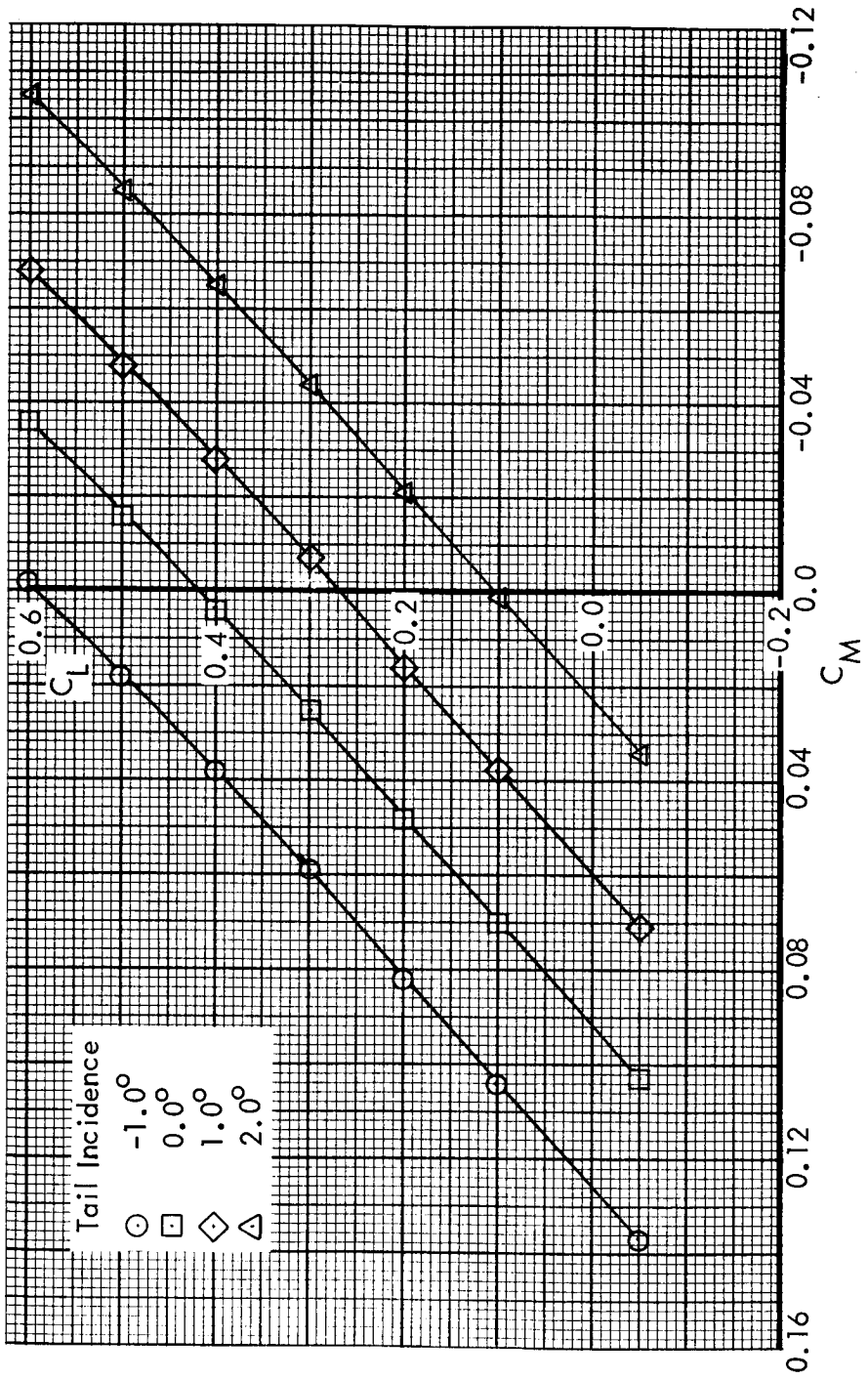
(b) M = 0.700

Figure 40. Continued

$R_N = 3.05 \times 10^6 / MAC$
Sting Position No. 4
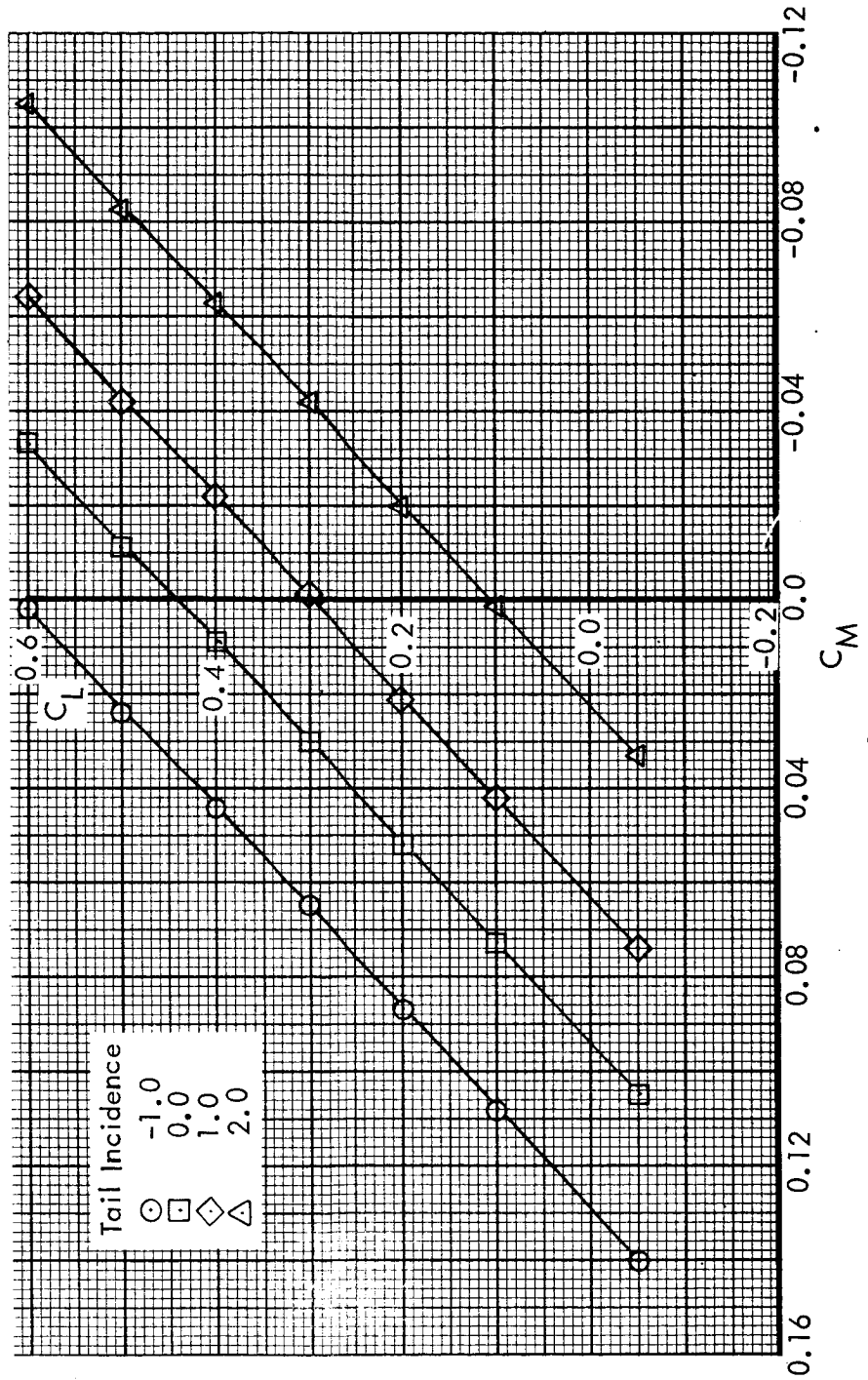
(c) $M = 0.750$

Figure 40. Continued

$R_N = 3.05 \times 10^6/MAC$
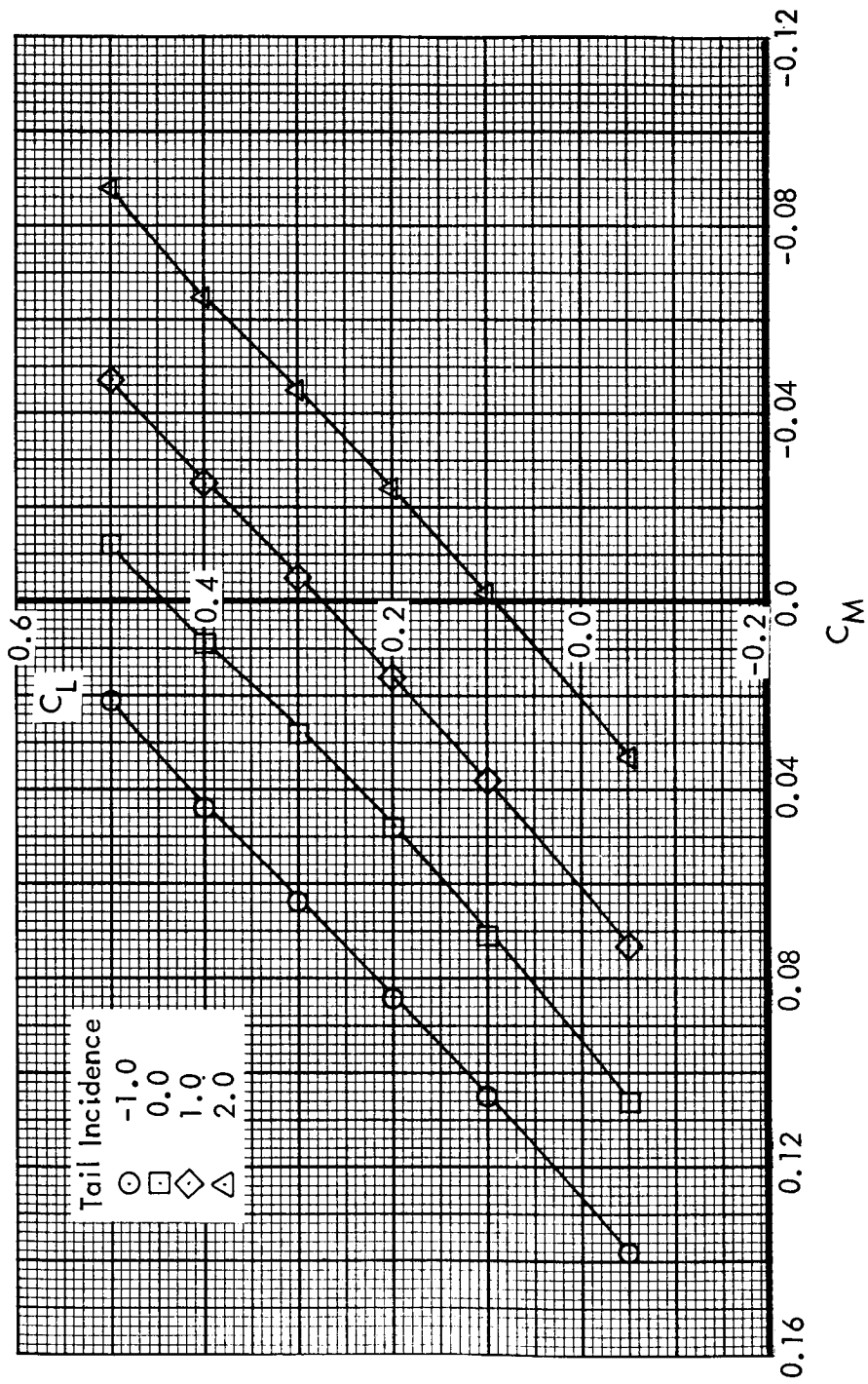
Sting Position No. 4

(d) M = 0.775
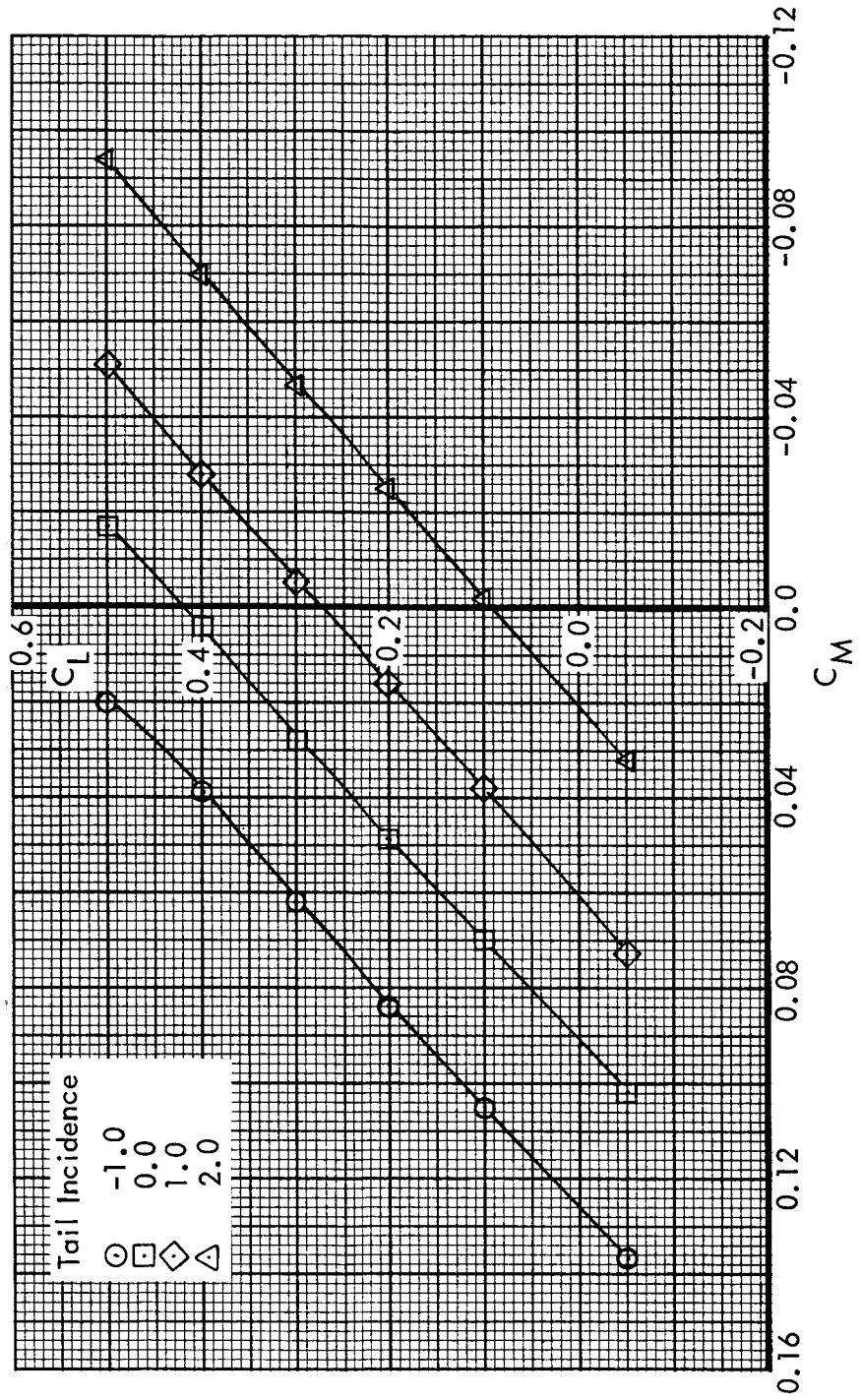
Figure 40. Continued

$R_N = 3.05 \times 10^6 / MAC$

Sting Position No. 4

Figure 40. Continued

(e) $M = 0.785$

99

Figure 40.   Continued

100
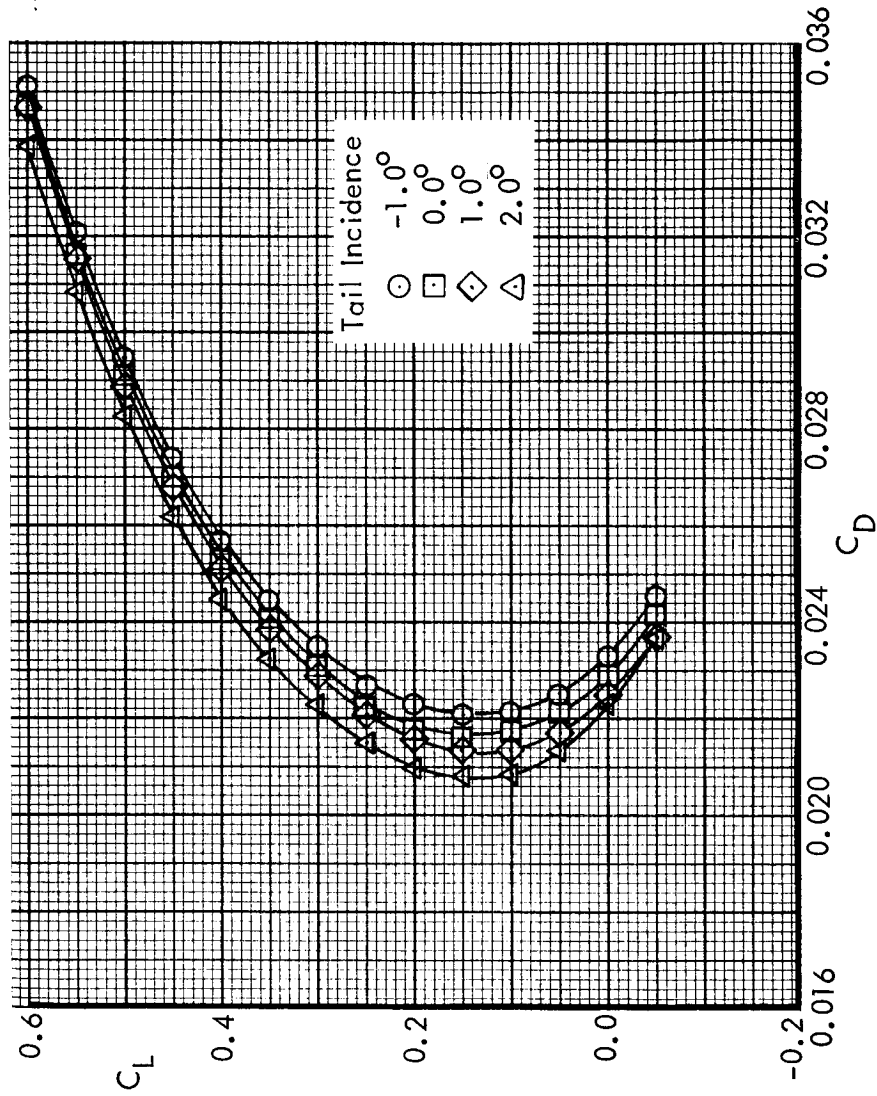
Figure 40. Continued

Figure 41. Effect of Horizontal Stabilizer Incidence on Drag. Data Corrected for Blade Tare and Interference.

102

Figure 41. Continued

(c) M = 0.75

Figure 41. Continued
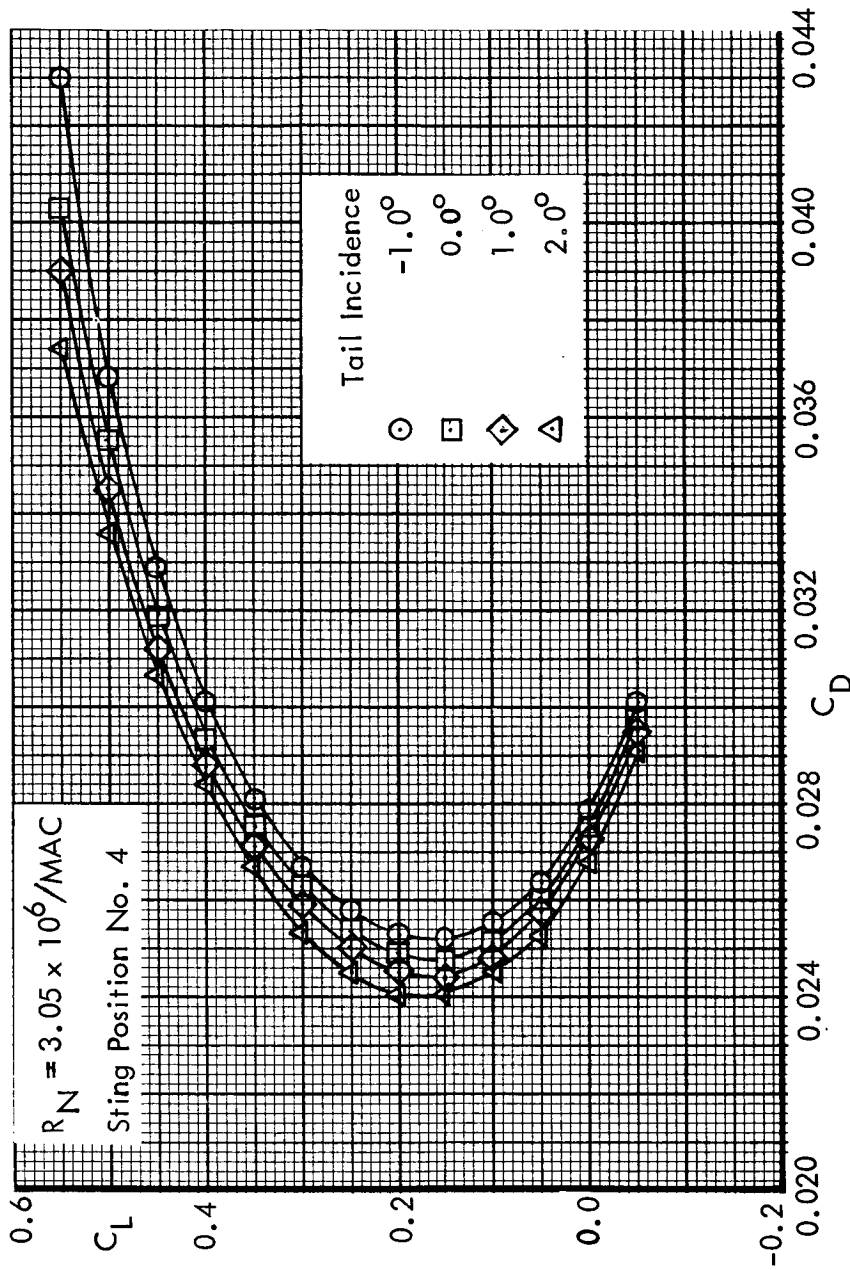
(d) M = 0.775

Figure 41. Continued
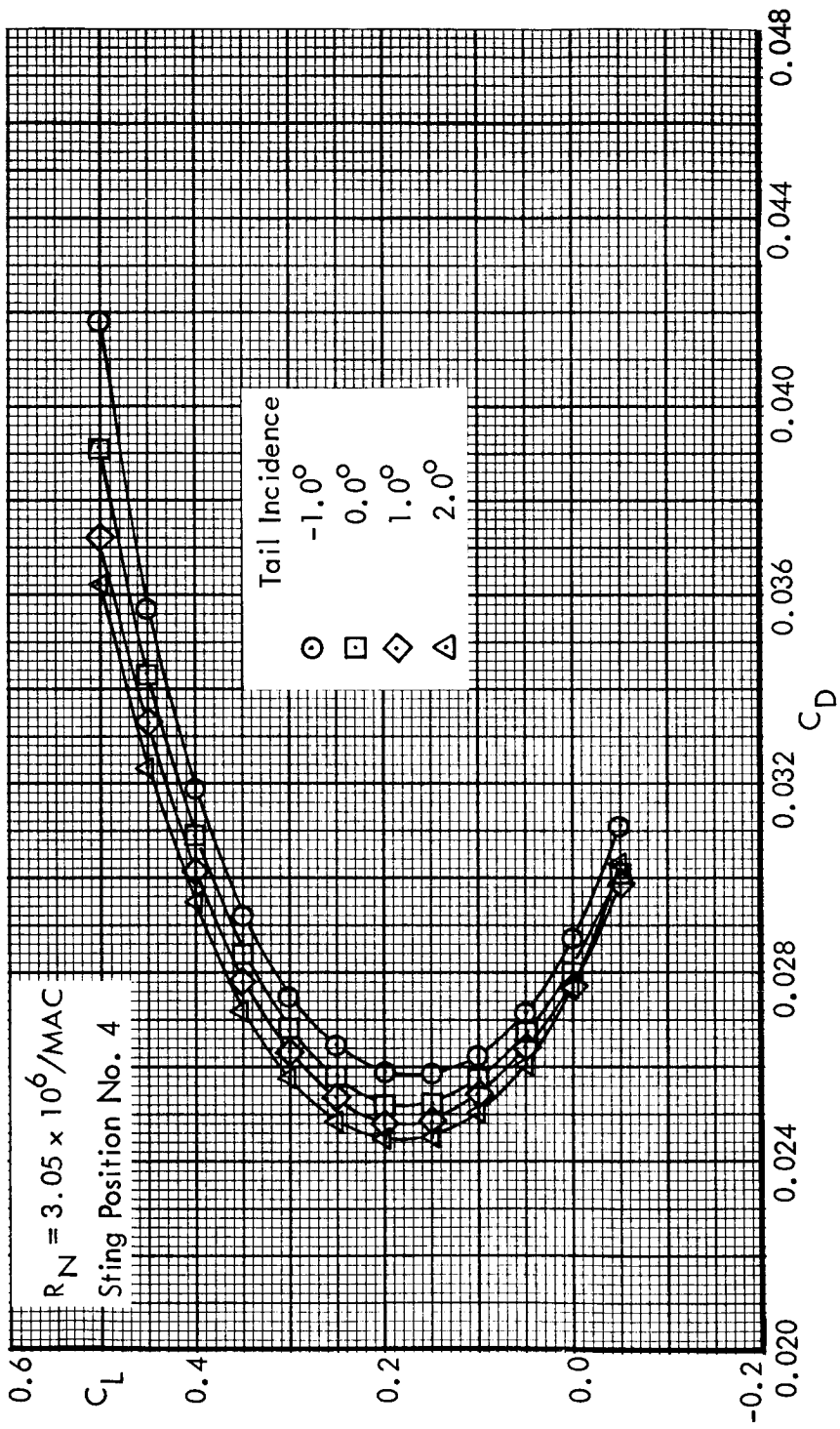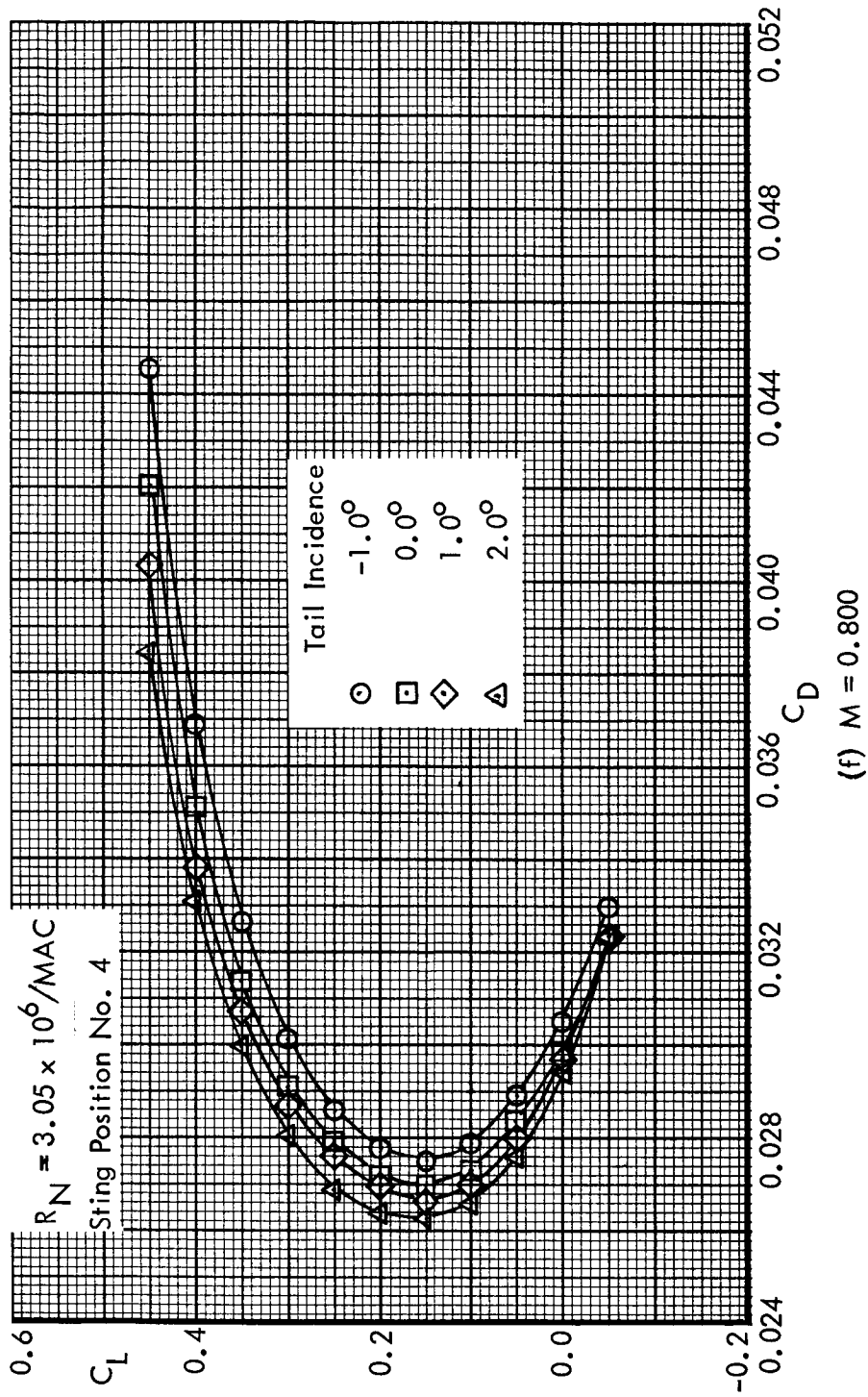
(e)   M = 0.785

Figure 41.   Continued

(f) M = 0.800

Figure 41. Continued

(g) M = 0.825
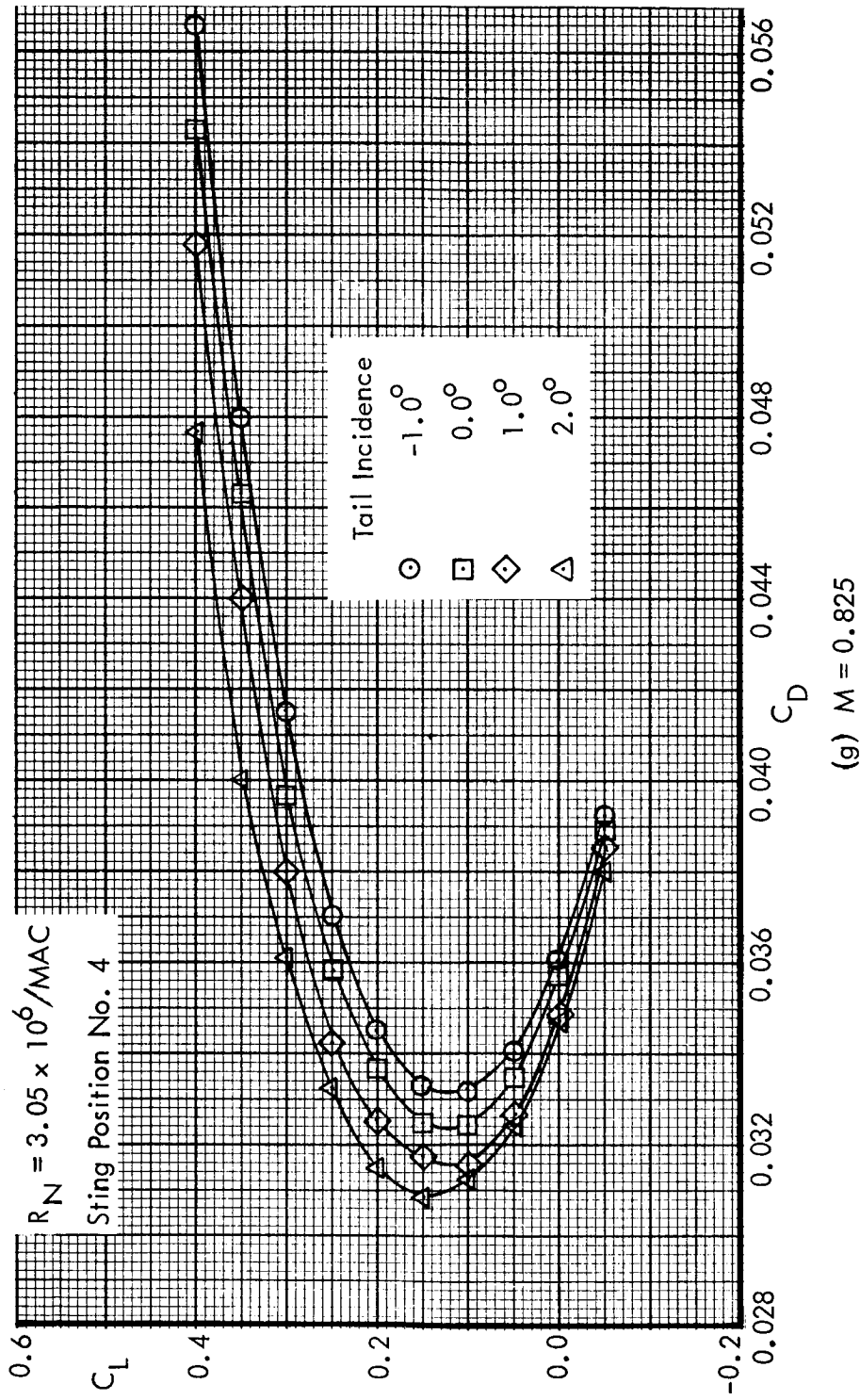
Figure 41. Continued

$R_N = 3.05 \times 10^6$/MAC

c.g. = 0.25 MAC

Blade and Sting Corrections Applied
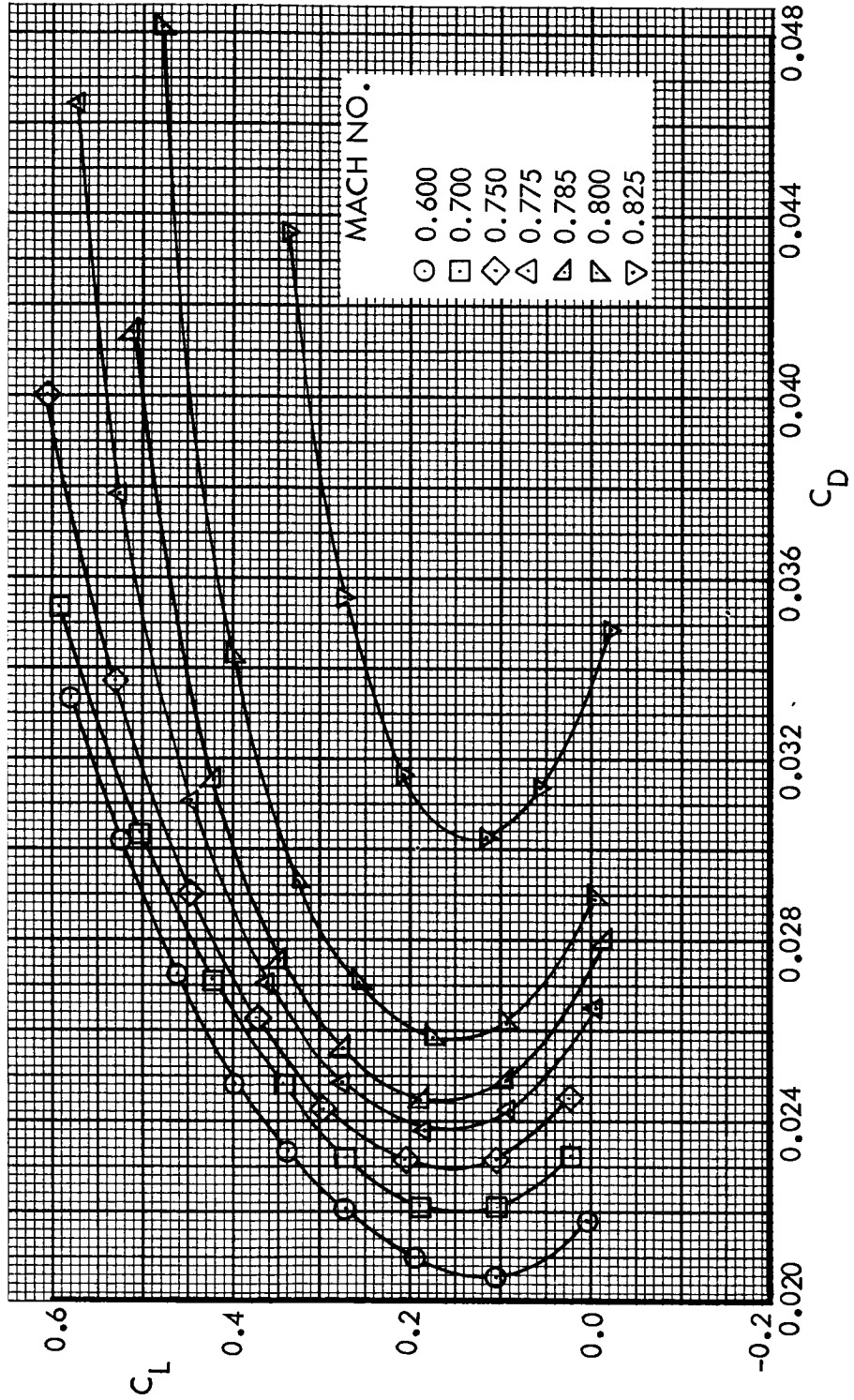
Figure 42.   Model Drag Polars Trimmed at c.g. = .25 MAC
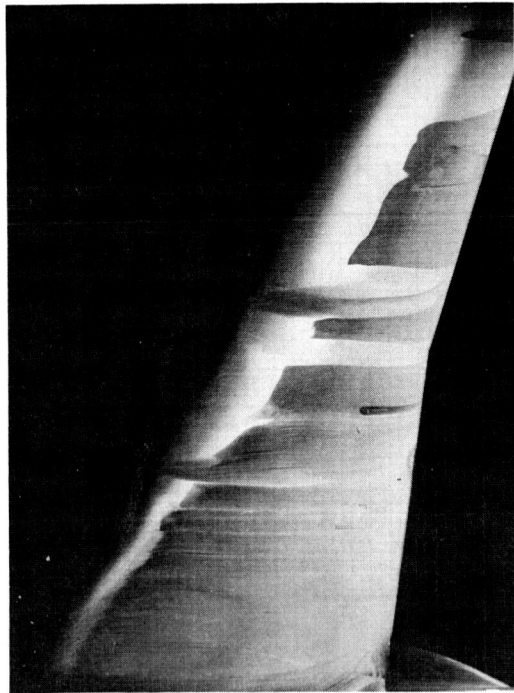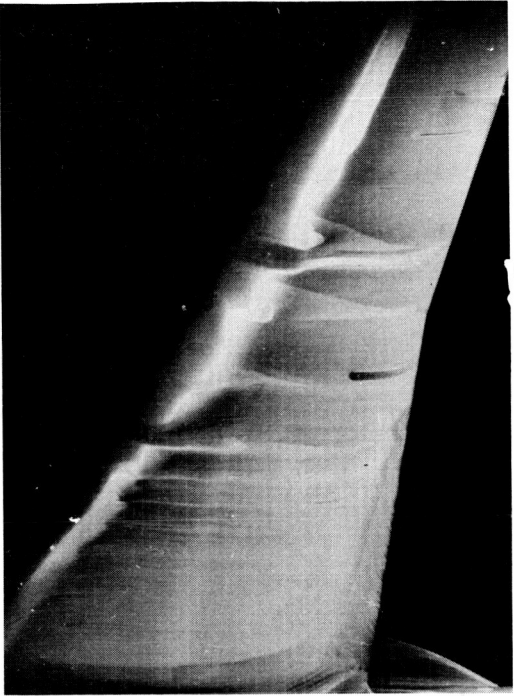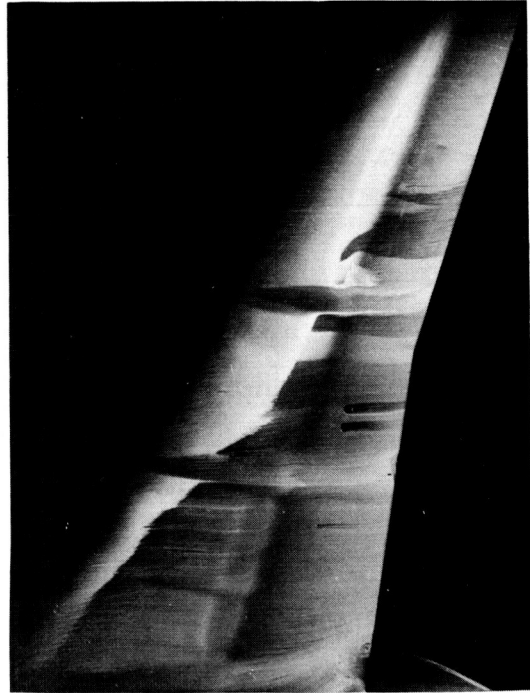
Figure 43. Oil Flow Visualization Photographs, Wing Upper Surface, Transition Free.

$\alpha_{FRL} = +2^{o}$

$\alpha_{FRL} = +2^{o}$

M = 0.750

M = 0.785

$\alpha_{FRL} = -1^{o}$

$\alpha_{FRL} = -1^{o}$
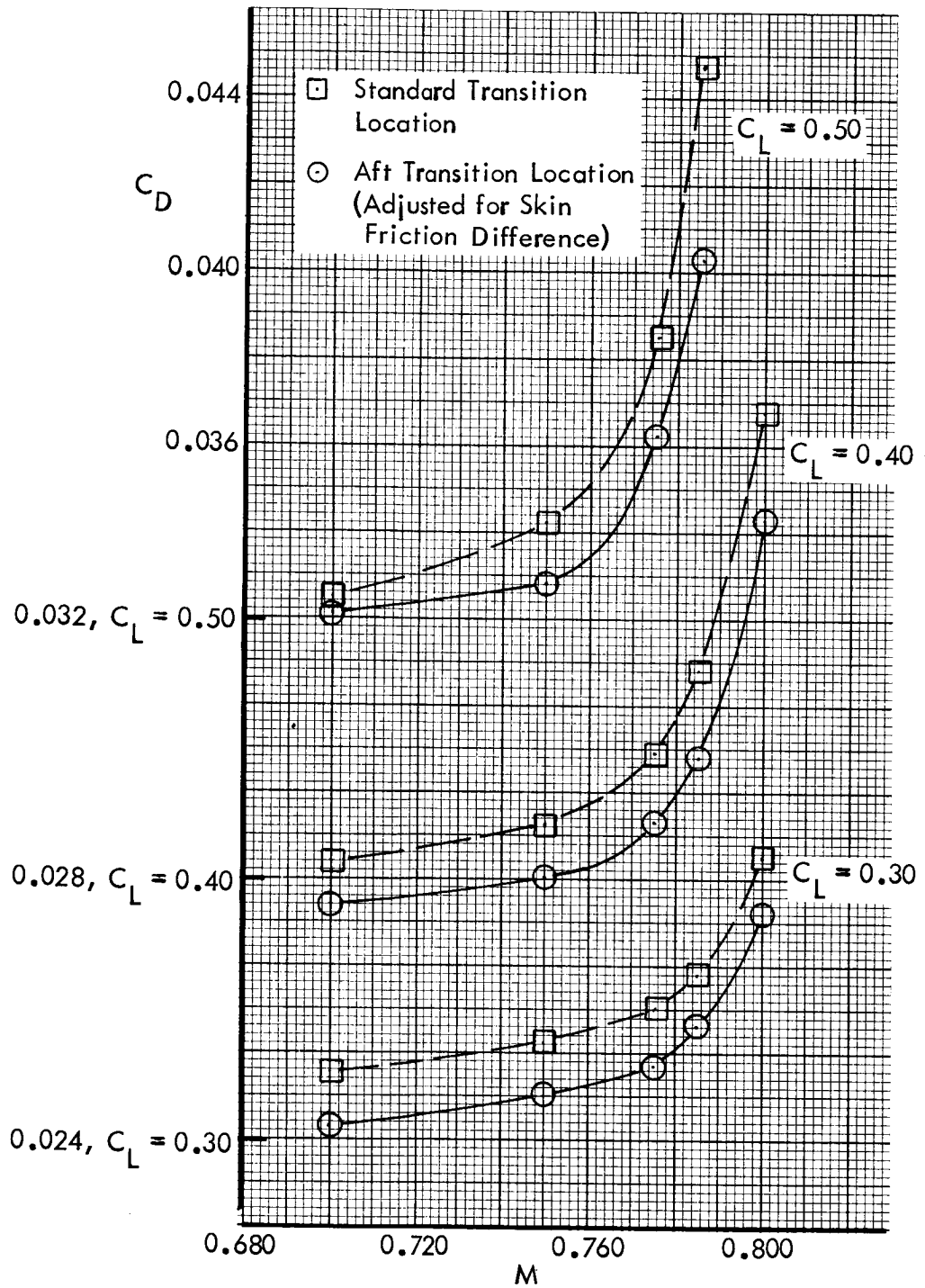
Figure 44. Effect of Transition Strip Location On Model Drag-Rise
Characteristics Trimmed. C.G. 25% MAC
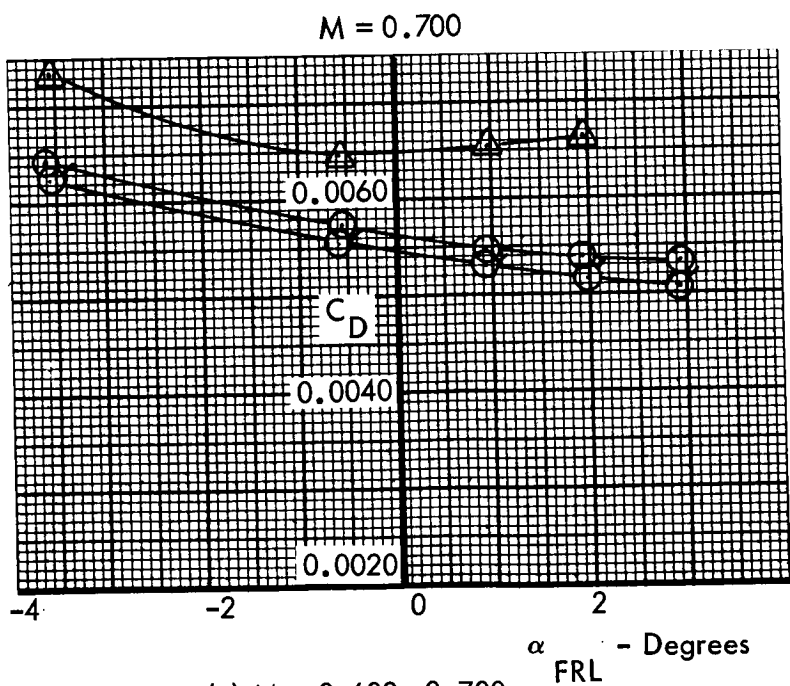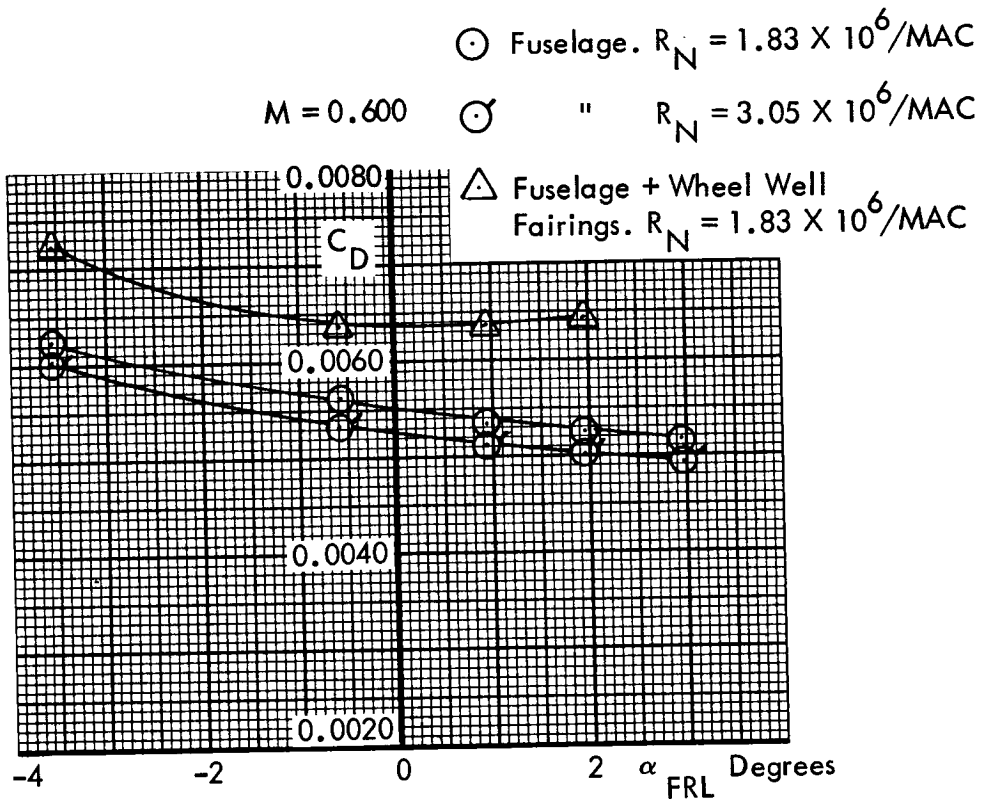
Figure 45.   Fuselage & Wheel Well Fairing
Drag.

M = 0.775

M = 0.785

Fuselage R_N = 1.83 X 10^6/MAC
" R_N = 3.05 X 10^6/MAC
Fuselage + Wheel Well
Fairings. R_N = 1.83 X 10^6/MAC
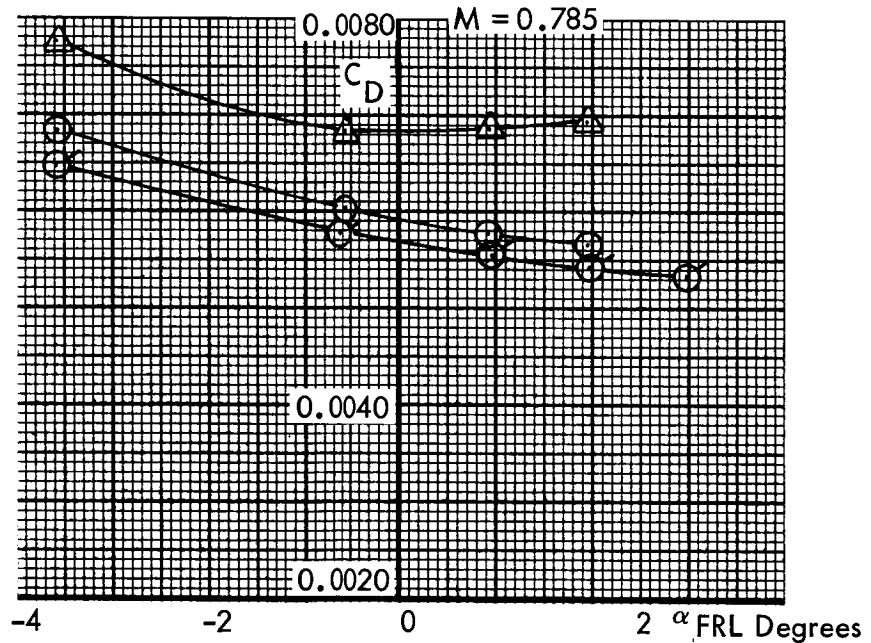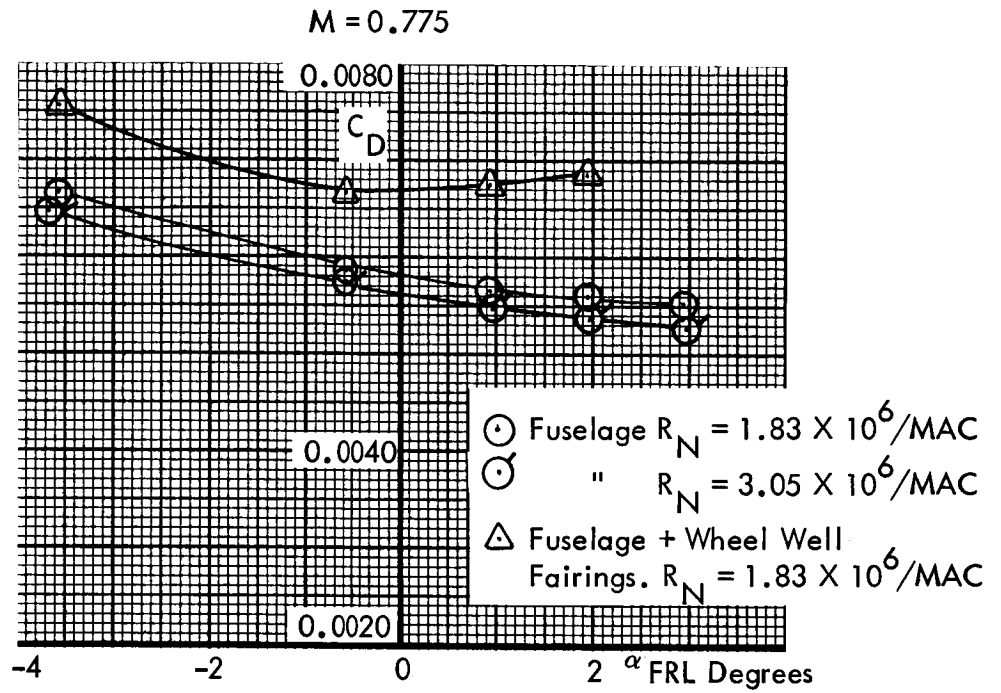
(b) M = 0.775, 0.785

Figure 45.   Concluded.
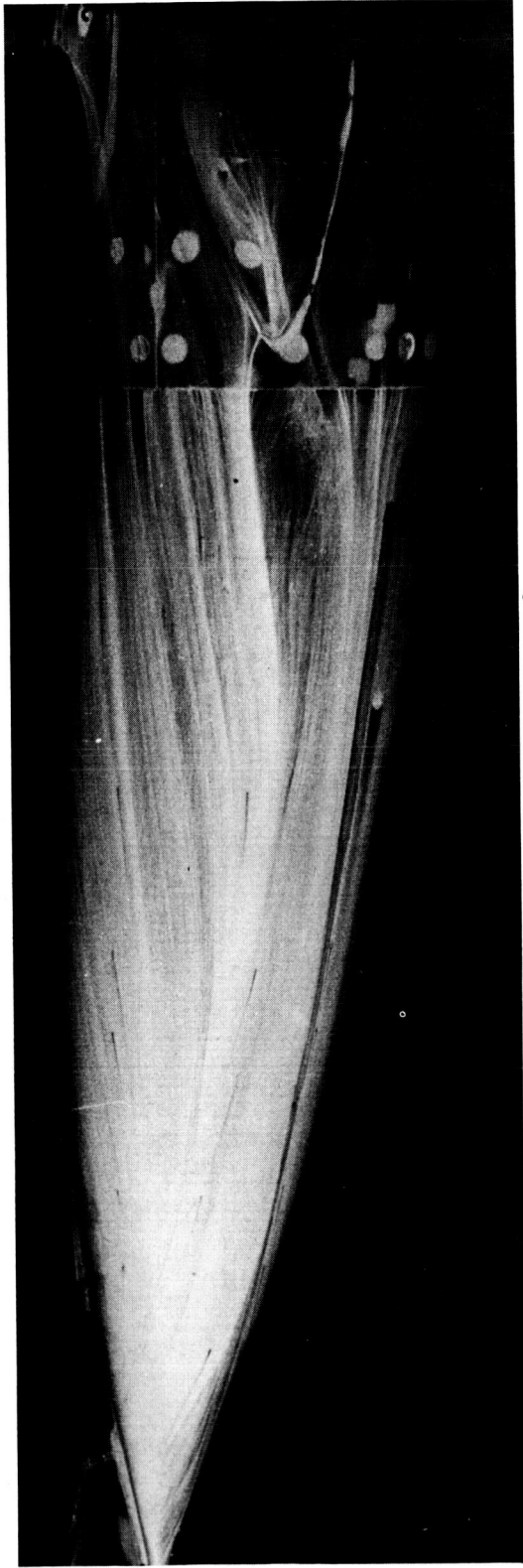
(a) $M = 0.785$, $\alpha_{FRL} = -1^\circ$
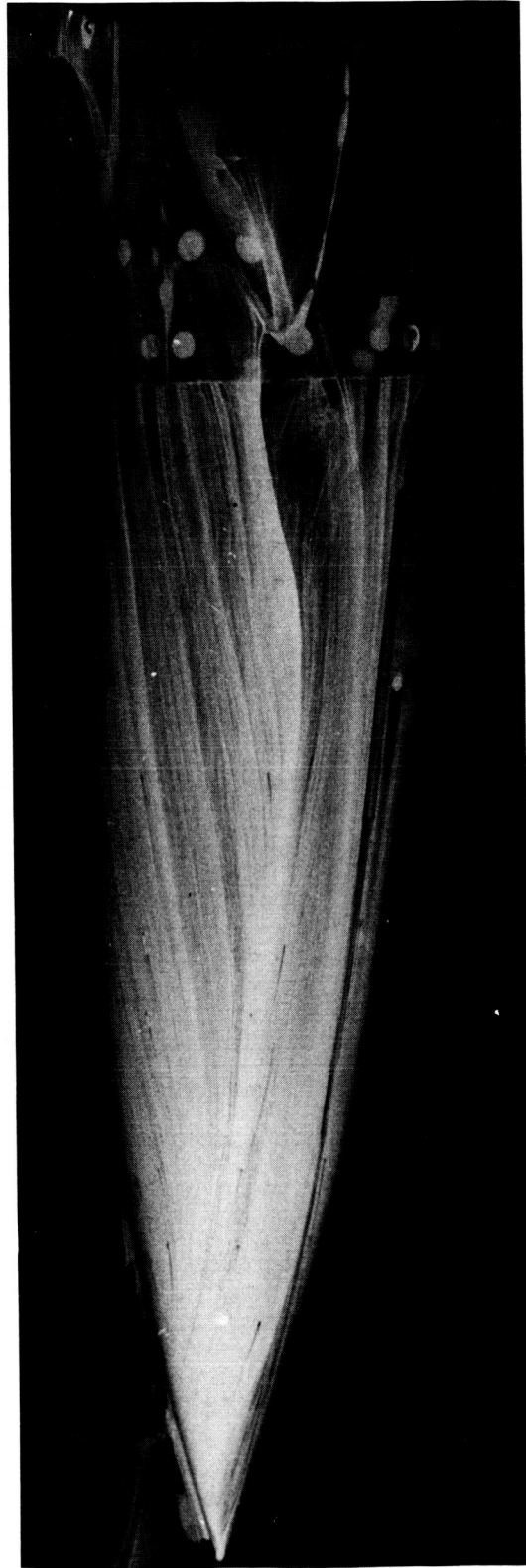
(b) $M = 0.785$, $\alpha_{FRL} = +2^\circ$

Figure 46. Oil Flow Photographs, Fuselage Afterbody
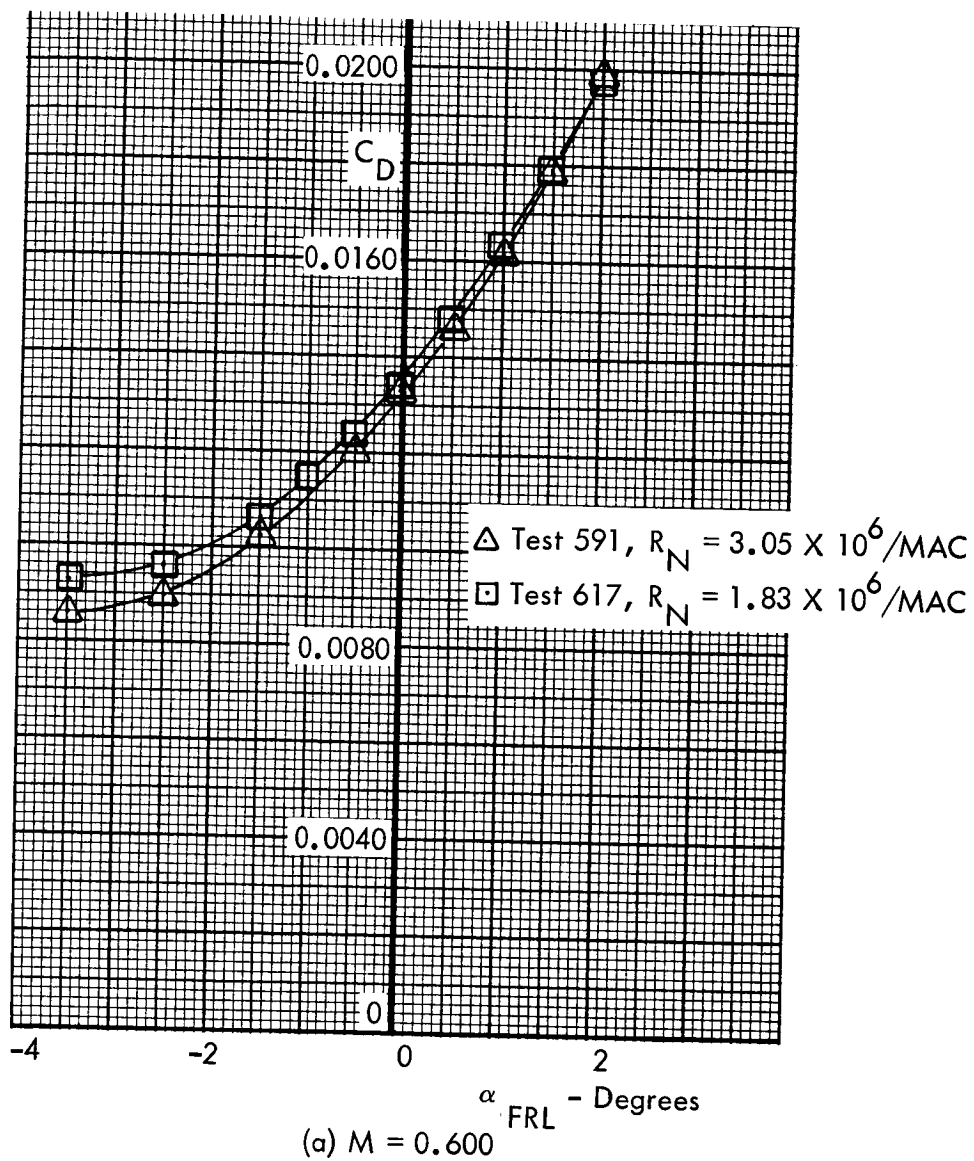
Figure 47.   Wing & Fillet Drag Increment.

(b) M = 0.700
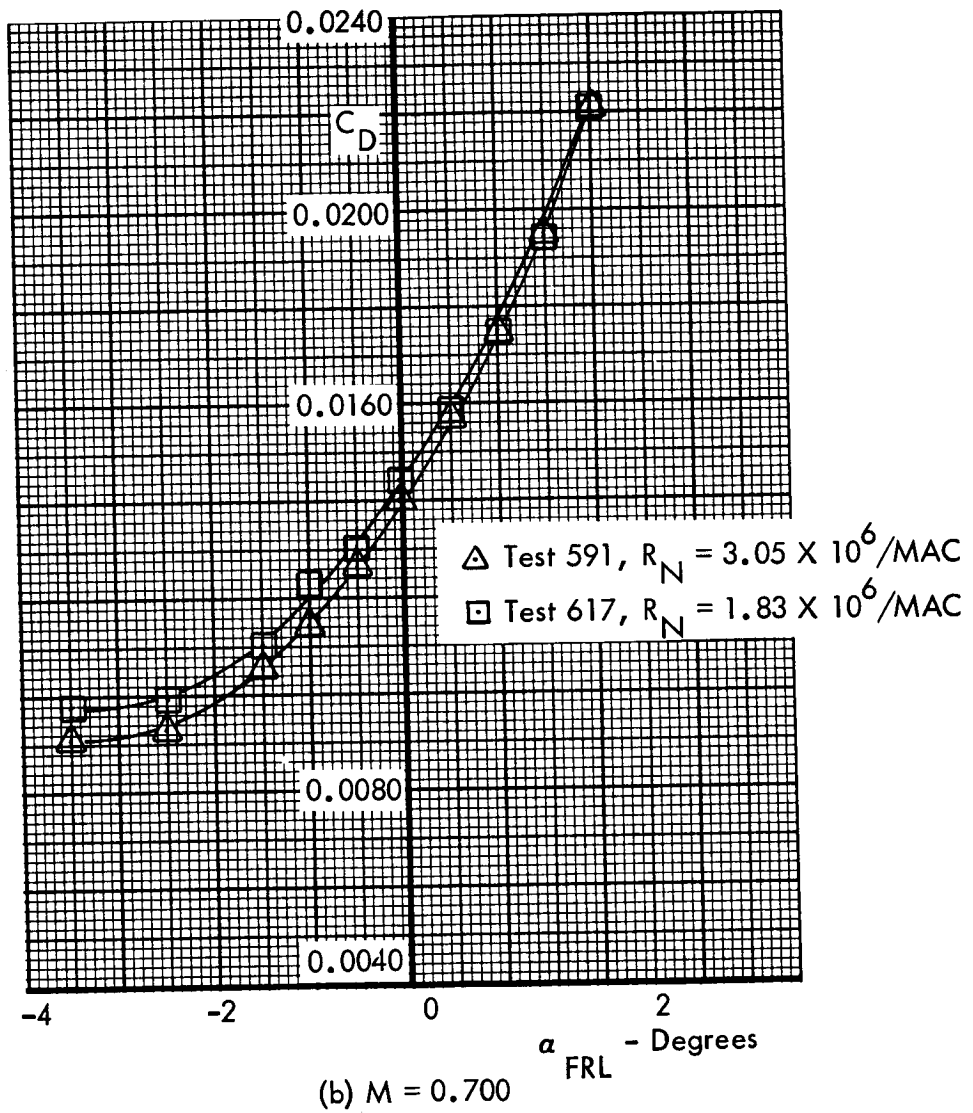
Figure 47.   Continued.
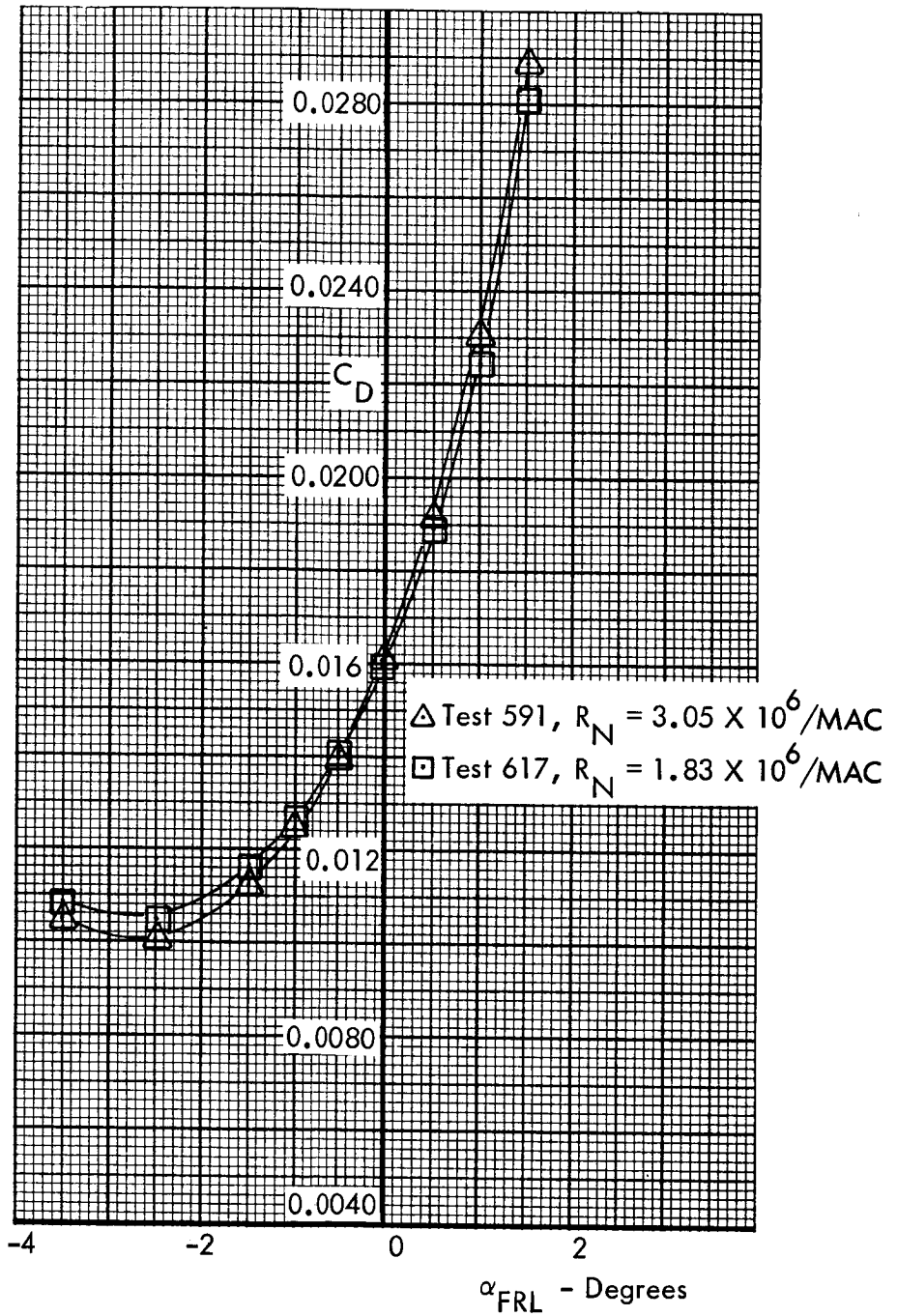
(c) M = 0.775

Figure 47.   Continued.
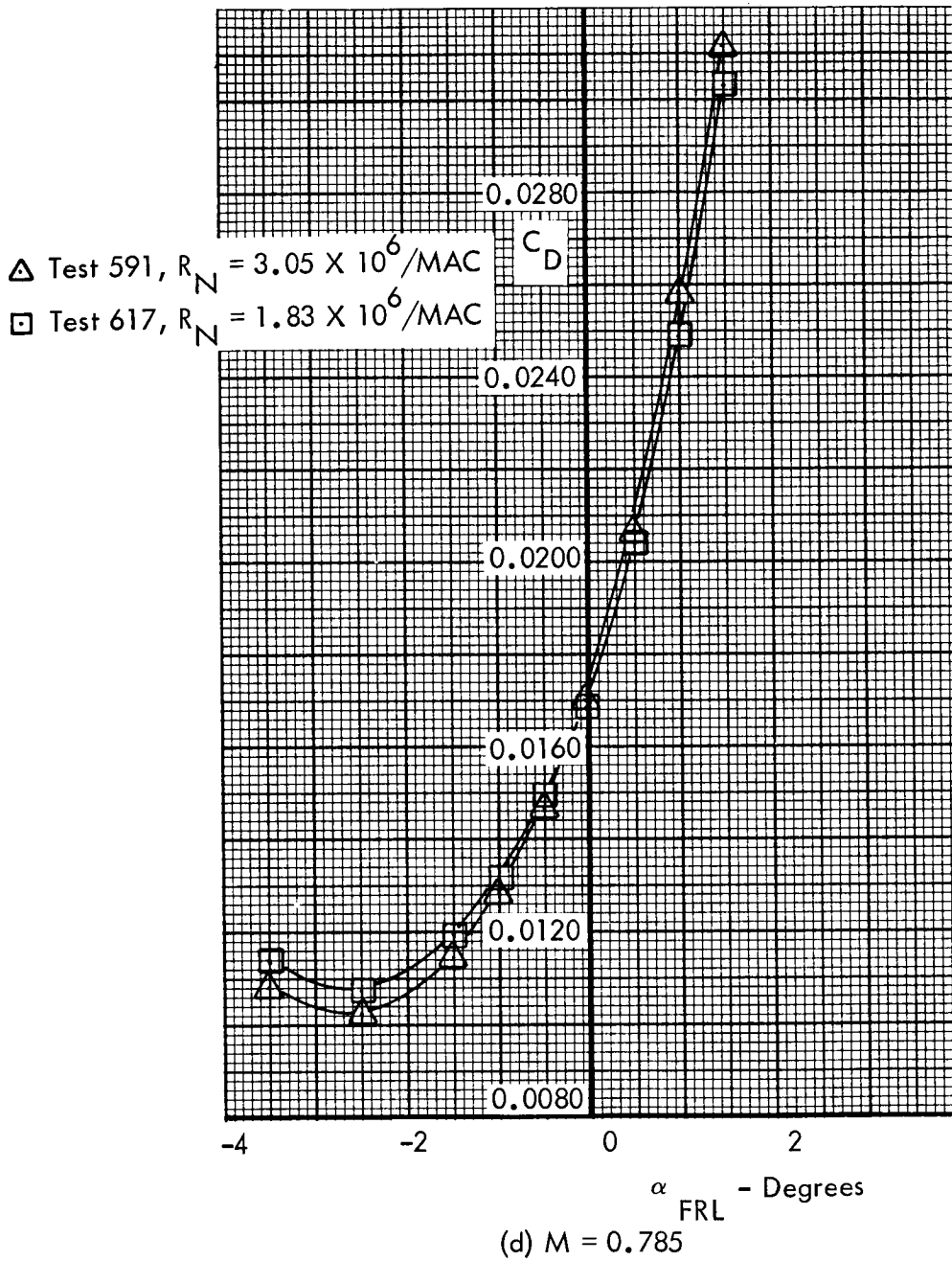
Figure 47.   Concluded.
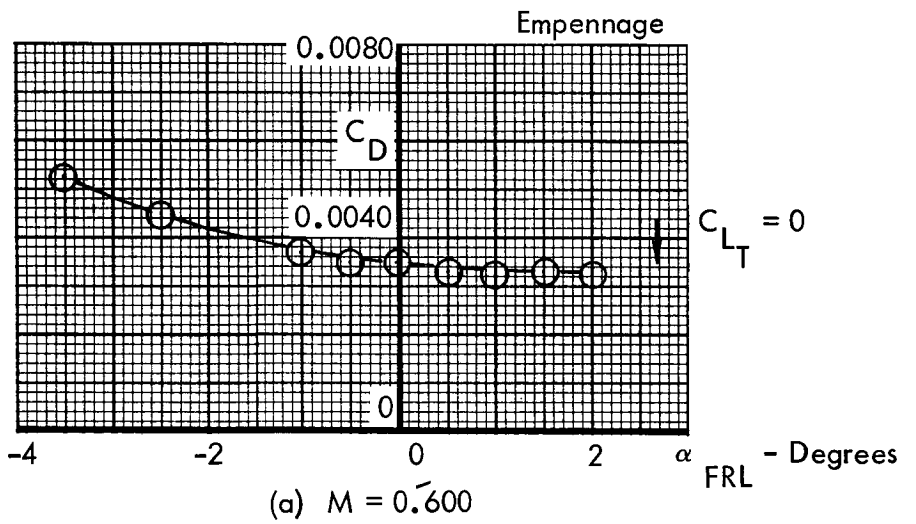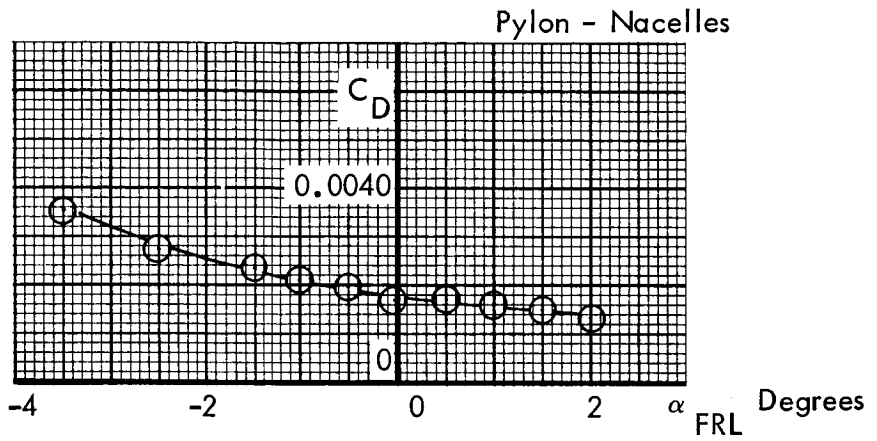
Figure 48   Pylon – Nacelles, Empennage
             Drag Increments.

(b) M = 0.700
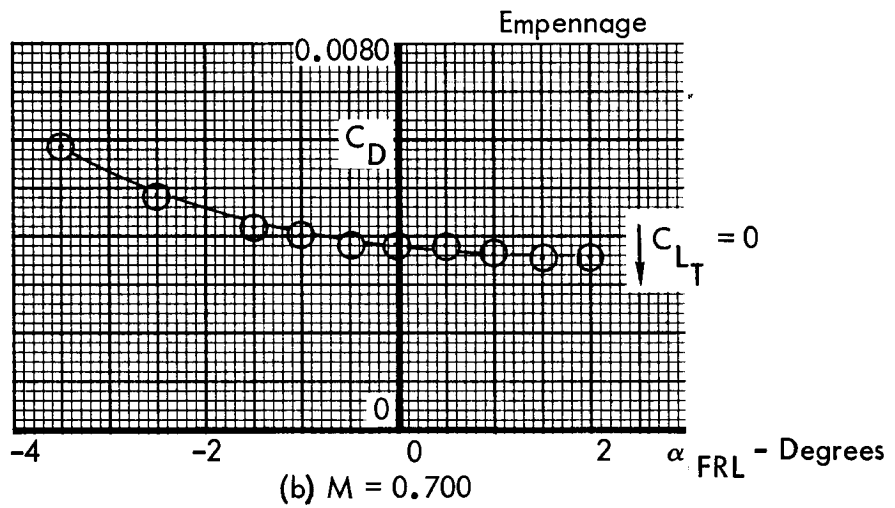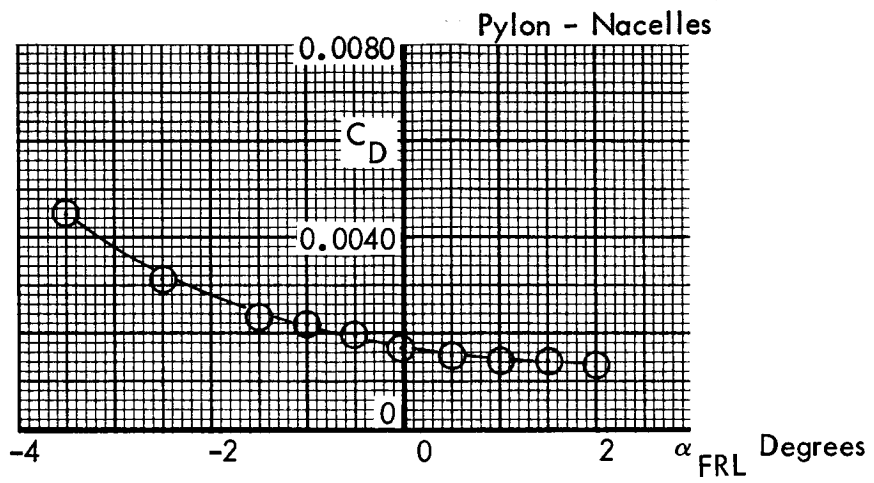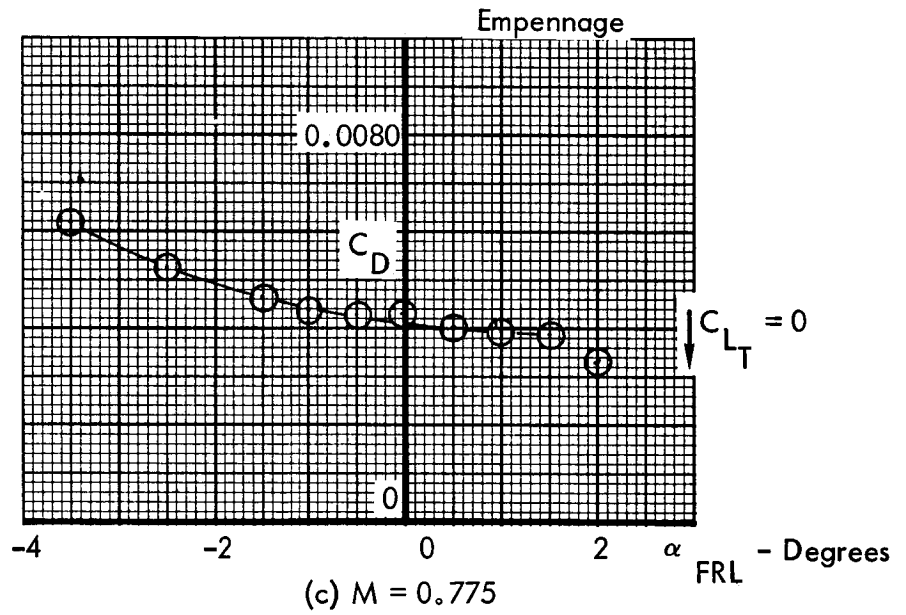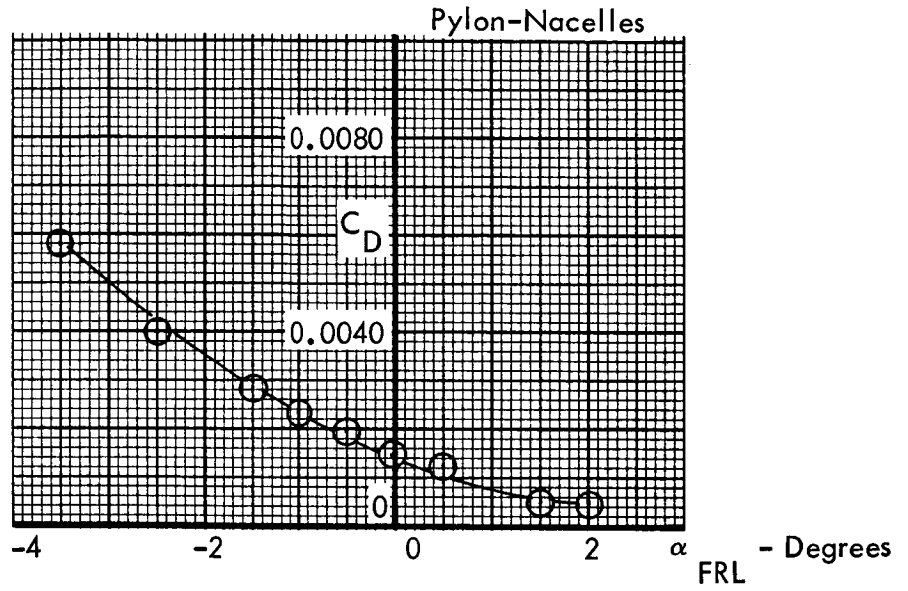
Figure 48.   Continued.

Figure 48.   Continued.

(c) M = 0.775

Pylon - Nacelles

(d) M = 0.785

Empennage
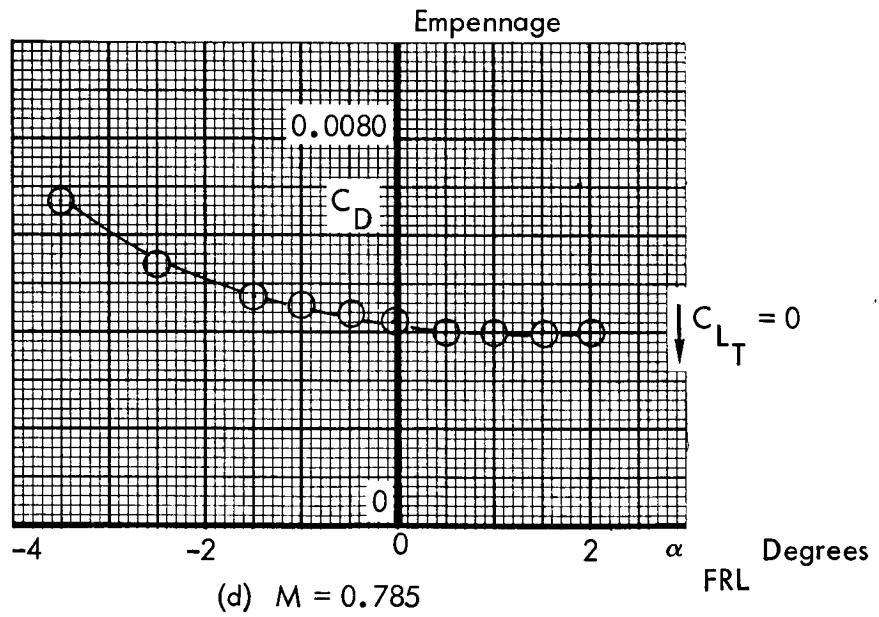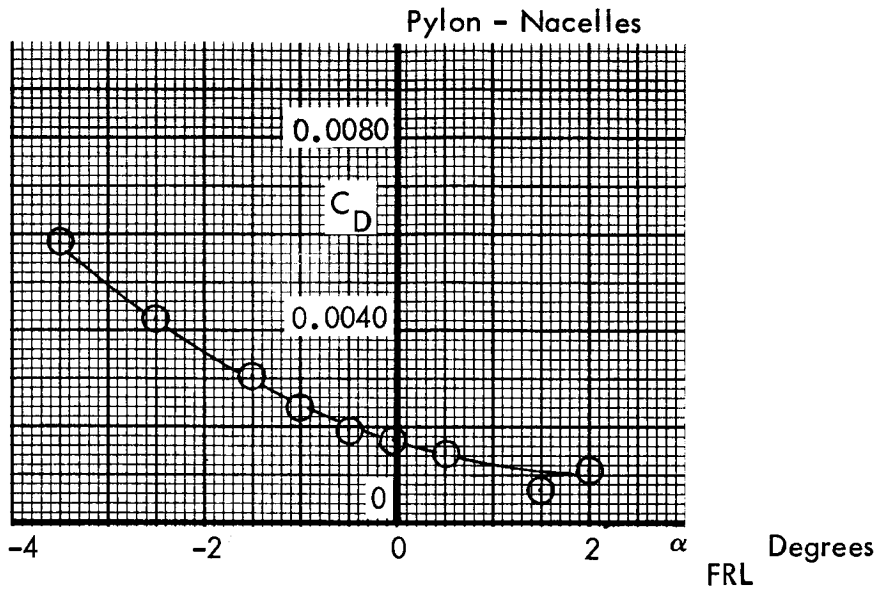
Figure 48.   Concluded.
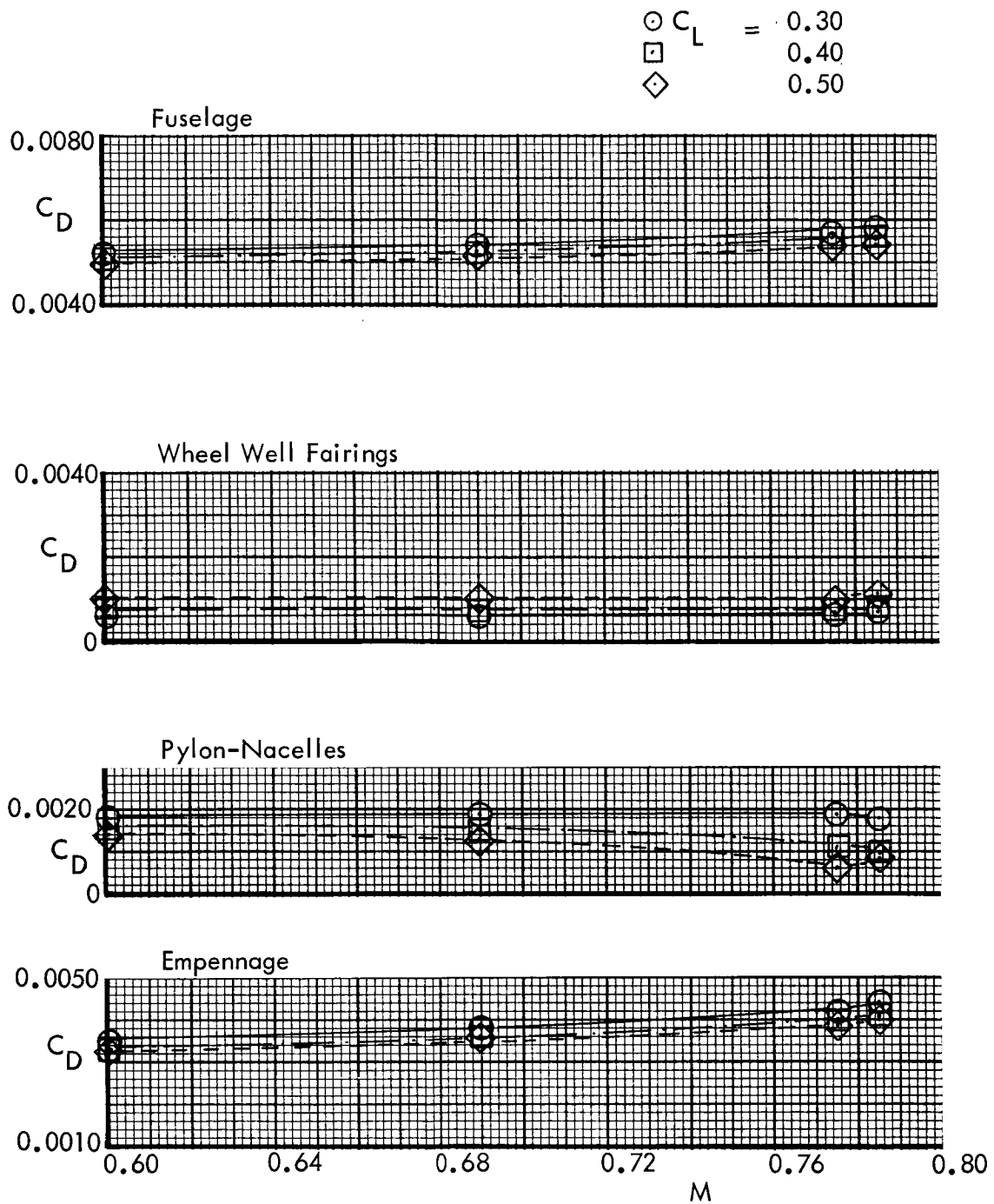
Figure 49.   Component Drag-Rise Characteristics
at C_L = 0.30, 0.40, 0.50
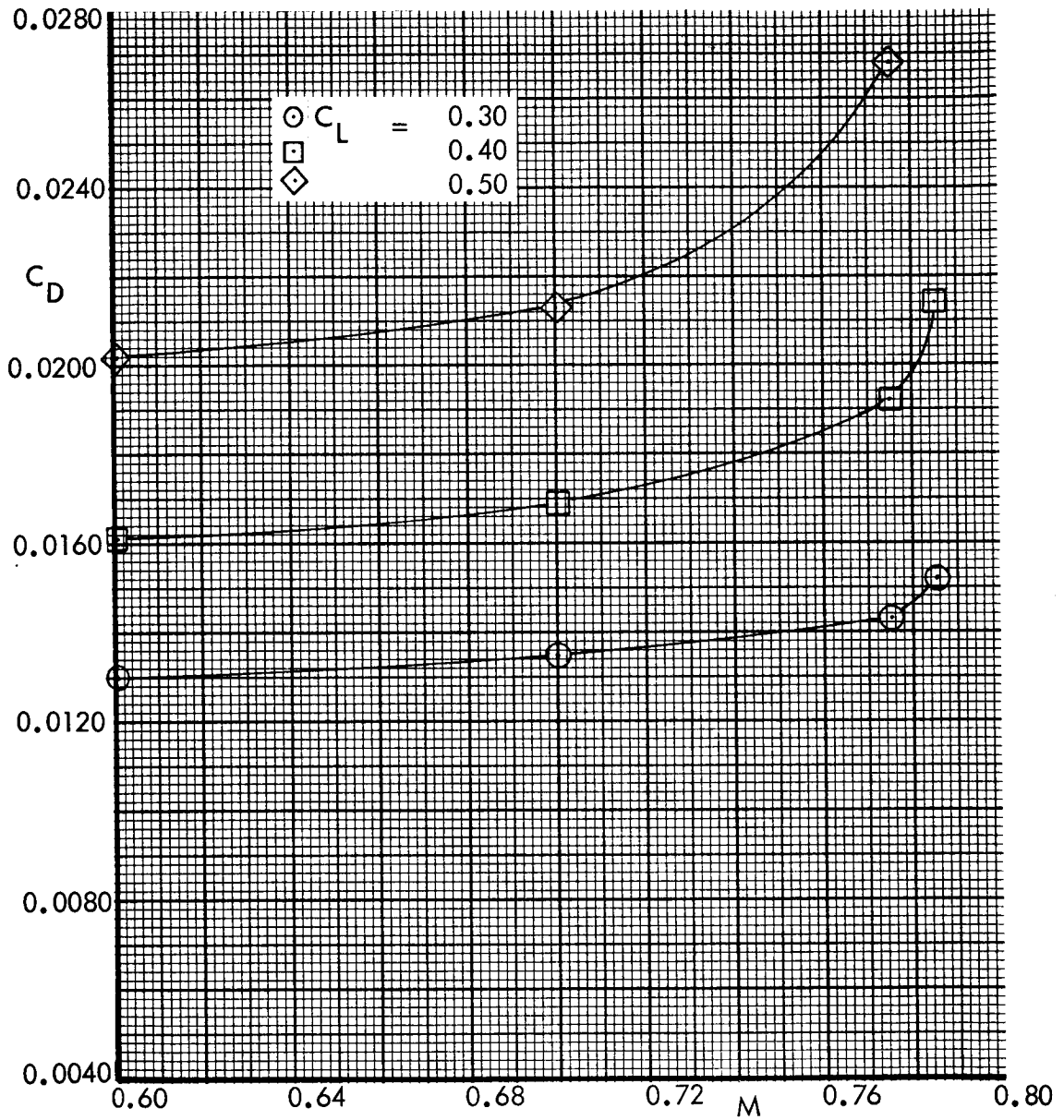
Figure 49. Wing & Fillet Drag Rise Characteristics
at C_L = 0.30, 0.40, 0.50

TABLE 2

SUMMARY OF EXPERIMENTAL COMPONENT PROFILE DRAG

Component M	.600	.700	.775	.785
Fuselage $(\Delta C_{D_p}$ Creep)	.0051 (0)	.0053 (.0002)	.0056 (.0005)	.0056 (.0004)
W. W. F. $(\Delta C_{D_p}$ Creep)	.0008 (0)	.0007 (−.0001)	.0007 (−.0001)	.0008 (0)
Wing + Fillet C_{D_p} $(\Delta C_{D_p}$ Creep)	.0088 (0)	.00945 (.00065)	.01105 (.0022)	.0126 (.0038)
Wing + Fillet C_{D_i} $(\Delta C_{D_p}$ Creep)	.0073 (0)	.00745 (.00015)	.00815 (.00085)	.0088 (.0015)
Pylon − Nacelles, (Int + Ext) $(\Delta C_{D_p}$ Creep)	.0016 (0)	.0015 (−.0001)	.0011 (−.0005)	.0010 (−.0006)
Empennage $(\Delta C_{D_p}$ Creep)	.0033 (0)	.0036 (.0003)	.0040 (.0007)	.0041 (.0008)
TOTALS $(\Delta C_D$ Creep) Net.	.0269 0	.0280 (.0011)	.0306 (.0037)	.0328 (.0059)
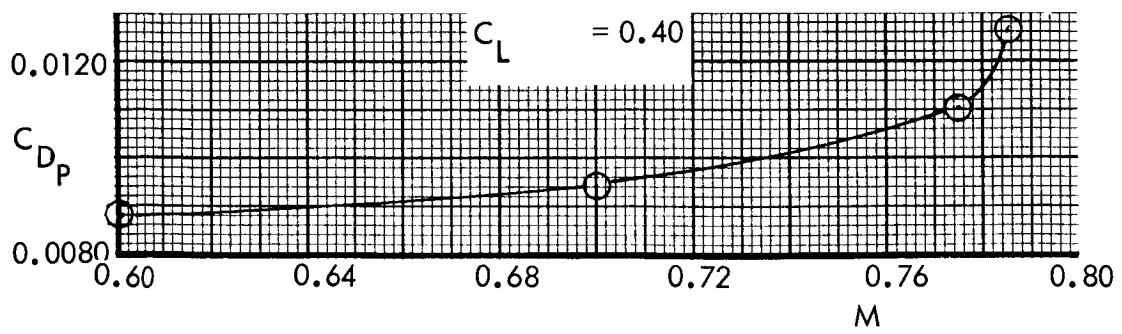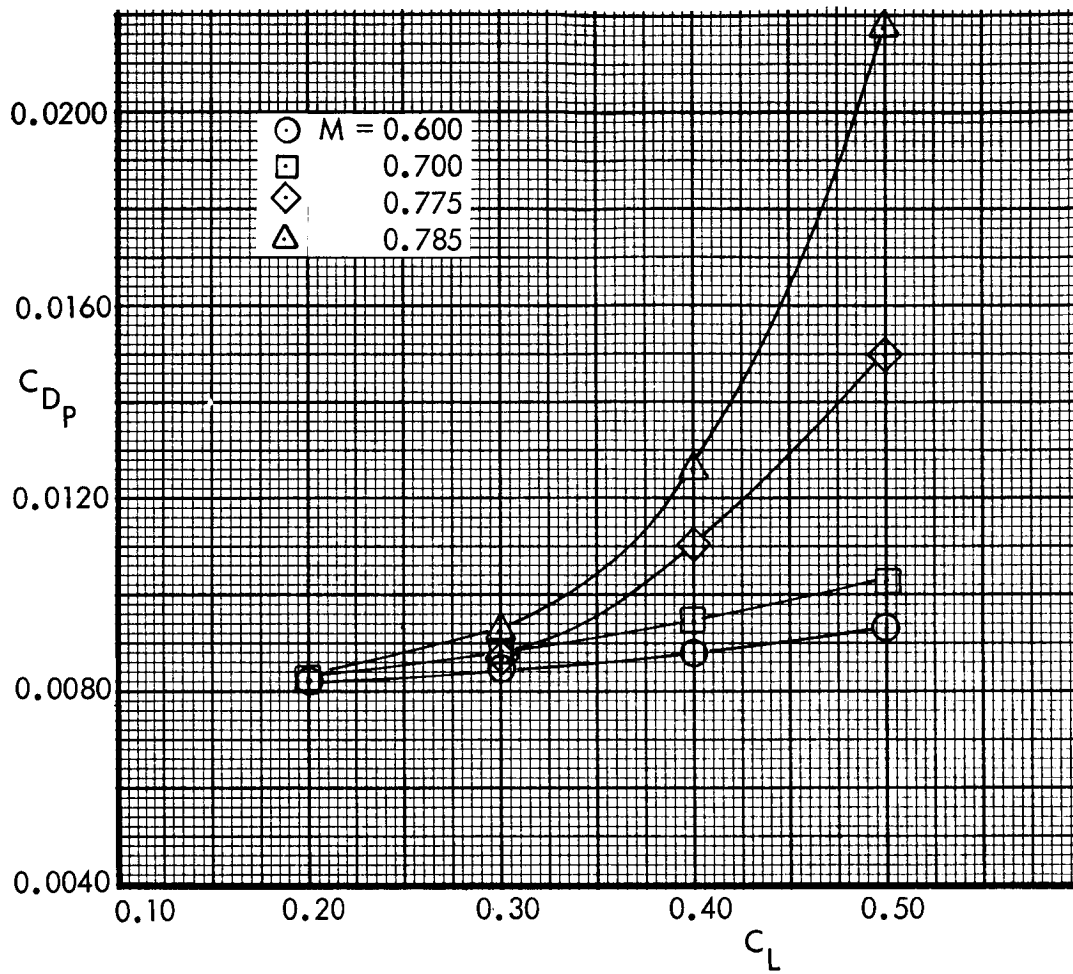
Figure 50. . Wing & Fillet Profile Drag Characteristics.

TABLE 3

COMPARISON OF MEASURED AND ESTIMATED PROFILE DRAG.

$M = 0.700.$ $C_L = 0.40.$ $R_N = 3.05 \times 10^6/\text{MAC}.$

Configuration	Estimate	Measured	$\Delta C_{D_{\text{Excess}}}$
Fuselage + Wheel-Well Fairings.	0.0051	0.0060 (0.00636 *)	0.0009 0.00126
Fuselage + Wheel-Well Fairings + Wing & Fillet	0.01233	0.01545	0.00312
Fuselage + Wheel-Well Fairings + Wing & Fillet + Pylon-Nacelles.	0.01463	0.01695	0.00232
Complete Model	0.01681	0.02055	0.00374 (0.0034 **)

* Corrected For Buoyancy

** Corrected For Buoyancy & Support Interference
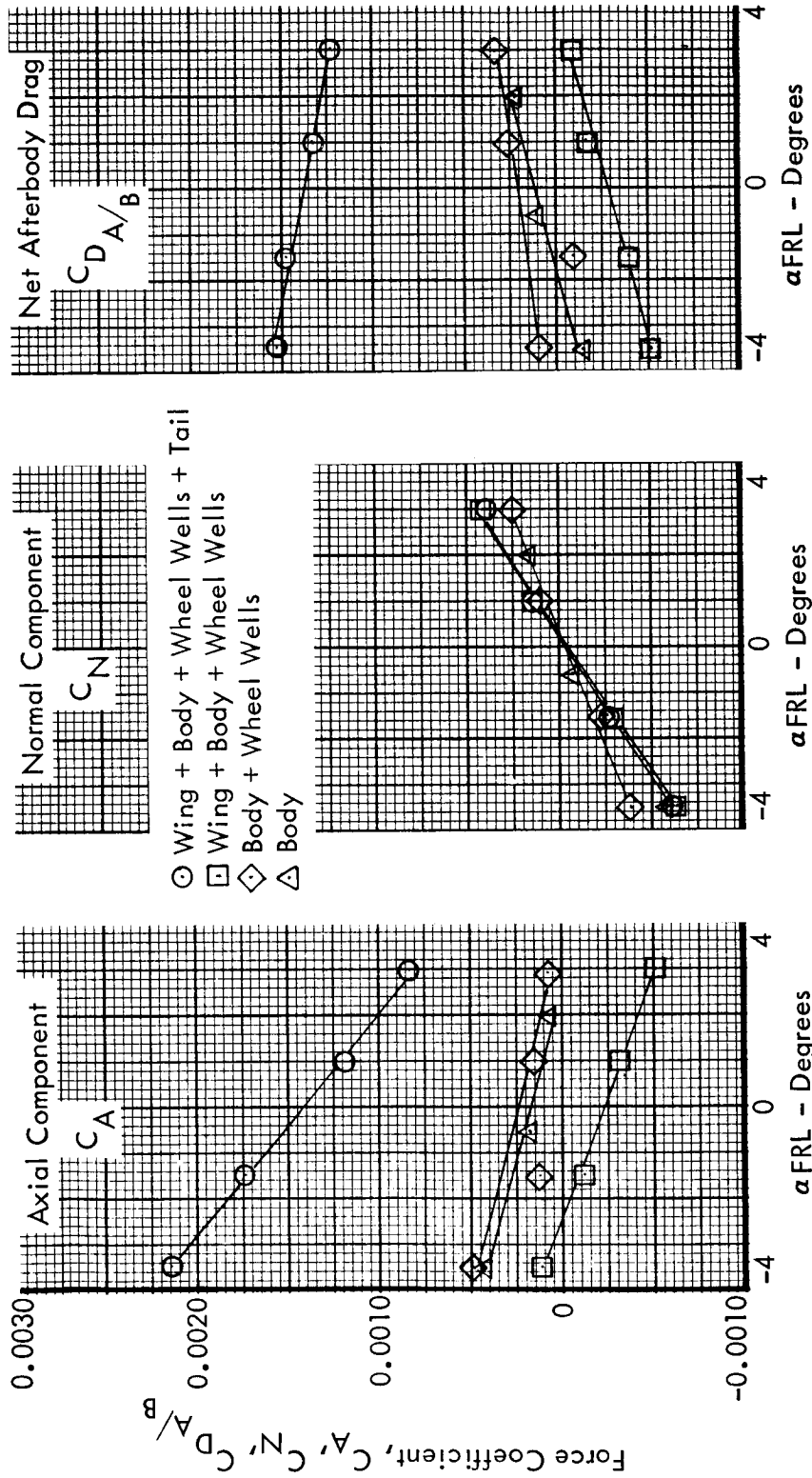
Figure 51.   Computed Afterbody Pressure Drag – Effect of
Wheel Well Fairings, Wing and Empennage.

128
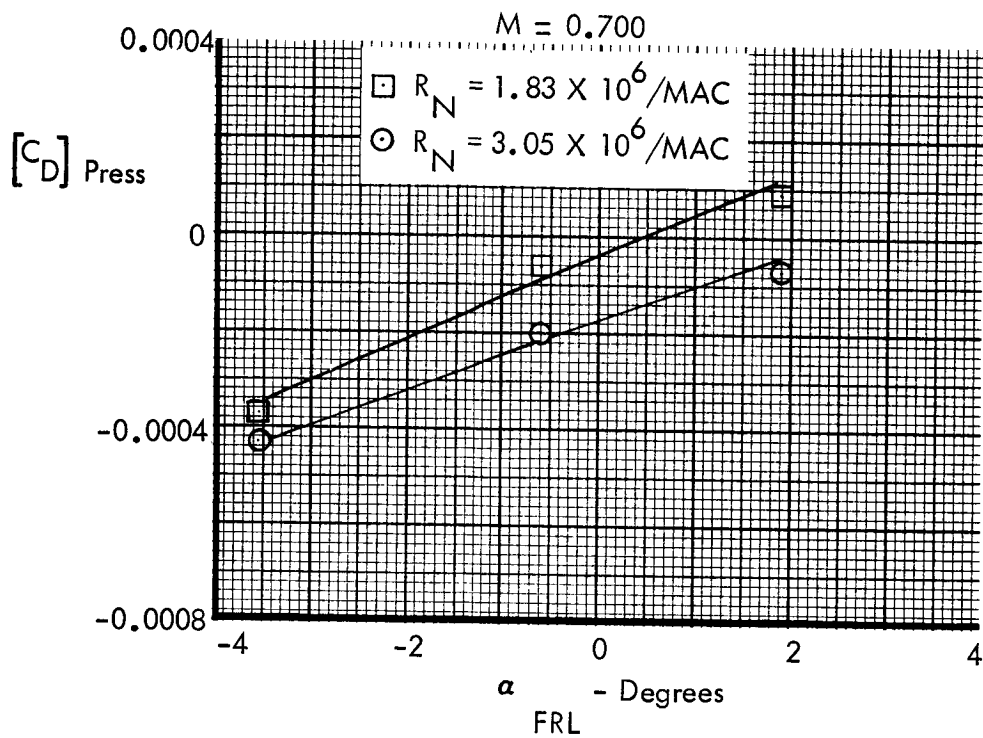
Figure 52.   Reynolds Number Effect on
              Afterbody Pressure Drag.

CORRELATION OF WIND TUNNEL AND FLIGHT DATA

Comparisons of the corrected wind tunnel data and flight test results are now discussed. Initially, the correlation at a subcritical Mach number of 0.700 is presented. Secondly, drag-rise characteristics are compared. The flight test data are taken from the previously reported analysis, Reference 1, in which equivalent rigid aircraft drag polars were determined.

The corrections required to develop profile drag from the support interference – corrected data, presented in figure 42, are as follows.

(i)   Wind tunnel buoyancy

(ii)   Model nacelle internal drag.

(iii)   Drag increment from model transition to leading-edge transition

(iv)   Induced drag on wing & tail.

Those corrections necessary for the full-scale prediction are,

(v)   Roughness

(vi)   Nacelle afterbody pressure drag

(vii)   Reynolds number effect on minimum profile drag

(viii) Reynolds number effect on lift-dependent profile drag

Wind tunnel buoyancy – The empty tunnel static pressure gradients in the Langley 8-foot tunnel resulted in a buoyancy correction of 0.00036 in C_D at M = 0.700, 0.00033 at M = 0.775, and 0.00032 at M = 0.800. These corrections were added to the uncorrected model data.

Model nacelle internal drag – The model nacelle internal drag was estimated to be an average of $\Delta C_D = 0.00046$ over the Mach number and angle of attack range of interest. This was deducted from the wind tunnel data.

Transition correction – The estimated correction from the model transition locations to an assumed full-scale location at the leading-edge of all surfaces was 0.00133 in C_D for $R_N = 3.05 \times 10^6/\text{MAC}$.

<u>Induced drag</u> – The drag polar was reduced to provide an overall configuration value of C_{D_P} by the following equation.

$$C_{D_P} = C_D - C_{D_{i_{WING}}} - C_{D_{i_T}} - C_{L_T} \tan \epsilon \qquad (18)$$

where $C_{D_{i_{WING}}} = \dfrac{C_{L_{A-h}}^2}{\pi A e}$

$$C_{D_{i_T}} = \dfrac{C_{L_T}^2 (S/S_H)}{\pi A_T e_T}$$

$C_{L_T} \tan \epsilon = $ drag component of the lift vector, which was a thrust
term in this case.

Thus, all trim drag terms which were lift-dependent were deducted from the total drag polar to give the required values of C_{D_P}. The estimated wing span efficiency factors for the equivalent rigid condition are given in figure 53, taken directly from reference 1.

<u>Roughness</u> – During the development period of the C-141A, considerable attention was given to estimating the combined drag increments of steps, gaps, protuberances, and leakage on the aircraft surfaces. This total drag increment was estimated using basic information from reference 14, supplemented by detailed boundary-layer calculations on individual surfaces. Table 4 summarizes these estimates. The total aircraft roughness drag was estimated to be $\Delta C_D = 0.0007$, and this increment is used in the correlation results of the current study.

<u>Nacelle afterbody pressure drag</u> – It will be recalled from the section that included figure 20 that the full-scale estimates for the nacelle afterbody pressure drag were included in the engine thrust levels. Therefore, to achieve compatability of model and full-scale drag, the corresponding model estimates are deducted from the wind tunnel results. This correction was estimated to be $\Delta C_D = 0.0007$ for the cruise Mach number range.

<u>Scale effect on minimum profile drag</u> – The variation of estimated minimum profile drag of the complete configuration with Reynolds number is taken from the component profile drag data given in table 1. The magnitude of drag predicted for each component is estimated to be that occuring on the component in isolation and at "minimum" drag conditions. The estimates for the fuselage, pylon-nacelles, and empennage thus refer to zero-angle of attack conditions. No interference drag is allowed for in this estimate. These effects are measured in the wind tunnel model and are discussed later.

Scale effect on lift-dependent profile drag - Apart from the minimum profile drag estimates, the lift-dependent drag of the wing was predicted using the subsonic viscous theory described in the previous sections. Results from figure 14 show that the effect of Reynolds number is a reduction in the increment ΔC_{D_P} with C_L from wind tunnel conditions to full-scale. The increment of C_{D_P} with C_L is inherent, of course, in the measured drag-due-to-lift of the model at wind tunnel Reynolds numbers, giving an overall effective span efficiency somewhat less than the computed vortex-induced span efficiency. Corrections have been applied to the model drag polars for this effect in order to predict full scale drag-due-to-lift. These corrections amounted to a reduction in the model drag of $\Delta C_D = 0.0002$ at $C_L = 0.25$, varying linearly to 0.0005 at $C_L = 0.50$.

The derivation of the predicted full-scale value of C_{D_P} at $M = 0.700$ is summarized as follows, using the data at $C_{L_{TRIM}} = 0.40$ as an example.

Trimmed wind tunnel data, corrected for support interference, model transition	$C_D = 0.02640$
Wind tunnel buoyancy correction	$\Delta C_D = 0.00036$
Nacelle internal drag correction	$\Delta C_D = -0.00047$
Transition from model location to leading edge	$\Delta C_D = 0.00133$
$C_{D_{i_{WING}}}$	$= -0.00760$
$C_{D_{i_T}}$	$= -0.00020$
$C_{L_T} \tan \epsilon$	$= 0.00083$
Equivalent $C_{D_{P_{min}}}$ at $R_N = 3.05 \times 10^6$/MAC.	$= 0.02065$
Roughness drag increment	$\Delta C_D = 0.00070$
Nacelle afterbody correction	$\Delta C_D = -0.00070$

$C_{D_{P_{min}}}$ Reynolds number correction Method (C) $\Delta C_D = -0.00580$

$C_{D_{P_{min}}}$ Reynolds number correction Method (B) $\Delta C_D = -0.00530$

$C_{D_{P_{C_L}}}$ Reynolds number correction $\Delta C_D = -0.00037$

Predicted full-scale Method (C) $C_{D_P} = 0.01448$

Predicted full-scale Method (B) $C_{D_P} = 0.01498$

The results in figure 54 compare the full-scale values of C_{D_P} at M = 0.700 for a Reynolds number of 32.5×10^6/MAC.

<u>Subcritical profile drag correlation</u> - The variation of profile drag with $C_{L_{A-h}}$ compares very favorably with the trends given by the flight test data points. The two levels shown for the predicted C_{D_P} represent the maximum spread in scale effect from the estimates of $\Delta C_D = 0.0005$ (Methods (B) and (C)). The results indicate that the predicted value of $C_{L_{A-h}}$ for minimum drag agrees very closely with full-scale evidence. Further, over most of the $C_{L_{A-h}}$ range of direct interest to cruise flight conditions, the variation of C_{D_P} with $C_{L_{A-h}}$ is in excellent agreement.

At this stage, it would be appropriate to discuss the correlation results achieved in relation to the expected accuracy of both the wind tunnel and flight test data.

Although the quoted accuracy of the balance axial force measurements is given in Volume 2 as ± 0.0005 in C_A, this is based on the maximum rating of the balance. Repeatability of the test data, based on loads of only one-half of the full rating, was shown to be considerably better than this, being of the order of ± 0.0001 to ± 0.0002 in C_D, as shown in figure 10(c) of Volume 2. Other accumulated errors of the instrumentation system are reflected in this figure. Thus, it is suggested that a more realistic figure based on the test experience should be of the order of ± 0.0002 in C_D. This represents $\pm 1.3\%$ of full-scale profile drag, or $\pm 0.8\%$ of total drag. Analysis of the flight test data conducted during Phase I of this program (ref. 1), concluded that the overall accuracy was $C_D = \pm 0.00074$, or $\pm 3.3\%$ of total cruise drag. Further, the apparent scatter in the data points was of the same order as the estimated accuracy. The correlation shown in figure 54 suggests that the agreement between prediction and flight is within the accuracy limits quoted from the wind tunnel test and flight data.

Wind tunnel and flight values of $C_{D_{P_{min}}}$ are shown in figure 55 as a function of Reynolds number. The magnitude of the extrapolated value of $C_{D_{P_{min}}}$ using method B, based on Karman-Schoenherr flat plate skin friction and a super velocity shape factor, shows agreement within 0.0001 in C_{Dp} of the statistical mean line of the flight data based on the method of least squares. This agreement should be assessed in the context of the review of flat plate skin-friction accuracy discussed previously, where it is shown that scatter in the measured C_f data results in an uncertainty in predicting full-scale drag of at least ± 0.0005 in C_D. The predicted value of $C_{D_{P_{min}}}$ based on a Reynolds number correction from viscous theory, method C, is seen to be 0.0006 less than the flight test mean line. This results from the slightly higher scale effects on form drag which are computed from the theory.

The correlation as it appears in figure 55 implies that the estimated full-scale roughness drag which has been added to the predicted values of C_{Dp} is substantially correct if the method B scaling correction is used, and underpredicted if the method C result is assumed. These conclusions are, however, dependent on the assumption that the excess profile drag of the total configuration is independent of Reynolds number. The results from the model component drag analysis (table 3) show that this consists primarily of wing-fuselage and afterbody pressure drag interference. It is seen also from figure 55 that the effective profile drag increment above estimate, accounting for trimming, is $\Delta C_{Dp} = 0.0030$. No confirmation of scale effects on the wing-fuselage interference is available over the Reynolds number range from $3.05 \times 10^6/\text{MAC}$ to flight values, although the results of the afterbody analysis indicate a reduction of $\Delta C_D = 0.0002$ in pressure drag over the range from $1.83 \times 10^6/\text{MAC}$ to $3.05 \times 10^6/\text{MAC}$.

With regard to the possibility of scale effects on the excess profile drag component, some justification may be made for assuming that this is dependent on the turbulent boundary layer parameters over the Reynolds number range from wind tunnel to flight. Thus, excess pressure drag from the wing and fuselage may reduce in the same proportion as the estimated profile drag of the configuration. Examination of the component interference drag increments indicate that if this approach is taken, the excess drag would reduce to approximately $\Delta C_D = 0.0020$ at flight Reynolds numbers, giving a predicted value of $C_{D_{P_{min}}}$ of 0.0135, based on method C, or 0.0140 for B.

Aside from the uncertainties of obtaining an exact correlation of $C_{D_{P_{min}}}$, the results in figure 55 confirm that the variation of profile drag with Reynolds number of the flight data is representative of smooth turbulent flow conditions on the aircraft surfaces. This implies that the effective distributed roughness is always less than the equivalent sand grain values which would be predicted from Nikuradses' criteria at these Reynolds numbers. From these results, the equivalent sand grain roughness of the wing, k_s, is estimated to be less than 0.00026 inches at flight Reynolds numbers up to $90 \times 10^6/\text{MAC}$. Reference 14 relates the equivalent sand roughness parameter, k_s, to the arithmetic average height of various surface grain structures, and $k_s = 0.00026$ inches corresponds to an average surface roughness, k, of approximately 150 micro-inches. This should be regarded as an upper limit, and more realistic values considerably less than this figure are implied.

<u>Drag polars and drag-rise characteristics</u> – Correlation of the configuration total drag polars for M = 0.700, 0.750 and 0.775 is shown in figures 56 (a), (b), and (c). These results indicate that the predicted full-scale drag in the range of $C_{L_{TRIM}} \approx 0.40$ is in good agreement with the flight data points at all Mach numbers. At lift coefficients less than 0.40, the full-scale predicted $C_{D_{min}}$ (as distinct from $C_{D_{P_{min}}}$ which occurs at $C_{L_{TRIM}}$ = 0.40) is less than flight levels by approximately 0.0010 at M = 0.700, increasing to 0.0020 at M = 0.775. Reasons for these discrepancies are not immediately apparent from examination of both wind tunnel and flight data. However, the following items are considered to be possible sources of error.

(i)   Errors in the flexibility corrections applied to the induced drag in the flight test data analysis, (ref. 1)

(ii) Further unknown wind tunnel corrections

(iii) Fuselage flexibility corrections

(iv) Transition underfixed on model wing lower surface at low C_L.

The induced drag flexibility correction analyzed in reference 1 was shown to be highly sensitive to the magnitude of wing-fuselage carry-over load distribution at low values of C_L, thus having a significant effect on the computed wing efficiency factor based on the total wing load. This item is considered to be the most likely source of error, and further study would be required to evaluate alternative methods of computing this correction. The other items listed above, notably (iii), the fuselage flexibility, would also require detailed analysis to determine the effect of large differences in tail download over the test C_L range on the fuselage and empennage flexibility. The possibility of further unknown errors in the support interference corrections is considered remote in view of the analysis of test data completed. In order to evaluate (iv) above, a sublimation check would be required on the wing lower surface in a new test in order to confirm that transition is properly fixed. The experience on the C-5A transition fixing program, however, would suggest that this is an unlikely source of error.

Drag-rise characteristics are presented in figure 57 as incremental figures relative to the subcritical drag level at M = 0.700. The results from flight test denote the equivalent rigid aircraft condition from the analysis of reference 1. The predicted drag-rise from wind tunnel data with the standard transition fixing technique shows that the drag-rise Mach number, defined arbitrarily as the Mach number for an increment of ΔC_D = 0.0020 above M = 0.700 levels, reduces more rapidly with increasing C_L than indicated by the flight data. The correlation with flight data is improved through use of the aft transition technique. In quantitative terms the wing & fillet drag-rise of 0.0031 in ΔC_D, discussed in the previous section is reduced by 0.0006. These results are now discussed with reference to previous data summarized in figure 58, in which the effects of transition location on shock movement and trailing edge pressure divergence with increasing Mach number are examined. In the

subcritical flow condition, fixing transition forward near the leading edge induces a thicker boundary layer at the trailing edge, and in the case of the C-141A wing, the tendency for a trailing edge pressure divergence and separation is magnified. Figure 58 also shows that, in the supercritical speed range, the rearward movement of shock position with increasing Mach number is retarded by this simulation technique, due to interaction of the rear separation and shock at drag-rise conditions. The over-riding effect is, however, the premature rear separation as induced by transition fixing, resulting in a less favorable drag-rise at low wind tunnel Reynolds numbers. These results confirm that fixing transition closer to the main shock location improves the full-scale simulation technique, but it should be emphasized that this result may not necessarily be achieved on other wing designs with different super-critical flow characteristics.
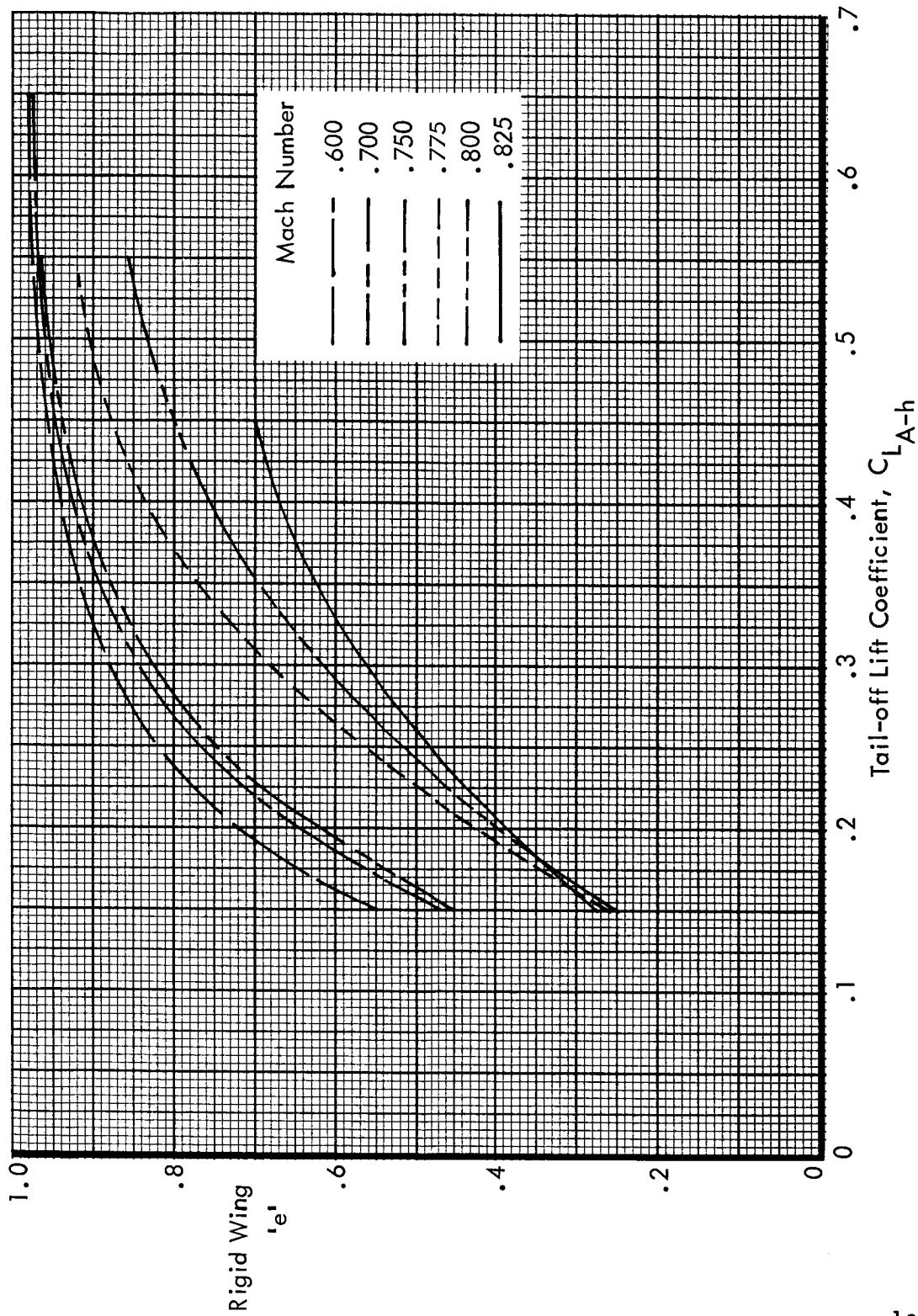
Figure 53. Rigid Wing Span Efficiency Factors

137

TABLE 4

C-141A ROUGHNESS DRAG ESTIMATE

ITEM	ΔC_D (COUNTS)
Antennae	2.337
Wing steps and gaps	1.250
Control surface vent gaps	0.890
Wing leading edge gaps	0.320
Wing fasteners	0.040
Fuselage steps and gaps	0.410
Fuselage fasteners	0.063
Fuselage doors	0.410
Empennage steps and gaps	0.350
Pylon steps and gaps	0.280
Leakage (Pressurization)	0.180
Total	* 6.530

* Total rounded off to 7 counts or $\Delta C_D = 0.0007$
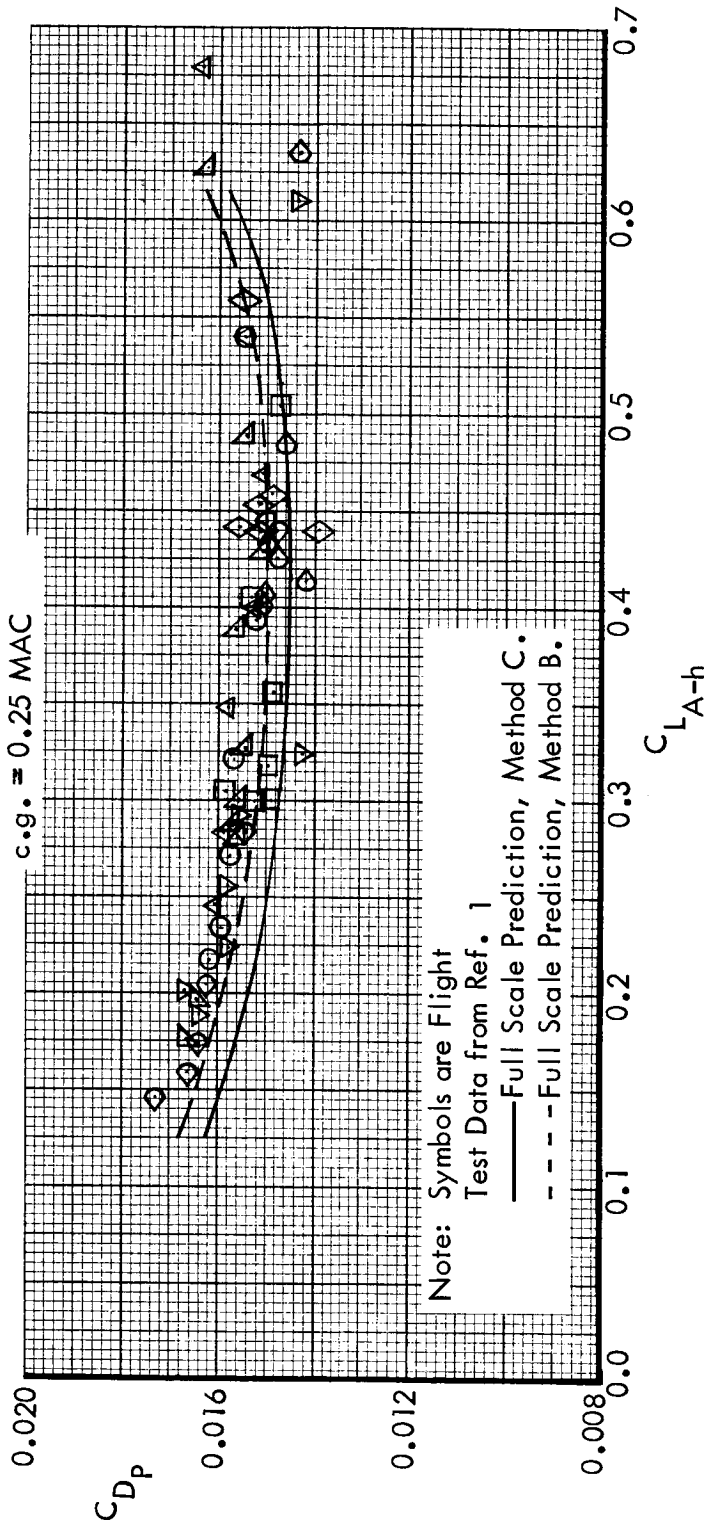
Figure 54. Comparison of Predicted Full Scale and Flight Test Profile Drag.
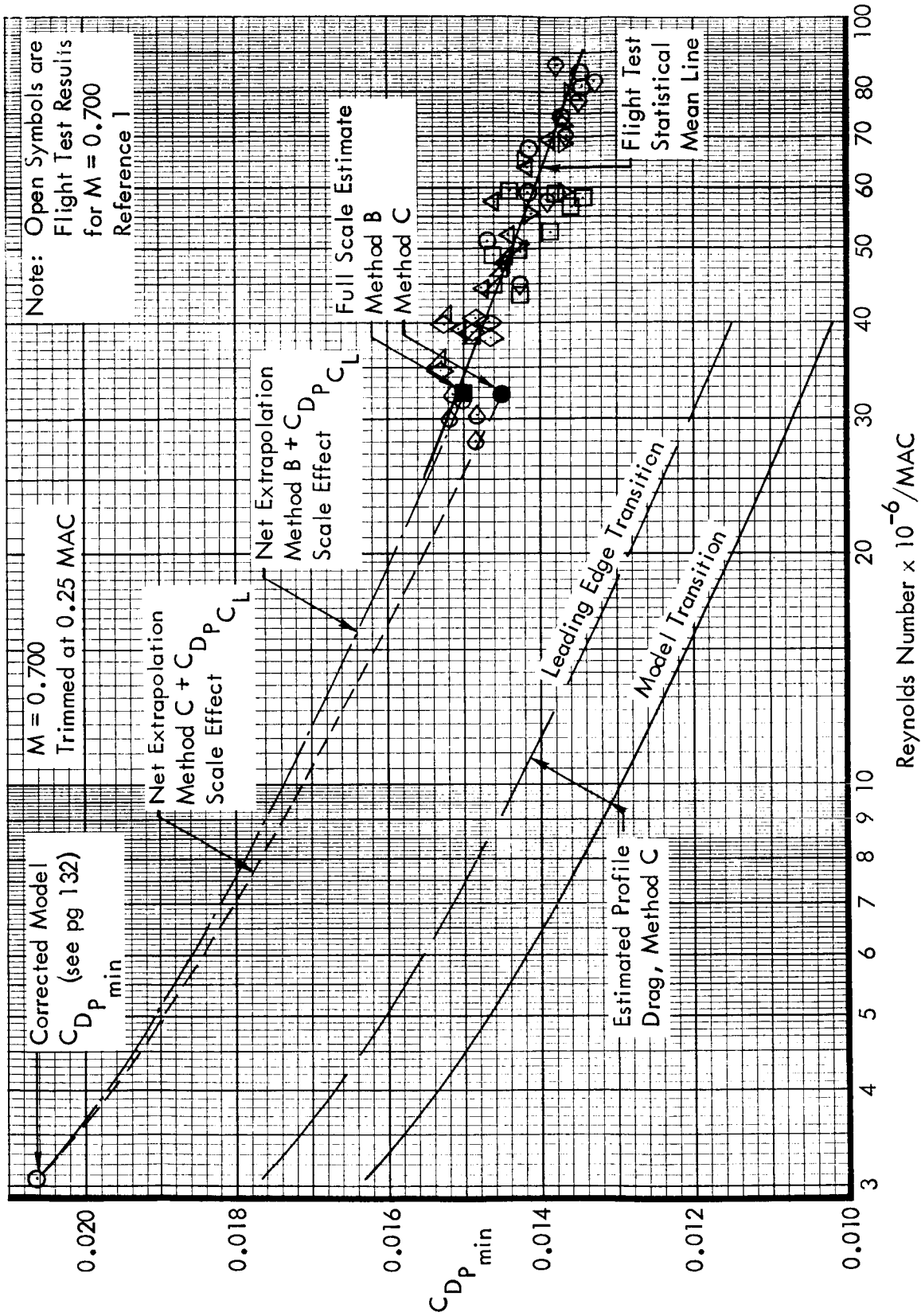
Figure 55. Correlation of Minimum Profile Drag

140
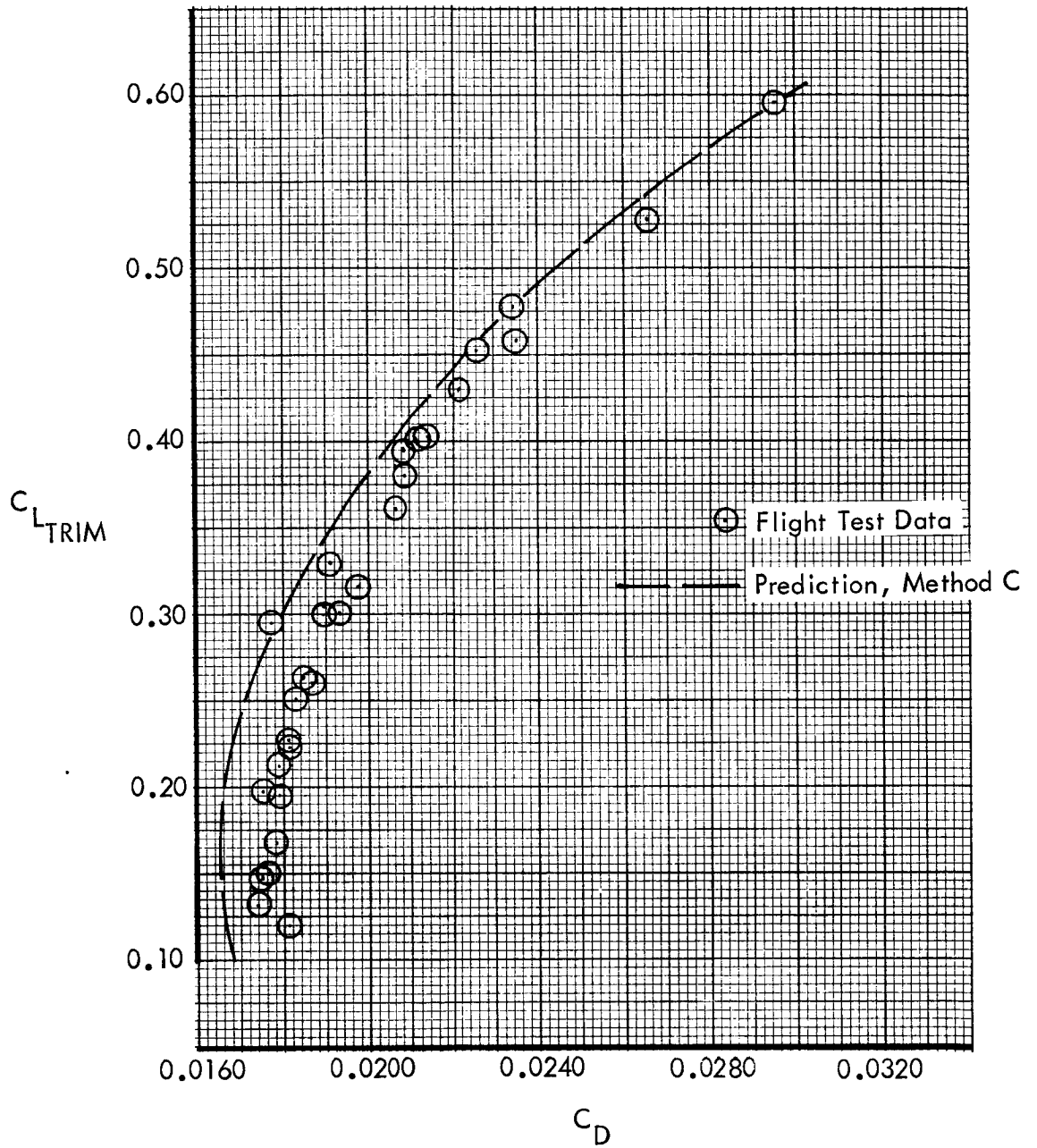
(a) M = 0.700

Figure 56. Correlation of Predicted Full Scale & Flight Test
Drag Polar. R_N = 55 x 10^6/MAC.
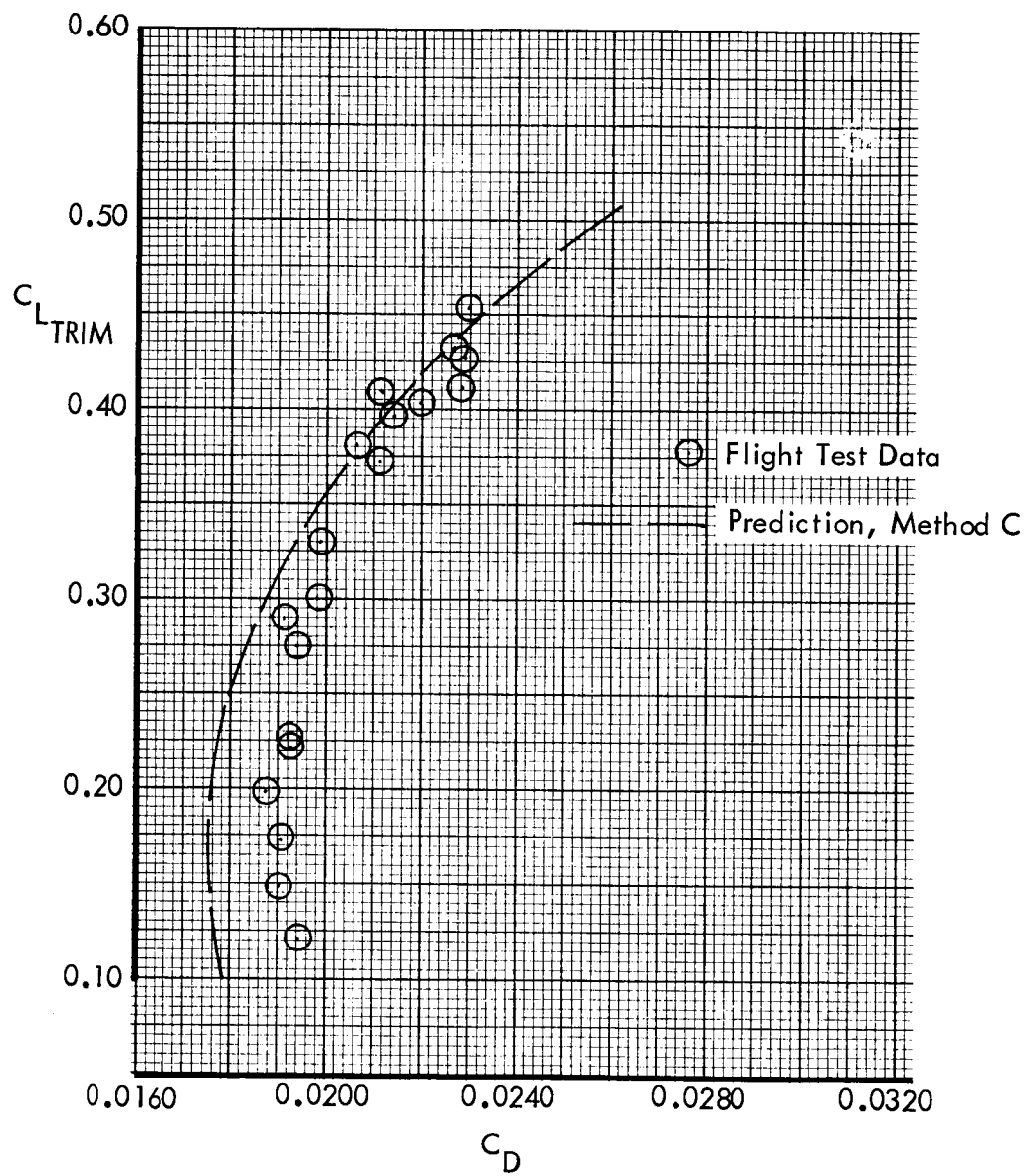
(b) M = 0.750

Figure 56. Continued

(c) M = 0.775
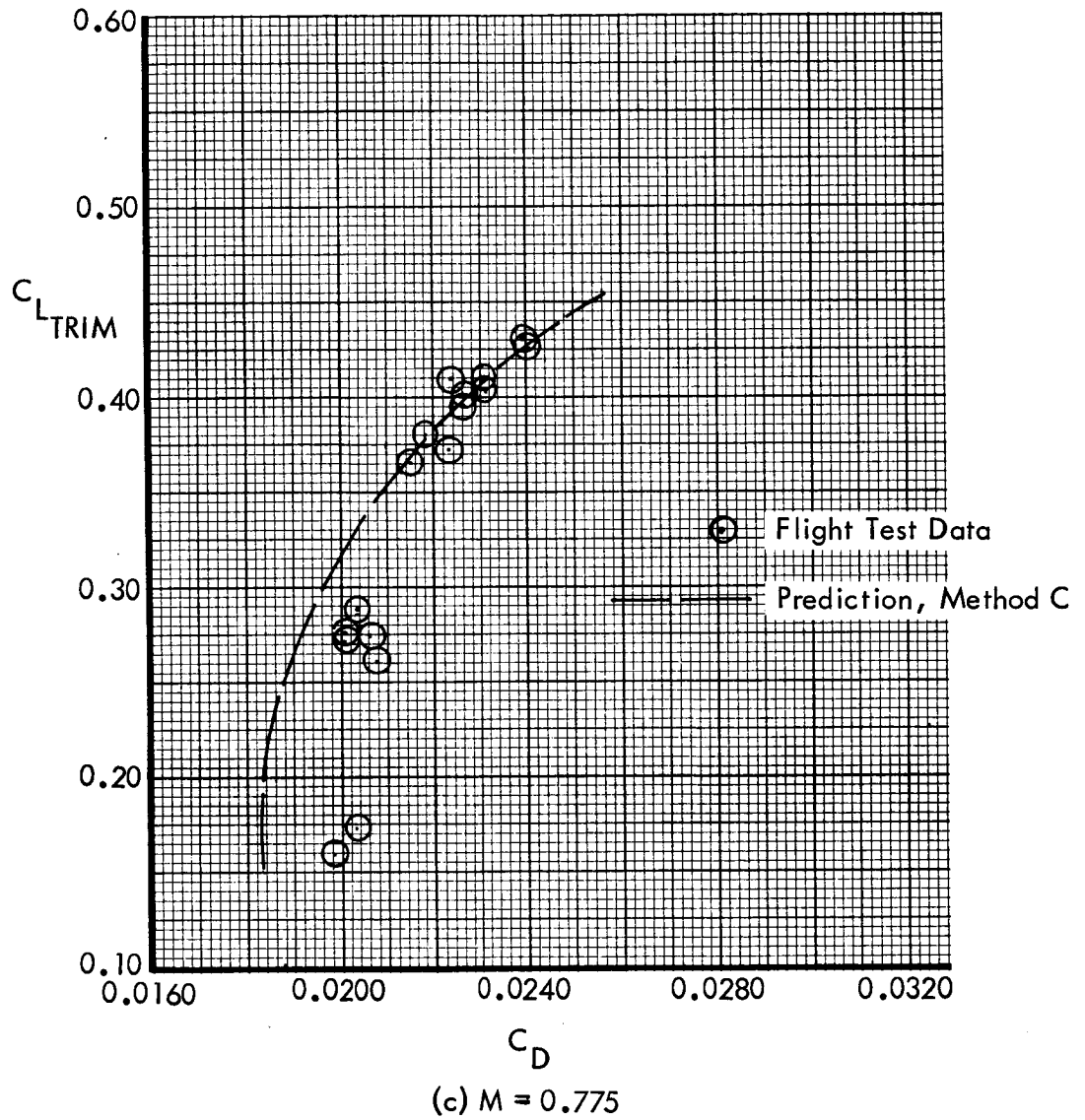
Figure 56. Concluded
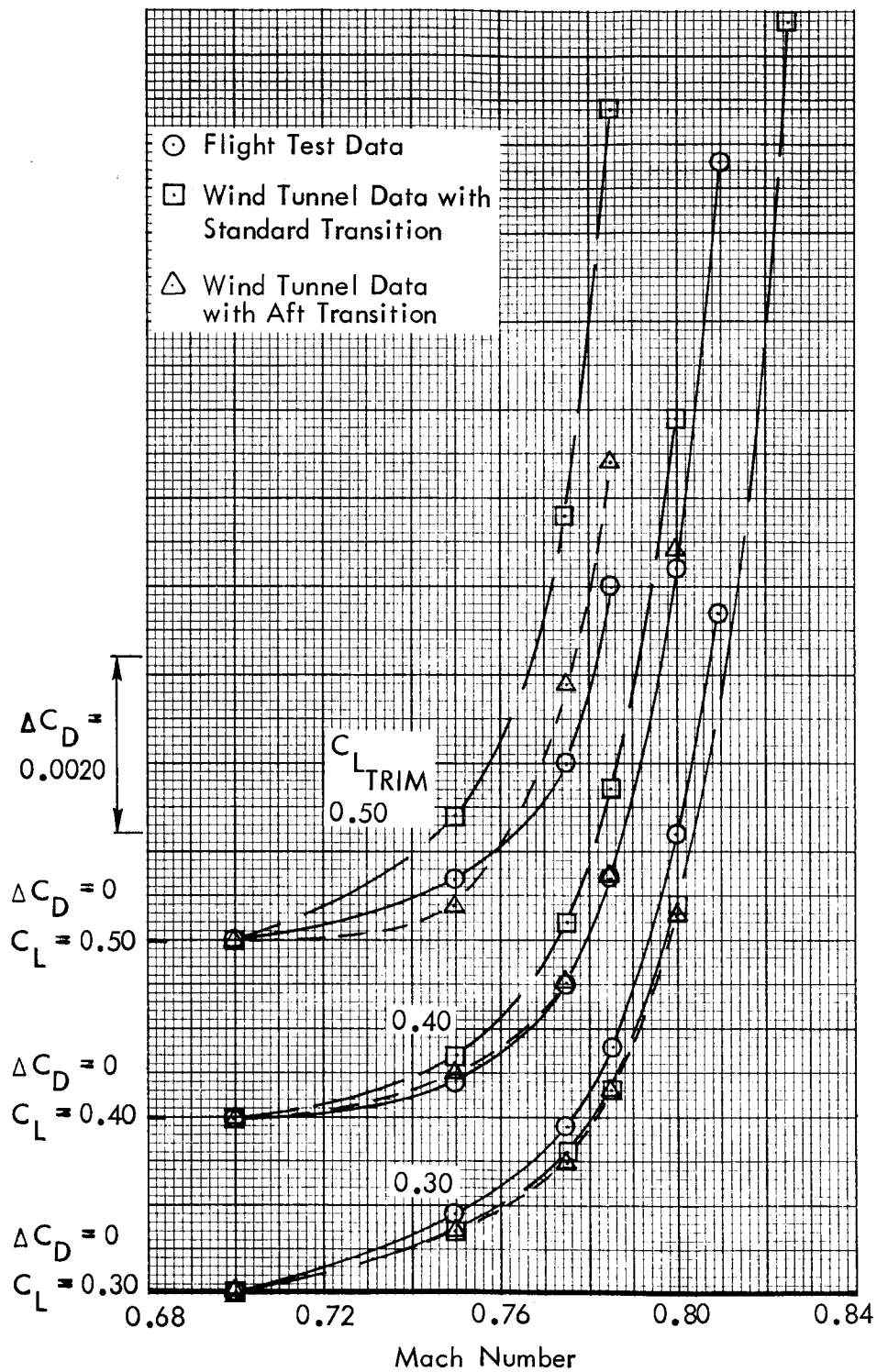
Figure 57. Drag Rise Characteristics. Trimmed
at c.g. = 25% MAC

○ U/S Transition, 0.075 c, k = 0.0025"

+ U/S Transition, 0.40 c, k = 0.0040"

▢ U/S Transition, 0.50 c, k = 0.0040"

◇ Trans. Free

$C_L = 0.4$

$R_N = 4.2 \times 10^6/\text{MAC}$

Shock Location % x/c η = 0.389

Flight Test

x/c_{Shock}

MACH NO.

$C_{P_{TE}}$

$C_{P_{TE}}$

Flight Test Data
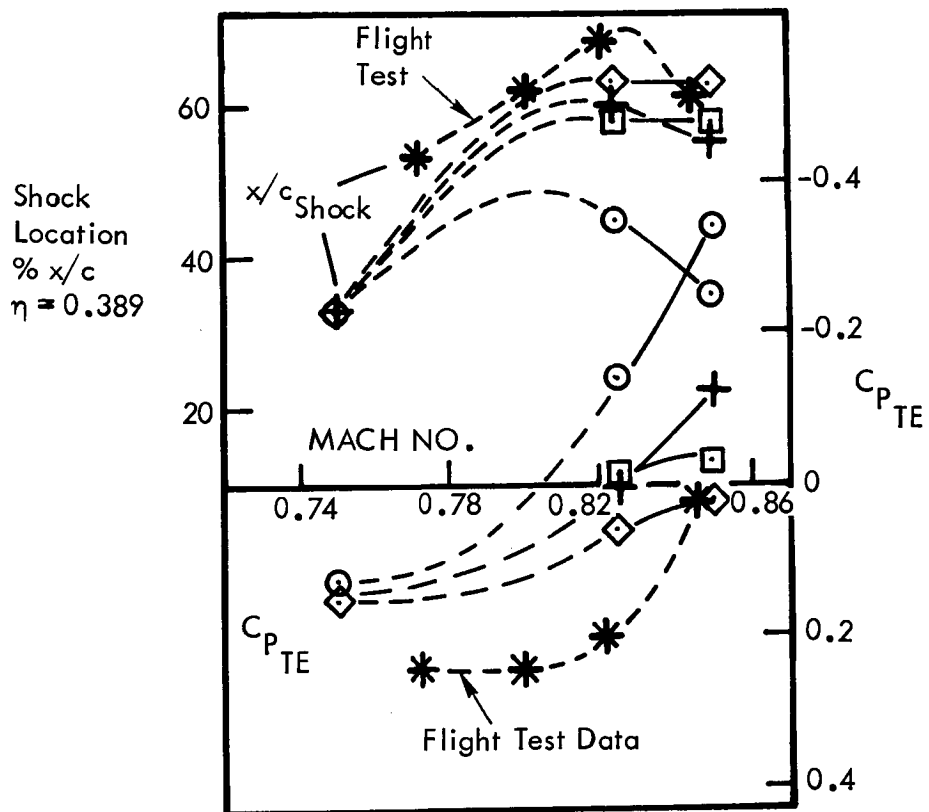
Figure 58. Effect of Transition Location on Drag Rise Characteristics $C_L = 0.40$

CONCLUSIONS AND RECOMMENDATIONS

A comprehensive analytical and wind tunnel test program has been conducted on the C-141A configuration in order to evaluate the degree of correlation attainable between predictions based on wind tunnel results and flight test cruise drag data. The principal conclusions follow.

(1) Review of a considerable quantity of test data on flat plate skin friction at incompressible speeds, which form the basis of several skin friction empirical laws, has identified sources which explain the considerable scatter ($\pm 10\%$) in the data in the Reynolds number range up to 40×10^6. It is concluded that use of flat plate skin friction to extrapolate low Reynolds number wind tunnel data to full-scale may result in uncertainties in predicted full-scale drag of a transport aircraft wing of ± 0.0005 in C_D.

(2) Use of the "flat plate x shape factor" approach to estimating profile drag can give inaccuracies, apart from those inherent in the flat plate skin friction, due to inadequate definition of a true shape factor, which should account for the exact degree of form or pressure drag in unseparated flows. Correlation of two-dimensional airfoil minimum profile drag test data suggests that use of existing empirical methods underpredicts $c_{d_{p_{min}}}$ by the order of 15 percent. A general lack of available good quality test data is identified, particularly for transition-fixed conditions, and very limited results are available over a wide Reynolds number range to determine scale effects on form drag.

(3) Detailed studies of wing profile drag for the C-141A configuration were conducted in order to determine a valid basis for extrapolating the wind tunnel data to full scale. The minimum profile drag from the strip-analysis super velocity method, (A), was calculated to be 0.0064 at $R_N = 3.05 \times 10^6/MAC$, compared with 0.0081 from method B, obtained by assuming the wing to be represented by the MAC for skin-friction purposes. A subsonic viscous flow theory developed at Lockheed-Georgia, method C, was shown to predict a corresponding value of 0.0077. The low value obtained from method A confirms the results of the airfoil correlation studies, and indicates that the derivation of shape factor by the super-velocity method does not account for the total viscous pressure drag on airfoils. The comparison of scale effects from the various methods shows that the viscous theory, Method C, predicts an increasing shape factor at Reynolds numbers below about $6 \times 10^6/MAC$, whereas the values from method B are assumed to be constant. Thus, Reynolds number effects on profile drag tend to be greater from method C, compared to method B. The estimated total difference for the C-141A configuration was shown to be 0.0005 in scale effect between method B and C.

146

(4) Systematic wind tunnel tests were conducted on a 0.0275-scale C-141A model to provide the necessary data for a correlation with the flight test results. A major portion of the test program was concerned with the evaluation of the model support system tare and interference corrections necessary to obtain equivalent free-air data. The interference of the lower support sting was shown to be positive at positions close to the model, resulting in typical values of $\Delta C_D = 0.0004$ at cruise conditions. The evaluation of the interference-free data for maximum sting-model displacement was found to be dependent on the effects of the tunnel ceiling interference on the tail downwash field for values of $1/D^2 < 0.40$, or $2h/B < 0.50$, where h = distance of tail from ceiling, and B = tunnel width. Use of a theoretical three-dimensional vortex lattice method to evaluate these interference effects was found to be very successful in substantiating in qualitative terms the trends measured in the model data. The main support blade drag interference on the model was found to be positive (0.0004 in C_D) at low Mach numbers, approximately zero at cruise Mach number and negative at $M > 0.750$, $\alpha_{FRL} > -1°$. The resulting effect on the model drag-rise characteristics was to reduce this by approximately 0.0010 in C_D over the full Mach number range.

(5) Fully-corrected model test data was extrapolated to full-scale Reynolds numbers by the estimated changes in component minimum profile drag for assumed, attached flow conditions. The comparison of the subcritical lift-dependent profile drag at $M = 0.700$ indicated good agreement between prediction and flight data in the variation of C_{D_P} with $C_{L_{A-h}}$ over the cruise-lift coefficient range. The predicted value of $C_{L_{A-h}}$ for minimum drag was also in good agreement with flight results.

The principal correlation technique used in the comparisons was based on the assumption that the excess profile drag of the configuration (0.0030 in $C_{D_{P_{min}}}$ based on method C) at $R_N = 3.05 \times 10^6/MAC$ was independent of Reynolds number up to flight values. Results from the model component drag evaluation showed that the main contributions to this excess drag were from wing-fuselage interference and empennage-afterbody drag. These increments were respectively 29 percent and 60 percent above the profile drag estimates for these components. Correlation of subcritical $C_{D_{P_{min}}}$ was shown to be within 0.0001 from the method B extrapolation or 0.7 percent of the statistical mean line of the flight points, and 0.0006 or four percent using the method C extrapolation. The results from method B imply that the estimated full-scale roughness drag which was applied to the prediction was substantially correct, but underpredicted if the method C approach was assumed. Both of these methods, however, assume that the respective excess pressure drag increments resulting from interference and separation are independent of Reynolds number. The possibility of a scale effect on the total excess drag, particularly from the afterbody pressure drag component, suggests that if this reduces in the same proportion as the minimum profile drag estimate, the full-scale prediction is 0.0016 in $C_{D_{P_{min}}}$ below the flight data, or ten percent. This result, therefore, represents an alternative approach to the correlation, and

must be included as a possibility in view of the absence of detailed knowledge on scale effects of the excess profile drag over the Reynolds number range from 3.05×10^6/MAC to full scale. These results should be viewed in relation to the degree of accuracy known from the different sources of data. Repeatability of the wind tunnel data was shown to be within 0.0002 in C_D, or $\pm 1.3\%$ of full-scale $C_{D_{P_{min}}}$, while the overall accuracy of the flight data was shown to be ± 0.0007 or $\pm 5\%$. In addition, scatter in the flat plate skin friction data, used to extrapolate wind tunnel results in method B, was shown to give a scale effect uncertainty of ± 0.0005 in $C_{D_{P_{min}}}$.

(6) The trends of $C_{D_{P_{min}}}$ noted in the flight test data confirm that the effective, distributed roughness of the C-141A configuration is representative of smooth, turbulent boundary layer conditions at Reynolds numbers up to 90×10^6/MAC. The equivalent sand grain values are thus always less than would be predicted from Nikuradse's criteria if these Reynolds numbers were assumed to be 'critical', i.e., representative of rough turbulent flow. It is concluded that the effective sand grain size, k_s, for the wing surface cannot be greater than 0.0026 inches, or an equivalent roughness height, k, of 150 micro-inches, and is likely to be considerably less than this figure.

(7) The comparison of total aircraft drag polars was shown to be good at cruise lift coefficients near 0.4. At values of $C_{L_{TRIM}} < 0.40$, the predicted values of $C_{D_{min}}$ were less than flight data by approximately 0.0010 in C_D at $M = 0.700$, increasing to 0.0020 at $M = 0.775$. The reasons for these discrepancies are possibly associated with the computation of the flexibility correction to induced drag for the flight test data points.

(8) At cruise-lift coefficients, the predicted drag-rise characteristics, based on model tests with transition-fixed at ten percent wing MAC from the leading-edge, resulted in a drag-rise Mach number 0.01 less than flight data. This correlation was improved by use of a transition location further downstream, but ahead of the main shock at cruise conditions. This technique is of limited use, however, and cannot necessarily be applied to other wing designs with different supercritical flow characteristics.

It is recommended that further research is initiated by the following:

(a) Evaluation of scale effects on two-dimensional airfoil profile drag at high Reynolds numbers through an experimental research program. Use of the Lockheed-Georgia CFF Facility is recommended where Reynolds numbers of up to 50×10^6 per foot can be achieved.

(b) Studies of configuration three-dimensional interference drag, through a combined analytical and experimental program.

(c) Continued use and development of the three-dimensional vortex lattice program as a method for evaluating model support interference effects.

148

(d) Evaluation of fuselage afterbody pressure drag scale effects through a flight test program on the C-141A aircraft.

(e) Continued acquisition of good quality wind tunnel data on a variety of different aircraft configurations in order to continue wind tunnel-flight correlation studies.

APPENDIX A

REVIEW OF EXPERIMENTAL AND ANALYTICAL
RESEARCH ON INCOMPRESSIBLE FLAT PLATE SKIN FRICTION

Experimental Research

Following the example of Schoenherr (ref. 7), and Hughes (ref. 5), and utilizing some results from their surveys, as well as from additional references, the general summary contained herein has been prepared. The discussion which follows centers around figure 1, introduced at the beginning of this report, which is a comprehensive summary of the important experimental results in both water tanks and wind tunnels. As Hughes points out, regardless of the method of experiment being used, it is impossible to avoid the results being affected by some of the following factors.

Form resistance;

Wave resistance (a consequence of form and speed in water tests);

Lack of absolute symmetry of the plane, resulting in side forces and possible further distortion of the plane if structurally weak;

Edge effects (extended laminar flow region or even laminar separation due to sharp leading edge);

Resistance of the turbulence tripping device.

Incomplete turbulence stimulation (whether or not equipped with transition fixing device);

Over-fixing of transition.

Interference from supports;

Air resistance of above-water structure;

Length-to-breadth ratio (degree of two-dimensionality of measured results).

Tests in water – Froude, 1872: The earliest experiments were conducted by William Froude, (ref. 2), and consisted of thin straight planks up to 50 feet in length, towed through water at varying speeds. According to Hughes (ref. 5), the l/b for the longer planks was quite large (31.6 for the 50 foot plank), possibly explaining the tendency for Froude's data to appear high at Reynolds numbers above 6×10^6. Although Froude made corrections for

the air resistance of the towing apparatus, there are several other features about his experiments which warrant attention. For example, the planks were completely submerged with the top edge only 1 1/2 inches below the surface, and it appears some interference would be inevitable. Also, the planks were quite flexible, having a thickness of only 3/16 inch, and the longer planks would tend not to be true planes because of the low thickness ratio; however, wave resistance would not be significant. Little is known about the extent of laminar flow over the forward part of Froude's planks, and since this is the case with most of the earlier work, every attempt is made in this analysis to exclude those experimental points which have obvious regions of laminar flow. Points attributed to Froude were obtained from Falkner's analysis of experimental results (ref. 8), where the resolution appears to be better than elsewhere.

Gebers, 1908, 1919: Gebers (ref. 3 and 4), repeated the work of Froude in 1908 and again in 1919 by towing planks up to ten meters long and at speeds up to eight meters per second. The data shown here were taken from Goldstein (ref. 30). Like Froude's planks, Gebers' planks were sufficiently thin to minimize wave resistance, but caused some distortion, especially at the higher speeds. These planks also had very sharp leading edges and, consequently, mixed flow conditions were more persistent than for planks with round leading edges. In his later test, Gebers had made allowance for edge effect and for form resistance. Hughes noted that Gebers' results indicated irregular patterns, but that at the higher Reynolds numbers a general effect of increasing drag with increasing 1/b could be seen. Data obtained for the smallest plank, one meter in length with a much greater thickness, appeared to have the best agreement with other test results. This is perhaps indicative of the importance of stiffness in these types of experiments. Generally, Gebers' data are lower than the average, a tendency which exemplifies mixed flow conditions.

Froude Tank, NPL, 1915: Baker (ref. 31), following the example of Froude and Gebers, investigated the resistance of a series of planks towed in water at the William Froude National Tank. These planks were shorter than previous examples, having lengths of 3, 8, and 16 feet and 1/b ratios of 1.63, 4.35, and 8.7, respectively. They were considerably thicker also, at 2.08 percent, and consequently should be affected somewhat by wave resistance and form drag. The results shown in figure 1 are considerably higher than the mean and thus lend support to this hypothesis.

Kempf, 1925: The results of Kempf (ref. 6), are of particular interest because, as can be seen in figure 1, they represent the only available flat plate skin friction data above 230 million Reynolds number, and are one of only two sets above 100 million. In view of the significance of Kempf's observations, a more careful assessment of his experiments is warranted.

Kempf employed the technique of a floating element device to measure local shear forces, instead of measuring total resistance as was done in previous testing. The apparatus consisted of movable plates, placed in the bottom of a long iron pontoon, and towed in the 350 meter Hamburg Tank. These plates were placed at distances from around 8 meters to about 69 meters from the nose of the pontoon and the surface resistance measured on the

plate. There are several sources for error in measurement recognizable in Kempf's experiments. Schoenherr, whose mean curve at high Reynolds numbers relies solely upon Kempf's observations, noted that Kempf's tests were made at fairly high speeds and would, therefore, probably be subject to considerable wave-making resistance.

Falkner (ref. 8), introduces the significance of the length of run in towing tests and asserts that a run of at least 6 - 12 lengths is required in order to achieve drag levels within one percent of the final value. This is more serious for measuring local resistances than when measuring total drag. Kempf's pontoon could not have exceeded run lengths of 3.7, 4.5, and 5.7 in the Hamburg Tank, and some error is implied. Finally, Falkner points out that because of the effect of the shape of the pontoon nose, there is an uncertainty in the distance between the nose and each measuring plate.

The sources of error would show up as form drag, due to wave resistance and nose shape, and mixed flow due to insufficient run length. Form drag tends to compensate for the lack of fully turbulent flow; however, the degree of cancellation is unknown.

Schoenherr/Washington Unpublished, 1932: Schoenherr's experiments, conducted at the David Taylor Model Basin (formerly the U. S. Experimental Model Basin), only covered a range of Reynolds numbers from 100,000 to about 2 million and consequently are not used here. However, results of previous tests conducted at the same site by other researchers, covering a higher Reynolds number range, are also reported by Schoenherr (ref. 7), and these data, which he attributes to Admiral D. W. Taylor, Captain McEntee, and Captain Eggert, are repeated here as "Washington Unpublished" (see figure 1). Although Schoenherr's results are not included in figure 1, a brief discussion of the technique and problems should provide further insight into the accuracy of these type experiments.

Following a suggestion from Captain Eggert, Schoenherr sought to overcome the stability problem of towing tests by using two parallel plates, held together above the water line by struts. This device he called a "catamaran friction plane." The testing tank used by Schoenherr was 35 feet long, 4 feet wide, and 22 inches deep. A 3-foot catamaran plane was first tested which had its twin planes 18 inches apart, had a taper thickness of from 1/2 to 1/8 inch and floated to a draft of 12 inches. Hughes points out that there would be a measurable interference effect under such restricted channel conditions, amounting to at least two percent form drag. Schoenherr reported that, at towing speeds in excess of three feet per second, appreciable wave making was experienced.

Another problem encountered by Schoenherr was mixed flow conditions. In some of his later testing, he fixed transition by applying sand particles from the leading edge back 4 inches, amounting to 11 percent of the total length for the 3-foot catamaran plane and 5.5 percent for the 6-foot plane. The roughness of this area corresponded to that of Number 2 sandpaper, approximately 0.15 inches, an amount which greatly over-fixes transition and should produce a significant grit drag.

With his 6-foot catamaran plane, Schoenherr also produced turbulent flow by towing two small, roughened struts just ahead of the plane. The measured strut resistance in this case was approximately 13 percent of the gross resistance, and therefore an appreciable wake would have been created by the strut, and the plane resistance alone, used by Schoenherr, would have been low because of this.

Hughes concludes that to account for all these effects, the published results should be reduced by a considerable amount. Although this statement cannot be made for the "Washington Unpublished" data, it is quite likely that these results would be similarly affected.

Hughes, 1952: Hughes (ref. 5), at the NPL tank, sought to clear up some of the confusion and lack of consistency accompanying the earlier skin friction research. He conducted two main sets of experiments: one using vertical plates or planks, with only one immersed longitudinal edge, where the total resistance of the wetted surfaces was measured, and a second set using shallow draft pontoons, similar to the Kempf experiments. Hughes experiments were very comprehensive in that he tested several materials (wood, glass, and metal) with differently prepared surfaces, with and without the transition fixed, and he varied the length to breadth ratio over a wide range. The results were corrected for air resistance, form drag and drag of the turbulence stimulation device.

His results showed a consistent variation of C_f with R_N as well as $1/b$, and provide valuable proof of the accuracy limitations of the earlier water tank tests. The extrapolated line for $1/b = 0$, corresponding to two-dimensional flow, is seen to be about eight percent below the Schoenherr line at $R_N = 20$ million.

The implications made by Hughes $1/b = 0$ line are quite interesting; however, the highest Reynolds number attained for the smaller $1/b$'s tested was only ten million, and trends at the higher R_N's would be strictly conjecture. In addition to conducting a comprehensive experimental investigation, Hughes also prepared a very thorough summary of a number of other water tests. This important work is highly recommended if the reader is seeking additional background information in the area of plane surface resistance.

Tests in air – Experiments were conducted in 1915 by Gibbons (ref. 9), on a 9.5 foot glass plate in the Navy Wind Tunnel at Washington. Wieselsberger (ref. 10), conducted similar experiments in Goettingen in 1925 using varnished cloth planes. Results from these experiments shown here and attributed to Gibbons and Wieselsberger were obtained from Goldstein, (ref. 30). The Gibbons' data appear compatible with the mean of all the measurements; however, the observations of Wieselsberger are somewhat higher. Schoenherr noted that the varnished cloth planes of Wieselsberger were of questionable smoothness, and this appears to be the case. A more consistent set of results was achieved later, in 1937, by Jones and Williams, at the NPL Compressed Air Tunnel. They determined the frictional restance of a plate by measuring the loss of momentum, and their observations, according to Falkner (ref. 8), must carry great weight because the experiment was practically free from known error. Since Falkner was writing a case against the Schoenherr line only a few

years after the Jones and Williams experiment, it is likely that this is an overstatement.

Smith and Walker, 1959: The great majority of the air test results shown in figure 1 are from the work of Smith and Walker (ref. 12). Their objective was to use "modern" wind tunnel investigative techniques to accurately define a skin friction law. Friction measurements were made on a flat plate which formed one wall of a channel mounted in the NASA Ames 12-foot pressure wind tunnel.

Local skin friction measurements were obtained using two methods. First, a floating element similar to that used by Kempf was employed to measure local shear at stations along the surface. Integration of these local shears converts these results into the corresponding drag loss. The second method is called the momentum defect method and involves computation of the skin friction drag by integration of measured boundary layer profiles. The floating element technique was quite sophisticated, being designed to eliminate or minimize problems with the gaps around the element inherent with this technique. Reynolds number range for the test was from two to around 50 million.

Spanwise and lengthwise checks on velocity profiles were made and indicated that good two-dimensional flow with essentially zero longitudinal pressure gradient was achieved. An air ejection-type boundary layer trip was utilized to stimulate turbulent flow and longitudinal velocity measurements, taken with varying amounts of airflow, which assured the attainment of turbulent flow with the least amount of disturbance. It is interesting to note that without the tripping device, measurements indicated a separation phenomenon near the leading-edge, this occurring despite a rounded leading-edge.

The care and precision of the Smith and Walker experiments imply that their results should receive considerable attention. As can be seen from figure 1, the consistency in these results is quite good with only a small amount of scatter. In the range of R_N from 3 to 30 million, Smith and Walker's measurements are lower by about one to two percent than the Schoenherr mean line, suggesting a different slope. This is important because, as seen earlier, differences in scale effect can be obtained with small slope differences over a large Reynolds number interval. However, no new law was proposed by Smith and Walker. Their reluctance was attributed to scatter in the values of parameters obtained from the experimental data and the limited Reynolds number range of their test.

Winter and Gaudet, 1966: Fairly recent investigations carried out by Winter and Gaudet (ref. 13), are of particular interest because of the high Reynolds number achieved. Their measurements were made on the sidewall of the RAE 8-foot by 8-foot wind tunnel over a Mach number range from 0.2 to 2.8. Surface shearing stress measurements were obtained directly, using a force balance as well as velocity and temperature profiles. The measuring station did not "float", as was the case in the Kempf and Smith-Walker experiments. All measurements were taken at one station and the variation in Reynolds number was obtained by varying the stagnation pressure. The effective length of run of the boundary layer was determined to be about 40 feet at subsonic speeds, giving Reynolds numbers up to 200 million at low speed, M = 0.2.

154

Most of the corrections discussed would not apply in the same manner to investigations of this type. The major problem with the single-point measurement on a tunnel sidewall is, of course, lack of information about the factors affecting the boundary layer ahead of the point. This apparently was of no consequence in the Winter-Gaudet experiments as they achieved excellent agreement with other skin friction results. Their observations confirm the variation of C_f with R_N established by the Kempf data at high values of R_N, at least up to the 200 million range. This is especially remarkable, in view of the vast differences in technique employed in these two experiments.

Analytical Research

Figure 59 shows a sample of five empirical formulae from analytical research on flat plate skin friction. Actually, none of these has evolved from a purely mathematical treatment of the flow over a flat plate, and at this time it is unlikely that one can produce anything but an approximation, or empiricism, based on some experimental results.

Early research followed the example of Prandtl, where the assumption was made that the velocity profile in the boundary layer of a flat plate is identical to that inside a circular pipe. This is sometimes called the 1/7 power velocity distribution law from which Prandtl derived his resistance formula for a flat plate,

$$C_f = 0.074 \, (R_1)^{-1/5}$$

where R_1 denotes Reynolds number based on length.
This formula is valid only over the range of R_N from 5×10^5 to 10^7 and, consequently, is not shown in figure 59.

In order to extend the range of validity of resistance formulae based on the 1/7 power law, substitution of the universal logarithmic velocity distribution law was made. Schlichting (ref. 32), obtained a modification to the Prandtl formula in this way. Calculations using the logarithmic velocity profiles become more cumbersome, and therefore Schlichting derived an empirical curve fit given by:

$$C_f = \frac{0.455}{(\log R_1)^{2.58}}$$

This formula is shown plotted on figure 59 as the Prandtl-Schlichting curve.

Based on the work of Von Karman, Schoenherr (ref. 7), was able to deduce an empirical formulae which approximated the mean line he had placed through a collection of experimental skin friction data. This has become the well-known Karman-Schoenherr line:

$$\frac{1}{C_f} = 4.13 \log (R_1 C_f)$$

Schultz-Grunow (ref. 33), set out to investigate the application of the logarithmic laws of velocity distribution within the boundary layer of pipe flow to flow along a flat plate. He made very careful measurements using plywood and metal plates mounted in the wall of a wind tunnel. Two types of measurements were made: velocity distributions within the free boundary layer and resistance of the plates. One means of measuring friction was to directly weigh the drag on a movable rectangular plate mounted at various locations in a sector of the principal plate. This was very similar to the movable plate technique employed by Kempf in his pontoon test.

Schultz-Grunow's measurements showed that the velocity profile in the outer portion of the boundary layer of the plate deviates systematically upwards from the logarithmic velocity distribution law of a circular pipe. Based on his results, he repeated the derivation of the resistance formula and obtained the following formula:

$$C_f = \frac{0.427}{(\log R_1 - .407)^{2.64}}$$

An excellent paper was written by Spalding and Chi (ref. 34), which reviews some twenty theoretical treatments of the turbulent boundary layer on a smooth flat plate. The major characteristics of these theories were summarized and their predictions compared with available experimental data. The root-mean-square error for each was computed for evaluation purposes, and a new calculation procedure was developed based on the accumulated knowledge. Consideration was not limited to the incompressible case.

The scope of the present work does not permit the type of detailed investigation which has been made by Spalding-Chi and the reader is recommended to consult reference 34 if seeking additional information.

Use of the Spalding-Chi equations directly is somewhat tedious, in that an iteration process must be used wherein the variation of local skin friction coefficient with Reynolds number is first determined, and then the mean skin friction is determined for a given combination of local skin friction and Reynolds number. The variation of mean skin friction with R_N is shown for comparison purposes in figure 59.

The final method shown in figure 59 is that due to Winter and Gaudet. Like the Spalding-Chi method, the Winter-Gaudet equations require an interation process. Details are to be found in reference 13.

APPENDIX B

METHOD FOR CALCULATING AFT FUSELAGE
PRESSURE DRAG FROM MEASURED PRESSURES

Pressure forces acting on any area are determined by the calculation,

$$Force = Pressure \times Area$$

or in coefficient forms

$$C = C_p \times A$$

where the pressure varies over an area, it is necessary to determine the average value acting on the total area.

For fuselage afterbodies, the average pressure acting in both the axial and normal directions must be determined. This is accomplished by an analysis of the forward facing and rearward facing pressures in the case of the axial component and the upper and lower surface pressures in the case of the normal component. Force coefficients referenced to wing area are calculated as

$$Axial: \quad C_A = \left[C_{P_{avg}} \left(\frac{S_{axial}}{S_{wing}} \right) \right]_{\substack{forward \\ facing}} - \left[C_{P_{avg}} \left(\frac{S_{axial}}{S_{wing}} \right) \right]_{\substack{rearward \\ facing}}$$

$$Normal: \quad C_N = \left[C_{P_{avg}} \left(\frac{S_{normal}}{S_{wing}} \right) \right]_{\substack{upper \\ surface}} - \left[C_{P_{avg}} \left(\frac{S_{normal}}{S_{wing}} \right) \right]_{\substack{lower \\ surface}}$$

The areas S_{Axial} and S_{Normal} are the projected areas of the fuselage afterbody in the axial and normal directions, respectively. Actual calculations of the average pressure and resulting pressure drag are made with the aid of a computer program using the following technique. Referring to the top diagram of figure 60, the area bounded by pressure orifices is divided into small incremental areas, ΔA, by subdividing the radius along each axis into a large number of increments, Δx and Δy.

Each element ΔA is then tested for its proximity to each pressure orifice and the assumption is made that the area, ΔA, experiences the pressure associated with the nearest orifice. In the example shown on figure 60, P_5 is the nearest orifice and thus the calculation

$$C_{P_5} \times \Delta A$$

is made. This process is repeated until the entire area has been treated and the overall average C_p is found from

$$C_{P_{avg}} = \frac{\Sigma \; C_p \Delta A}{\Sigma \; \Delta A}$$

This method, in effect, defines the total area influenced by each orifice. An example for one orifice is shown in the bottom sketch of figure 60. This area is defined by midpoints between P_5, in this case, and all the surrounding orifices. The area around P_5 is assumed to have pressure based on C_{P_5} over its entirety. Having calculated the average pressure, the computer program can then calculate the force, axial or normal, and the afterbody pressure drag coefficient can be determined by resolving the two components:

$$C_{D_{press}} = C_A \cos \alpha_{FRL} + C_N \sin \alpha_{FRL}$$

158
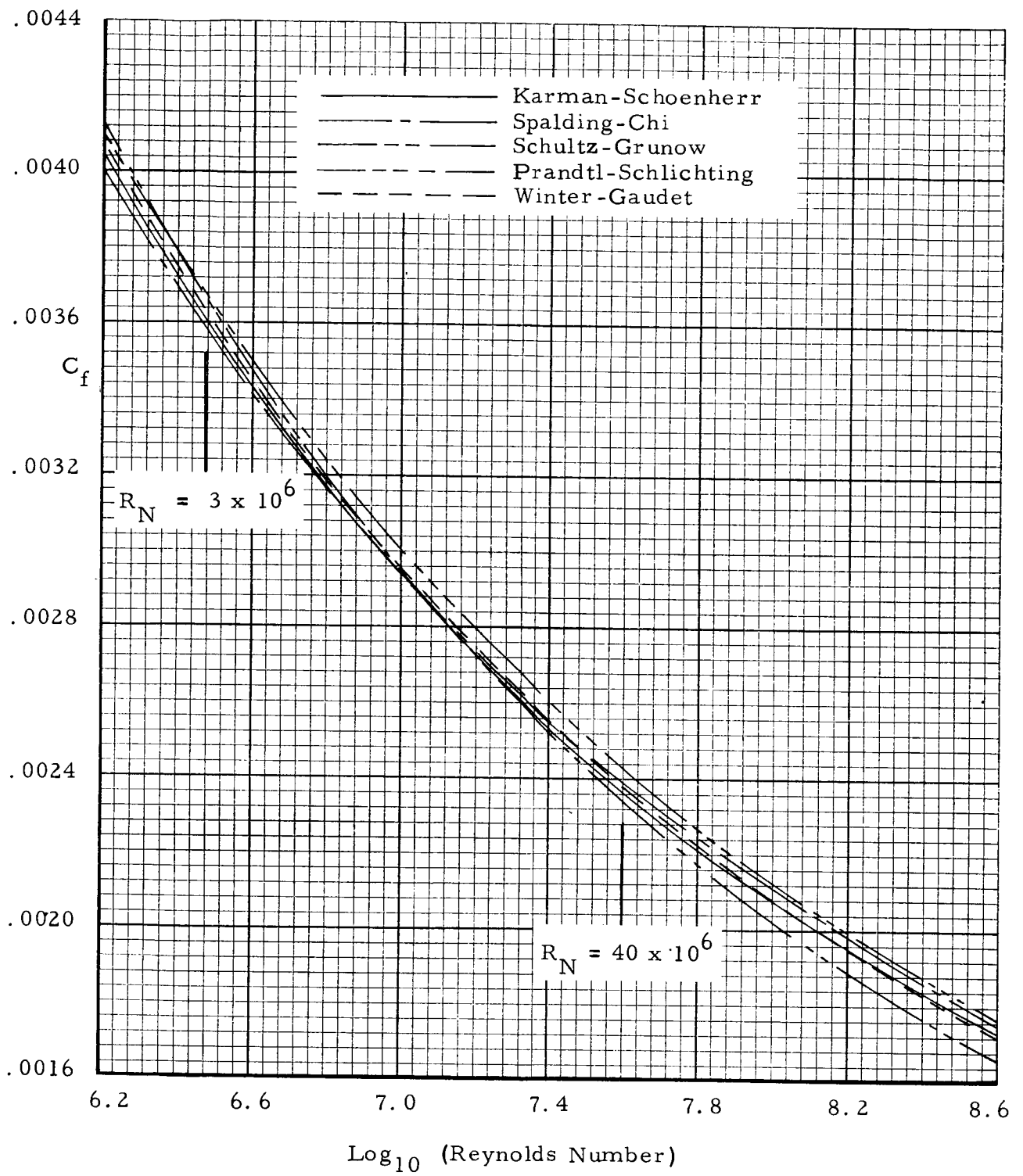
Figure 59. Comparison of Empirical Flat Plate Skin Friction
Formulae for Incompressible Turbulent Flow.
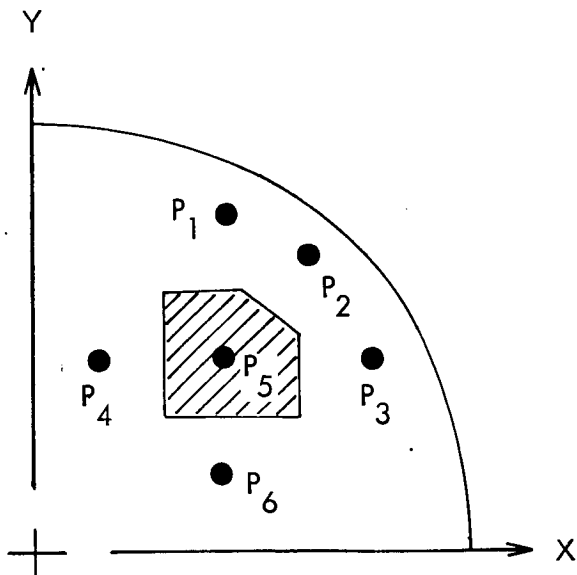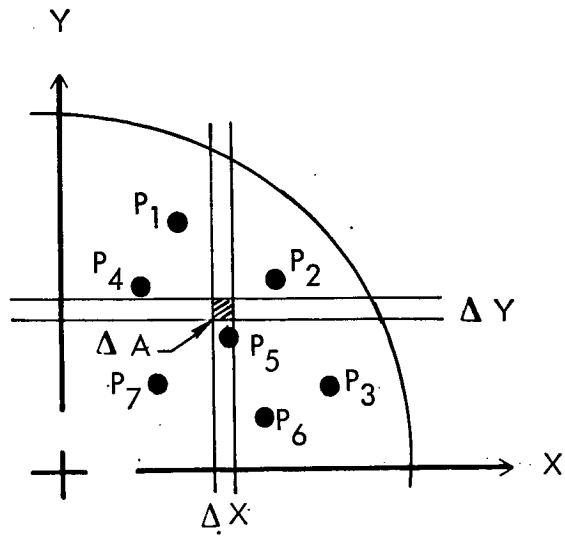
Figure 60. Elements of Fuselage Pressure Integration Technique

REFERENCES

1. Paterson, J. H.; Blackerby, W. T.; Schwanebeck, J. C.; and Braddock, W. F.: An Analysis of Flight Test Data on the C-141A Aircraft. NASA CR-1558, 1970.

2. Froude, W.: Experiments on Surface Friction Experienced by a Plane Moving Through Water. British Association Reports, 1872.

3. Gebers, F.: Ein Beitrag Zur Experimentellen Ermittlung des Wasser-widerstandes gegen bewegte Koerper. Schiffbau, Vol. 9, 1908.

4. Gebers, F.: Das Aehulichkeitsgesetz bei im Wasser geradlinig fortebewegter Platten. Schiffbau, Vol 22. Nos. 29-33, 35, 37-39, 1919.

5. Hughes, G.: Frictional Resistance of Smooth Plane Surfaces in Turbulent Flow. New Data and a Survey of Existing Data. Trans. Inst. Naval Architects, vol. 94, no. 4, Oct. 1932, pp 287-322.

6. Kempf, G.: Neuere Ergebuisse der Widerstandsforschung. Werft Reederei U. (Hafen), 1929.

7. Schoenherr, K. E.: Resistance of Flat Surfaces Moving Through a Fluid. Trans. Soc. Naval Architects and Marine Engineers, vol. 40, 1932, pp 279-313.

8. Falkner, V. M.: The Resistance of a Smooth Flat Plate with Turbulent Boundary Layer. Aircraft Engineering, vol. 15, no. 169, Mar. 1943.

9. Gibbons: Skin Friction of Various Surfaces in Air. First Annual Report of the NACA, 1915.

10. Wieselsberger: Untersuchungen ueber den Reibungswiderstand stoffbespannter Flaechen. Ergebnisse der Aerod. Versuchsanstalt Goettingen, Vol. I, 1925.

11. Jones, R.; and Williams, D. H.: The Profile Drag of Aerofoils at High Reynolds Numbers in the Compressed Air Tunnel. A.R.C. R&M, 1804.

12. Smith, Donald W.; and Walker, John H.: Skin-Friction Measurements in Incompressible Flow. NASA TR-R-26, 1959.

13. Winter, K. G.; and Gaudet, L.: Some Recent Work on Compressible Turbulent Boundary Layers and Excrescence Drag. Agardograph 97, 1966.

14. Hoerner, S. F.: Fluid Dynamic Drag. Second ed., S. F. Hoerner (Midland Park, N. J.), 1965.

15. Abbott, I. R.; Von Doenhoff, A. E.; and Stivers, L. S.: Summary of Airfoil Data, NACA Rept. 824, 1945.

16. Thwaites, B.: Incompressible Aerodynamics. Clarendon Press (Oxford), 1960.

17. Brown, C. E.; and Chuan Fan Chen: An Analysis of Performance Estimation Methods for Aircraft (Contract NAS1-5816) NASA CR 921, Hydronautics, Inc., Laurel, Maryland. 1967.

18. Squire, H. B.; and Young, A. D.: The Calculation of the Profile Drag of Airfoils. R&M 1818, Nov. 1937.

19. R.Ae.S. Data Sheets. Wings, 02.04.02,03.

20. Anon: C-141A Investigation of Wing Modifications to Delay Trailing Edge Separation Using a 0.044 Scale Model in the NASA Ames 11-Foot Transonic Tunnel. Lockheed-Georgia Company Report ER-7337, 1964.

21. Cebeci, T.; and Smith, A. M. O.: Calculation of Profile Drag of Airfoils at Low Mach Numbers, Journal of Aircraft, vol 5, no. 6, Nov. -Dec. 68.

22. Maddox, B. W.; and Honrath, J. F.: C-141 High Speed Wind Tunnel Investigation of a .0275 Scale Pressure Model, Phase II. Lockheed-Georgia Company Report ER-5075, 1963.

23. Anon: C-141A Aerodynamics Substantiating Data Report (Revised), Lockheed-Georgia Company Report ER-4982, 1961.

24. Young, A. D.: The calculation of the Total and Skin Friction Drags of Bodies of Revolution at Zero Incidence, A.R.C. R&M, 1874, April 1939.

25. R.Ae.S Data Sheets, Bodies. 02.04.01/2

26. Gyorgyfalvy, D.: Effect of Pressurization on Airplane Fuselage Drag. Journal of Aircraft, Nov. -Dec. 1965.

27. Bahr, W. C.; and Ferrill, R. S.: Engineering Flight Test Data Analysis Methods. Lockheed-Georgia Company Report ER-4936, 1963.

28. Hudson, W. G.: High Speed Wind Tunnel and Static Investigations of Nacelle Afterbody Configurations. Lockheed-Georgia Company Report ER-5080, 1962.

29. McDonald, H.; Hughes, P. F.: A Correlation of High Subsonic Afterbody Drag in the Presence of a Propulsive Jet or Support Sting. Journal of Aircraft, vol. 2, no. 3, Nov. 1964.

30. Goldstein, S., ed.: Modern Developments in Fluid Dynamics. Vol. II. Dover Publications, 1965.

31. Baker, G. S.: Notes on Model Experiments. North East Coast Inst. of Engineers and Shipbuilders, Translations. 1915.

32. Schlichting, H.: Boundary Layer Theory. Fourth ed., McGraw-Hill Book Co., Inc., 1960.

33. Schultz-Grunow, F.: New Frictional Resistance Law for Smooth Plates. NACA TM 986, 1941.

34. Spalding, D. B.; and Chi, S. W.: The Drag of a Compressible Turbulent Boundary Layer on a Smooth Flat Plate With and Without Heat Transfer. J. Fluid Mechanics, vol. 18, part 1, 1964, pp. 117-143.